THE MICROSTRUCTURE, MECHANICAL PROPERTIES AND SURFACE TRANSFORMATIONS OF A SYALON CERAMIC

by

Stephen Mason

A thesis submitted for the degree of Ph.D. to
The University of Warwick
Department of Physics

November 1988

CONTENTS

SUMMARY

The potential application of nitride based ceramics in structural applications is dependent on their performance at elevated temperatures. To meet these demands the microstructure of a syalon ceramic has been refined. Improved processing techniques, by the use of high purity powders and "balanced" compositions, have been shown to improve the degree of intergranular crystallisation. The key aspects are the reduction of impurity levels, particularly calcium, and the use of high nitrogen compositions such that full crystallisation is achieved. The achievement of complete crystallisation results in the elimination of subcritical crack growth during fracture and high temperature creep processes dominated by non-cavitational grain boundary diffusional processes.

The mechanism for oxidation has been identified by determination of the kinetics, surface and sub-surface reactions. A temperature limit of 1300°C has been identified by the reversion of YAG to a eutectic liquid by reaction with the SiO_2-rich oxidation layer. In this regime oxidation rates are determined by the YAG reversion and cation out-diffusion to the oxide layer. Oxidation effects have been shown to be responsible for the onset of sub-critical crack growth at temperatures above 1300°C, where crack extension results directly from YAG reversion effects.

Enhanced high temperature performance above and beyond 1300°C by surface transformation and surface coating was investigated. Surface microstructures based upon β' and Si_2N_2O have been shown to increase oxidation resistance upto 1375°C but are difficult to form without substantial surface degradation. Si_3N_4 and SiC coatings deposited by chemical vapour deposition (CVD) were found to have similar effects, increasing oxidation resistance beyond 1300°C.

Glossary

Chemical Vapour deposition (CVD) - reactive deposition of a solid material from gaseous precursors.

Fracture toughness - material parameter defining the resistance to crack initiation and propogation.

Hot isostatic pressing (HIP) - fabrication process in which densification is achieved by the simultaneous application of high isostatic pressures and temperature.

Janecke prism - schematic three-dimensional phase representation of a 5 component system e.g. Y-Si-Al-O-N.

LCS 201 - tradename for yttrium sialon marketed by Lucas-Cookson-Syalon.

Modulus of rupture - stress value at which there exists a 50% failure probability.

Polytype - layered structure which preserves a constant chemical composition but differs in the way the atomic layers are stacked.

Polytypoid - polytype structure where both composition and unit cell dimension exhibit a systematic variation with structure type.

Sintering - thermally activated particle agglomeration.

Sintering, liquid phase - agglomeration by capillary action of a liquid, and diffusion through that liquid.

Weibull parameter (m) - a measure of the variation of a set of statistical data.

YAG - yttrium aluminium garnet, $Y_3Al_5O_{12}$.

List of Figures

CHAPTER ONE

CHAPTER TWO

CHAPTER THREE

CHAPTER FOUR

CHAPTER FIVE

CHAPTER SIX

CHAPTER SEVEN

CHAPTER ONE - INTRODUCTION AND OBJECTIVES

In this first chapter, the concept of engineering with ceramics at high temperatures will be introduced. The historical background outlining the basic motivations behind the development will be discussed, defining the major areas of application for such materials, with an indication of the level of world commitment. The principle ceramic contenders for high temperature engineering applications will be defined leading into an introduction to Silicon Nitride and Sialon ceramics. Finally, the objectives of this research project are presented.

1.1 The Need for Engineering Ceramics

Advances in the use of metals in structural and engineering applications are limited by their intrinsic high temperature properties. As a result of this, much interest has been generated over the past decade into the development of new materials which may partially or totally replace existing metallic components. Of the many possible fields of application, the development of alternative materials for use in diesel and gas turbine engines has become one of the major goals (figure 1.1). The principle motivation for such a development stems from the world oil crises of 1973 and 1979. Large increments in fuel prices, and the projected shortages of oil in the next century stimulated the design and development of engines which would operate more efficiently, in order to reduce the dependence of the industry on the variations of the world oil market.

The current generation of gas turbine engines, using superalloy components, are limited to maximum surface temperatures of 900°C-1000°C (1). Any improvements gained by increasing the operating temperatures are limited by the subsequent need to force cool the metallic

Figure 1.1 The Rolls-Royce Gem 60 turboshaft demonstrator engine used to develop ceramic materials.

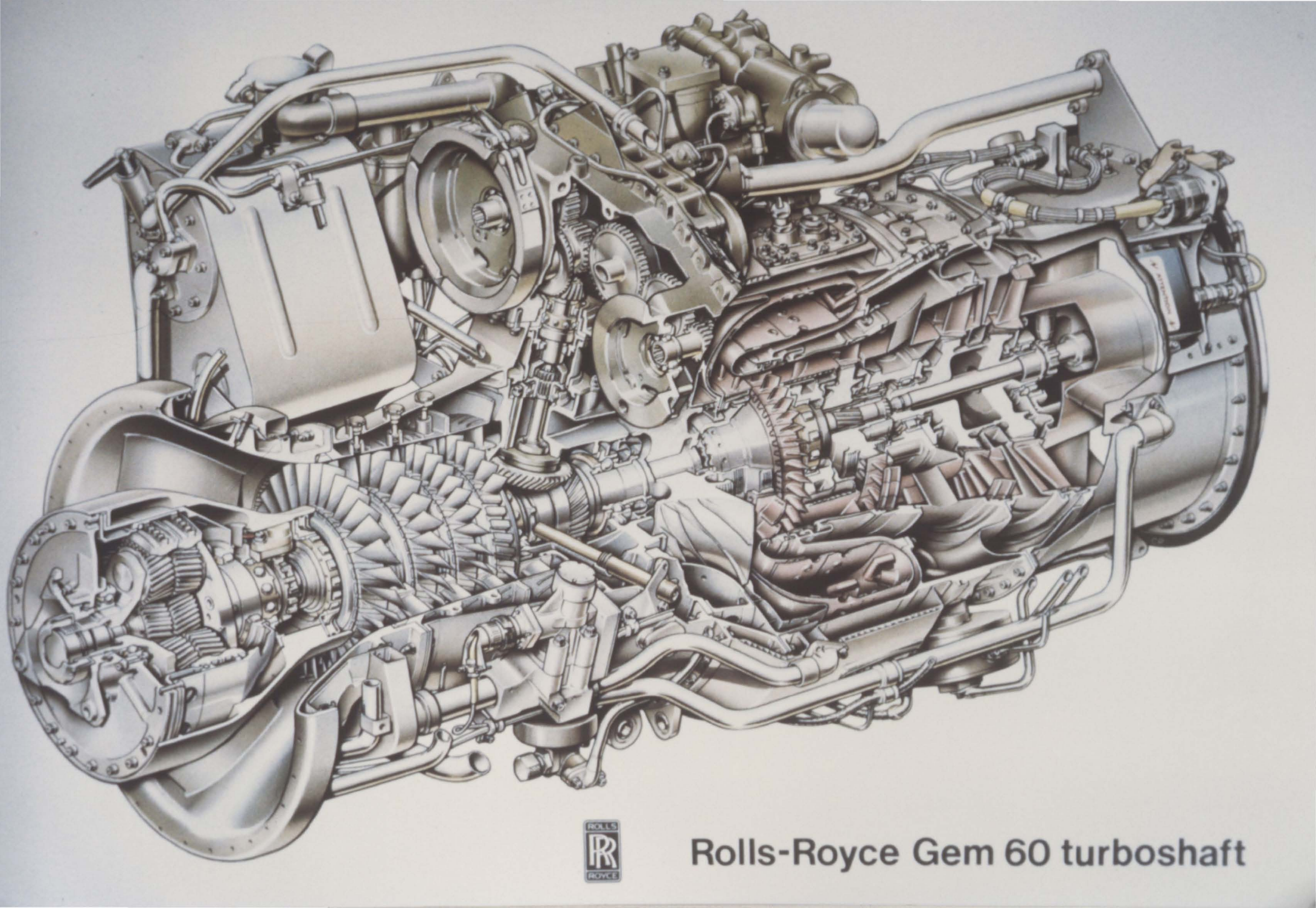

Rolls-Royce Gem 60 turboshaft

components, resulting in a loss of the overall efficiency. In addition high operating temperatures increase the possibility of component failure as a result of plastic deformation or chemical attack. With projected operating temperatures for gas turbines in development for the 1990's exceeding 1375°C, it became apparent at a very early stage that alternative materials would have to be considered and developed for the next generation of engines.

It was already well known that ceramics showed the desired properties required for such a material (2,3,4) i.e.

(i) High decompositional temperature

(ii) High oxidation resistance

(iii) Good thermal shock resistance

(iv) Low coefficient of friction

(v) High elastic modulus to specific gravity ratio

(vi) Low thermal expansion coefficient.

The advantages of using such a material are numerous. Due to the refractory nature of these materials, much higher operating temperatures without the need for elaborate cooling systems appeared possible, resulting in an overall increase in efficiency and power output (figure 1.2). In addition to gains in fuel efficiency, the substitution of ceramic components for superalloys would reduce the industry's critical dependence on the scarce and expensive raw materials used in the current generation of superalloys. Some materials used in nickel based superalloys, such as hafnium are extremely scarce, and cost in excess of £100,000/tonne! Many ceramics are based upon more abundant and cheaper materials such as silicon and aluminium, reducing both the basic cost for materials and the manufacturers' sensitivity to variations and shortages in the world market, resulting ultimately in a more cost effective product.

Figure 1.2 The increases in efficiency and power output possible by the application of ceramic materials in gas turbine engines.

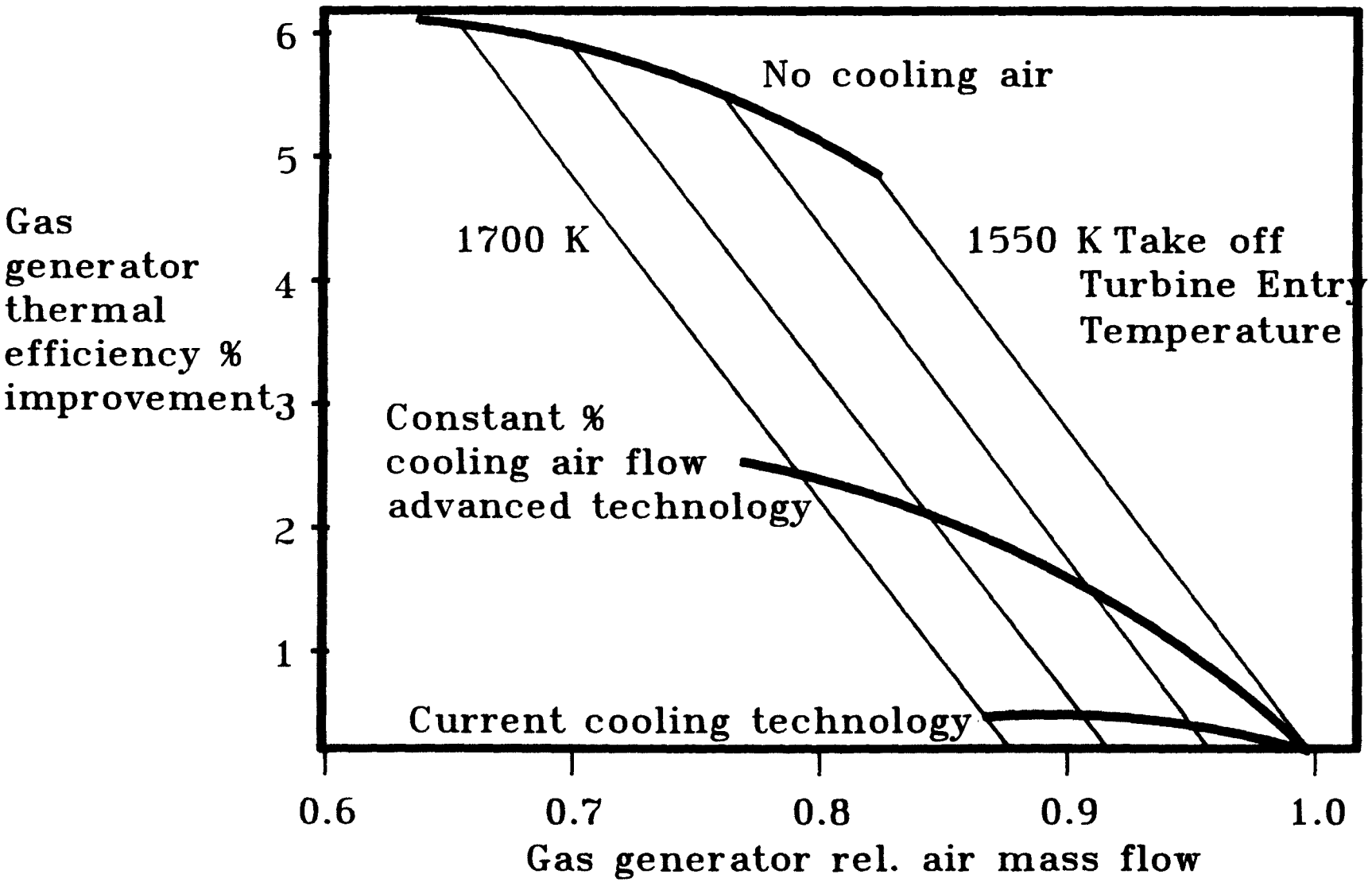
Gas generator thermal efficiency % improvement
6
5
4
3
2
1
No cooling air
1700 K
1550 K Take off Turbine Entry Temperature
Constant % cooling air flow advanced technology
Current cooling technology
0.6
0.7
0.8
0.9
1.0
Gas generator rel. air mass flow

The development of engineering ceramics has been accelerating rapidly over the past decade. Much research is centred in the United States (5) and Japan (6,7) where in the former, large scale projects initiated by the US Government's Advanced Research Projects Agency, finance the Army Materials and Mechanics Centre (AMMRC) and the Ford Motor Company into the development of high temperature gas turbine engines. The funding associated with this project and others over the past decade has been of the order of $250 million with at least this amount already committed for the next. In Japan, ceramic development has grown to the degree that currently one-half of the current world production is now centred there (8). The United Kingdom, once a world leader in this field, now has fallen behind from substantial reductions in research and development commitment during the 1970's, now having only modest programmes compared with the US, Germany or Japan. The research efforts around the world have resulted in the establishment of the appropriate methods for powder processing, densification, and better definition of the requirements, capabilities and limitations of materials under trial in severe environments.

Traditionally, the majority of ceramic development has been in the field of monolithic ceramics eg. alumina, silicon carbide, silicon nitride. However, recent technological developments have re-established the field of fibre-reinforced ceramic composites as a contender for gas turbine applications (9). Therefore, current development can be categorized into two distinct areas:

(i) Monolithic ceramics

(ii) Ceramic composites.

1.2 Monolithic ceramic contenders for engineering applications

It was quickly discovered that many of the desirable properties required for the development of ceramic components for diesel or gas

turbine engines were to be found in a large number of metal oxide, carbide and nitride ceramics. However, of the wide range of ceramics available, those based on silicon nitride, silicon carbide and aluminium oxide have shown the greatest potential. A comparison of properties of a wide range of heat engine contenders can be found in figure 1.3.

1.2.1 Aluminium oxide (Alumina) based ceramics: These exhibit good corrosion and oxidation resistance and a high decompositional temperature (~2045°C). This has meant that alumina ceramics have already found wide application in industry, as a replacement to cemented Titanium Carbide (TiC), being widely used for the high speed machining of cast iron. However, the poor thermal shock resistance and its inadequate toughness has severely restricted development in a wider range of applications, including heat engine design.

1.2.2 Silicon Carbide (SiC) based ceramics: These ceramics have recently found limited success as structural components in the development of advanced heat engines. Silicon Carbide may be fabricated to a fully dense ceramic (10) by hot-pressing (HP-SiC), sintering (S-SiC), and by a form of reaction sintering between Silicon Carbide and silicon in the vapour phase -siliconised Silicon Carbide (Si-SiC). The general properties of Silicon Carbide ceramics are summarised in figure 1.3. Densification to near full theoretical density requires the use of sintering aids, usually Boron Carbide (B_4C) or Alumina (Al_2O_3) (11), the former resulting in a more deformation resistant grain boundary, a factor desirable for the mechanical properties at elevated temperatures. However, B_4C also promotes grain growth during sintering, resulting in an overall reduction in strength. Alumina, on the other hand, inhibits grain growth, leading to an increase in strength, but leaves an amorphous residual alumino-silicate grain boundary phase, an important factor in the degradation of the high temperature mechanical properties.

Figure 1.3 A comparison of properties of a range of materials used in engineering applications.

MATERIAL	Crystal Structure	Theoretical Density (g/cm^3)	Transverse Rupture Strength (MPa)	Fracture Toughness (MPam)	Poisson Ratio	Youngs Modulus (GPa)	Thermal Expansion ($10^{-6}K^{-1}$)	Melting or Decompositional Temp (^oC)
Si_3N_4	α-hexagonal β-hexagonal	2.7-3.3	250-1000	3.6-6.0	0.24	138-304	3.0	1897(d)
SiC	α-hexagonal β-cubic	3.2	250-600	2.6-5.0	0.19	207-483	4.3-5.6	2723(d)
Mullite	Orthorhombic	2.8	185	2.2	0.25	145	5.7	
Al_2O_3	Hexagonal	3.97	270-1000	2.7-4.2	0.26	380	7.2-8.6	2027(d)
PSZ	Cubic, monoclinic tetragonal	5.7-5.75	600-700	8-9	0.23	205	8.9-10.6	2680(m)
FSZ	Cubic	5.56-6.1	245	2.8	0.23-0.32	97-207	13.5	
Glass Ceramics	Variable	2.4-5.9	70-350	2.4	0.24	83-138	5-17	Variable
TiC	Cubic	4.92	241-276	-	0.19	430	7.4-8.6	
TiB_2	Hexagonal	4.5	700-1000	6-8	0.09-0.13	514-574	8.1	
Graphite	Hexagonal	2.21	0.48-207	0.5-1.8	0-0.22	1.4-34.5	0.1-19.4	
Cast Irons	Cubic	5.5-7.8	90-1186	37-45	0.17	83-211	8.1-19.3	

Fig. 1.3 Comparison of properties of heat engine and common ceramic materials.

The strength characteristics of silicon carbide ceramics are generally intermediate to those of its rivals (Si_3N_4 and Al_2O_3). SiC ceramics show superior microstructural stability, oxidation/corrosion resistance (12) and creep resistance (13,14,15), mainly being due to low volumes of sintering additive and high purity of powders. Fracture toughness levels in silicon carbide are relatively low (~3-4 $MPam^{\frac{1}{2}}$) (16), often as a result of factors such as grain size and anisotropy, as a result of processing. The low toughness levels have posed questions about its suitability for engineering applications, however, excellent high temperature stability coupled with a lack of slow crack growth at elevated temperatures (17) has made it a contender for use at temperatures in excess of 1300°C.

1.2.3 Toughening of ceramics using Zirconia (ZrO_2) additions: Zirconia based ceramics in many differing forms are currently being assessed for application in heat engines, predominantly in low temperature (~1000°C), high stress applications. One specific class of material partially stabilised zirconia (PSZ) (18,19) has been of particular interest for three reasons (i) highly refractory (ii) very low thermal conductivity (iii) dramatic increase in fracture toughness derived from a process known as transformation toughening.

The toughening effect is derived from the ability to control crystal structure transformations by the addition of impurities such as Y_2O_3, MgO, or CaO for instance. The mechanisms for transformation toughening have been reviewed by Lewis (20) and will not be presented in detail. The toughening process mechanism generally involves a stress induced tetragonal-to-monoclinic transformation accompanied by a volume expansion. This generates stress fields in the transformed region generating microcracks, resulting in a dramatic increase in fracture toughness, fracture energy and strength. Increases in strength of ceramics which have been transformation toughened have been

observed compared with monolithic cases. The precise mechanism relating the transformation process to the increase in strength is not well understood and is subject to many explanations including crack deflection, branching or energy absorption by the transformation process itself. Whatever the mechanism, the transformation toughening has been successfully used to increase the strength in a range of monolithic ceramics including ZrO_2, Al_2O_3 and Si_3N_4.

1.3 Ceramic composites

The strengthening of monolithic ceramics by addition of fibres and whiskers within the structure has been the growing focus of widespread investigation over recent years (9,20). Much interest in these composite ceramics has been motivated by the relatively poor strength and toughness exhibited by the current monolithic ceramics, coupled with the emergence of new, small diameter (~10μm), high strength fibres and whiskers such as SiC and Si_3N_4.

The emergence of new ultra-fine single crystal whiskers has provided the necessary technology to now reevaluate the potential that ceramic composites have in the field of high temperature engineering ceramics. Of the range of whiskers available, oxide based materials were found unsuitable due to the high reactivity in the presence of silicate liquids. α-Silicon Nitride is also unstable in silicate liquids at temperatures in excess of 1000°C, leaving β-SiC whiskers, which is due to their high oxygen resistance, high strength, and low reactivity as the most promising development.

Fabrication of a ceramic with a whisker reinforced matrix follows a similar route to that for monolithic ceramics - ceramic

powders/whiskers are intimately mixed, compacted and sintered. Hot die pressing has been found to promote preferential whisker orientation, resulting in an anisotropy in the strength characteristics. However, alternative methods, ie pressureless sintering, hot isostatic pressing may be employed to produce a fully dense composite with properties desirable for engineering applications.

Investigations into whisker reinforced ceramics has shown useful improvement (20) in the levels of fracture toughness, K_{IC}, (typically 2-4x the monolithic values), and Weibull modulus, m, (upto 2-3x the monolithic values). However, the addition of the reinforcing phase has been seen to have minimal effect on the strength of the materials, being due to a compromise between the increase in the K_C value and the influence of whiskers as critical flaws. Although the increases in strength characteristics indicate the potential usefulness of these materials in engineering applications, the high temperature properties have yet to be proven especially under severe environmental conditions where whisker-matrix interface reactivity and dependence on high stresses have yet to be investigated.

The second class of ceramic composite currently under development utilise semicontinous fibres as a means of toughening (21,22). These composites offer the potential for 'pseudo-plastic' behaviour, ie large strains to failure by a load transfer mechanism during matrix microcracking, and an insensitivity to flaws when compared to monolithic ceramics. However, the lack of a suitable high temperature fibre and experience in composite fabrication are currently the two major reasons hindering further development of this class of materials.

1.4 Silicon Nitride and the development of Sialon ceramics

Silicon Nitride based ceramics have shown the optimum properties desired for application to heat engine design, and have become the most highly developed of all the engineering ceramics discussed. Figure 1.4 summarises the prospective areas of application for this range of ceramics. The principle goal for the development of this family of ceramics is for advanced turbine engines where potential uses include turbine blades, shroud rings, blisks and gas bearings, examples of which are shown in figure 1.5. A review of the development of Si_3N_4 and Sialon ceramics will be presented in Chapter 2.

1.4.1 Crystal structure of Silicon Nitride

Silicon Nitride (Si_3N_4) exists in two distinct crystallographic forms, α- and β-Si_3N_4, built up of covalently bonded SiN_4 tetrahedra joined at the corners, forming a three dimensional network (figure 1.9). β-Si_3N_4 is formed form the stacking of successive hexagonal layers along the c-axis to give a stacking sequence ABABAB... with lattice parameters a=7.608Å and c=2.911Å (figure 1.6(b)). The atomic arrangement of β-Si_3N_4 is in fact consistent with the structures of beryllium silicate (Be_2SiO_4) and zinc silicate (Zn_2SiO_4), indicating the simple principles of silicate crystal chemistry also apply to the nitride family (23). α-Si_3N_4 exhibits a similar structure to the β form, but has an elongated c-axis dimension due to a 180° rotation of two basal stacking planes, giving a stacking sequence ABCDABCD...., and a unit cell dimension a=7.753Å and c=5.617Å. It has been suggested (24) that α-Si_3N_4 is in fact a defect structure, where approximately 1 in 30 nitrogen atoms is replaced by an oxygen atom, with an equivalent number of silicon sites remaining vacant to maintain overall charge neutrality.

Figure 1.5 Areas of application for silicon nitride ceramics

a) Shroud rings

b) Bearings

c) Turbine blades

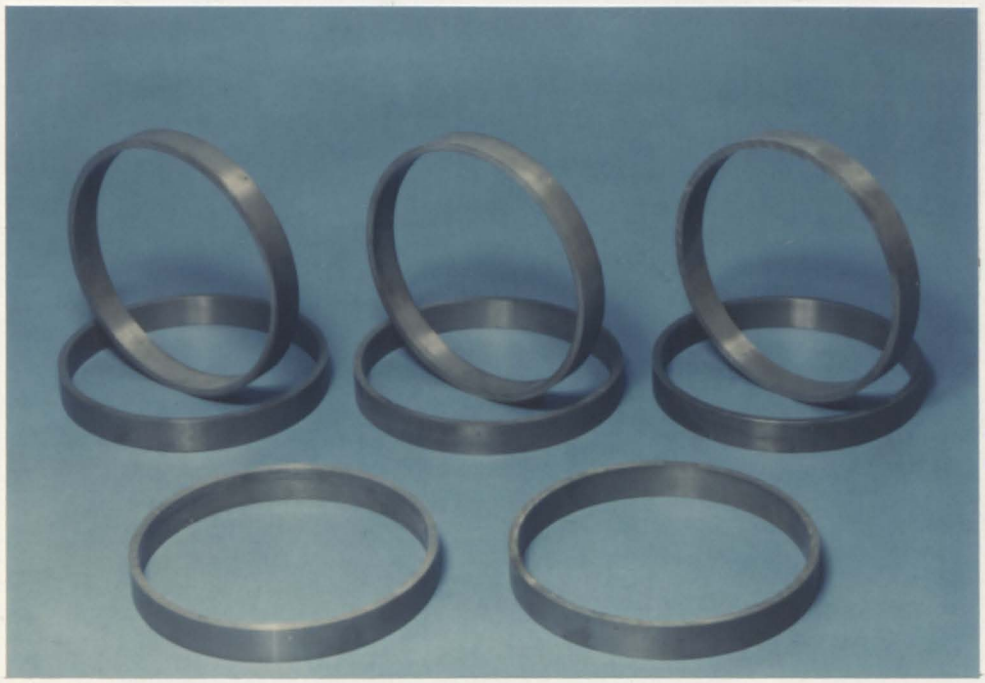

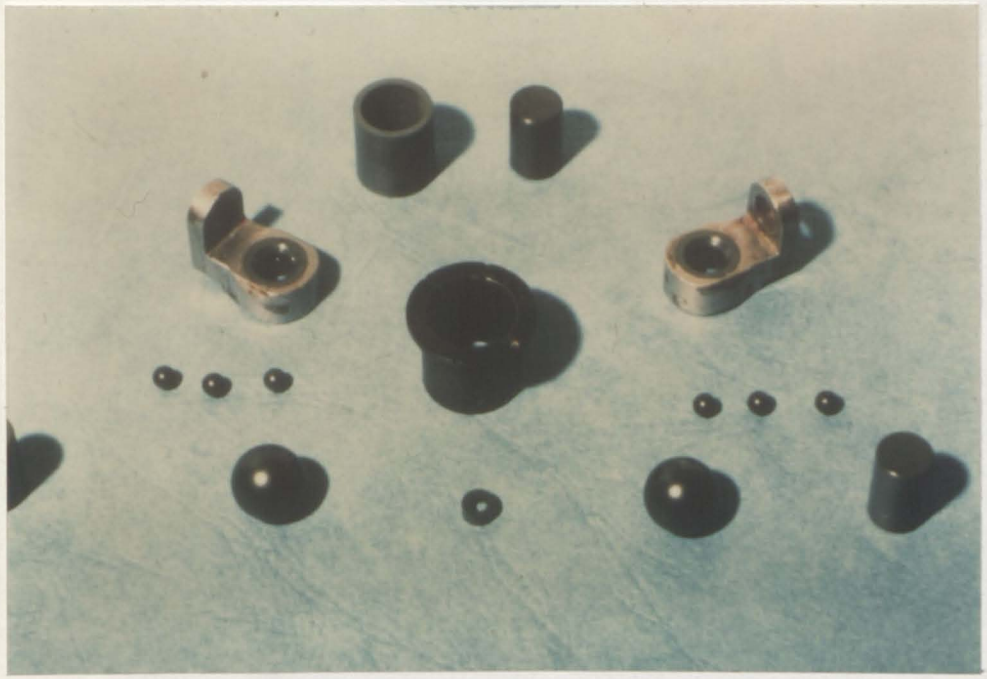

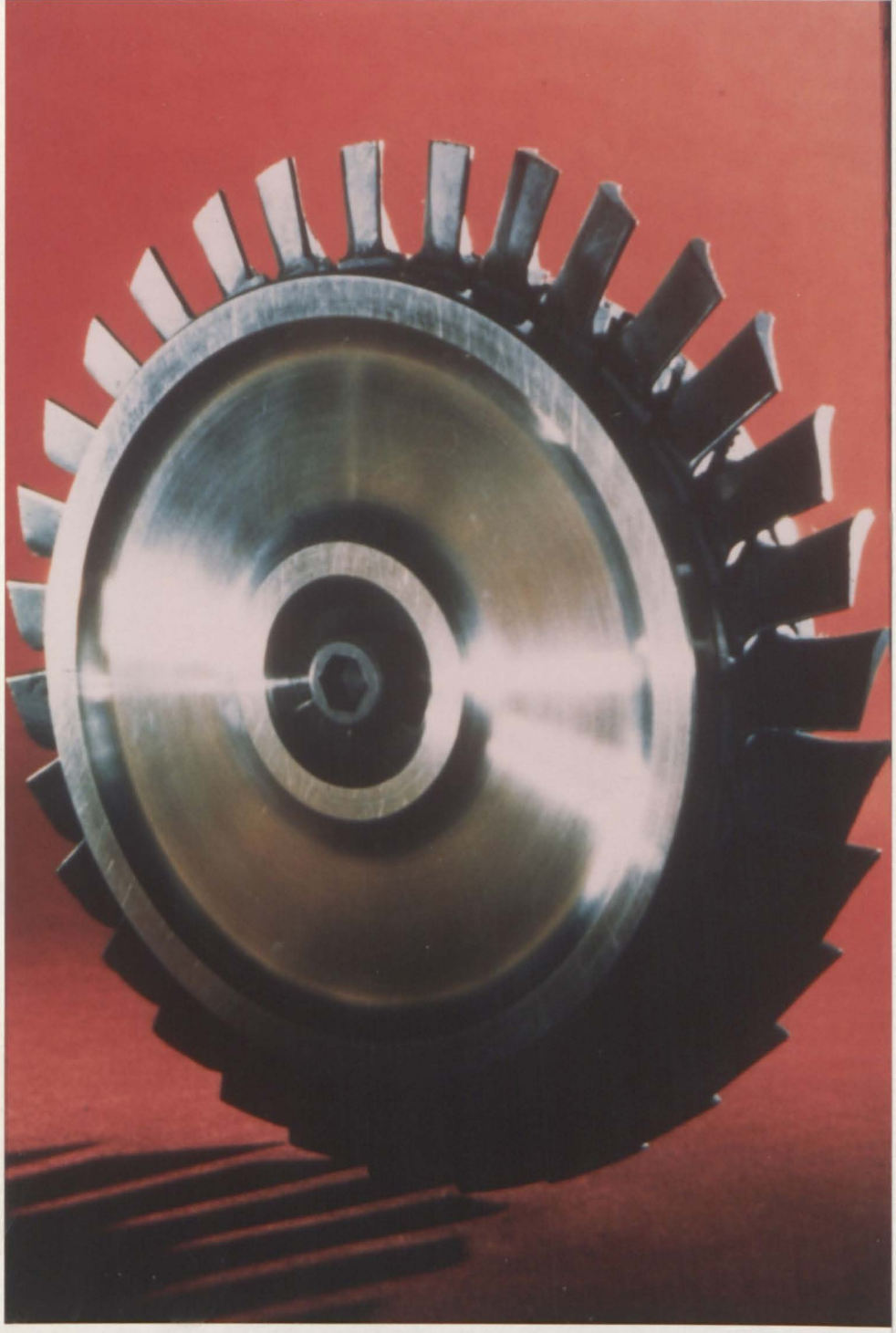

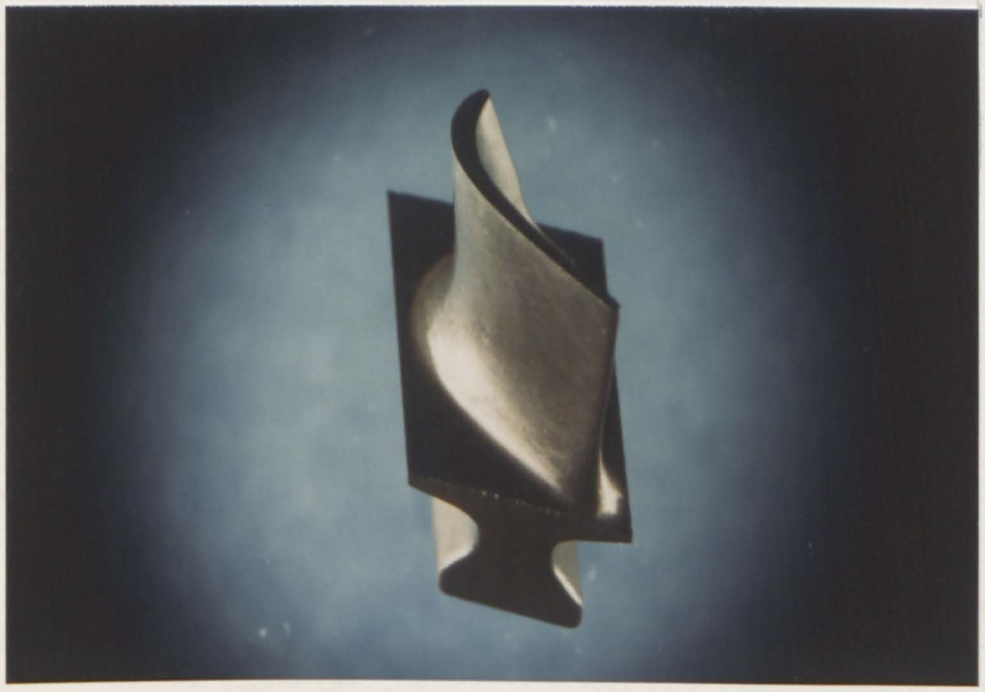

Figure 1.6 The relationship between the α and β silicon nitride crystal structures.

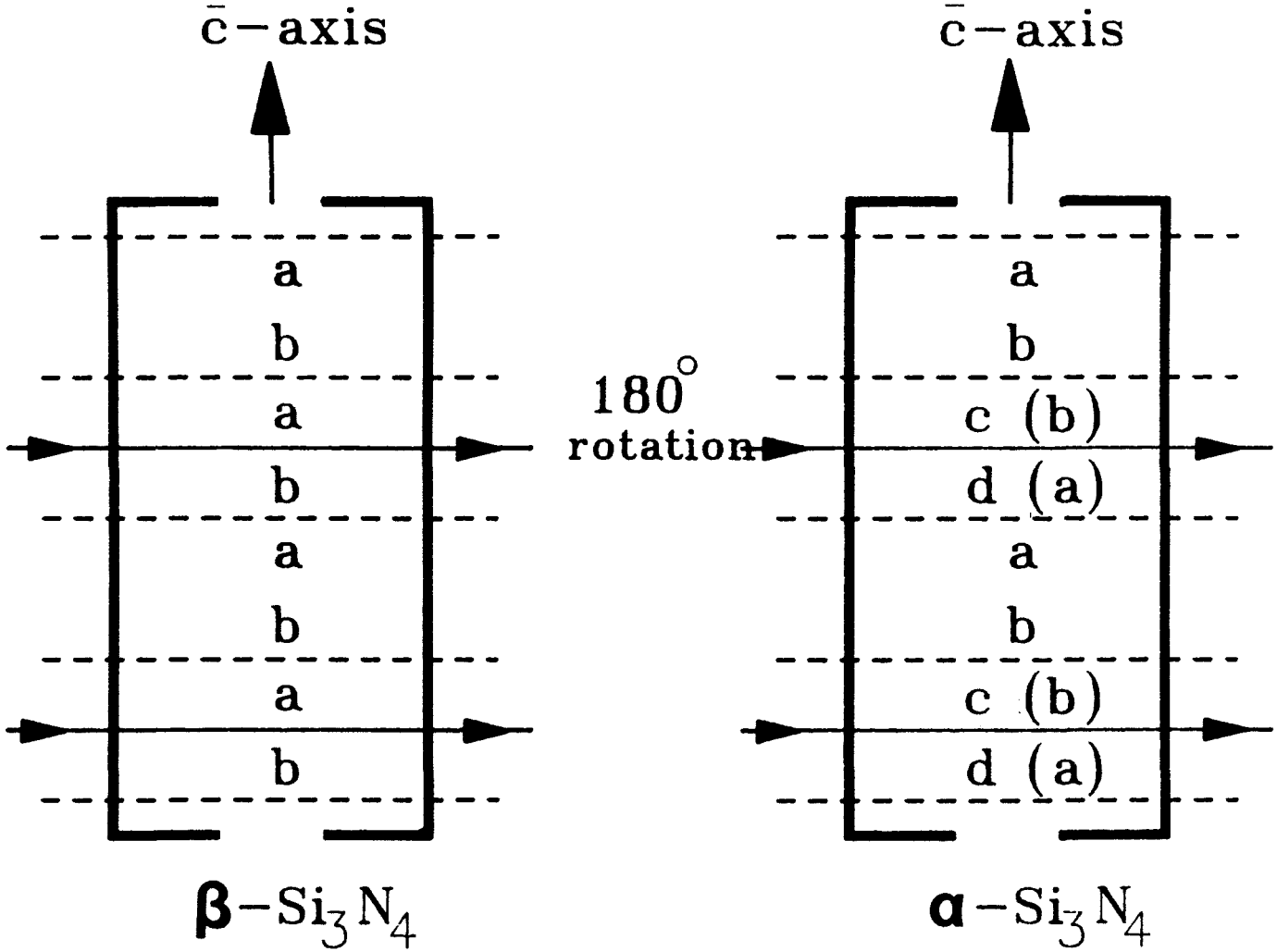

Figure 1.6 The relationship between α and β silicon nitride crystal structures.

1.4.2 Fabrication and sintering of Silicon Nitride

Silicon Nitride does not occur naturally. Ultra-fine silicon nitride base powders are produced commercially by various different processes. Traditionally, the powder was produced by the direct nitridation of silicon metal powder (25). This process occurs spontaneously at temperatures above 1100°C, producing mainly α-Si_3N_4 in the form of fine whiskers. However, several problem areas exist in the process. Firstly, silicon like many other pure metals, spontaneously oxidises at room temperature, forming a protective SiO_2 layer on the particle surface, of the order of 3nm in thickness. This acts as a barrier to both diffusion of nitrogen to the silicon surface, and volatilisation of silicon away from the grain, inhibiting nitridation. Secondly, due to the sluggish nature of the nitridation process, a catalyst is often necessary to aid the reaction, usually iron (26,27). Some of the iron is found to remain after powder manufacture, forming iron silicides upon sintering, resulting in a degradation in the ceramic properties. Other impurities often found as a result of powder processing are calcium, fluorine, all of which have been shown to degrade properties. Recently, alternative powder production routes have been developed (28,29,30) to a commercial level which provide powders of exceptional purity and physical form.

One major problem associated with the the development of silicon nitride ceramics has been the problem of fabricating a fully dense material. Due to the highly covalent nature of the bonding in silicon nitride, the self diffusivity is low, and densification does not take place under normal circumstances (31,32). The use of combinations of high temperatures and pressures (~5GPa) including explosive compaction (33,34,35) have caused some densification of pure Si_3N_4 powders, but all have proved unsuccessful in obtaining full densification.

Early production of silicon nitride ceramics was by 'reaction-bonding' or 'reaction-sintering' (36,37,38,39) where the required shape is cast from commercial grade silicon powder, 'pre-sintered' at temperatures of approximately 1200°C in argon. After the pre-sintering process, the compact is machined to the shape and dimensions of the required product, and heated to a temperature in the range 1200°C-1450°C in nitrogen at atmospheric pressure, when the reaction-bonding process takes place. During this final process, very little change in dimension occurs, so that very close tolerances, approximately 0.1%, on the dimensions of the component may be obtained. Recently, methods such as slip casting, injection moulding, extrusion and die pressing have been developed, enabling the silicon compact to be formed directly to the component size and shape, reducing the need for expensive machining. Reaction-bonding of Si_3N_4 produces a ceramic with ~25% porosity, a major factor which excludes this type of material from applications at high temperatures and stresses.

Fully dense Si_3N_4 ceramics were first produced by 'hot-die pressing' silicon nitride powder under moderate loads at temperatures up to 1700°C (40). This was acheived by the addition of sintering aids, usually metal oxides and some nitrides (usually Y_2O_3(41,42,43), MgO(44,45), Sc_2O_3(46), Ce_2O_3(47,48), Li_2O(49) and ZrO_2(50)). Densification is a result of the formation of a liquid phase by the reaction of the metal oxide additive with all constituents above a eutectic temperature, figure 1.7(b) ie

$$\alpha\text{-}Si_3N_4 + SiO_2 + M(\text{metal oxide}) + \text{contaminants} \rightarrow \beta\text{-}Si_3N_4 + \text{liquid} \qquad (1.1)$$

The SiO_2 is derived from the oxide layer present on all Si_3N_4 powders. The type and amount of contaminants is generally a function of the powder manufacturing route, iron and calcium being the most common. The mechanism for sintering of silicon nitride ceramics may therefore

be described as the simultaneous solution- reprecipitation of particles as proposed by Kingery (51). The three main stages proposed by the model are summarised in figure 1.7(a) (54):

1. Particle rearrangement following the formation of the liquid phase. The rate and extent of shrinkage is dependent on the viscosity and volume of the liquid.

2. Solution-precipitation: solid particles react and are dissolved into the liquid. α-β transformation begins, and the volume change is given by

$$\frac{\Delta v}{V_o} \alpha\ t^{-1/n} \qquad (1.2)$$

where t is time.

If n=3 then the rate controlling step is solution/ precipitation, or if n=5 the rate is controlled by diffusion through the liquid.

3. Solid-solid interaction: Ostwald ripening, liquid phase sintering effectively ceases, residual porosity is removed, and theoretical density is achieved.

The resultant ceramic, known as hot-pressed silicon nitride (HPSN), was found to be multiphase, consisting of small equiaxed β-Si_3N_4 grains surrounded by a continuous glassy phase, a residue of the sintering liquids, distributed along the grain boundaries and triple junctions (52). This grain boundary phase acts as a sink for the metallic ions used as sintering additions (Mg, Mn etc) and any impurity atoms (eg Fe, Ca) which may be present, and has been shown to drastically effect the high temperature properties (53) of the ceramic (oxidation, fracture, strength and creep resistance). A discussion of these effects will be presented in Chapter 2.

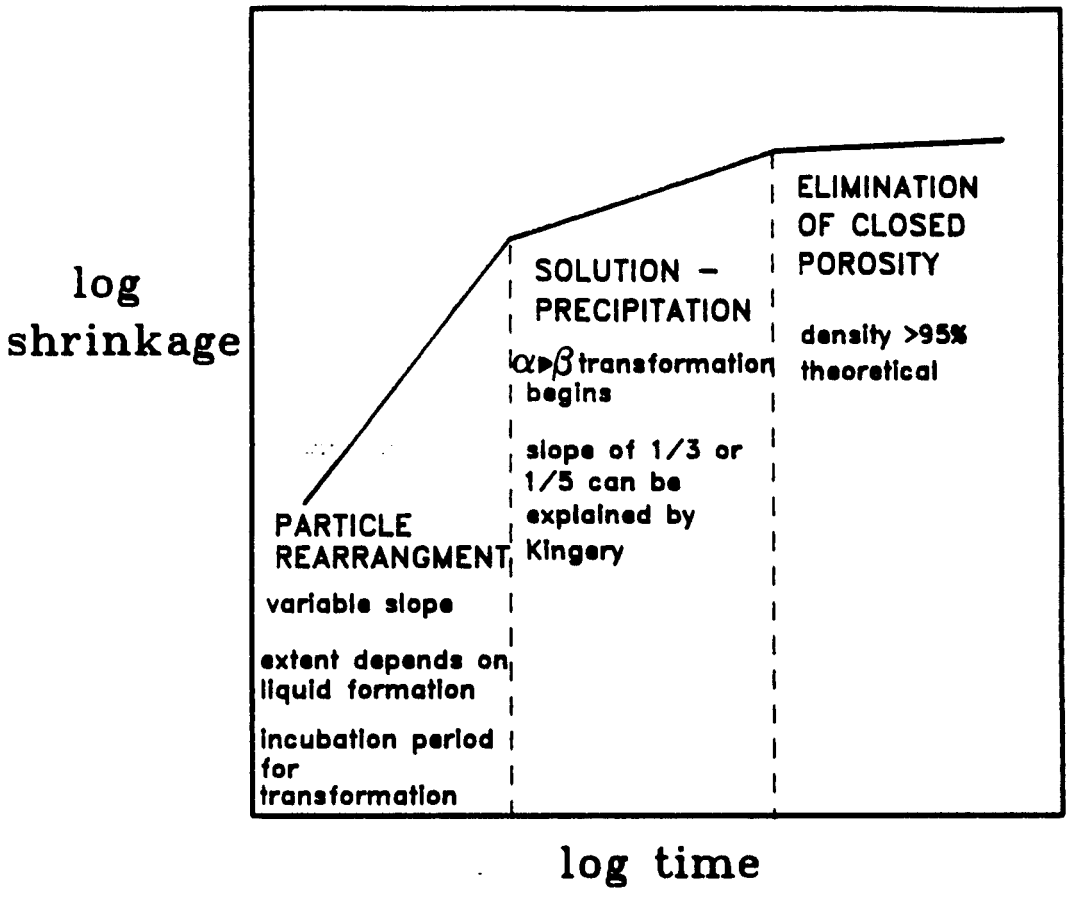

Figure 1.7(a) Kingery model plot for sintering of nitrogen ceramics

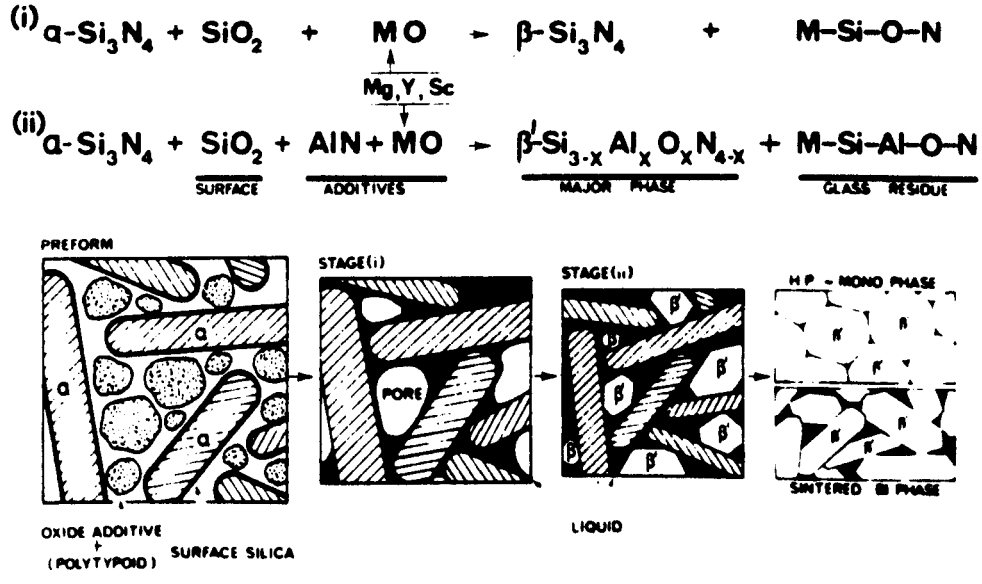

Figure 1.7(b) Schematic representation of the sintering mechanism in nitrogen ceramics

Although the hot-pressing of silicon nitride produced fully dense ceramics, the method suffered from various limitations. Firstly, the process is limited to the production of simple shapes only. As many components required were complex in shape, ie gas turbine rotor blades, expensive machining would be required to form the final article. Secondly, the application of a uniaxial load during fabrication results in preferred directional grain growth, leading to an anisotropy in mechanical properties.

In an effort to alleviate these problems, pressureless sintering has been adopted as an alternative fabrication method to uniaxial pressing. However, without the aid of pressure to assist the densification, as in the case of HPSN, larger sintering liquid volumes are necessary. Simply increasing the sintering temperature to enhance the densification kinetics results only in rapid decomposition of the silicon nitride with evolution of SiO and N_2.

The sintering aids appropriate for use for the pressureless sintering of silicon nitride are essentially those described for HPSN earlier. All form a low temperature eutectic liquid and hence reduce the liquid viscosity at the sintering temperature. Densification is then attained by enhanced atom transport in the low viscosity liquid.

In comparison to hot-pressed silicon nitrides where residual liquid volumes are ~1%, residues of liquid in pressureless sintered Si_3N_4 are significantly greater, up to 15% in extreme cases, amplifying the degradation effects at high temperatures (55). Although greater flexibility in shape is allowed by the use of pressureless sintering technique, shrinkage variations during fabrication has resulted in the requirement for machining to final dimensions. This coupled with the desire to reduce residual glass volumes has recently stimulated investigations into alternative fabrication methods.

One such method, which is having reasonable success in the formation of silicon nitride ceramics with reduced additive levels is Hot Isostatic Pressing (HIP) (56,57,58,59,60). In this process, the compacted premoulded powder, which may or may not be encapsulated in a silica (SiO_2) envelope, is subjected to both high temperature (~1800°C), and high isostatic pressure using a gas transfer medium. Pressures used are commonly in the region of 70-300 MPa, compared with 15-30 MPa employed in uniaxial hot-pressing. The resulting ceramic is virtually pore free, with minimal residual glass phase, in a near finished shape, precluding the need for expensive post sintering machining. The structure and properties of HIP'ed Si_3N_4 will be briefly discussed in Chapter 2.

1.4.3 Ceramic alloying and the development of Sialon ceramics.

It was suggested (61) that it was possible to substitute N^{3-} atoms by O^{2-} atoms in the Si_3N_4 structure, if at the same time Si^{4+} was replaced by Al^{3+} to maintain overall charge neutrality. This predicted a whole new variety of ceramics based upon the Si-Al-O-N system, and were subsequently discovered simultaneously both in England (62) and Japan (63) in 1971. These materials, known by the acronym 'sialon' or 'syalon'* (4,64) are based upon the aluminium substituted α and β forms of silicon nitride, α' (alpha prime), and β' (beta prime) respectively, having an expanded hexagonal structure similar to Si_3N_4 (65) with only a small increase in a and c parameters, depending on the level of aluminium substitution into the structure, figure 1.8.

β'-Sialons may be fabricated by sintering suitable mixtures of α-Si_3N_4 and Al_2O_3. However, this approach was found to result in the formation of residual glass at the grain boundaries (66), as a result

---

* Trademark of Lucas-Cookson-Syalon.

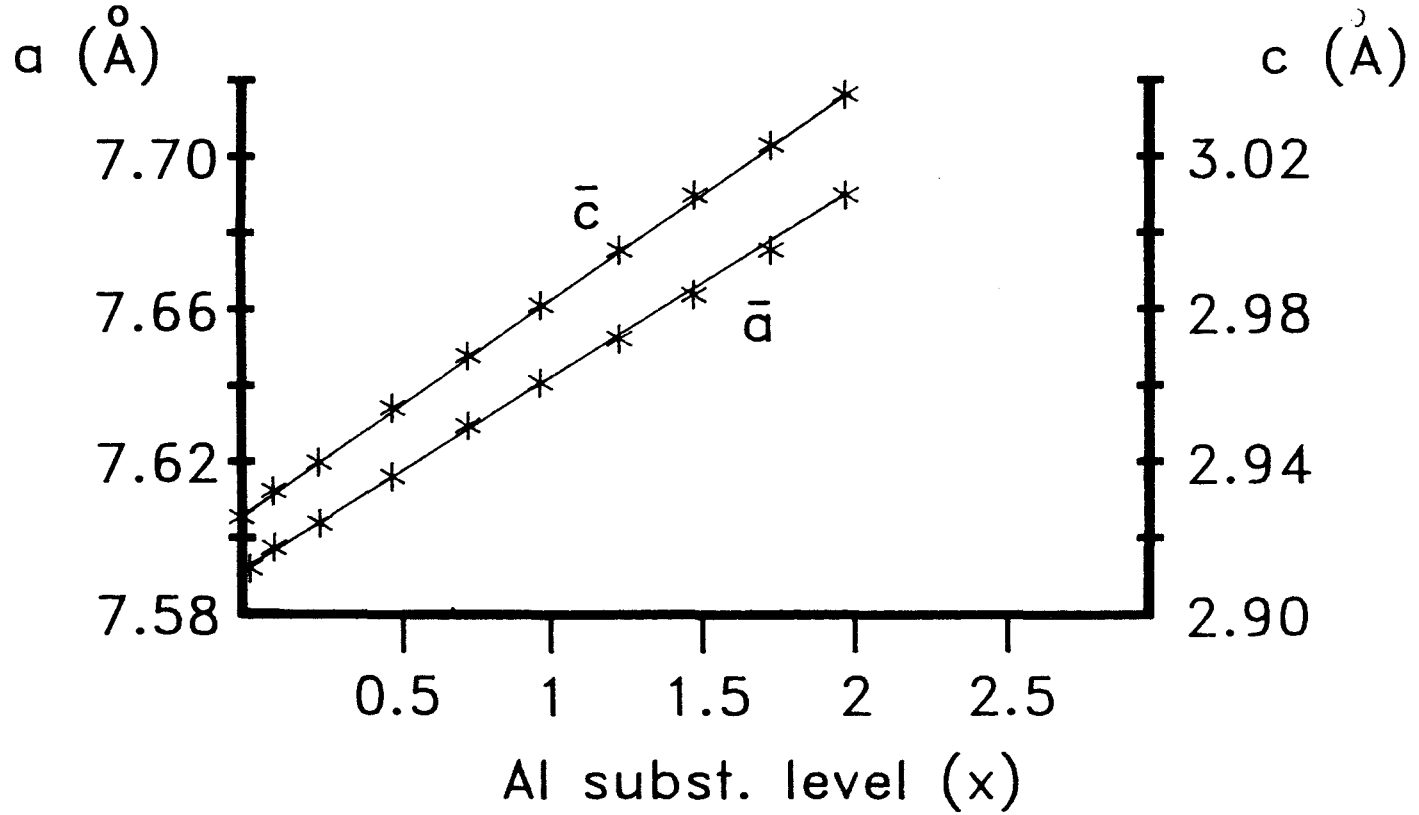

Figure 1.8 Calculated relationship between lattice parameter with aluminium substitution level

of reaction with SiO_2 found as an unavoidable impurity layer on the surface of the silicon nitride. Single phase materials were obtained using a mixture of α-Si_3N_4, $\{SiO_2\}$, Al_2O_3 and AlN or AlN polytypoid where AlN additions "balanced" the SiO_2 impurity levels. The composition of the balanced materials were identified generally of the form

$$Si_{3-x}\ Al_x\ O_x\ N_{4-x} \qquad (1.3)$$

where x is the aluminium substitution level in the structure and was found to form a continuous solid solution up to x=2 (67).

Densification generally occurs by liquid phase sintering mechanism, similar to hot-pressed and pressurelessly sintered silicon nitride ceramics. Again full densification may only be attained by the use of metal oxides (Y_2O_3, MgO etc) which lower the liquidus temperature of the liquid phase. This is further modified by the addition of aluminium compounds, allowing "balanced" compositions to be fabricated with minimal residual glass levels. The Janecke prism , figures 1.9 and 4.2, is a convenient representation of the relationship between stoichiometric components in the M-Si-Al-O-N system, where in this case M=yttrium.

This concept has been demonstrated by Bhatti et al (44), successfully crystallising Y-Si-Al-O-N glass residues to yttrogarnet, $Y_3Al_5O_{12}$, producing a material with promising high temperatures properties. However, these properties were not retained at elevated temperatures because of the severe environmental reaction above 1300°C.

As well as β'-sialons, there also exists two types of ceramics based on related structures, figure 1.9.

(i) α'-Sialons: These ceramics are based upon the substituted form of α-Silicon nitride, namely α'-Sialon (68,69,70,71). Here the Si-N

Figure 1.9 The Si-Al-O-N system

Fig 1.9

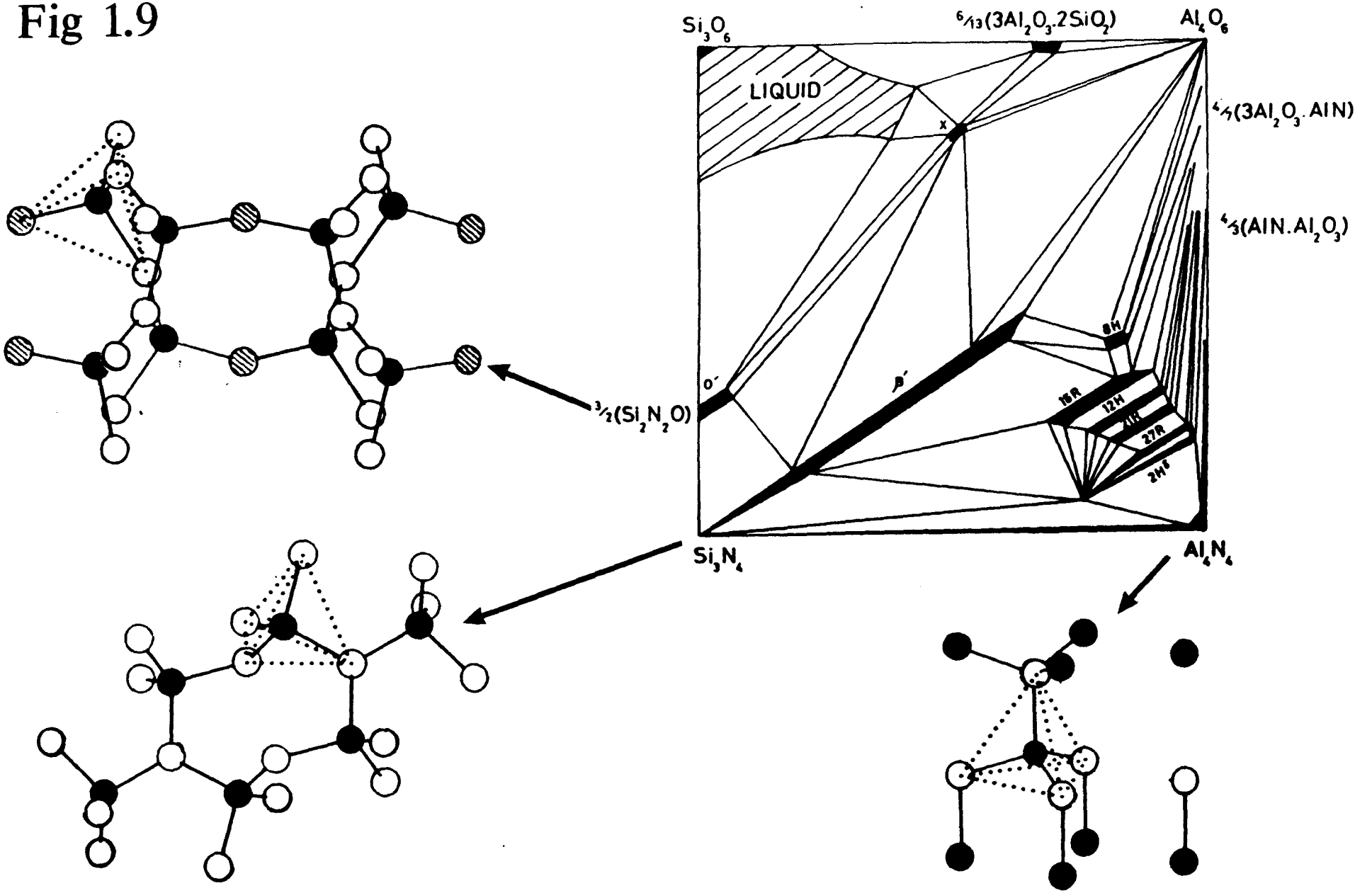
Si_3O_6
$^6/_{13}(3Al_2O_3.2SiO_2)$
Al_4O_6
LIQUID
X
$^4/_1(3Al_2O_3.AlN)$
$^4/_3(AlN.Al_2O_3)$
$^3/_2(Si_2N_2O)$
O'
β'
8H
15R
12H
21R
27R
2H
Si_3N_4
Al_4N_4

bonds are replaced by Al-O bonds, as in β'-sialons, and also by Al-N bonds to a degree, resulting in a charge imbalance. Electrical neutrality is preserved by the incorporation of suitable metal cations (72) such as lithium, calcium, yttrium and rare earth metals (except lanthanum and cerium) into the two intersticial sites in the unit cell at positions (1/3, 2/3, Z) and (2/3, 1/3, 1/2+Z) (68,73). The general formulae of α'-sialons can be expressed as the following;

$$M_x\ Si_{12-(m+n)}\ Al_{(m+n)}\ O_n\ N_{16-n} \qquad (1.4)$$

where M is the metal cation and x<2.

The most significant and promising aspect of α'-sialons is that the metal oxide densification aid may be incorporated into the crystal structure, unlike in β'-sialons which, due to the stacking order of the atomic planes, contains no intersticial sites, and therefore cannot accommodate the metal cations within its structure. This would reduce or even eliminate the residual glassy grain boundary phase, producing a truly single phase ceramic, and would avoid the dominant effects that the grain boundary structure has on properties at high temperature.

(ii) O'-Sialons: The second group of ceramics which have received little attention to date are those based upon the silicon oxynitride (Si_2N_2O) structure (74). Comparatively little attention has been given to this family of ceramics due to their inferior sinterability and hence mechanical properties (75) to silicon nitride (Si_3N_4) based ceramics. Sintering in these ceramics is limited by the decomposition of Si_2N_2O at high temperatures (>1600°C) via the reaction:

$$3Si_2N_2O \rightarrow Si_3N_4 + 3SiO + N_2. \qquad (1.5)$$

Therefore, in order to achieve densification, metal oxide additions (eg Y_2O_3, Al_2O_3) are again necessary to promote liquid phase sintering, resulting in enhanced mass transport and densification.

However, these additions, as in the case of the silicon nitride ceramics, result in the formation of an intergranular residual glass phase, which at elevated temperatures causes degradation of the mechanical and thermal properties.

In these ceramics, it is seen that it is possible to replace Si-N bonds by Al-O in an expanded lattice to form O'-sialons (O'-O-prime). The equation for such a reaction is as follows:

$$(2-x)\ Si_2N_2O + xAl_2O_3 \rightarrow 2\ Si_{2-x}\ Al_x\ O_{1+x}\ N_{2-x} \qquad (1.6)$$

Solubility of aluminium in the silicon oxynitride structure is significantly less than is possible in silicon nitride ceramics, such that the substitution level, x, is <0.2.

The reliability of pressureless sintered sialon materials at elevated temperatures is dependent on the nature of the intergranular phase. Only by the elimination of residual glass phases by the increased use of "balanced" compositions and high purity starting materials may the properties of sialon ceramics be improved. The materials in this study constitute the continued development of yttrium sialon ceramics towards those ends.

1.5 Research Objectives

The objectives of this research programme may be summarised as follows:

(i) To determine the effects that both increased purity and "balanced" compositions have on the sintered and crystallised microstructures based upon the Lucas-Cookson-Syalon 201 composition.

(ii) The high temperature stability in oxidising environments will be determined of materials with YAG matrices leading to an investigation into various methods of surface transformation asan effective barrier against instability of these materials at temperatures above 1300°C.

(iii) To investigate the consequences that the above factors in (i) and (ii) have on the short term fracture properties, and longer creep rupture behaviour at temperatures up to 1500°C.

(iv) To study the relationship between the creep resistance and crystallisation of the matrix phase. The effect of oxidation resistant layers on the high temperature deformation will also be investigated.

(v) To investigate the possible use of Si_3N_4 and SiC coatings formed by chemical vapour deposition (CVD) onto the Y-Si-Al-O-N substrate.

CHAPTER 2 - OXIDATION AND DEFORMATION OF SILICON NITRIDE CERAMIC SYSTEMS - A REVIEW

This chapter will review the current status of monolithic ceramic development today. The aspects of the role and nature of the grain boundary phase will be presented, being subsequently related to their role in dictating the high temperature properties eg oxidation, fracture and creep. The relevant theory and mechanisms concerning all the high temperatures properties will also be presented.

2.1 The nature of the grain boundary phases in Si_3N_4 based ceramics densified with yttria additions

As has been shown already in Chapter One, it is necessary to utilise metallic oxides to aid the densification process. Ceramics densified using yttria additions have shown probably the greatest promise for use in high temperature regimes (76). Early work on the sintering processes showed that the residual glass phase was mainly concentrated at three grain junctions although high resolution dark field and 'lattice' imaging (77,78) have indicated that small volumes of residual phase are also present at two grain junctions. Recent analysis by Clarke (79) has shown that it is possible that thin intergranular films can adopt an equilibrium thickness in polycrystalline ceramics. The analysis, based upon two continuum approaches, one being derived from relative interfacial energies and the other from force balance normal to the grain boundary, both indicate there will exist a stable film thickness at two grain boundaries which will differ according to the nature of the grain boundary. This conclusion has been supported experimentally by Shaw (80) where it appeared that the thickness of the intergranular phase had one value at boundaries between like phases, and another value between dissimilar phases. A volume increase of the intergranular phase does not result in a thickening of the boundary film at two

grain junctions, most of the volume increase is accommodated at three grain junctions.

2.2 Oxidation of Silicon Nitride based ceramics

Oxidation in silicon nitride based ceramics is strongly dependent on many factors, the most important being the nature of the residual grain boundary phase. The grain boundary phase in this range of ceramics is often in the form of a glass, and at elevated temperatures this acts both as a 'short-circuit' for diffusion through the microstructure increasing the oxidation rate compared with "pure" silicon nitride.

2.2.1. Oxidation mechanisms in Silicon Nitride

Oxidation of silicon nitride at elevated temperatures may occur by two different processes. At low oxygen potentials, usually confined to temperatures below 1400°C for 'pure' silicon nitride, active (linear) oxidation reaction occurs i.e.

$$Si_3N_4\ (s) + \frac{3}{2}\ O_2(g) \rightarrow 3SiO(g) + 2N_2(g) \qquad (2.1)$$

and for non-gaseous sources,

$$Si_3N_4\ (s) + 3SiO_2(s) \rightarrow 6SiO(g) + 2N_2(g) \qquad (2.2)$$

Active oxidation kinetics are characterised by an overall loss in weight during oxidation, due to the development of the gaseous oxidation species derived from the above equations.

Passive (parabolic) oxidation occurs at high oxygen potentials, such as normal atmospheric conditions, usually obeying the parabolic rate law by the reaction;

$$Si_3N_4(s) + 3O_2(g) \rightarrow 3SiO_2(s) + 2N_2(g) \qquad (2.3)$$

Passive oxidation is generally characterised by the formation of a protective silica layer during the early stages of oxidation.

The nitrogen ions liberated by the oxidation of the silicon nitride either diffuse out through the oxide layer, or as is more usual, combine to form gaseous nitrogen (N_2), which due to low solubility in the silica layer forms as gaseous bubbles in the layer, causing disruption and spalling of the layer. Passive oxidation of silicon nitride ceramics is characterised by an overall weight gain of the material.

Oxidation of β'-Sialon materials occurs in a similar manner to that of β-Si_3N_4 materials, represented by;

$$Si_{3-x}Al_xO_xN_{4-x} + (3-\frac{3}{4}x)O_2 \rightarrow (3-x)SiO_2 + \frac{x}{2}Al_2O_3 + (\frac{4-x}{2})N_2. \qquad (2.4)$$

2.2.2 Oxidation in "pure" Silicon Nitride

The intrinsic oxidation behaviour of Si_3N_4 is difficult to assess due to the fact that in most cases the presence of various impurities in the form of residual grain boundary phases often dominates this behaviour at high temperatures. However, silicon nitride deposited by chemical vapour deposition (CVD) provides the most effective means of preparing high purity, dense Si_3N_4.

The oxidation kinetics for this were found to be parabolic in nature, oxidation taking place by the formation of a protective silica (SiO_2) layer at the surface by the direct oxidation of the exposed Si_3N_4 grains on the surface (81). This layer increases with weight in addition to acting as a diffusion barrier as the thickness increases. Analysis of the oxidation mechanism proposed by Wagner (82) and Singhal (83) indicated that passive oxidation, i.e. parabolic kinetics should be expected at temperatures of up to 2000°C at oxygen pressures of 35 kPa. It was concluded from this study that passive oxidation should be observed in most circumstances for the oxidation of silicon nitride. The rate determining mechanism for oxidation of this mechanism is diffusion of oxygen through the viscous oxide layer. The measured activation energy for this at temperatures between 1100°C and

1300°C was ~145KJmol^{-1} (44). This value was similar to those found for the oxygen diffusion through SiO_2 (84). Therefore it can be concluded that oxidation of pure Si_3N_4 depends only on diffusion of oxygen through the silica layer. The nature of this layer then determines the rate of oxidation, at 1100°C a discontinuity in both rate and activation energy arises due to crystallisation of the amorphous layer; Above 1400°C another discontinuity in the kinetics takes place, being due to the dissociation of Si_3N_4.

2.2.3 Oxidation of reaction-bonded Silicon Nitride

Reaction-bonded silicon nitride ceramics, fabricated by the direct nitridation of silicon powders without metal oxide additives, are often very pure, containing typically 0.5-1% cation levels. Due to these facts, the ceramics are often porous and oxidation in these materials occurs in two stages. First, internal oxidation within the pores occurs. Davidge (85) found that at temperatures of around 1000°C, oxidation proceeded rapidly due to the non-closure of the open porosity. Therefore, at these temperatures oxidation is predominantly internal. At higher temperatures it is found that the oxidation rate decreases, due to the rapid in-filling of the pores resulting in pore closure. At this stage oxidation may only occur at the outer surface, forming the protective SiO_2 layer at the surface. The effective decrease in oxidation rate at the higher temperatures may be explained by an overall reduction in the surface area accessible to atmospheric oxidation by the closure of pores by silica formation.

The oxide layers formed during oxidation were found to be mainly crystalline silica, either tridymite, or cristabolite (86), with activation energies for oxidation measured to the ~150 KJmol^{-1} and 250-290KJmol^{-1}. These values equal those expected for diffusion of oxygen through silica (~120KJmol^{-1}), and interstitial diffusion of oxygen through amorphous silica (~298KJmol^{-1}).

2.2.4 Oxidation of Hot-Pressed Silicon Nitride

Oxidation kinetics of hot-pressed silicon nitride (HPSN) ceramics (including HP-Sialons) have been shown to be parabolic in nature. However, unlike the two previous cases, the oxidation mechanism is dominated by the out diffusion of the metallic cations at the grain boundary into the oxide layer.

Dense HPSN which contain varying amounts of additives have been found to exhibit accelerated oxidation kinetics when compared with pure Si_3N_4, ie CVD (87) with an associated increase in the rate constant. This has been shown to be caused by the diffusion of the metallic cations into the SiO_2 layer from the intergranular regions below the SiO_2-Si_3N_4 reaction interface (88). The formation of the SiO_2 layer creates a chemical potential across this interface, providing the driving force for cation mobility. The sources for this are,

(i) minimising of the free energy of mixing (ie maximising the entropy of the system).

(ii) the reduction of the total free energy by the reaction of Me^+ with SiO_2 or O_2 to form crystalline silicates at the surface.

The diffusion of metallic cations into the SiO_2 layer causes an overall reduction in the viscosity, increasing diffusion of O_2 species to the SiO_2-Si_3N_4 reaction interface from the atmosphere. The oxidation kinetics are therefore determined by the concentration and diffusion rate constant for the metallic cations in the grain boundary. This diffusion out from the grain boundary to the SiO_2 layer results in the formation of a sub-surface region depleted of cations (46). Evidence that the oxidation rate was determined by viscosity modifying cations was observed by Cubiccioti et al (81), where parabolic oxidation kinetics were observed during the formation of an oxide layer after prior removal of an existing oxidation layer. The oxidation rate was not dependent on the thickness of the SiO_2

layer, but on the viscosity which is controlled by the rate of diffusion out from the intergranular regions.

An alternative mechanism proposed is that where the oxidation rate is controlled by the formation of crystalline silica at the Si_3N_4-SiO_2 interface, by the dissolution of Si_3N_4 grains. The rate determining step proposed by this model is the diffusion of oxygen through this crystalline SiO_2 layer. This mechanism as yet has little evidence to support it.

The nature and form of the grain boundary phase has been shown to dramatically affect the kinetics of oxidation. The volume of grain boundary phase has been shown to have a detrimental effect on oxidation resistance (46,90,91,92,93). Babini et al (93) discussed oxidation phenomena in terms of a simple diffusion model assuming constant grain boundary composition. This model although basic, accounts for both kinetic and thermodynamic variations observed with amount and composition of grain boundary phases.

The oxidation rate has also been shown to be markedly affected by the form of the intergranular phase. In HPSN densified with MgO and Mn_2O_3 additives, the grain boundary phase has been shown either to be amorphous or crystalline, depending on the initial composition. If the grain boundary phase is amorphous, the reduction in viscosity at elevated temperatures provides a fast channel for the diffusion to the surface oxide layer of metallic species, and rapid indiffusion of O_2. In these materials, crystalline grain boundary phases may be obtained by careful balancing of the initial composition. The crystalline matrix phase would be expected to reduce cation mobility at elevated temperatures, thus reducing the susceptibility to oxidation. Indeed, some cases (93,94) have shown that in the yttria system the formation of stable crystalline oxides such as yttrium disilicate ($Y_2Si_2O_7$) has lead to a highly oxidation resistant grain boundary phase up to 1400°C.

However, processing problems often results in variations in the composition during sintering, sometimes resulting in the formation of unstable crystalline phases. Babini et al (93) and Lange (95) have shown that the formation of one or more of the four quaternary phases, $Y_{10}Si_{17}O_{23}N_4$ (H-phase), $Y_2Si_2O_4N_2$ (K-phase), $Y_4Si_2O_7N_2$ (J-Phase) and $Si_3Y_2O_3N_4$ which occur in compatability fields other than Si_3N_4-Si_2N_2O-$Y_2Si_2O_7$ and Si_3N_4-Y_2O_3-SiO_2, can cause catastrophic oxidation at intermediate temperatures (~1000°C). Under these conditions, oxidation or reaction with SiO_2 leads to transformation associated with a large molar volume change, shown in figure 2.2. This transformation causes the creation of large compressive stresses, which can only be accommodated by the formation of surface cracks. In extreme cases (96) cracking becomes so extensive that specimen disintegration ensues.

Hot-pressed sialon ceramics exhibit similar oxidation reactions to the HPSN ceramics. Parabolic kinetics are generally observed, due to the formation of a SiO_2 protective oxide layer. The addition of Al_2O_3 and AlN polytypoid to form "balanced" compositions was shown to increase the oxidation resistance by removal of the intergranular glass phase which acts as a "short-circuit" diffusion path for cations at elevated temperatures (97). However, compositions removed from the "balanced" compositions exhibited inferior oxidation resistance. This was attributed directly to glass formation in intergranular regions (98).

2.2.5 Oxidation in Pressureless Sintered Ceramics

Oxidation of pressureless sintered ceramics has been shown to occur in a similar fashion to the hot-pressed Si_3N_4 based ceramics. The nature of the grain boundary chemistry and form dominate the kinetics.

Secondary Phase	Oxidation Product	Vol Change %
$Y_2Si_3O_3N_4$	$Y_2Si_2O_7 + SiO_2$	+30
$YSiO_2N$	$0.5\ Y_2Si_2O_7$	+12
$Y_5(SiO_4)_3N$	$0.75\ Y_{4.67}(SiO_4)_3O + 0.75\ Y_2SiO_5$	+4
$Ce_5(SiO_4)_3N$	$5CeO_2 + 3SiO_2$	+8
$CeSiO_2N$	$CeO_2 + SiO_2$	+14
$Ce_2Si_2O_7$	$2CeO + 2SiO_2$	+7
$ZrO_{2-x}N_{4x}$ (x=0.2)	ZrO_2 (monoclinic)	+5

Fig. 2.2 Molar volume changes of unstable secondary phases compatible with Si_3N_4.

Upon sintering the grain boundary phase is often amorphous (46,99). Ceramics with high viscosity grain boundary phases (such as Y_2O_3, Sc_2O_3) show high oxidation resistance, whilst the additives which form low viscosity liquids (MgO) have been shown to have inferior oxidation resistance. The generally larger volumes of grain boundary results in increased oxidation kinetics when compared with the hot-pressed ceramics due to the larger amounts of modifying cations which may diffuse into the SiO_2 layer.

Similarly, as with the hot-pressed materials, oxidation in sintered silicon nitride materials may be reduced by crystallisation of the grain boundary phase, reducing cation mobility. If the crystalline grain boundary is stable with respect to reaction with the SiO_2 oxide layer, such as with yttrium disilicate ($Y_2Si_2O_7$) grain boundary phases, oxidation resistance is high. However, if the grain boundary phase reacts with SiO_2, to form a eutectic liquid, the kinetics revert to that found in ceramics containing amorphous grain boundary phases. This is of particular significance to ceramics with yttrium aluminium garnet, YAG, ($Y_3Al_5O_{12}$) grain boundary phases, where reaction with the SiO_2 oxidation forms a eutectic liquid, the mechanism generally referred to as 'YAG reversion', occurs at temperatures above 1300°C. In this regime, this reaction causes reversion of YAG to a glass, resulting in catastrophic oxidation and strength reduction.

2.3 Fracture of Ceramics

The mechanical properties of silicon nitride ceramics are generally dominated by two processes. At low temperatures, failure is usually 'brittle', derived from the catastrophic extension of pre-existing flaws. Secondly, there is delayed fracture or stress rupture, which occurs at sub-critical stress levels, by the slow extension of a single or multiple crack front.

2.3.1 Brittle fracture of ceramics

Most ceramic materials exhibit measured strengths far below those calculated from theoretical considerations of a crack propagating through an elastic solid. Explanations for this behaviour were developed by Inglis (100) and Griffith (101) in 1913 and 1920 respectively, demonstrating the significance that microscopic flaws have on the strength. Inglis showed that notches serve as stress concentrators which locally magnify the applied stresses in a solid, i.e. that

$$\sigma = 2\sigma_{app}\left(\frac{a}{r}\right)^{\frac{1}{2}} \qquad (2.5)$$

where σ_{app} - applied stress

a - crack length

r - crack step radius where $r = \frac{b^2}{a}$ for elliptical notches.

Failure occurs when the amplified stress (σ) exceeds the theoretical stress limit of the solid. In ceramic materials the magnitude of the stress concentration is estimated to be of the order of 100 to 1000x.

Griffith considered crack stability from a mechanical energy viewpoint. In this model, the energy required to create two new surfaces was equated to the mechanical energy lost as the crack propagated. This analysis results in the familiar Griffith equation;

$$\sigma_f = \left(\frac{2E\gamma}{\pi a}\right)^{\frac{1}{2}} \qquad (2.6)$$

where E - Youngs modulus

γ - surface energy

a - crack length.

Both of the Inglis and Griffith analyses are simply alternative methods of describing fracture in brittle solids, in the former the

material parameters control fracture, and in the latter energy terms control. However, they both show that the strength is inversely proportional to the square-root of the flaw size.

These basic models for the fracture of brittle solids now form the basis of linear elastic fracture mechanics. Irwin (102) considered the Griffith concept by defining a new energy parameter, namely the strain energy release rate G. In this approach fracture occurs when the value of G reaches some critical value G_c, being defined by the equation;

$$G = \tfrac{1}{2} \left(\frac{\partial U}{\partial A} \right) \qquad (2.7)$$

when U - total mechanical energy

A - unit area.

Irwin's method suggests that a crack will only propagate when the stored energy release rate (G), exceeds the energy required to form two new surfaces ie $G_c \geq 2\gamma$. However, unlike the Griffith approach which assumed a totally reversible mechanism, Irwin suggested that the creation of new surfaces is not the only method of energy dissipation that the existence of a plastic zone at the crack tip is also possible. Hence the Griffith equation (eqn. 2.6) becomes;

$$\sigma_f = \left(\frac{EG}{\pi a} \right)^{\frac{1}{2}}. \qquad (2.8)$$

Brittle fracture has been shown to occur in three distinct modes; mode I, crack opening; mode II, crack sliding; and mode III, crack tearing (figure 2.3). In brittle materials it is found that cracks tend to propogate in a direction perpendicular to the applied stress. Thus the strain release energy parameter G may be written to describe the energy release confined to a specific mode of crack propagation i.e. G_c may be re-written as G_{Ic} for mode I crack propagation. G_{IIc} and G_{IIIc} as similarly identified. Likewise the

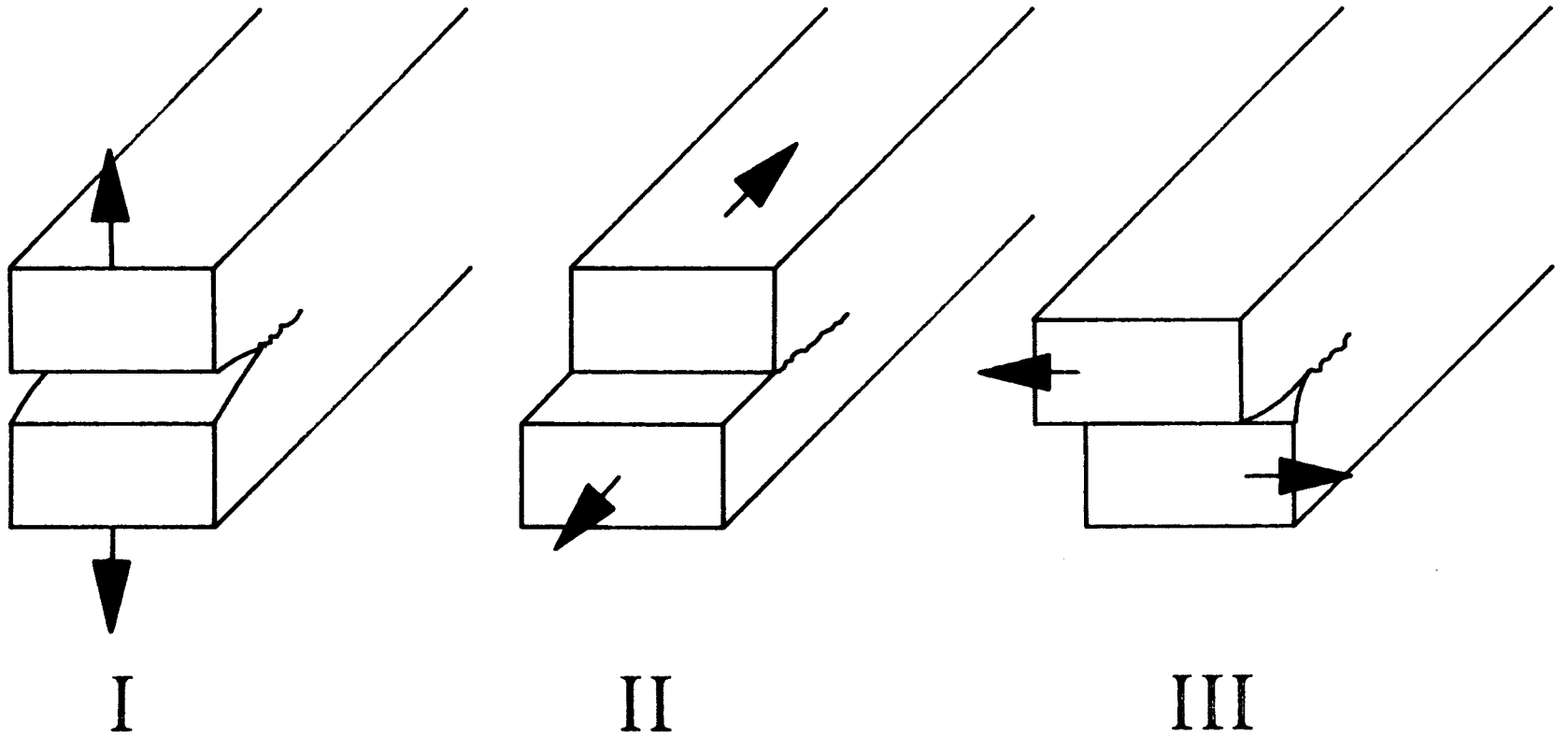

Figure 2.3 The three modes of fracture

'stress intensity factor', K_c is defined from Irwin's theory by the equation

$$K_c = \sigma\sqrt{a}\, Y \qquad (2.9)$$

where a - crack length

σ - applied stress

Y - dimensionless constant.

Similarly K_c may be defined with respect to the seperate modes of crack opening, i.e. K_{Ic}, K_{IIc}, K_{IIIc}. For mode I failure in ceramics when the stress intensity reaches a critical level, K_{Ic}, crack propagation ensues. A simple relationship exists between G_{Ic} and K_{Ic}, as during loading, the strain energy is related to K_{Ic} by the equation

$$G_{Ic} = \frac{(1-\nu^2)\pi K_{Ic}^2}{E} \qquad (2.10)$$

where ν - Poisson's ratio.

Both of these parameters measure the resistance of a material to crack propagation, commonly known as the "fracture toughness". Unlike the fracture stress which is dominated by statistical flaw distributions, the fracture toughness is independent of these, being unaffected by the surface flaws inherent in most materials.

2.3.2 Sub-critical crack growth

In materials there often exists mechanisms by which pre-existing cracks may propagate under stresses far below those associated with catastrophic failure. This phenomena is generally known as "sub-critical crack growth", which manifests itself as a gradual strength loss during long term loading (mechanical, thermal, chemical), and often is the determining factor when considering the expected life of the material in use.

2.3.3 Fracture in Silicon Nitride ceramics

Fracture phenomena in polycrystalline silicon nitride based ceramics has been studied for a wide range of material compositions, over a wide range of temperatures. The basic methods have been used for determining the intrinsic strength of materials; 3 or 4 point bend tests, measuring the ultimate strength or modulus of rupture (MOR), and measurement of fracture toughness (K_{Ic}). The former relates to the ultimate fracture stress the normally processed bar will withstand, being modified by the flaw distribution on or near the stressed surface. This method is often used to construct the Weibull plot for the determination of the flaw population (104).

The measurement of K_{Ic} nominally allows the assessment of the material strength independently of flaw size or distribution, or specimen configuration. Many methods for the measurement of K_{Ic} are available (105,106,107,108,109), but the most popular being the single edge notched beam method (SENB) due to its overall simplicity, where a known critical flaw is introduced into the specimen. Hence K_{Ic} may be regarded as a true material parameter being unaffected by flaw population. However, K_{Ic} has been shown on many occasions to be affected by material parameters such as grain size, aspect ratio although the exact relationship is unclear, the effect appearing to be contradictory in various materials (110).

The lowest K_{Ic} values in silicon nitride materials are generally found in reaction bonded ceramics (RBSN) (111). K_{Ic} values are lower, typical 2-4 $MPam^{\frac{1}{2}}$ than generally found in similar dense materials. The origin of this low fracture toughness is porosity forming critical flaws under stress. However, RBSN materials are very pure, containing little or no additive phase, and thus the properties are maintained at elevated temperatures, even increasing at high

temperature. This is thought to be a result of oxidation, causing the formation of a protective SiO_2 layer blunting critically sharp flaws.

The fracture properties of ceramics densified with the aid of sintering additives fall into two broad categories. At low temperatures, failure occurs catastrophically. Many investigations into the effect of different additive type on the strength have been undertaken (112,113,114,115,116,117). In this regime, like the RBSN materials, failure is dominated by structural parameters ie residual porosity, average grain size, grain anisotropy, agglomerates, rather than microstructural parameters ie grain boundary structure. Variations in K_{Ic} values have been observed in hot-pressed materials as a result of severe grain anisotropy. In addition, higher strength and K_{Ic} values have been observed in materials with high aspect ratio grains. It is thought that energy dissipative mechanisms near to the crack tip may be responsible for this effect. The energy for fracture (118) has been found to increase dramatically with additive levels (usually associated with more elongated grain growth due to reduced sintering liquid viscosity).

The second regime of fracture occurs at elevated temperatures. Materials with residual grain boundary phases show increased susceptibility to degradation at temperatures in excess of 1000°C. The exact temperature where this degradation occurs depends critically on the nature of the grain boundary phase. Magnesia based materials eg Norton NC132 (116), have been shown to have increased susceptibility to strength degradation at high temperatures when compared with the yttria materials (112,115,119,120), being due to the formation of a less refractory grain boundary phase. An increase of 100°C is often observed before time dependent failure occurs when comparing Y-based and Mg based materials.

Failure at elevated temperatures becomes dominated by sub-critical crack growth (section 2.3.2). Failure is observed to be intergranular, the crack following a tortuous route via the grain boundaries. In this regime, processing flaws and surface defects are found to have little effect on failure, often being blunted by oxidative reactions (121). Subcritical crack growth has been proposed to occur by a grain boundary sliding-cavity formation and linkage mechanism (122). Grain boundary sliding has been found to be the basic step by which large stresses sufficient to create cavities at triple junctions, essential for the formation of microcracks (123). An alternative mechanism proposed by Lange (124) involves an energy dissipation mechanism by the formation of glass fibrils between Si_3N_4 grains as the crack advances.

Two approaches may be taken to improve the high temperature strength of Si_3N_4 based materials. First is the removal of additives which would form grain boundary silicate phases during sintering. This has been demonstrated (125,126) to reduce the susceptibility to sub-critical crack growth at elevated temperatures. However, in general this usually results in difficulties in forming a dense ceramic. A second approach is to eliminate the residual glass phase by crystallisation using a post-sintering heat-treatment, resulting in the formation of a refractory hard materials as a secondary grain boundary phase. This should reduce viscous flow, and grain boundary sliding, and hence cavity and microcrack formation. The difficulty in sintered ceramics, due to the large volumes of grain boundary phase, is that complete crystallisation is difficult to attain (127), and hence sub-critical crack growth is difficult to eliminate.

Crystallisation of the grain boundary phase has been shown to increase the strength at elevated temperatures. Tsuge et al (115,128)

observed increases in strength in Si_3N_4 densified with Y_2O_3+Al_2O_3 with a crystalline grain boundary phase. Similar observations of Y_2O_3 densified materials were made by Smith and Quackenbush (129). However, in a more recent study (121), no strength increase was observed in a material with a similar crystalline grain boundary phase. In this study it was found that the strength was dominated by processing flaws. It has been suggested that variations in the intrinsic strength upon crystallisation is due to internal stresses produced by a slight volume change upon devitrification. The stress would be dependent on the form of the crystallised phase, thus determining whether a strength increase or decrease ensues.

2.4 Creep behaviour of Silicon Nitride ceramics

The proposed uses for this type of ceramic material includes that at high temperatures. At these temperatures, all ceramics exhibit time dependent plastic deformation under load, the process generally termed as creep. The measurements of the creep properties of materials is an important factor in determining the long term stability under stress.

Upon application of a stress, σ, at elevated temperatures, the material will start to creep. A conventional creep curve, ε versus time t, obtained under these circumstances (ie at constant load and temperature) may be divided into three regions (figure 2.4). Initially, upon application of the load, the material undergoes an instantaneous strain ε_o, followed by three regions of creep behaviour;

Stage I: Primary Creep ($\dot{\varepsilon}_p$) - this is characterised by a continuously decreasing creep rate with increasing strain and time. Primary creep may be represented by the equation (130);

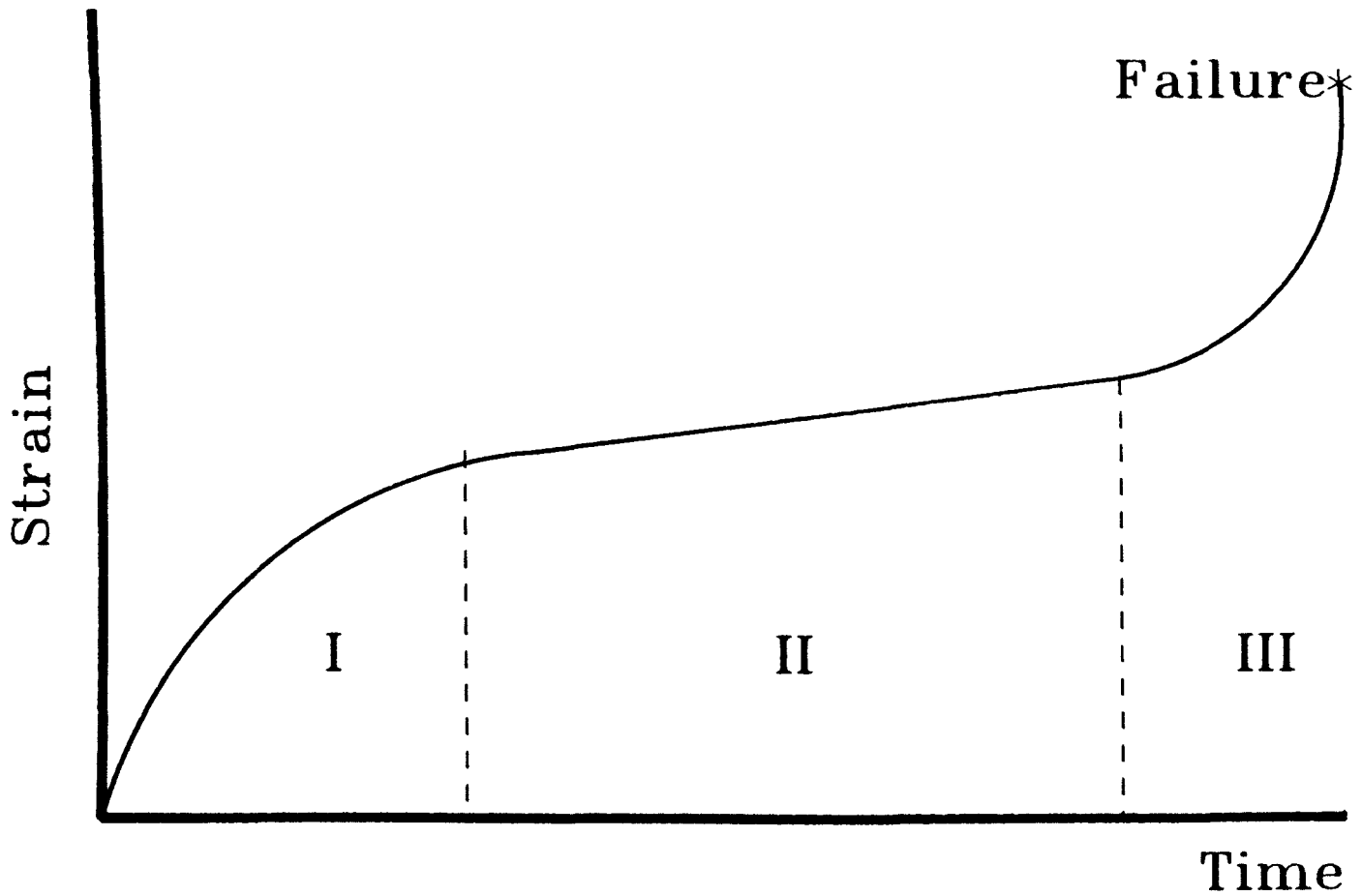

Figure 2.4 Deformation behaviour, 3 stage creep curve at constant temperature and stress

$$\dot{\varepsilon}_p = \left(A \frac{\sigma}{a^{1.5}} \exp\left(\frac{-Q}{RT}\right)\right) t^{m-1} \qquad (2.11)$$

where A,a - constants

σ - stress

Q - activation energy

t - time

m - stress exponent.

Stage II: Secondary or Steady State Creep ($\dot{\varepsilon}_s$) - in this regime it is found that the creep rate is constant with increasing strain and time. Most ceramic systems have been shown to obey empirical relationships of the form;

$$\dot{\varepsilon}_s = A\, \sigma^n \exp(-Q/RT) \qquad (2.12)$$

$$\dot{\varepsilon}_s = A'\, \sigma^n \left(\frac{1}{d}\right)^m \exp(-Q/RT) \qquad (2.13)$$

$$\dot{\varepsilon}_s = A'' \frac{DGb}{kT} \left(\frac{b}{d}\right)^m \left(\frac{\sigma}{G}\right)^n \qquad (2.14)$$

with $D = D_o \exp\left(\frac{-Q}{RT}\right)$

where A,A',A" - constants

d - grain size

m - exponent of grain size

n - stress exponent

Q - activation energy for diffusion process

G - shear modulus

b - Burgers vector.

D - appropriate diffusion factor

D_o - frequency factor

For most ceramic systems it has been found that the equation 2.12 is most useful. The secondary creep rate is most influenced by the terms associated with the stress exponent n,

and the Arrhenius term exp ($^{-Q}/RT$). Knowledge of the stress exponent, n, the activation energy, Q, and an assumption that the structure parameters do not change significantly during creep allows some conclusions to be drawn regarding the mechanisms of creep present. It should be noted that these parameters are not constant being dependent on stress (σ), total strain (ε) and temperature (T). Therefore one must be careful to draw detailed conclusions beyond the empirical nature of the mechanisms defined by the equations 2.12, 2.13 and 2.14. Difficulties arise also from multiplicity of the creep process in real materials, where many seperate mechanisms are superimposed to produce the measured creep rate. Therefore, the measured values of n and Q may be an average of many different effects, resulting in problematic deduction. This is especially true for the activation energy Q. The measured value does not include the effects that variation of the shear modulus G and the 1/kT term, thus may only be termed as the apparent activation energy (131). This factor only becomes significant when n is large when the true activation energy is generally found to be lower than the measured value. For $1 < n < 2$, as found in a wide range of ceramic materials, the two are essentially equal.

Stage III: Tertiary Creep ($\dot{\varepsilon}_t$) - this stage of creep involves a rapid increase in the observed creep rate. Tertiary creep involves conventional creep processes, modified by the formation and growth of cracks, ultimately leading to catastrophic failure. This region of creep is not often observed in ceramic materials, often being preceeded by catastrophic failure.

2.4.1 Creep in Silicon Nitride

The high temperature creep of a large range of materials based upon Si_3N_4 and SiC structures have been widely studied (99, 125, 126, 133, 134, 135, 136, 137), figure 2.5. The form of observed creep was well predicted by theory, consisting of elastic strain, a region of primary creep, secondary creep and finally tertiary creep preceeding failure.

It has been found that in these materials, there is little evidence for creep behaviour dominated by dislocation motion. This is primarily due to the covalent nature of the materials resulting in very high bond energies, ~ 335 kJ mol^{-1}. Therefore, creep processes by this mechanism do not become important until very high temperatures. There is, however, substantial evidence for creep processes dominated by grain boundary sliding as a result of the presence of grain boundaries, and what may be present there. It has also been shown that not only is the creep rate dependent on the existence of grain boundaries and the associated additives, but it is critically dependent on the nature of the phases at the grain boundary (ie whether it is amorphous or crystalline).

In many Si_3N_4 based materials, the additives required for densification result in the formation of amorphous or crystalline grain boundary phases (138). Fully crystalline grain boundary phases are not easily observed, often containing small volumes of residual glass at triple junctions. It is these regions which are of prime importance, glassy phases may be the cause of uncontrolled viscous properties during creep. The volumes of glass phases have been attributed, at least partially, to large primary components observed during creep. Lange et al (134) and Arons et al (136) observed long periods of primary creep in materials known to have residual glassy grain boundary phases, being attributed to effects caused by grain boundary sliding accommodated by elastic deformation at g.b asperities

Figure 2.5 A comparison of creep behaviour of a range of engineering ceramics.

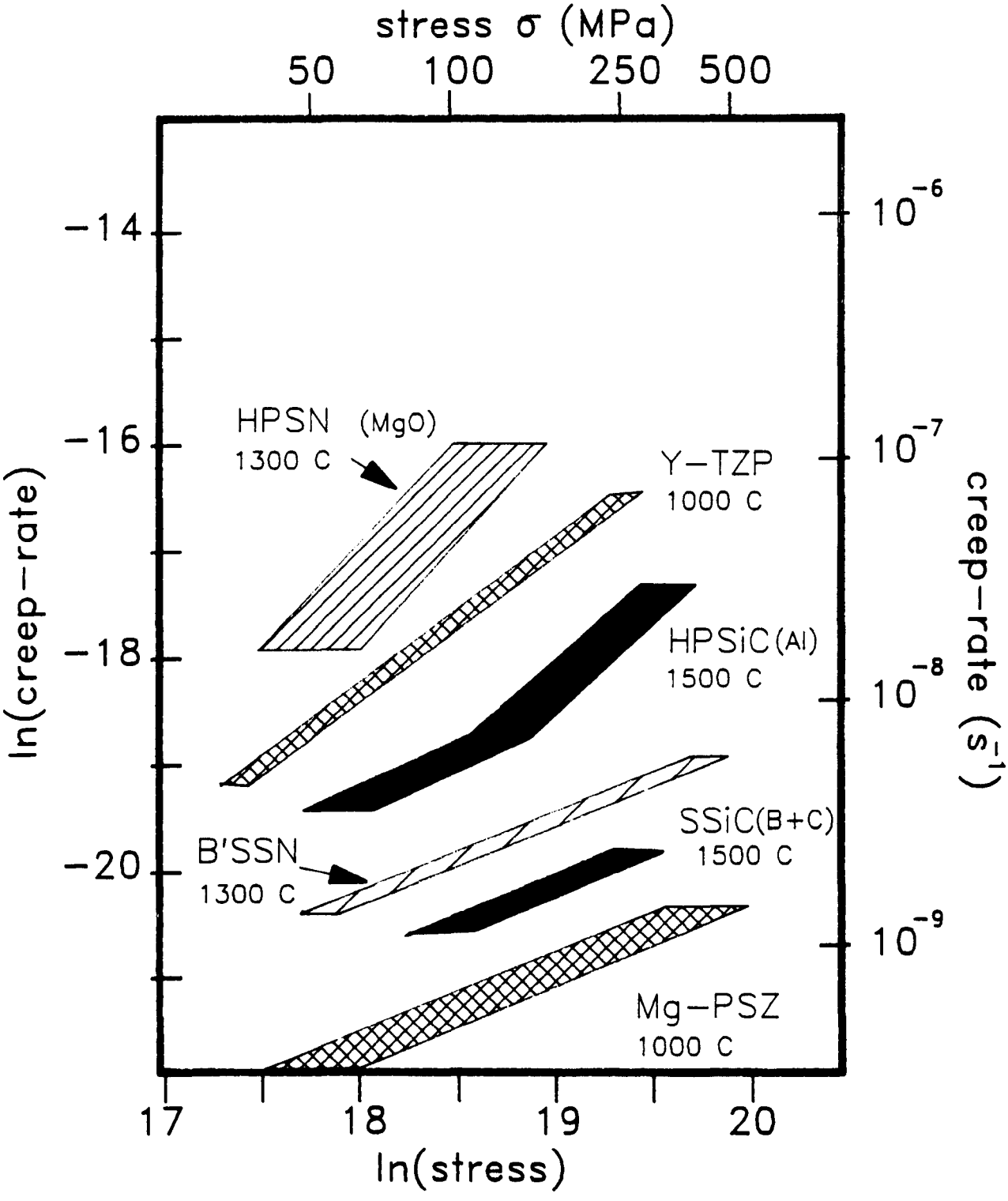
stress σ (MPa)
50
100
250
500
−14
−16
−18
−20
ln(creep−rate)
10^{-6}
10^{-7}
10^{-8}
10^{-9}
creep−rate (s^{-1})
HPSN (MgO)
1300 C
Y−TZP
1000 C
HPSiC(Al)
1500 C
B'SSN
1300 C
SSiC(B+C)
1500 C
Mg−PSZ
1000 C
17
18
19
20
ln(stress)

and/or adjacent grains. The existence of fully crystalline grain boundary phases would be expected to result in a dramatic reduction in the viscoelastic component to the primary stage of creep.

After reasonably short regions of primary creep, most ceramic materials move into an extended region of steady-state creep. The importance of the grain boundary structure in relation to the observed creep rates was clearly shown by considering the creep behaviour of a range of hot-pressed sialons, with and without amorphous grain boundary phases (125, 126). Studies of the deformed microstructure of the ceramics with an amorphous phase revealed the presence of grain boundary voids, or cavities which had formed during creep. These were, at low total strains, usually observed at three grain junctions. However, at larger strains cavities have been observed to form along two grain junctions, eventually coalescing to form microcracks, and ultimately leading to failure (139). The controlling mechanism in this case was found to be grain-boundary sliding facilitated by the amorphous grain boundary phase, which is accommodated by the formation of intergranular cavities. The associated stress exponent values obtained from the creep behaviour were $1.5<n<1.6$.

In contrast to this behaviour, a similarly fabricated ceramic, but with no glassy phase at the triple junctions exhibited a stress exponent n=1 indicating a diffusion controlled creep process (140,141). Microstructural evidence in these materials indicate no cavitation occurs until very high stress levels. Shape accommodation in this case is purely diffusion from the compressive to tensile facets via the grain boundaries.

It must be noted that extended annealing at high temperatures has the effect of reducing the creep rate and the value of the stress exponent n=>1 ie diffusional creep, with the suppression of cavitational effects. This has been explained by outward metallic impurity diffusion into the SiO_2 oxidation layer, depleting the grain

boundaries, such that the microstructure tends towards that observed in the non-cavitating ceramic.

Pressureless sintered ceramics exhibit similar creep properties to the hot-pressed materials. Due to the larger volumes of sintering aids, cavitating due to amorphous grain boundaries is more commonly observed. Stress exponent values in this case have been found to be appreciably greater than unity, resulting from cavitation due to grain-boundary sliding effects. Removal of the glassy phase in these materials is difficult; post sintering heat-treatments at temperatures around 1400°C causes the crystallisation of the matrix phase. During this process, impurity species eg Ca, F are rejected at the crystallisation front. These form stable glass pockets at triple junctions, providing sites for nucleation of cavities. This has been observed in a previous range of development sialon ceramics (127), where impurities, particularly fluorine and calcium derived from the starting powders, were found to be responsible for the incomplete crystallisation of the Y-Si-Al-O-N intergranular matrix glass. The resultant high temperature creep and creep-rupture properties were found to be dominated by cavitational effects severe enough to ultimately lead to failure, being directly attributed to the presence of impurity rich residual glass regions, generally at triple junctions. These regions not only dominate the creep mechanism, but also severely affect the temperature at which these effects occur and become catastrophic. Winder (173) showed that the presence of residual intergranular glass caused enhanced creep rates at temperatures far below those targeted for its use.

Hence, the reduction or removal of residual glass regions by superior powder processing, and by the use of "balanced" compositions will result in ceramics with enhanced creep properties, approaching the targeted values.

The creep properties of this range of ceramics is additionally affected by the environment in which it is deforming. At high temperatures, nitride ceramics form oxidation products in the appropriate atmosphere as reviewed in section 2.1. The high temperature creep properties may be significantly altered by the change in both chemical and physical states of the material eg flaw size changes, blunting effect, chemical depletion. Hence the creep behaviour may be radically altered, with creep rupture and/or sub-critical crack growth mechanisms becoming dominant.

2.4.2 Stress Rupture in Silicon Nitride based ceramics

Theoretical considerations have indicated that high temperature failure in ceramics is similar to that in metals (142), where processes such as nucleation growth -coalescence of cavities formed by the creep processes, and growth of cracks to critical size from pre-existing flaws, dominate failure. Theoretical and experimental considerations showed that creep failure could be modelled by the following two relationships; the Monkman-Grant relation

$$t_f \dot{\varepsilon}_s = \text{constant} \qquad (2.15)$$

and the Orr-Sherby-Dorn relation;

$$t_f \exp(^{-Q}/RT) = f(\sigma) \qquad (2.16)$$

where t_f - time to failure

$\dot{\varepsilon}_s$ - steady state creep rate

T - temperature

Q - activation energy for the rate limiting step in the failure process.

In equation 2.15 the function $f(\sigma)$ is dependent on the failure mechanism, for steady-state viscous creep $\varepsilon \alpha \sigma$ and $t_f \alpha \sigma^{-1}$. If crack growth is the rate limiting step, $t_f \alpha \sigma^{-3}$ (143).

The applications of ceramics into high temperature and stress regimes in real situations requires a full understanding of the

time-temperature-stress dependence of the materials. The simplest assessment of this is to extend the conventional creep experiments until specimen failure. This is easiest done in four point bending or tensile modes of creep, as the strength of this type of material is lower in these modes than in compressive. This method of testing allows the assessment of a material's performance over realistic time periods, not relying on the measurement of fast cracks to predict lifetimes eg double torsion testing techniques (125,126).

Stress rupture is the general term used to describe failure after a finite time after stress is applied. Specifically, failure usually occurs by one of three modes; stress corrosion, the extension of cracks and flaws by chemical attack in stressed materials. Secondly, there is creep rupture, entailing the formation of microcracks by coalescence of cavities, and thirdly, there is slow crack growth, the extension of a crack from a pre-existing flaw. These modes of stress rupture have been extensively observed by Evans et al. in fine grain alumina (144,145,146).

Stress rupture in ceramic materials is strongly dependent on composition and particular history of the material. Hence it has been observed that the lifetimes of Norton NC132 showed large differences between samples from two billets (147). Extensive studies on the stress rupture on a wide range of silicon nitride and carbide ceramics has been performed by Quinn (148, 149, 150, 151, 152). Stress rupture was observed at elevated temperatures in four point bend. Fracture surfaces revealed prominent crack growth zones, including in several instances, crack zones which did not intersect the surface. The mechanism of failure in HPSN was found to occur by various mechanisms, depending on the temperature. At moderately low temperatures, failure occurs mainly by stress corrosion at stresses very near the critical failure stress. Failure at intermediate temperatures, was due to slow

crack growth from pre-existing flaws at relatively high stresses. At higher temperatures failure was found to be due to creep rupture at stresses far below the critical value. In this regime, critical pre-existing flaws undergo local deformation about the crack tip causing crack blunting such that these defects will not grow. In this case deformation is large, and the failure damage zone is usually a good proportion of the fracture surface. The origin of failure for this mode of failure is difficult to observe, often due to severe oxide layer formation, and that in most cases the nucleation zone and growth zone are indistinguishable in most cases.

Models have been produced to describe stress rupture in silicon nitrides based upon a fracture mechanics approach (153, 154, 155). These have failed to give consistent results, the theory being relevant to slow crack growth mechanisms, but due to the highly complex nature of creep rupture processes these models are irrelevant.

This chapter will describe the general experimental techniques used for the microstructural and mechanical property assessment of the ceramics used.

3.1 Material preparation and composition

The research programme has been based upon a range of yttrium Sialons fabricated and supplied by Lucas-Cookson-Syalon Ltd., Solihull, England of compositions as shown in figure 3.1. All these materials are based upon the commercially available sialon, LCS201, and as a consequence of the industrial nature of the ceramic, some information regarding the composition and fabrication processes may not be published.

The starting material powders, high purity α-Si_3N_4, AlN-polytypoid, Y_2O_3 were mixed to the proportions as shown in fig. 3.1, and milled in isopropyl-alchohol with alumina media to ensure fine grain size (<1μm), and intimate dispersion of the powders. During this operation, approximately 3 to 4% alumina was 'picked-up' from the milling media, a factor accounted for in the initial powder preparation. The milled powder was then dried, and isostatically pressed in rubber containers to form billets ready for pressureless sintering. The compacted billet was placed in a bed of boron nitride, and sintered in one atmosphere of nitrogen for the times and temperatures as shown in figure 3.1, using a graphite resistance furnace. At completion of sintering the furnace was shut down, and the samples were allowed to furnace cool before removal.

3.2 Techniques for microstructural observation and evaluation

3.2.1 Transmission electron microscopy

(a) Sample preparation

Electron transparent specimens suitable for transmission microscopy were prepared by initially cutting thin slices (~0.5mm)

Fig. 3.1 Treatments	α-Si_3N_4	AlN*	Y_2O_3	Al_2O_3	Theoretical Density (gcm^{-3})	Measured Density (gcm^{-3})	Sintering Conditions	Crystallisation Conditions	Additional
201/8	86	8	6	3.69-3.76	3.26	3.24-3.26	1650 C 2hrs + 1800 C 5hrs (or 1750 C 5hrs)	1250 C 7hrs 1400 C 5hrs	
201/2	86	2	6	4			1650 C 2hrs 1800 C 5hrs	1250 C 7hrs 1500 C 5hrs	
201/4	86	4	6	4			1650 C 2hrs 1800 C 5hrs	1250 C 7hrs 1400 C 5hrs	
201/6	86	6	6	4			1650 C 2hrs 1800 C 5hrs	1250 C 7hrs 1400 C 5hrs	
201/8a	86	8	6	4			1650 C 2hrs 1800 C 5hrs	1250 C 7hrs 1400 C 5hrs	
201/0	86	8	6	0			1650 C 2hrs 1800 C 5hrs	1250 C 7hrs 1400 C 5hrs	HIP'ed for 1 hr 1800 C after sintering

from a billet using a high speed annular diamond saw. The cut section was mounted on a glass slide using 'Lakeside' wax and mechanically ground using SiC paper to a thickness of 50-70μm followed by diamond lapping of both surfaces to a finish of 1 μm. The sections were mounted on brass rings with quick setting epoxy resin, removed from the glass slide and cleaned in acetone to remove any residual Lakeside wax from the surface of the specimen. Final thinning to produce an electron transparent specimen was performed using a 5 KV argon ion beam at an angle of approximately 30°. Finally, in order to avoid charge build up on the specimen, a thin carbon coating was evaporated onto the surface.

(b) Microstructural analysis.

Microstructural analysis was performed on a JEOL 100C 100 KV transmission electron microscope fitted with an EDAX 9100 energy dispersive X-ray analyser for semi-quantitative compositional analysis, using conventional modes of operation, ie. bright and dark field imaging, electron diffraction, and high resolution lattice imaging.

3.2.2 Scanning electron microscopy

(a) Sample preparation

Specimens for SEM analysis for which a flat surface was required were mounted in a conducting bakelite block and mechanically ground using SiC paper to form a flat surface. Finally, the specimen was diamond lapped to a surface finish of 1μm and ultrasonically cleaned in acetone. A thin layer of carbon was evaporated onto the surface of the specimen to avoid charge build up. Fracture surfaces were studied by mounting the specimen vertically on an aluminium stub using quick setting epoxy resin. To avoid charge build up, the sides

of the specimen were painted with conducting carbon paint, and a thin layer of carbon was evaporated onto the fracture surface.

b) Microstructural analysis.

Microstructural analysis was performed using a Cambridge Stereoscan 250 Mark III scanning electron microscope, fitted with a lanthanum Hexaboride (LaB_6) filament. Both scanning and back-scattered (atomic number contrast) modes were extensively used, that latter being of high importance for the visual identification of phase distribution and changes within the specimen. Quantitative X-ray microanalysis was performed using a Link 860 energy dispersive X-ray analyser fitted with a windowless detection system. This allows the characteristic X-rays associated with light elements, specifically the oxygen and nitrogen lines to be directly observed, previously impossible due to absorption of low energy X-rays in the beryllium windows protecting the detector. Due to severe overlap of the nitrogen and oxygen K lines, and high self absorption of the low energy X-rays, quantitative measurements of nitrogen levels was not possible, only a semi-quantitative estimation could be made.

3.2.3 Optical microscopy

Macroscopic changes in the microstructure were observed by the use of dark field reflection microscopy.

Unlike bright field microscopy where the image is derived from the direct illumination of the surface of the specimen, dark field reflection microscopy uses an incident light source reflected at a low angle onto the surface of the specimen enabling the observation of effects arising from changes in the microstructure.

Specimens used were simply those prepared for analysis in the SEM, before a carbon coating was evaporated onto the surface, which tended to obscure the microstructural detail. A Zeiss Ultraphot II

photographic microscope was used for all optical microscopy, specimen illumination being provided by a 200 watt high pressure mercury lamp.

3.2.4 X-Ray diffraction

X-ray diffraction identification of crystalline phases present in the range of materials available was performed using a Philips PW 13800/00 horizontal scanning diffractometer. X-rays of average wavelength 1.54Å were generated from a copper target at 40 KV and 30 mA. These were passed through a nickel filter to remove the characteristic X-rays associated with the CuK_β component, leaving only the combined $CuK_{\alpha 1}$ and $CuK_{\alpha 2}$ components. Characteristic Bragg diffraction spectra were obtained from flat, polished (6μm) samples over a range $5°\theta$ to $35°\theta$. Analysis of these diffraction patterns with reference to the ASTM Powder Diffraction file enabled the major crystalline phases present to be identified. In addition, approximate determination of the interplanar spacings d_{hkl}, were calculated via the Bragg equation

$$n\lambda=2d\sin\theta \qquad (3.1)$$

where n = the order of the given reflection

λ = the wavelength of the incident X-rays - 1.54Å for CuK_α radiation.

θ = the Bragg angle of deflection.

3.3 Post-sintering heat-treatments in the temperature range 1000°C-1800°C

3.3.1 Oxidation studies in the temperature range 950°C to 1400°C

Oxidation kinetics and subsurface reactions were studied over a range of temperatures 950°C to 1400°C for periods up to 100 hours duration. Studies were performed on selected materials; 201/3 in both as-sintered and heat-treated conditions, and 201/0 in as-sintered, heat-treated and HIP'ed conditions.

All specimens were cut to minimum dimensions of 5mmx5mmx5mm with at least one surface being the original billet surface from the sintering of the material. A single cut surface was ground and polished to 1μm finish, as in SEM sample preparation, and ultrasonically cleaned in preparation for oxidation. The original billet surfaces were left untreated, in the original state that they were fabricated for comparison with the processed surface.

Oxidation heat-treatments at all temperatures were performed under static air conditions at normal atmospheric pressures in a horizontal tubed open-ended SiC resistance furnace controlled by a stepless Eurotherm temperature controller to an accuracy of ±5°C.

Specimens were supported by platinum wire in an alumina boat, to reduce the possibility of reaction between the two, and were introduced into the hot zone of the furnace at a constant rate in order to reduce any anomalies in the observed oxidation kinetics which may be due to effects of thermal shocking.

The measurement of the oxide layer thickness as a function of time was used to determine the oxidation kinetics at various temperatures. The use of this method instead of weight gain vs time measurements was preferred because continuous removal and reintroduction of the specimen into the hot zone of the furnace resulted in extensive cracking and spalling of the oxide layer (via stresses introduced from the thermal expansion mismatch between the oxide layer glass and the substrate ceramic.

The oxide layer surfaces were analysed by EDAX in SEM and by X-ray diffraction to observe the phases present, and cross-sections were prepared for SEM and TEM to observed sub-surface reactions resulting from the oxidation treatment.

3.3.2 Heat-treatment studies upto 1500°C in inert gas atmosphere

The study of the microstructural development at both the surface and in the bulk of the as-sintered 201/3 ceramic. Specimens

for heat-treatment were prepared in a similar fashion to those for oxidation (Section 3.3.1), but polished to a finish of 1μm on all surfaces.

Heat treatments were performed in various atmospheres, nitrogen, argon to vacuum (10^{-05} torr) in a purpose-built vertical tube dual spiral SiC resistance furnace (figure 3.2). The temperature was controlled to an accuracy of ±5°C at maximum temperature by a stepless Eurotherm, monitored by a Pt-13%Rh/Pt thermocouple. The specimens, wound in platinum to avoid reaction with the alumina supports inside the furnace were lowered into the furnace while at room temperature, the furnace sealed to air, and the desired atmosphere admitted. Nitrogen and argon atmospheres were maintained at a slight overpressure to minimise the possibility of leakage of oxygen into the furnace. The furnace was then taken to the desired temperature for the required period of time, and following the heat-treatment allowed to cool via radiative heat loss to room temperature before removing the specimen from the furnace. The specimen was then sectioned and polished as described in Section 3.2 for microstructural analysis in TEM, SEM, optical microscopy and by X-ray diffraction.

3.3.3 Heat-treatment studies at temperatures in excess of 1600°C

The effects on the surface and bulk microstructure of the as-sintered and heat-treated 201/3 material at temperatures approaching the original sintering temperatures (~1800°C) was studied. Specimens for heat-treatment were similarly prepared as in Section 3.3.2, but were large in dimension (usually 10mmx10mmx10mm) due to the expected large scale surface reactions occurring at the high temperature. The specimen was coated with a viscous slurry made of a mixture of AlN or SiO_2 and Collodion, and set into a powder bed of boron nitride in a closed graphite crucible.

Figure 3.2 Schematic representation of the furnace used for heat-treatments in inert atmospheres.

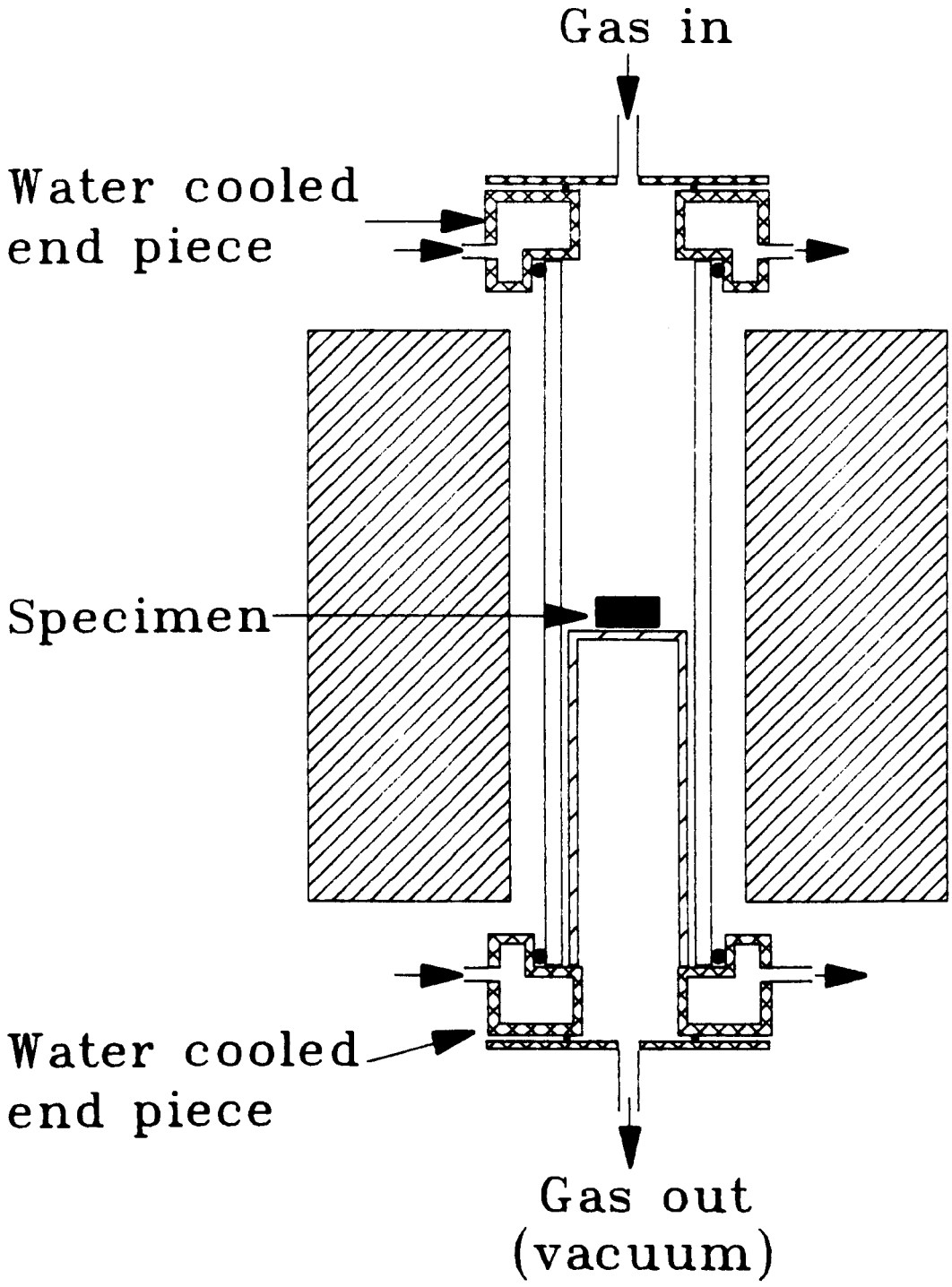
Gas in
Water cooled
end piece
Specimen
Water cooled
end piece
Gas out
(vacuum)

Heat treatment was performed in a vertical tubed inductively heated furnace in a nitrogen atmosphere similar in design to the one used in the previous section. A slight overpressure of nitrogen was maintained to avoid oxygen leakage into the furnace and subsequent reaction with the specimen.

3.4 Mechanical property and high temperature deformation

3.4.1 High temperature fracture - K_{IC} - temperature relation

The fracture toughness (K_{IC}) temperature relationship was investigated for material 201/3 in both the as-sintered and heat-treated variations, using the single-edge notched beam method (109) at temperatures between room temperature and 1500°C. Testing was performed on an Instron unit fitted with a double spiral SiC resistance furnace mounted vertically about the Instron cross head axis (figure 3.3), capable of operating at temperature with various bottled gases, eg. nitrogen, argon or vacuum (10^{-5} Torr) atmospheres.

The specimens used for all SENB tests were cut from billets with an annular diamond saw, and ground to rectangular bars of dimensions 20x4.8x2.4mm. Using a clock gauge, a notch 30% of the bar height (1.44mm) was cut using the annular diamond saw (figure 3.3). This depth of notch, (a/w)=0.3 was used to allow accurate K_{IC} values to be obtained. The bars were diamond polished to a standard 1µm finish to remove any surface flaws produced in the initial machining of the specimen. This procedure was necessary to minimize the effects that residual stresses have on the strength properties of the ceramic. It has been well established (156,157) that such machining introduces large compressive and tensile stress fields in the near surface regions of the material which may act as strength degrading zones. Therefore, every care was taken to ensure these residual stress zones were minimised by careful polishing.

Four point bend loading was chosen for all SENB tests in preference to three point loading to avoid interaction between the contact stresses and that at the root of the crack (105), and

Figure 3.3 Schematic representation of;

a) High temperature Instron testing System

b) Loading arrangement for fracture toughness determination

c) Specimen configuration

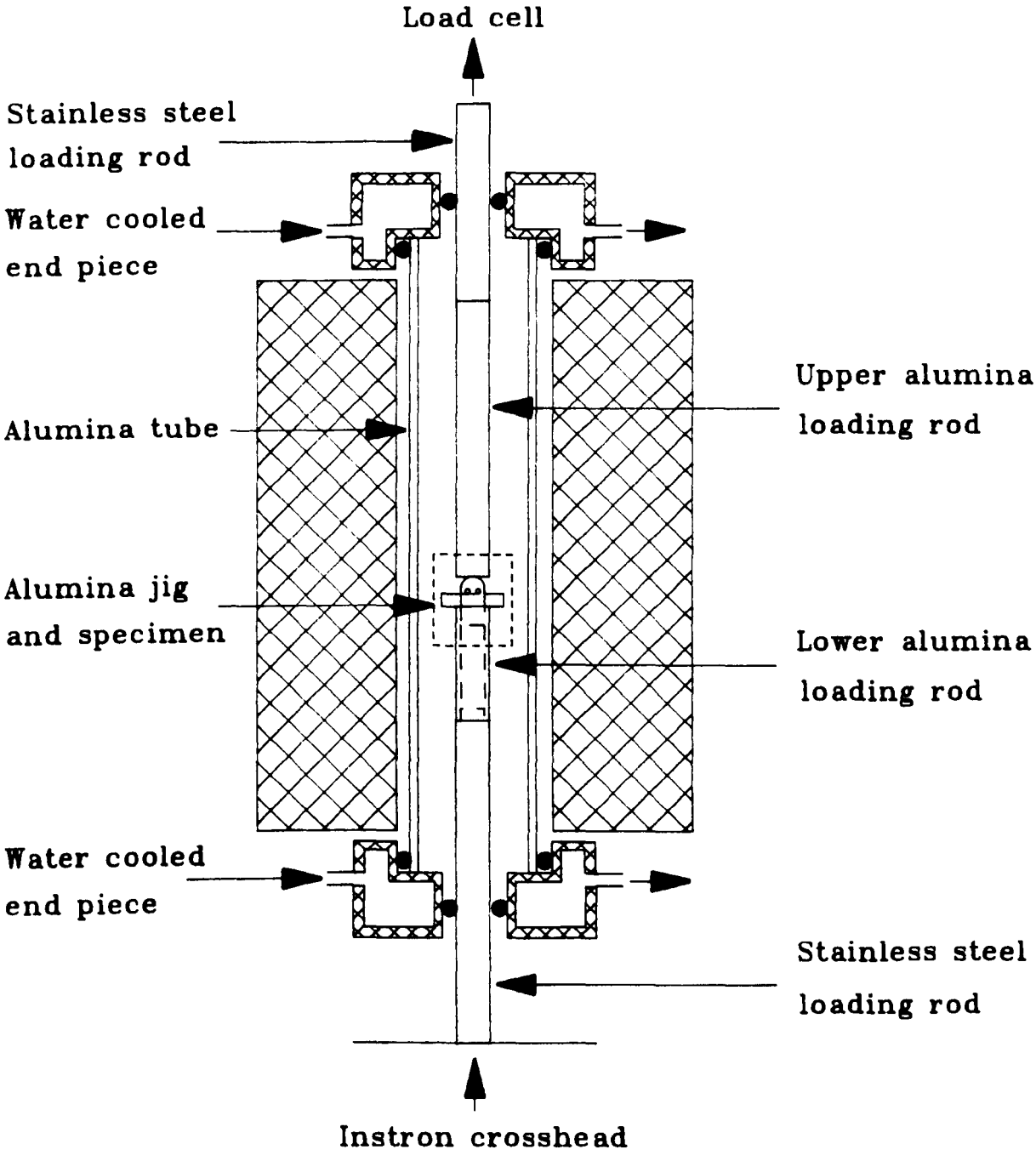
Load cell
Stainless steel loading rod
Water cooled end piece
Alumina tube
Alumina jig and specimen
Water cooled end piece
Upper alumina loading rod
Lower alumina loading rod
Stainless steel loading rod
Instron crosshead

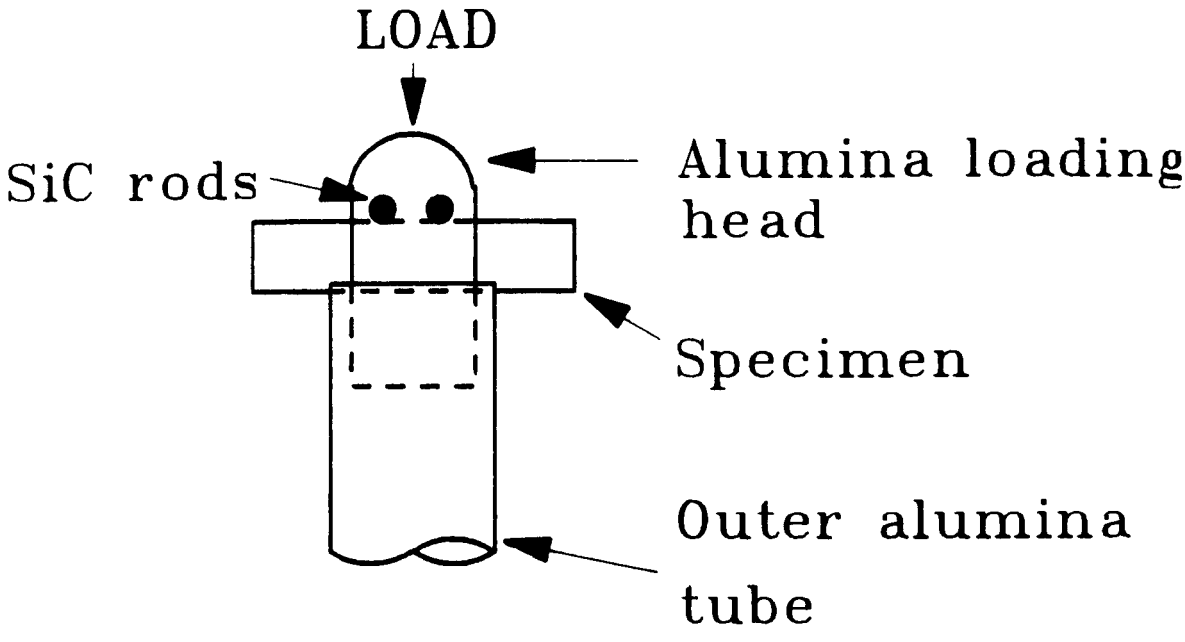
LOAD
SiC rods
Alumina loading head
Specimen
Outer alumina tube

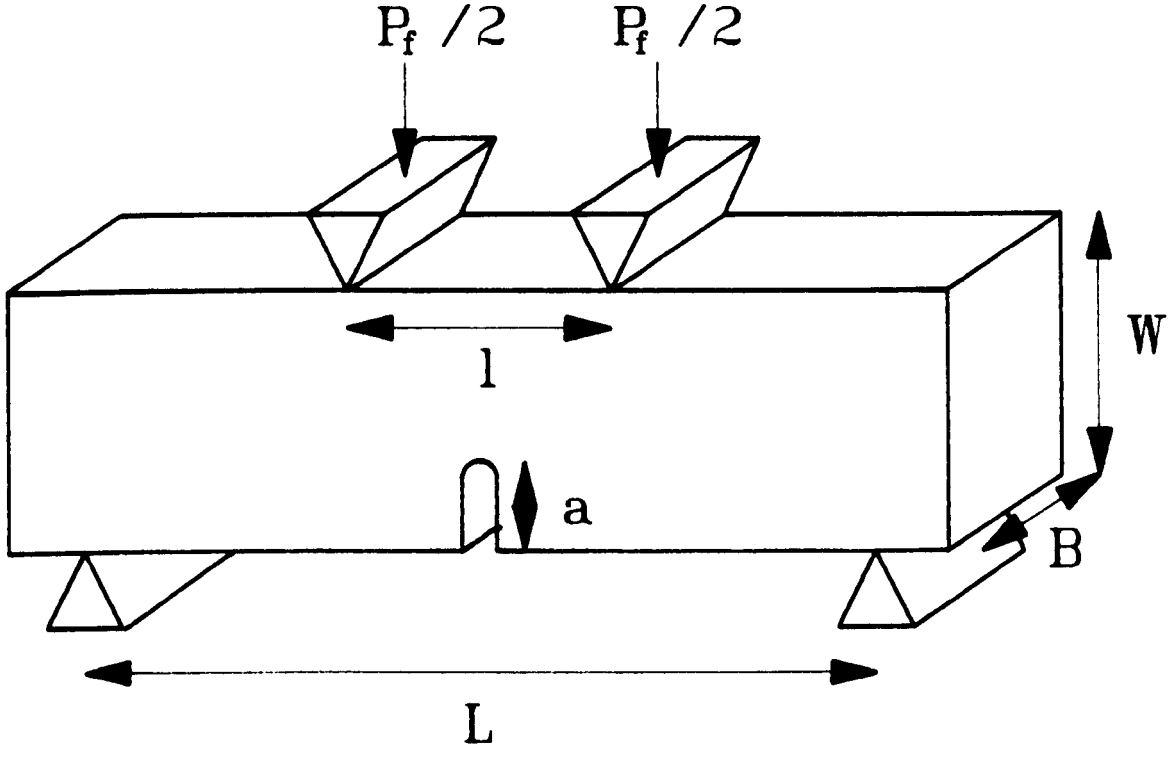
P_f /2
P_f /2
l
W
a
B
L

difficulties with the alignment of the specimen such that the upper loading rod is directly over the notch. The loading arrangement is shown in figure 3.3(b). The upper loading system consists of two SiC rods mounted in a recrystallised alumina rod. The upper part of the head was ground to a hemisphere to ensure that loading was equal about the two loading points. The lower loading points were the edges of a recrystallised alumina tube.

For testing, the specimen was carefully aligned in the jig as shown in figure 3.3(a), and fixed into place using Durafix glue to stop any movement of the specimen during introduction into the furnace. The specimen was introduced into the furnace, and raised into the hot zone region of the furnace to within approximately 2mm of the upper loading rod. The furnace was slowly heated to 500°C in air to burn off the glue fixing the specimen, then sealed (if necessary) to allow the gas or vacuum atmosphere to be admitted. Once this atmosphere was established, the furnace temperature was slowly run up to the desired temperature. The temperature was controlled by a stepless Eurotherm to an accuracy of ±5°C at temperature, monitored by a Pt/13% Rh/Pt thermocouple. The furnace temperature was allowed to equilibrate, and the cross-head was slowly moved up at a constant rate of 0.002 cm min^{-1} until fracture of the specimen. The fracture toughness (K_{IC}) was determined using the fracture stress P_F using the relationship

$$K_{IC} = \frac{3\, P_F(L-\ell)}{2bd^2}\, a_o^{\frac{1}{2}}\, Y(a_o') \qquad (3.2)$$

where $Y(a_o') = [3.86 - 6.15a_o' + 21.7(a_o')^2]^{\frac{1}{2}}$

P_F - load at fracture

$(L-\ell)$ - bending arm

a_o - notch depth $\quad a_o' = a_o/d$

b - specimen depth

d - specimen depth

Upon fracture, the furnace, jig and specimen was allowed to cool slowly to avoid the possibility of thermal shock of any part of the system. The broken bars were then removed from the furnace, and mounted and prepared for analysis in the optical and scanning microscopes, as described in section 3.3.2.

3.4.2 High temperature creep and stress rupture

The creep and creep rupture behaviour of a range of syalons was investigated over a range of temperatures up to 1400°C in both uniaxial compression and four point bending modes in ambient air atmospheres. These methods of testing were chosen for two reasons, (1) ease of specimen production and (2) ease of loading, both from the design of the loading arrangement and the calculation of the maximum stresses. All creep testing was performed using standard SiC resistance furnaces powered by a stepless Eurotherm controller with the hot zone temperature monitored by two parallel Pt/13%Rh/Pt thermocouples to an accuracy of ±5°C. The furnaces were of split design, allowing direct access to all of the loading system (figure 3.4). All testing was performed in a laboratory fitted with a thermostatically controlled air conditioning unit. This was necessary to reduce the effects of variations in the ambient air temperature which were found to affect the measured creep rates markedly. This was particularly essential for compressive creep measurements because of the inherently small deflections associated with the design of the specimen and method of testing.

(a) Creep data collection and recording

Recording of creep deflections in all creep experiments was performed by a linear variable differential transducer (LVDT) Type 1071B in conjunction with a Model 22 DC-DC signal conditioner, rigidly clamped onto the alumina loading rod (figures 3.4 and 3.5). A

capacitive type transducer was chosen in preference to the inductive type because of its greater thermal stability. The signal from the transducer is passed into an analogue to digital converter (ADC) unit where it was digitised and passed into a BBC model B microcomputer for storage. Due to the long term nature of creep experiments it was necessary to build an ADC unit whose stability was guaranteed over long periods (± 1 bit in 8192 over 250 hours). The ADC unit was able to input up to 4 channels, data from two creep experiments each consisting of one input from the transducer and one input from a silicon diode monitoring the temperature at the LVDT such that corrections to the creep rate from variations in the ambient temperature could be made if necessary. Data from each experiment was collected at 15 minute intervals and simultaneously displayed graphically on screen and stored on cassette tape. Upon termination of the creep experiment, the data was transferred from cassette tape to floppy disc for analysis. All collection and analysis of data was controlled through software written by the author, listed in appendix one.

(b) Compressive creep testing

Specimens for compressive creep testing were cut from a billet using a high speed annular diamond saw to dimensions of 5mm x 3mm x 3 mm. Care was taken to ensure that all faces and both ends were square, to avoid non-axial loading causing buckling of the specimen. The length (l) and width (w) ratio has been found to be a critical factor in compressive loading, for if ℓ/w is low, barrelling of the specimen may occur (158), and if ℓ/w is large, buckling may occur (159). These two effects have been found to be minimized for uniaxial loading if ℓ/w lies within the range 1.5 to 2.5 (159), in this case $\ell/w=1.66$. The specimen was polished to a finish of 1 μm on all faces and its dimensions recorded before being placed in the creep

furnace under the loading arrangement shown in figure 3.4. Loading of the specimen was by a lever system, where the applied load P_1 was amplified by a factor of 10.2 along the length of the lever arm, and applied by a vertical loading system directly to the specimen (P_2). The creep specimen was situated between two hot-pressed Sialon platens. These were chosen because of their known stability to temperatures in excess of 1300°C and their low reactivity with the Sialon creep specimens in comparison with either alumina or silicon carbide.

All creep experiments were conducted at constant temperature. Creep rates were observed at constant load for a period of 100 hours before the application of additional load to increment the stress. A period of 100 hours was allowed between loading to enable the observation of apparent steady state creep of the specimen. On completion of the experiment, the specimen was sectioned of analysis by X-ray diffraction, SEM and TEM.

c) Four-point bend and stress-rupture testing

Specimens for testing were cut from a billet using an annular diamond saw to dimensions 35mmx3mmx3mm. The specimen was polished to 1 μm on all four faces, with special attention being paid to the finish of the tensile face as failure is known to be initiated from surface flaws in brittle materials. The sharp corners were rounded off using 1200 grit SiC paper and 1μm diamond paste to reduce any effects caused by flaws. The specimen dimensions were recorded and placed in the creep furnace under the loading arrangement as shown in figure 3.5. Unlike the loading of the compressive specimen, load P was applied directly to the loading rod, magnification caused by loading on the arm was not necessary as the required stresses for four-point bending were easily attained by this method of loading.

Figure 3.4 Schematic representation of the compressive creep apparatus and loading arrangement.

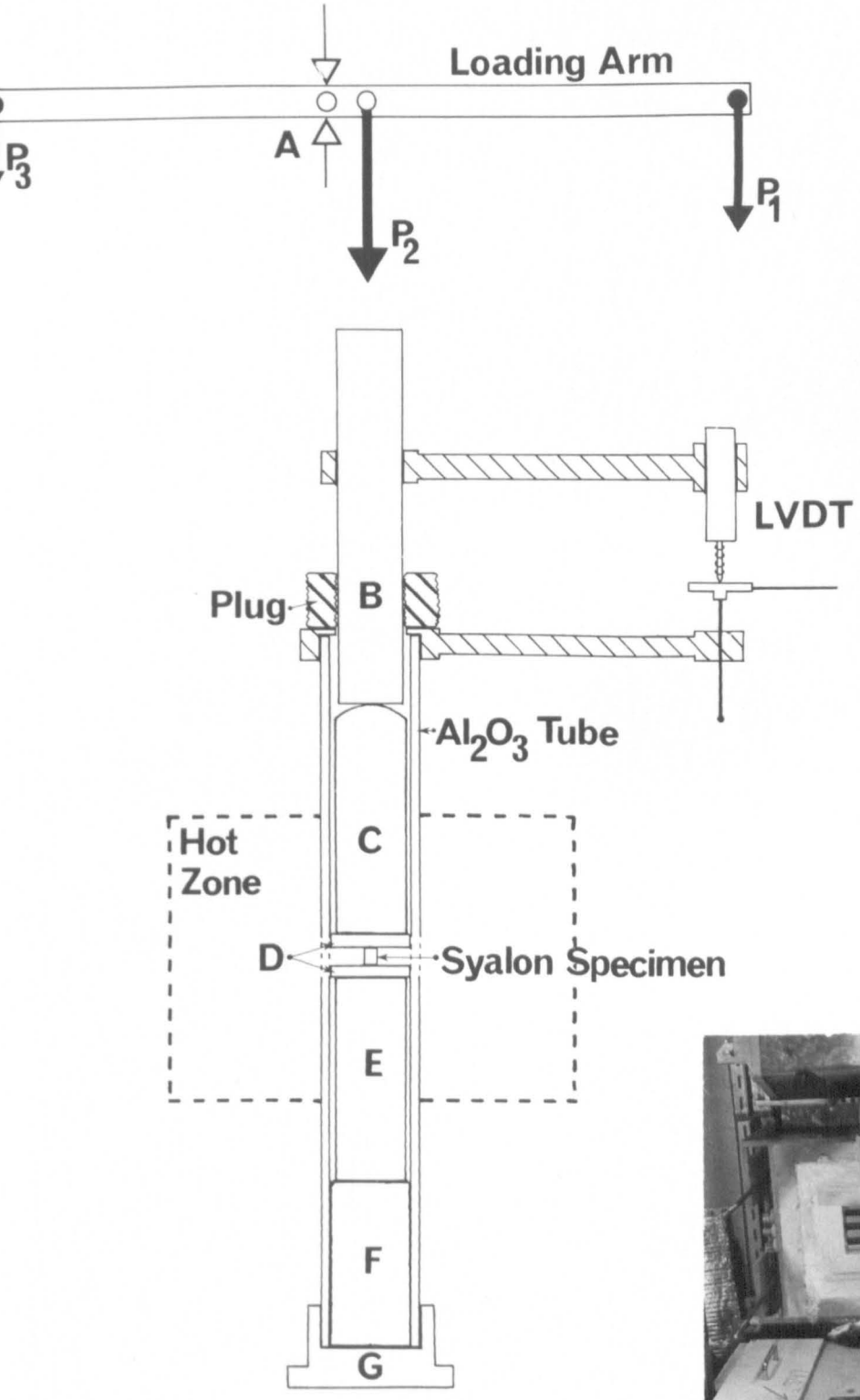
Loading Arm
A
P_3
P_2
P_1
LVDT
Plug
B
Al_2O_3 Tube
Hot Zone
C
D
Syalon Specimen
E
F
G

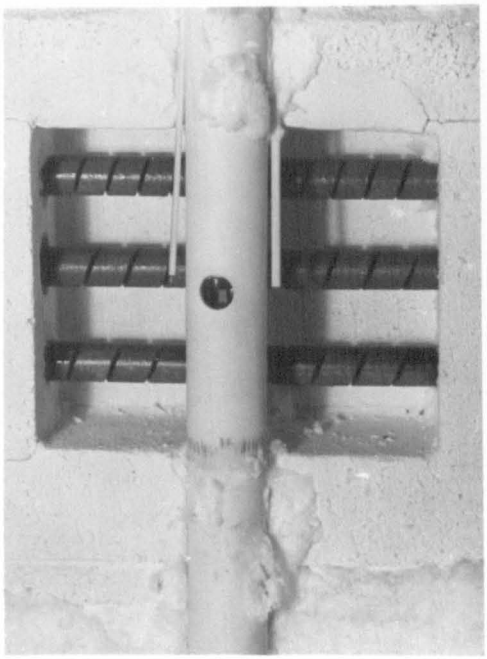

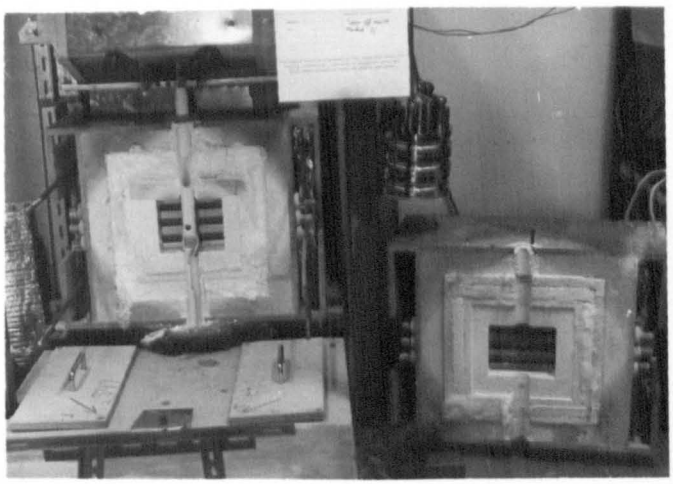

The specimen was loaded in four point bend configuration between four hot pressed Sialon cylindrical pins, the upper points being set 15mm apart, and the lower 30mm apart. The upper loading points were mounted in a recrystallised alumina head whose top had been carefully domed to ensure axial loading. The lower loading points were set into a 'Refel' SiC beam. Stress and strains on the outer fibre in four point bend were calculated from the relationships given by G.W. Hollenberg et al (160)

$$\sigma_{max} = \frac{3(L-\ell)P}{bh^2} \quad \frac{(2N+1)}{3N} \tag{3.3}$$

$$\varepsilon_{max} = \frac{2h(N+2)}{(L-a)(L+2a)} \cdot Y_L \tag{3.4}$$

where σ_{max} and ε_{max} are the stress and strain in the outer fibre, ie. at Z=h/2.

Creep experiments were conducted under isothermal conditions, with incremental loading at 100 hour intervals, so that the apparent steady state creep rates could be monitored. All data was collected and stored by a BBC microcomputer. Creep-rupture experiments were conducted under isothermal conditions. The specimen was loaded to a predetermined stress at temperature and left until failure.

Upon removal, the specimens were prepared for analysis in TEM, SEM and X-ray diffraction.

Figure 3.5 Schematic representation of the four point bend creep apparatus and loading arrangement.

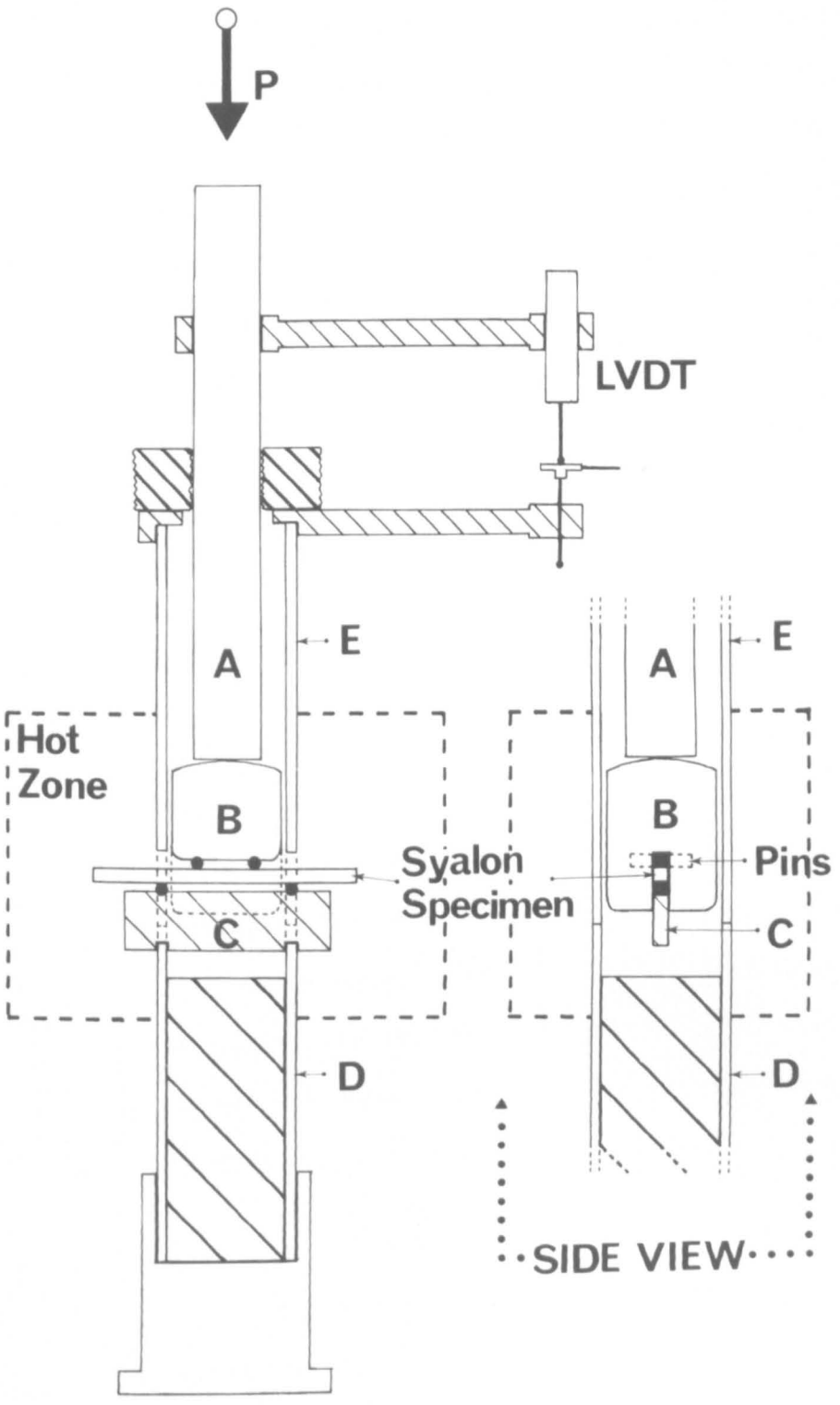
P
LVDT
A
E
Hot
Zone
B
Syalon
Specimen
C
D
A
E
B
Pins
C
D
SIDE VIEW

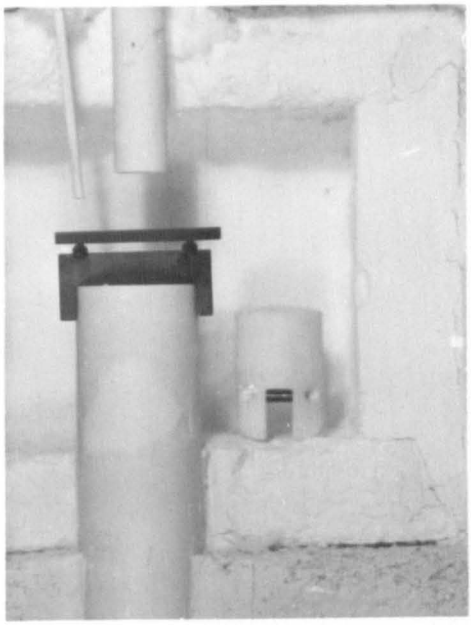

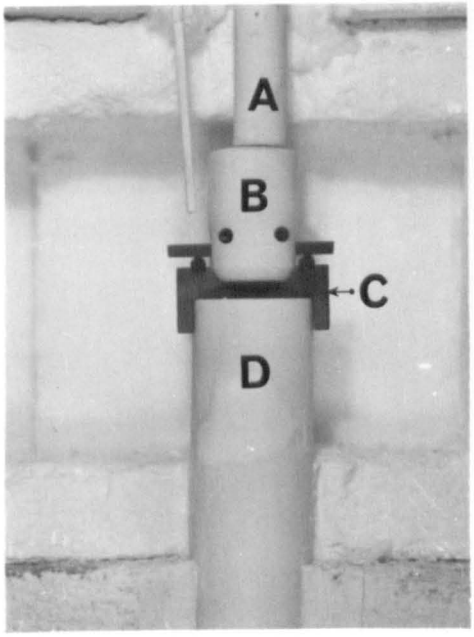
A
B
C
D

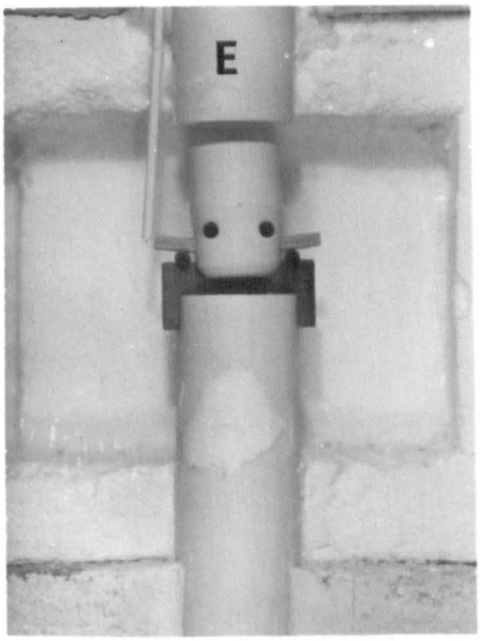
E

CHAPTER 4 - MICROSTRUCTURE AND CRYSTALLISATION

This chapter describes the microstructure and crystallisation kinetics of the current range of Syalon ceramics manufactured by Lucas-Cooskon-Syalon Ltd. Emphasis is placed upon the requirement to attain a fully crystalline β'/YAG ceramic through careful balancing of the composition, and reduction in the impurity levels, particularly calcium and fluorine which have been shown to seriously effect the devitrification of the grain boundary phase.

4.1 Microstructural characterisation of sintered ceramics

4.1.1 Microstructure of sintered LCS201

The microstructure of the ceramic following the sintering cycle described in section 3.1 is shown in figure 4.1. The microstructure consists of mainly small β'-Sialon grains, <1μm to 5μm across the basal plane, and up to 10μm along the c-axis, and a small amount of a second crystalline sialon phase which was identified as the related α'-Sialon phase (68,161). α'-Sialon is stabilised by the incorporation of yttrium into the crystal structure (162) hence making it easily identifiable using back-scattered imaging in the SEM. α'-grain size was found to be similar to that of β' grains, 1μm to 5μm across the basal plane and up to 10μm along the c-axis. The ratio β'/α' was measured by X-ray diffraction using the relationship,

$$\frac{\beta}{\alpha} = \frac{I_{101}(\beta) + I_{201}(\beta)}{I_{102}(\alpha) + I_{210}(\alpha)}. \qquad (4.1)$$

The α' levels in these sintered materials was calculated to be approximately 7-8% by volume.

Analysis of these phases show the aluminium substitution level in the β' to be x~0.3 hence giving an approximate composition from the general relationship (67) as;

$$Si_{2.7}\ Al_{0.3}\ O_{0.3}\ N_{3.7} \qquad (4.2)$$

Figure 4.1 The microstructure of sintered LCS 201

a) Backscattered (atomic number contrast) with EDX analysis of α' and β' phases

b) Transmission electron micrographs with selected area diffraction pattern from β'. Light element EDX if the glass phase is given (top) in comparison with a comparable low nitrogen containing sialon glass phase.

	Glass Composition (at %)	Eutectic Composition (at %)
Al	28.2 ± 0.4	27.6
Si	50.2 ± 0.5	52.1
Y	21.6 ± 0.4	20.3

Fig 4.1

(a)

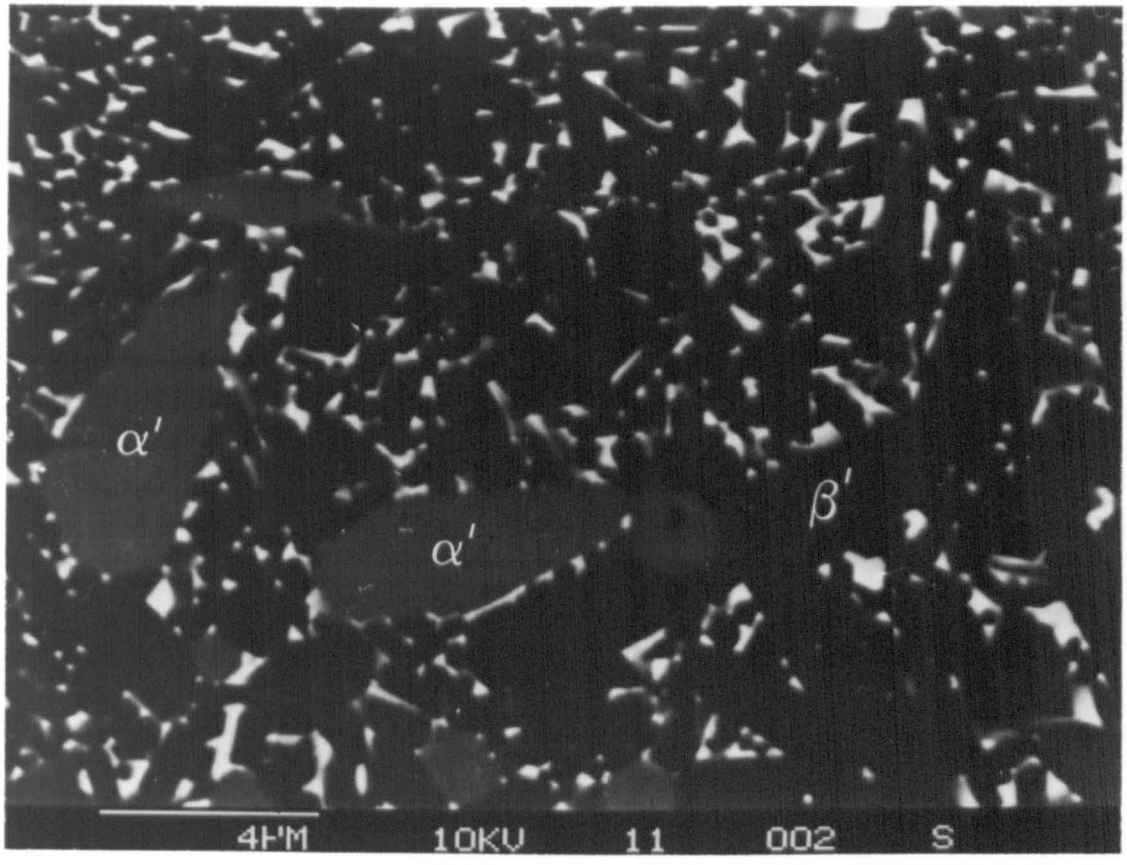

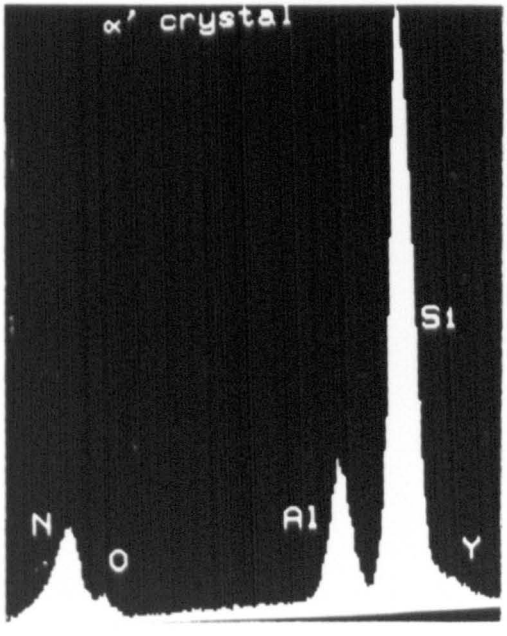

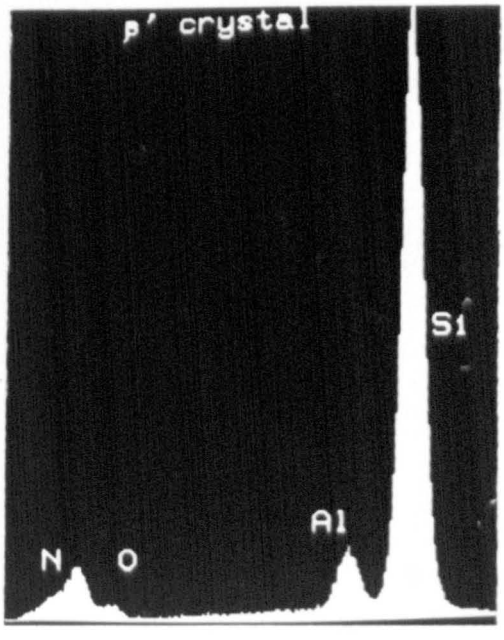

Fig 4.1

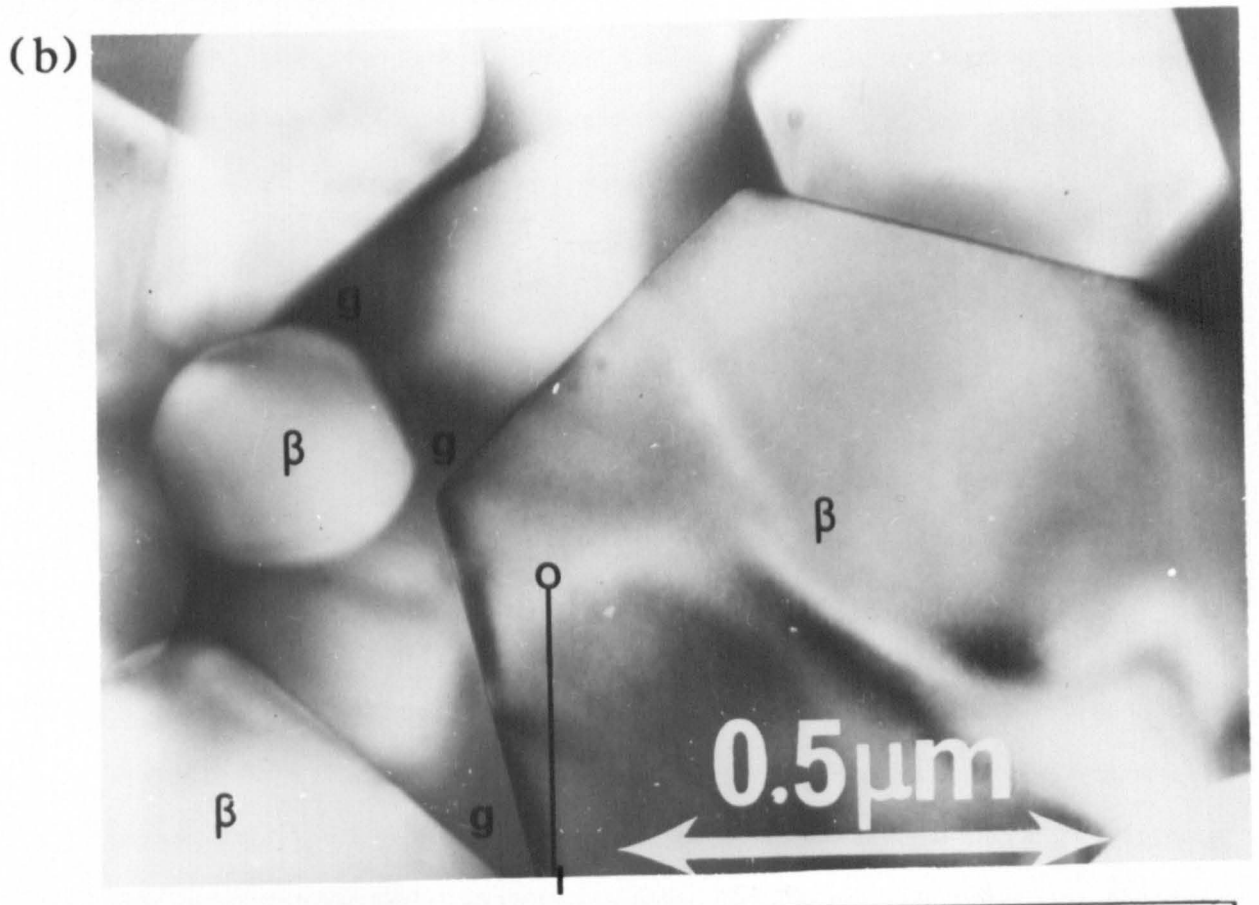

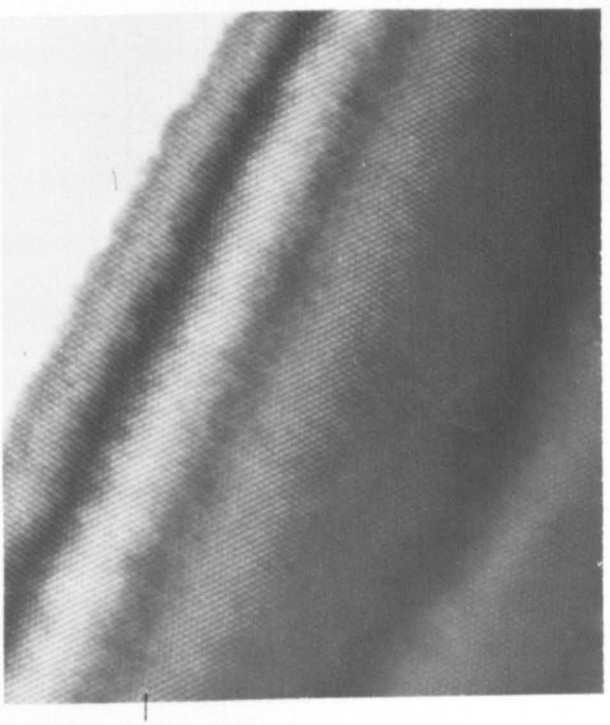

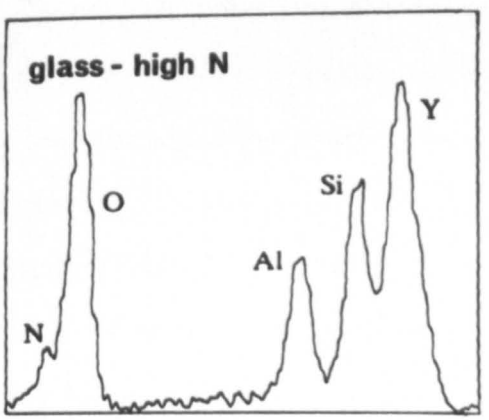

β′ [0001]

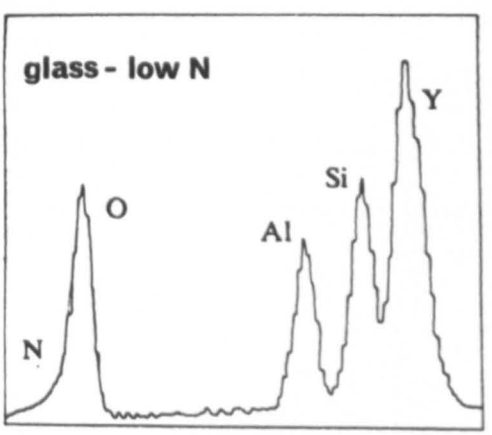

Similarly α' was found to have a higher aluminium substitution level and a small amount of yttrium which stabilises the structure. Light element EDX analysis of this phase semi-quantitatively indicates that the O/N ratio is similar to that in the β', the composition having been shifted from the β' solid solution line along a line of constant O/N ratio to the point intersecting with the $M_x(Si,Al)_{12}(O,N)_{16}$ plane, figure 4.2, having a composition, from the general composition by Jack (162).

$$Y_{0.41}\ Si_{10.4}\ Al_{1.6}\ O_{1.2}\ N_{14.8} \quad (4.3)$$

The second phase is a semi-continuous Y-Si-Al-O-N glass phase (figure 4.1). This phase showed no diffraction contrast on tilting, only a weak diffuse diffraction pattern, and was easily damaged by prolonged exposure to the electron beam. Dark field imaging using the diffuse ring obtained in selected area diffraction (figure 4.1b) shows the glass matrix phase to be continuous throughout the structure, even along two grain β'-β' grain boundaries. Two trace intergranular phases were identified. Firstly yttrium N-α-wollastonite ($Y_2Si_2O_4N_2$) was detected by XRD. No crystalline intergranular phase was detected microscopically, and as only the strongest diffraction peaks were evident, it was concluded that the yttrium wollastonite phase only occurred in trace amounts. The existence of this phase is of particular concern as studies in the Si_3N_4-SiO_2-Y_2O_3 pseudoternary system by Lange (95) has shown an instability of a range of quaternary phases in the Y-Si-Al-O-N system. These compounds show catastrophic oxidation properties at temperatures around 1000°C due to transformation to yttrium disilicate ($Y_2Si_2O_7$) with associated volume changes as shown in figure 2.2. The existence of the yttrium α-wollastonite phase, even in small quantities may have two possible detrimental effects on the properties of the ceramic at temperatures

around 1000°C. Firstly, the transformation will increase the oxidation kinetics to unacceptable levels at this temperature, and secondly, internal stresses due to the transformation to $Y_2Si_2O_7$ may if severe enough cause cracking, or at least cause a reduction in strength.

The second trace impurity detected was analysed as containing major amounts of iron and silicon. The inclusions are mainly present in the form of discrete particles dispersed throughout the intergranular sites of the structure, as shown in figure 4.3(a). Occasionally the iron forms large agglomerates, ~10μm, within the structure (figure 4.3b). Iron is commonly found as a result of the nitriding of silicon, from the production of the powder. During sintering, Fe enhances the decomposition of Si_3N_4 forming a highly distorted iron silicide ($FeSi_2$) structure (26).

EDX analysis of the intergranular phase indicates the composition lies close to the ternary eutectic of the Y-Si-Al-O-N system. If the nitrogen content is neglected, then the glass phase can be represented as metallic oxides and may be more conveniently plotted on the Y_2O_3-SiO_2-Al_2O_3 ternary phase diagram as shown in figure 4.2.

The glass phase shows no evidence of impurities such as fluorine or calcium. The presence of these in the intergranular regions has been shown to seriously inhibit complete crystallisation (42,163), by stabilisation of regions containing high concentrations of impurity ions. These regions remain glassy even after prolonged thermal cycling, resulting in severe degradation at elevated temperatures.

Current technological advances now allow the detection of light elements ($Z \leq 9$) by windowless EDX and electron energy loss spectroscopy (EELS). The former is simply a direct extension of the widely used

Figure 4.2 The Y-Si-Al-O-N phase diagram.

Fig 4.2

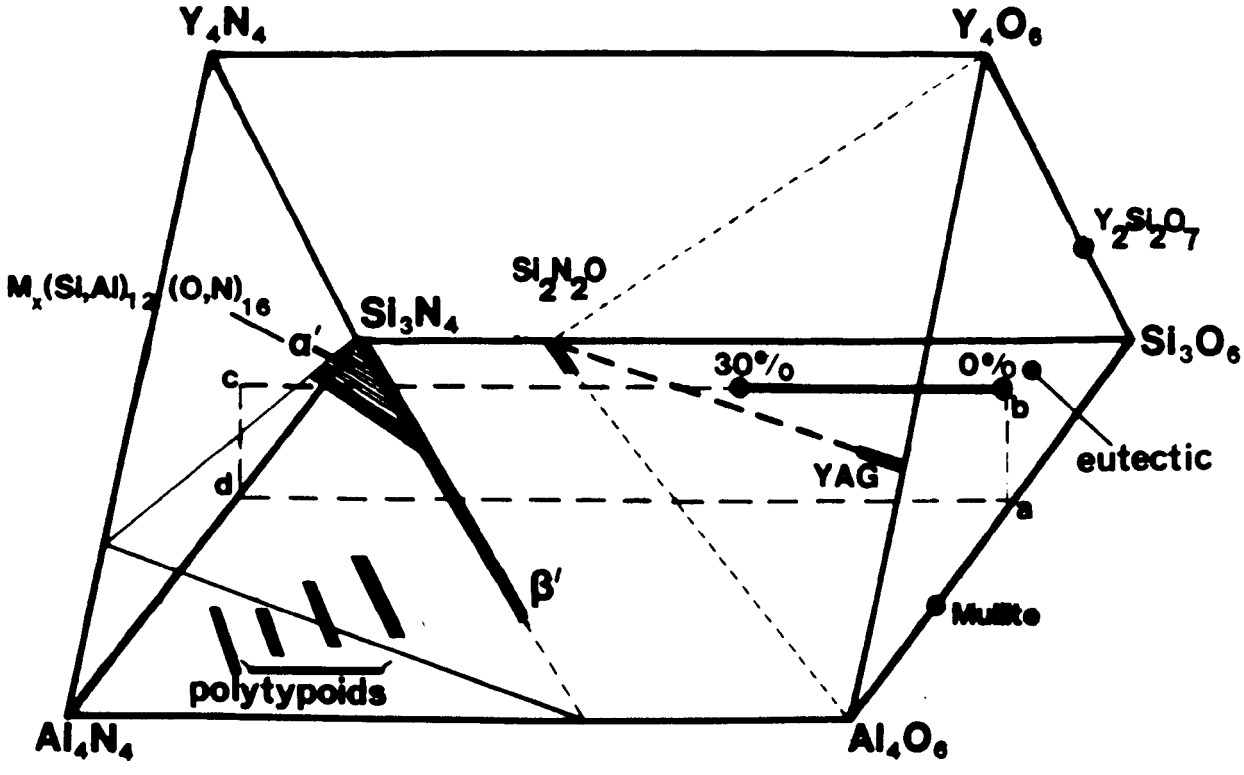
Y4N4
Y4O6
Y2Si2O7
Si2N2O
Mx(Si,Al)12(O,N)16
α'
Si3N4
Si3O6
c
30%
0%
b
eutectic
YAG
d
a
β'
Mullite
polytypoids
Al4N4
Al4O6

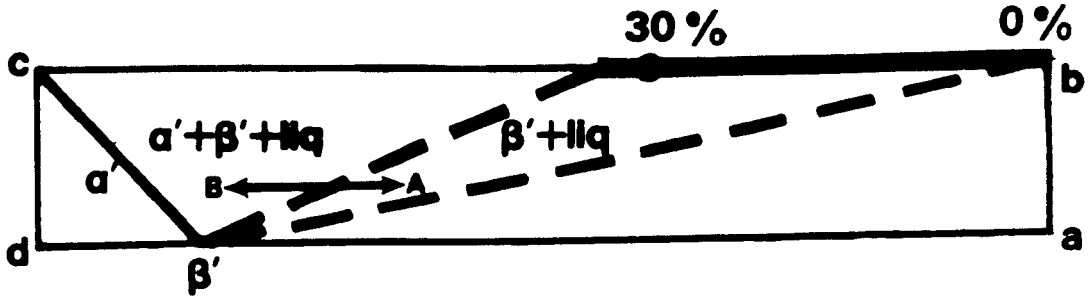
30 %
0 %
c
b
α'+β'+liq
β'+liq
α'
B
A
d
a
β'

Figure 4.3 SEM backscattered image of a large iron silicide inclusion

Fig 4.3

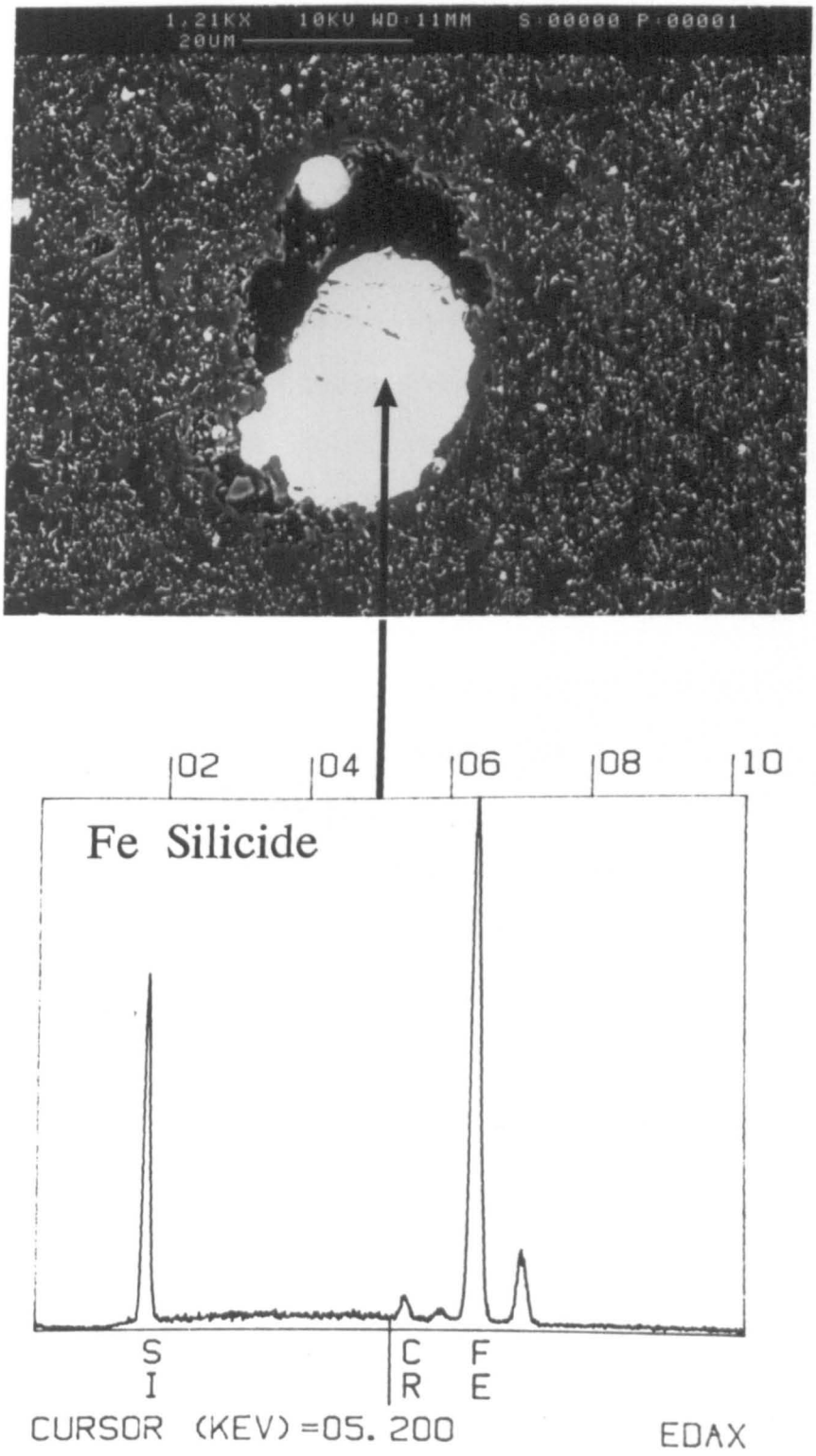
1.21KX 10KV WD:11MM S:00000 P:00001
20UM
02
04
06
08
10
Fe Silicide
S
I
C
R
F
E
CURSOR (KEV) =05. 200
EDAX

EDX technique, with the beryllium window removed to avoid the adsorption of low energy x-rays. The latter utilises the characteristic energy losses due to interaction between the electron beam and the specimens inner electron shell.

Analysis using these two methods show measureable levels of nitrogen in the intergranular glass (figure 4.1, 4.4). Care had to be taken in the detection of the light element levels using high energy electron beams (400KV) in the TEM. Electron beam damage imparted to the specimen was found to cause a measured decrease in the nitrogen levels. Over extended count times the detected levels of nitrogen in the intergranular regions dropped to zero. Evolution of nitrogen as a result of the irradiation damage is thought to be responsible for this effect. Therefore it was necessary in all these analyses to use short collection times to avoid this phenomena.

The use of light element detection techniques give direct evidence of significant levels of nitrogen present in the grain boundary glass in the high polytypoid additive materials.

4.1.2 Microstructural development with increasing polytypoid content

The variation in the polytypoid addition has been found to have observable effects upon the microstructure of the sintered ceramic. The starting compositions of these materials are shown in figure 3.1. Figure 4.5 shows backscattered images contrasting the differences between the low polytypoid ceramic (2% addition) and the high polytypoid 201 ceramic (8% addition). The most significant observable effect the increasing addition has on the microstructure is the formation of α' with increasing levels. Figure 4.6 shows X.R.D. traces for ceramics with polytypoid levels ranging from 2% to 8%. Up to 6% addition, the only crystalline phase detected is β', the only other phase being detected was glass. With the addition level

Figure 4.4 EELS spectra obtained from

a) Low nitrogen LCS 101 glass

b) High nitrogen LCS 201 glass

c) LCS 201 β' crystal

d) Silicon oxynitride

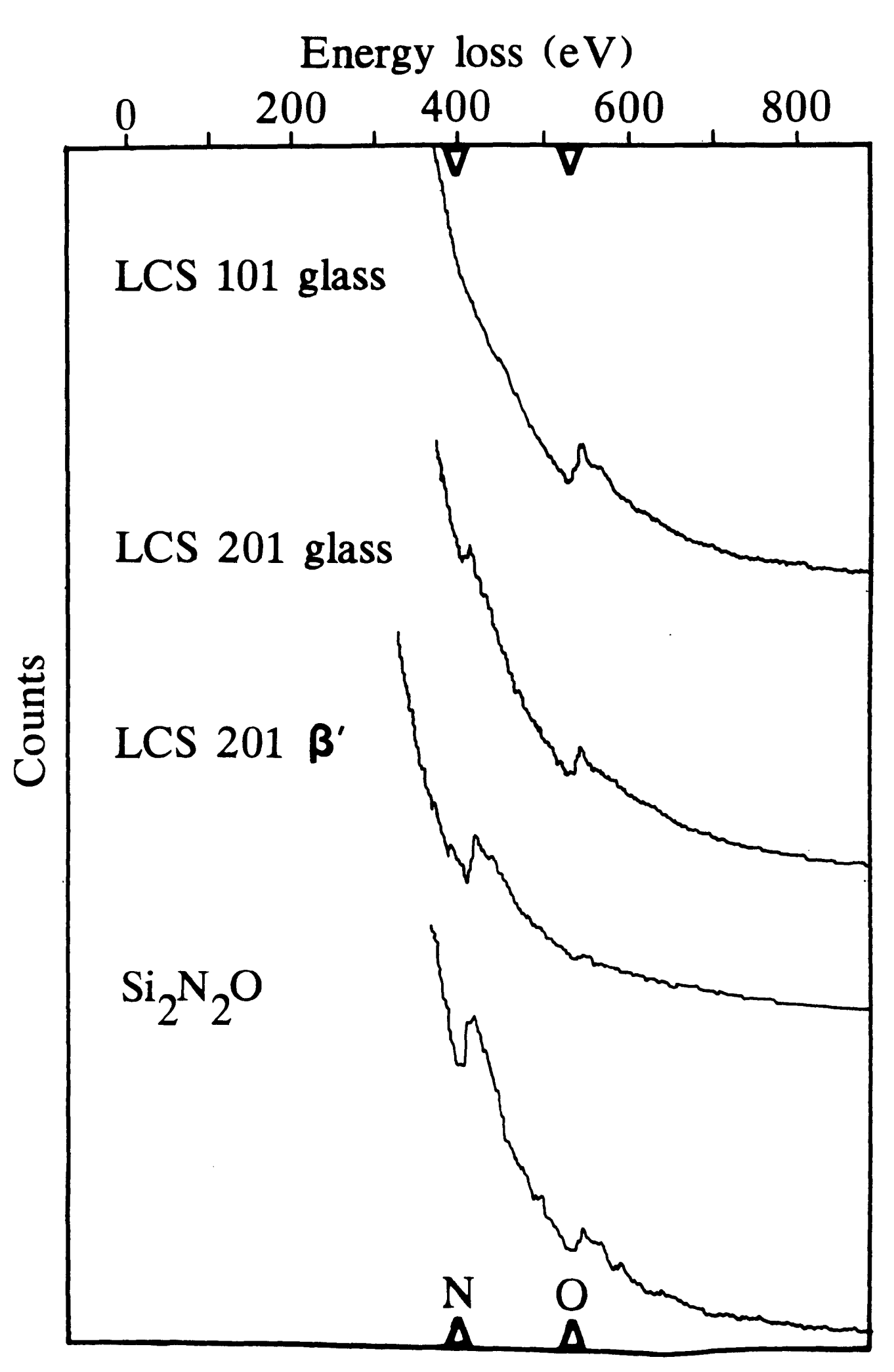
Energy loss (eV)
0
200
400
600
800
LCS 101 glass
LCS 201 glass
LCS 201 β′
Si2N2O
N
O
Counts

Figure 4.5 Backscattered electron micrographs of ceramics fabricated with varying AlN/21R polytypoid additions;

a) 201/2 - 2% polytypoid

b) 201/4 - 4% polytypoid

c) 201/6 - 6% polytypoid

d)→f) billet surface microstructures of the above compositions

g) variation of aluminium substitution levels with increasing polytypoid addition.

(a)

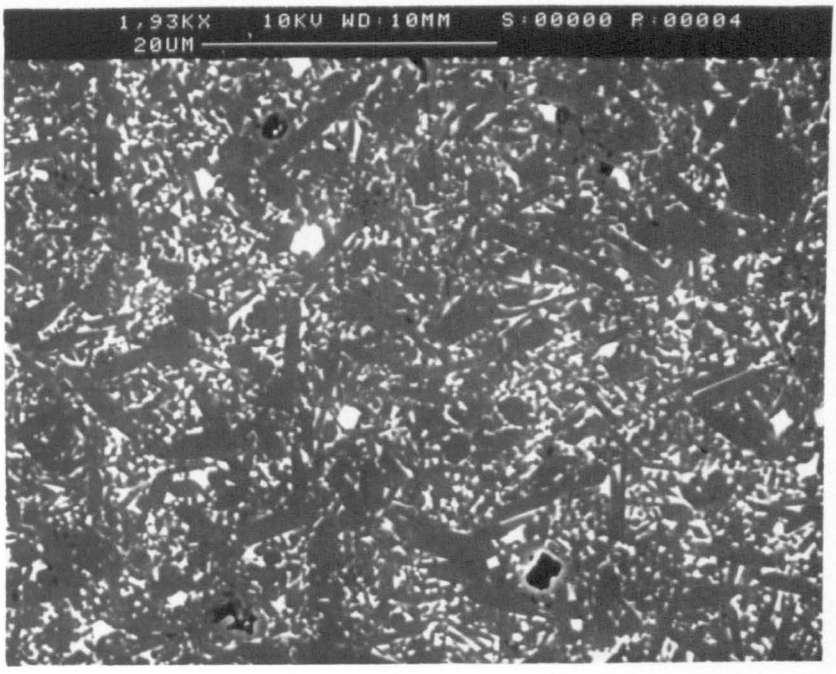
1,93KX 10KV WD:10MM S:00000 P:00004
20UM

Fig 4.5

(b)

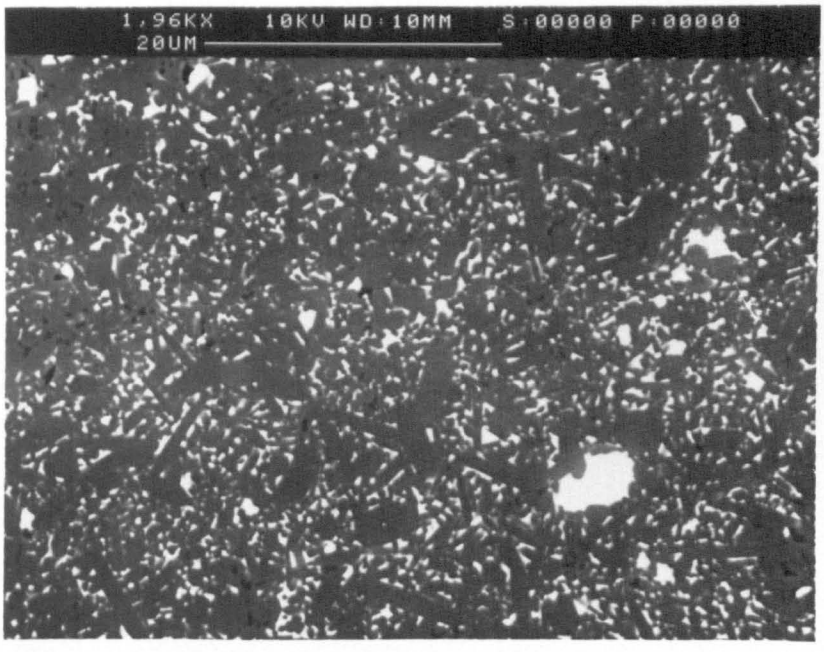
1,96KX 10KV WD:10MM S:00000 P:00000
20UM

(c)

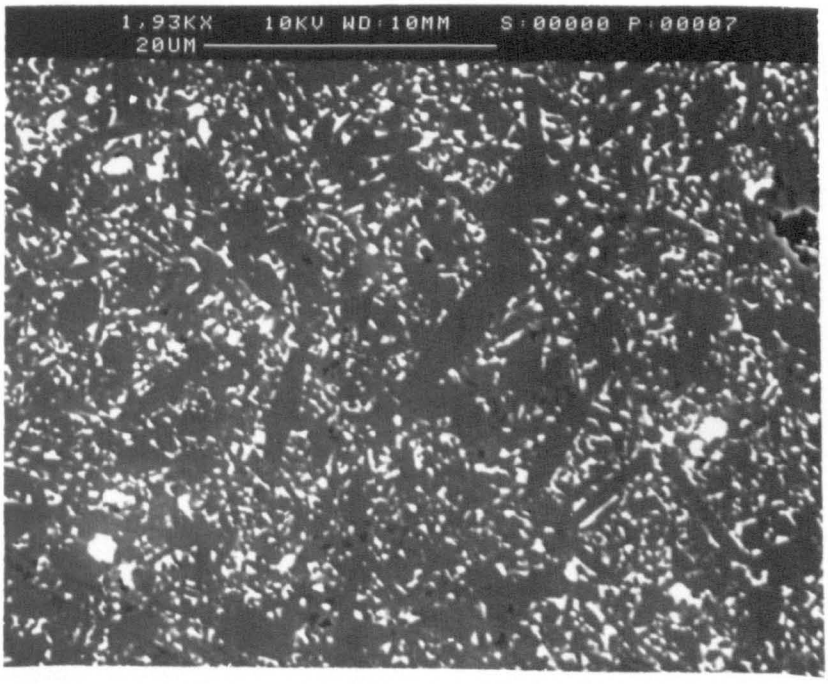
1,93KX 10KV WD:10MM S:00000 P:00007
20UM

Fig 4.5

(d)

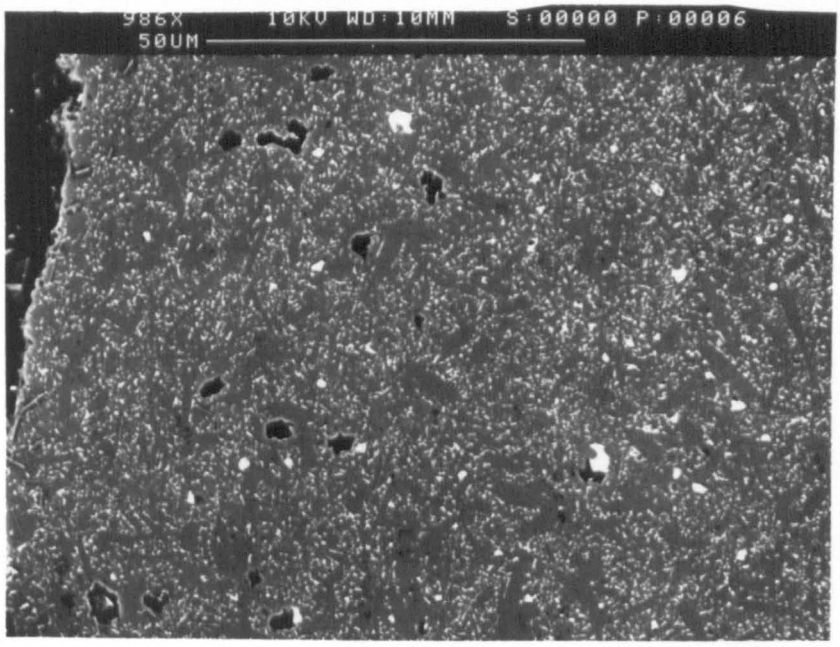
986X 10KV WD:10MM S:00000 P:00006
50UM

(e)

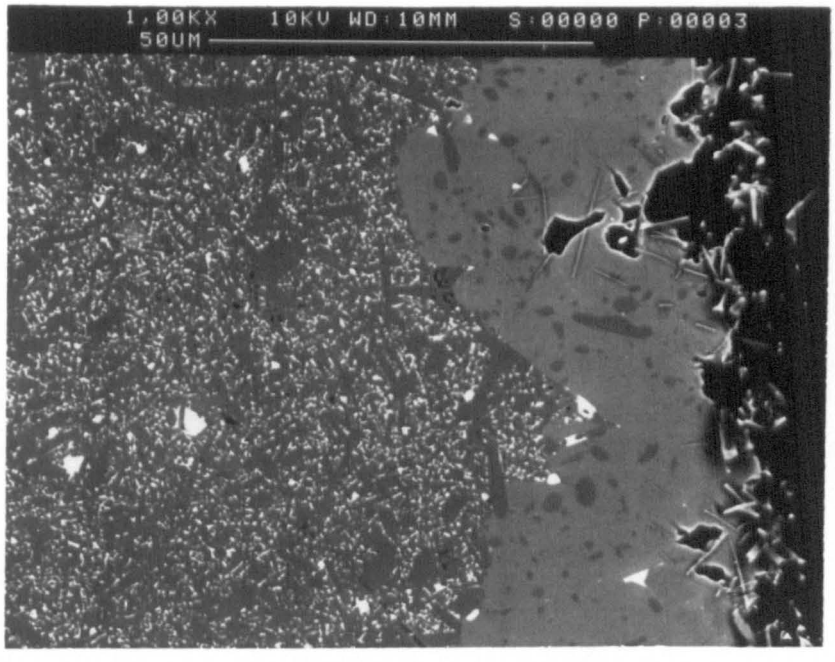
1,00KX 10KV WD:10MM S:00000 P:00003
50UM

(f)


493X 10KV WD:10MM S:00000 P:00009
100UM

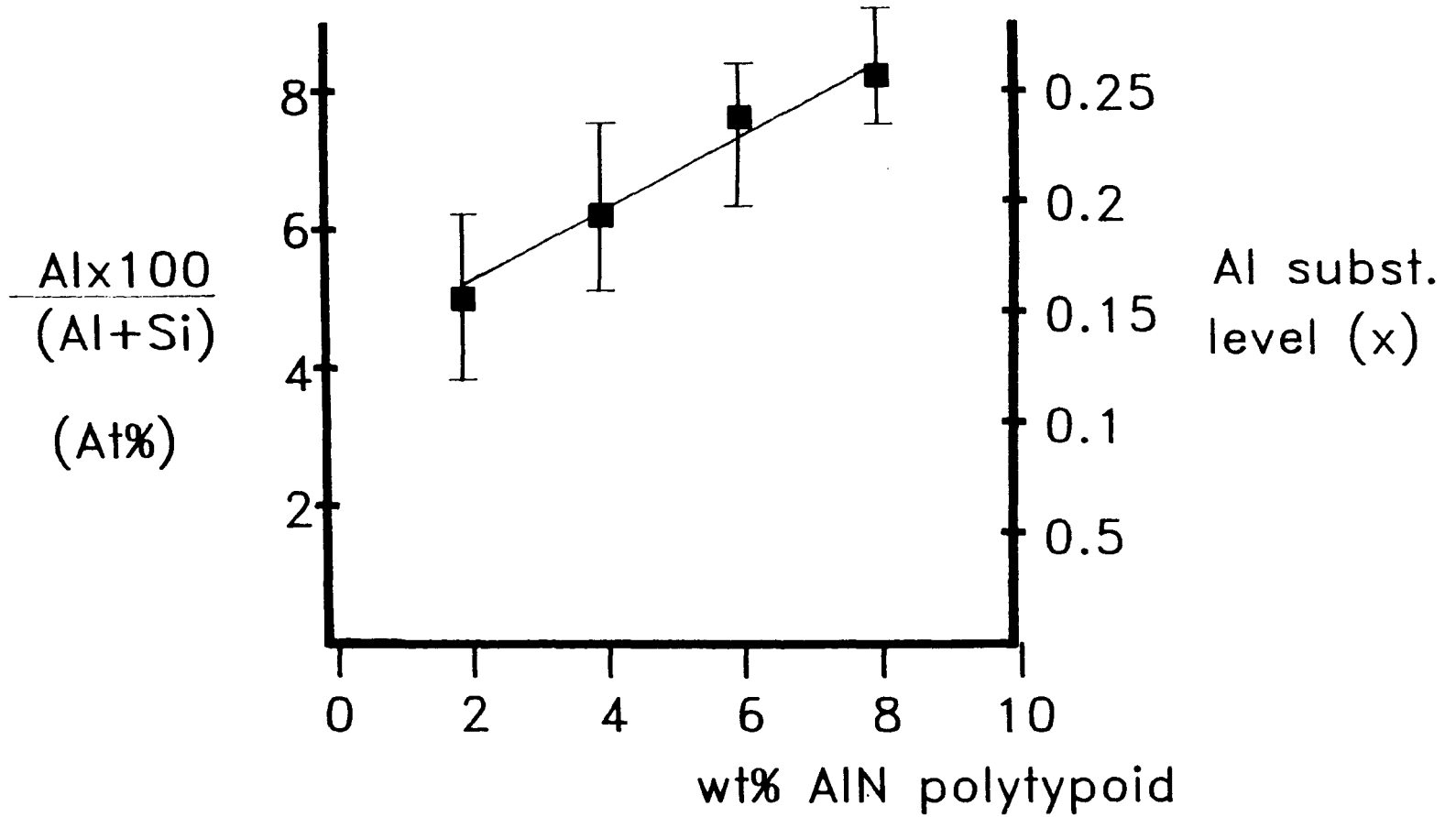

Figure 4.5 Variation of substitution level with increasing polytypoid addition

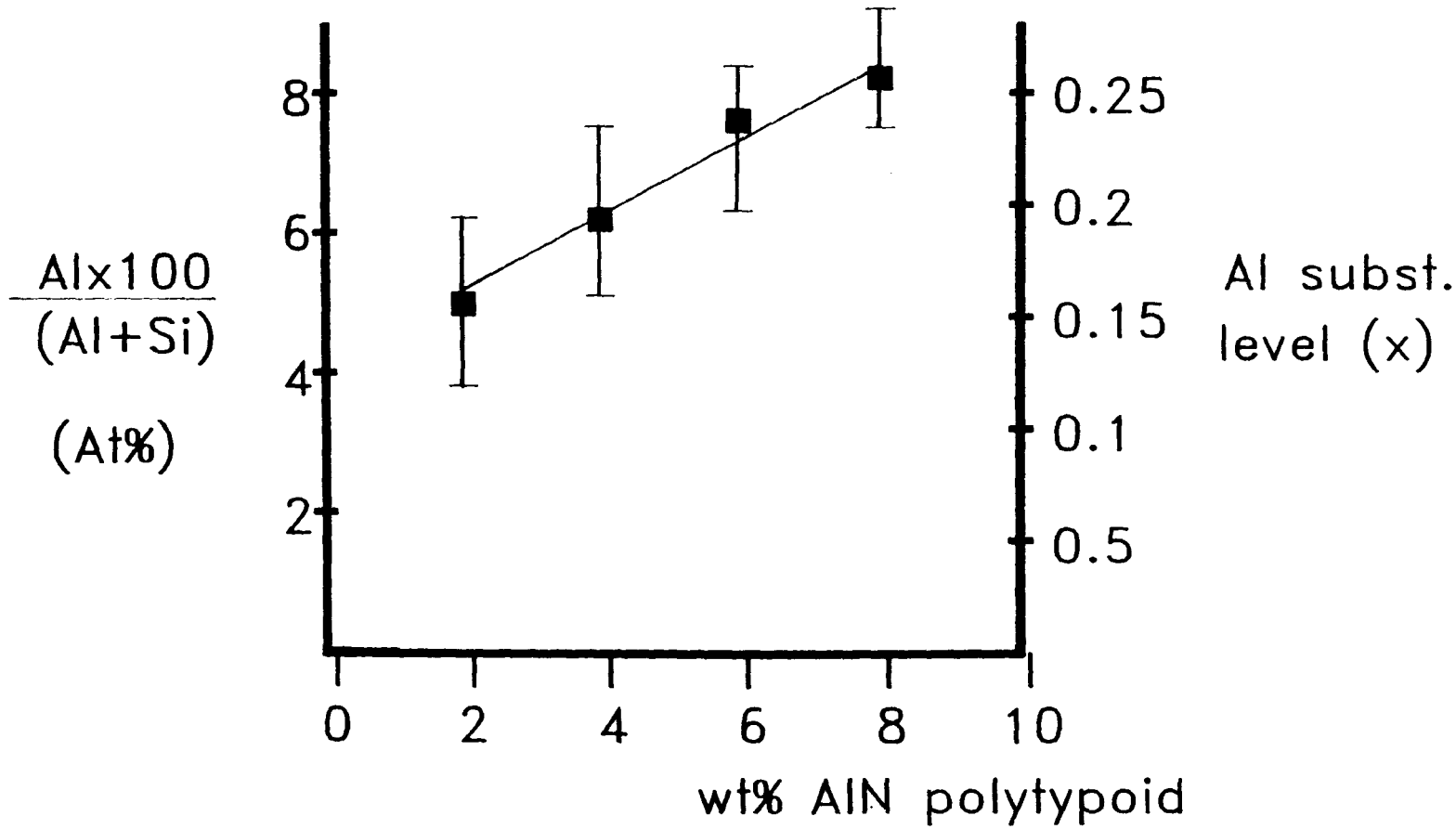

Figure 4.5 Variation of substitution level with increasing polytypoid addition

Figure 4.6 X-ray diffraction spectra of ceramic fabricated with varying polytypoid additions.

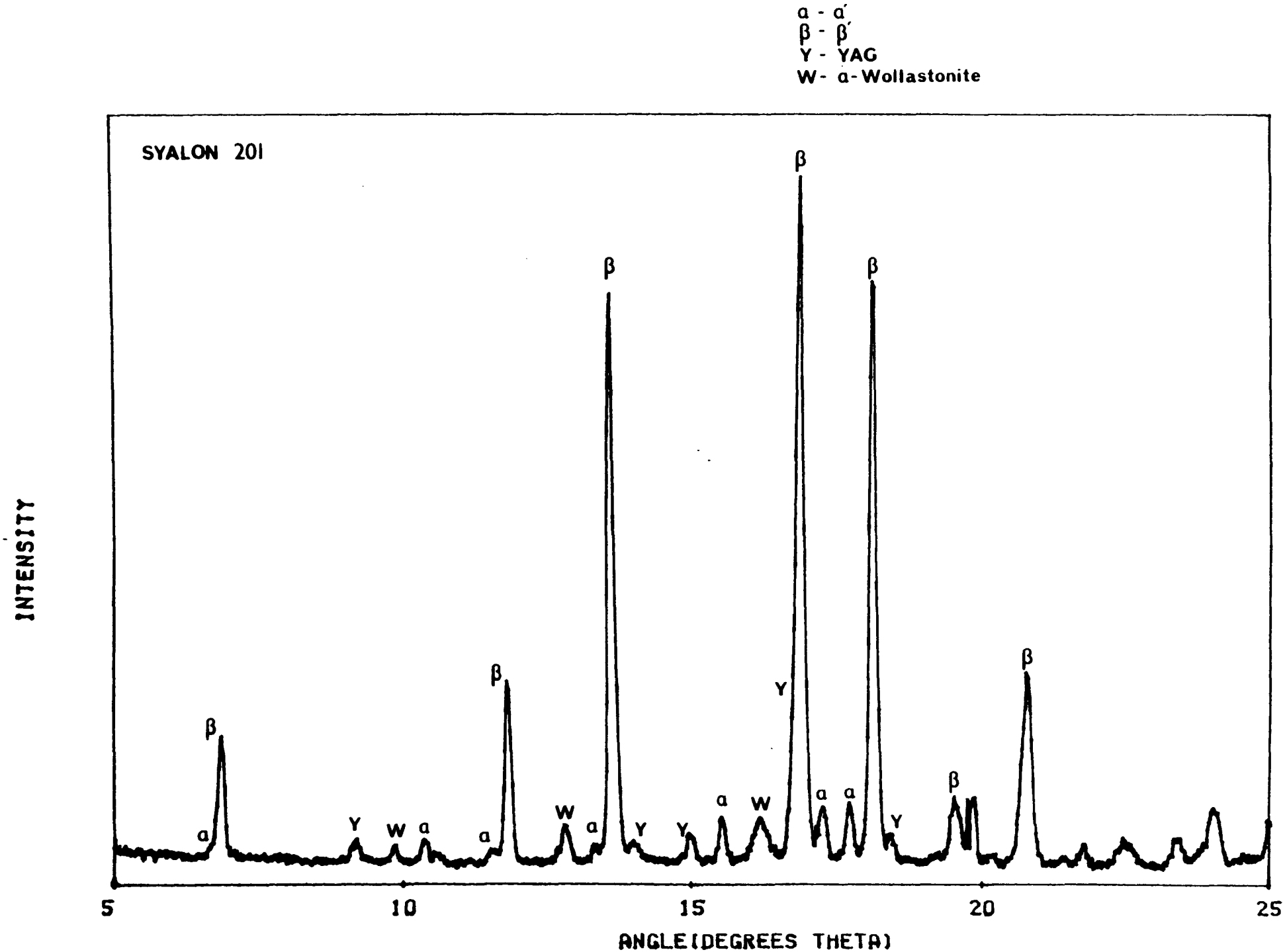
α - α'
β - β'
Y - YAG
W - α-Wollastonite
SYALON 201
INTENSITY
5
10
15
20
25
ANGLE(DEGREES THETA)

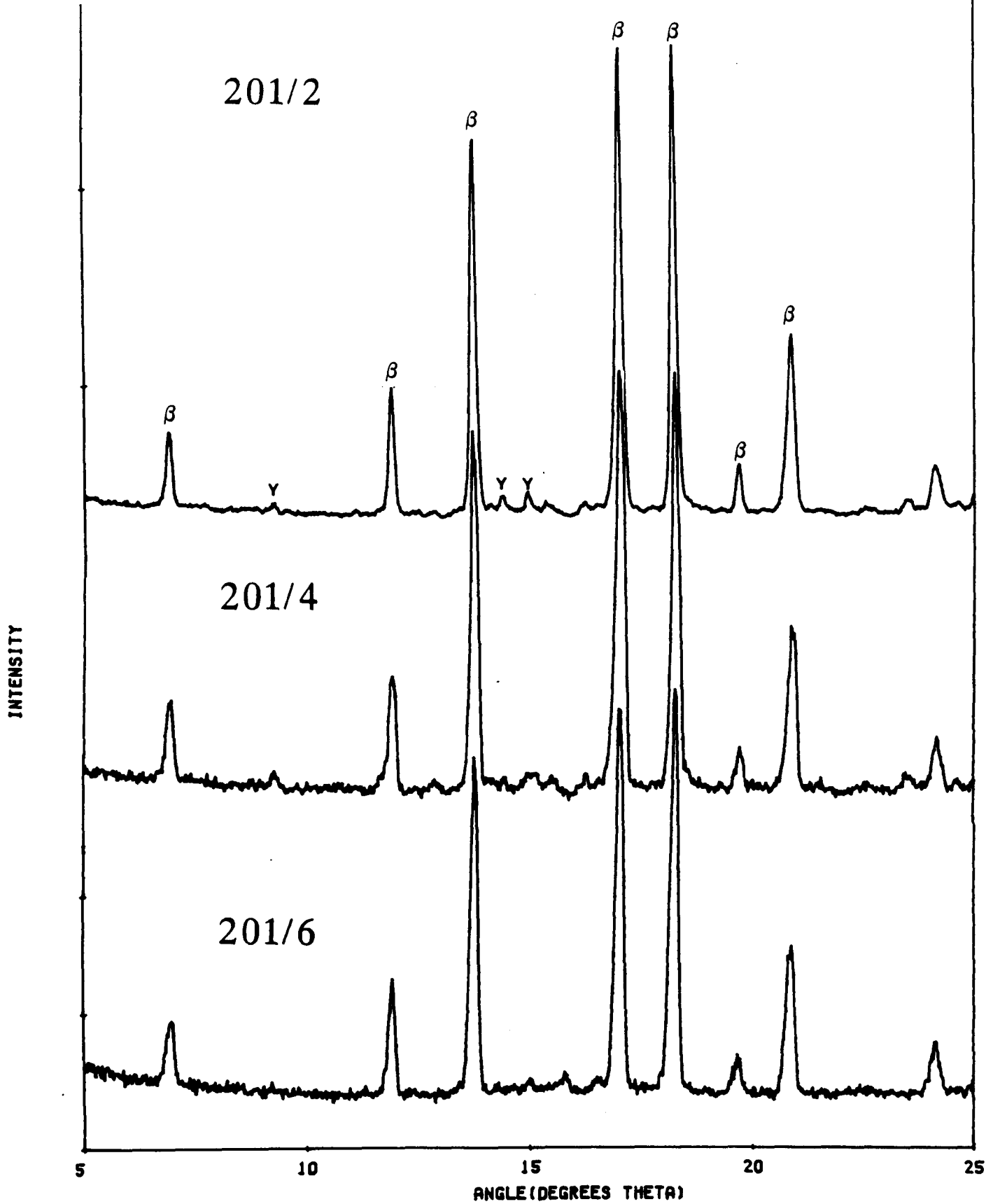
201/2
201/4
201/6
β
γ
INTENSITY
5
10
15
20
25
ANGLE(DEGREES THETA)

increased to 8%, the nitrogen level of the sintering liquid increases to such a level where the average composition moves from A to B, schematically shown in figure 4.2. The α' phase in the varying ceramics shows that the composition remains constant, having composition shown in section 4.1.1.

If this is plotted on the alpha-sialon phase plane proposed by Spacie et al (164) as shown in figure 4.7 the calculated compositions are found to be outside the field of existence found by these workers. This is consistent with the findings of Chatfield et al (165) where the increasing polytypoid content results in α' formation with composition

$$Y_{0.3\pm0.1}Si_{10.2\pm0.4}Al_{1.8\pm0.1}O_{1.3\pm0.1}N_{15.7\pm0.5} \qquad (4.4)$$

similar to that found in this case. When these compositions are plotted on the α' phase plane proposed by Spacie et al (164) as shown in figure 4.7, it is found that α' compositions in these ceramics lie at the maximum possible aluminium/oxygen level within the (α'+β') phase field.

The other effects that varying the polytypoid addition have on the microstructure may be summarised as follows:-

(i) The residual glass volumes after sintering decrease with increasing polytpoid addition. This is a result of the average composition of the sintering liquid shifting to both aluminium and nitrogen rich values, away from the ternary eutectic position of the pure oxide glass. Calculation of relative phase volumes of glass associated with this shift in composition indicate that the increase in polytypoid level will have the effect of reducing glass volumes. In addition to this, the appearance of α' with increasing levels will also have a similar effect on glass volumes. Unlike β', the α' structure may accommodate Y ions within the crystal structure, so to maintain a mass balance, the volume of glass phase decreases.

Figure 4.7 The Mx $(Si,Al)_{12}(O,N)_{16}$ phase diagram.

A - $Y_6Si_3N_{10}O$

C - AlN

D - YSi_3N_5

E - $Y_2Si_3N_6$

J - $Y_4Si_2N_7O_2$ - $Y_4Al_2O_9$ ss

L - Liquid

M - $Y_2Si_3O_3N_4$

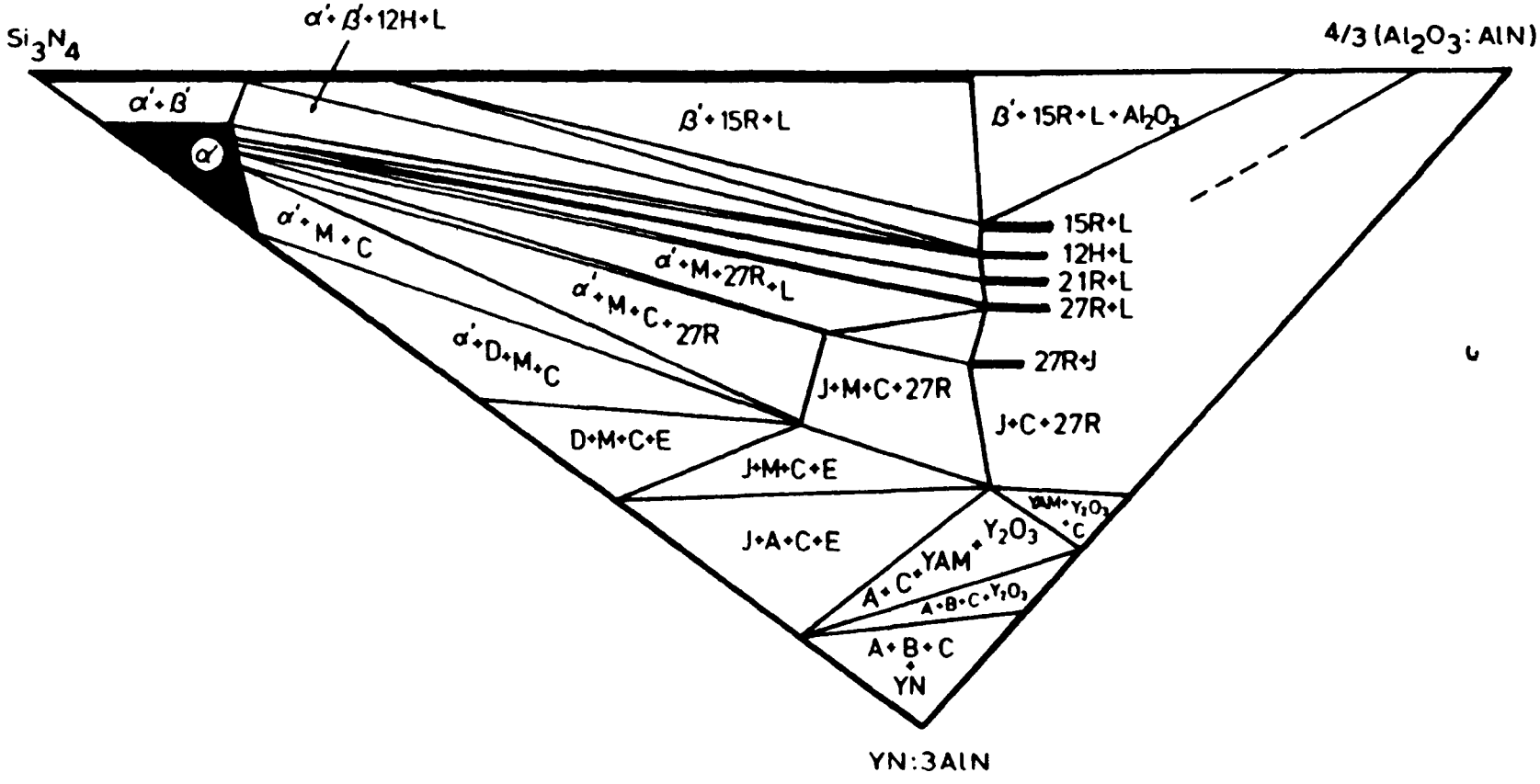
Si_3N_4
α'+β'+12H+L
4/3 (Al_2O_3: AlN)
α'+β'
α
β'+15R+L
β'+15R+L+Al_2O_3
15R+L
12H+L
21R+L
27R+L
α'+M+C
α'+M+27R+L
α'+M+C+27R
α'+D+M+C
27R+J
J+M+C+27R
J+C+27R
D+M+C+E
J+M+C+E
J+A+C+E
YAM+Y_2O_3+C
Y_2O_3
A+C+YAM
A+B+C+Y_2O_3
A+B+C
YN
YN:3AlN

(ii) β' growth and composition vary with changing polytypoid level. An increase in the nitrogen level increases the viscosity of the liquid during sintering (166,167). This inhibits grain growth reducing the aspect ratio, ie. c/a ratio. Ceramics with low polytypoid additions tend to have more elongated prismatic β' grains, with a greater distribution in grain size. EDS analysis of β' grains in these materials shown a marked increase in the aluminium substitution, x, figure 4.5. This is a direct result of shifting the average composition towards the aluminium corner of the ternary phase diagram. This implies rejection of Si and N into the intergranular glass phase, enhancing the nitrogen level. This O/N compositional variation has previously been shown to significantly affect the crystallisation kinetics of these materials (168,169). This effect will be discussed in greater detail in Section 4.3.

(iii) EDS analysis of the residual glass phase shows little variation from the eutectic composition of the ternary oxide Y-Al-Si system.

As with the 201 ceramic described in the previous section, the major impurity detected in the ceramic was iron silicide ($FeSi_2$). As with the previous section, the silicide phase segregates to the grain boundary regions. However, in the lower polytpoid ceramics, the $FeSi_2$ regions are more agglomerated, forming regions often 4-5 μm in size. This is in contrast to the higher polytpoid ceramics where the $FeSi_2$ is more finely and uniformly dispersed. This contrasting behaviour may be caused by the different transport characteristics of the sintering liquid due to variations in the O/N ratio. With high nitrogen levels, high viscosity coupled with a higher nucleation density of β' crystals reduces transport and agglomeration of the iron

silicide, hence a more finely distributed morphology. With lower polytypoid levels, the sintering liquid viscosity is reduced and transport is greater, hence a more agglomerated morphology.

4.1.3 Microstructure of ceramics with 0% Al_2O_3 additions

This family of ceramics differs from the ones previously described, in that no Al_2O_3 is added to the composition during fabrication. Alumina is usually derived as an accidental addition from the ball-milling of the powder prior to sintering. However, advances in processing techniques developed at Lucas-Cookson-Syalon have removed this accidental and unpredictable addition, such that any quoted Al_2O_3 additions are deliberately added in a controlled manner. Thus, the composition of this range of ceramics may be seen to be that of the 8% polytypoid 201 ceramic as described in section 4.1.1 without the Al_2O_3 addition. This maximises the possible nitrogen level possible within this system, oxygen only being derived from yttria (Y_2O_3) and silica (SiO_2) on the surface of Si_3N_4 crystals.

Figure 4.8 illustrates the typical microstructure of this ceramic. Backscattered imaging shows a significantly higher α'-sialon content in the ceramic. Using the relationship (equation 4.1) the α' content in this ceramic is calculated to be approximately 25%. EDX analysis of this phase indicates a similar composition to that found in the ceramics of lower nitrogen level where α' precipitates (ie. 6-8% polytypoid ceramics). Significantly, even though the system has much lower aluminium levels than the previous cases, precipitation of α' occurs to a greater extent. This implies that at high nitrogen levels, the α' phase field extends down to low overall aluminium levels. Analysis of β' grains show a low aluminium substitution level, x~0.15. β'/α' grain growth is markedly reduced, with the loss of long elongated grains, although the randomly orientated interlocking morphology is retained.

Figure 4.8 The microstructure of sintered 201/0, fabricated with 0% Al_2O_3 addition.

a) Backscattered electron micrograph

b) EDX spectra of major phases

c) and d) Transmission electron micrographs of areas of amorphous and crystalline intergranular phases

Fig 4.8

(a)

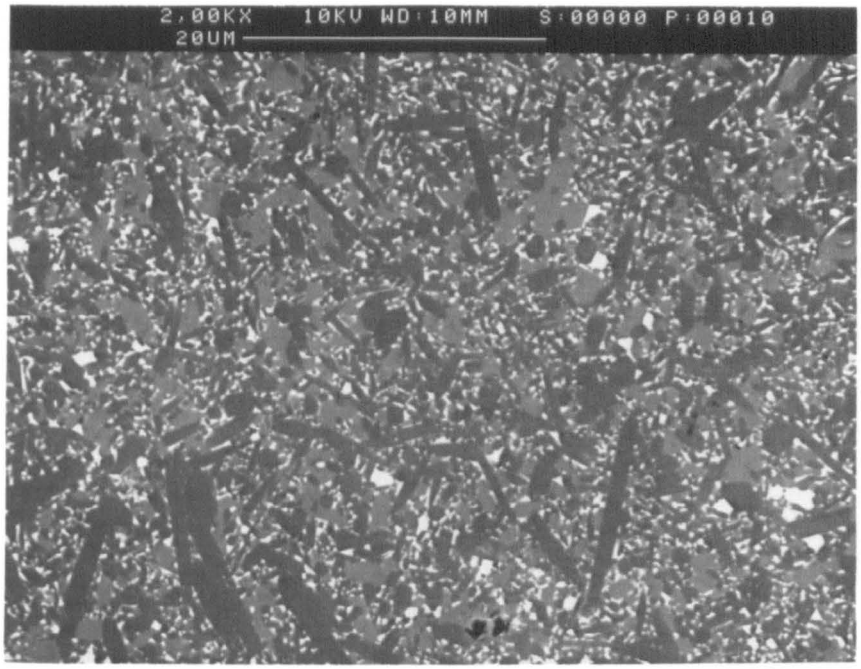

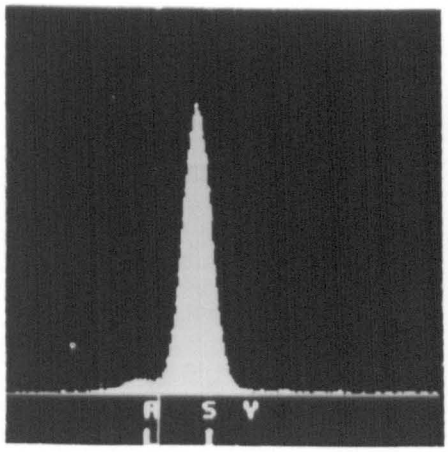

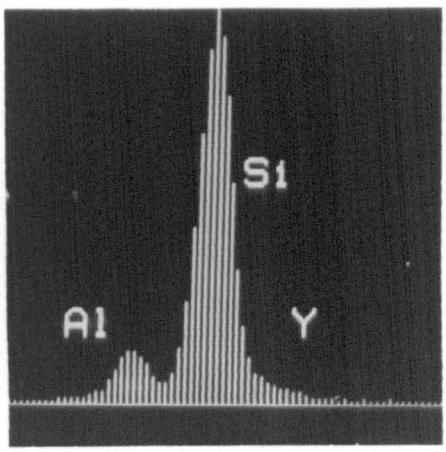

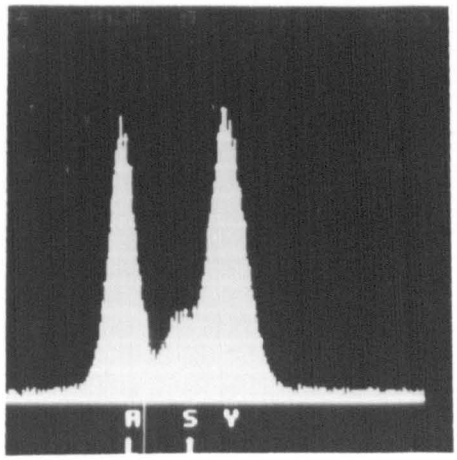

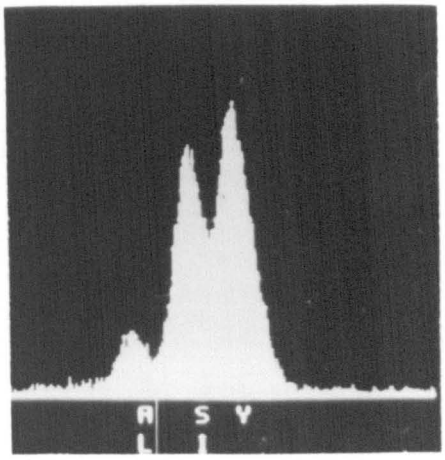

Fig 4.8

(c)

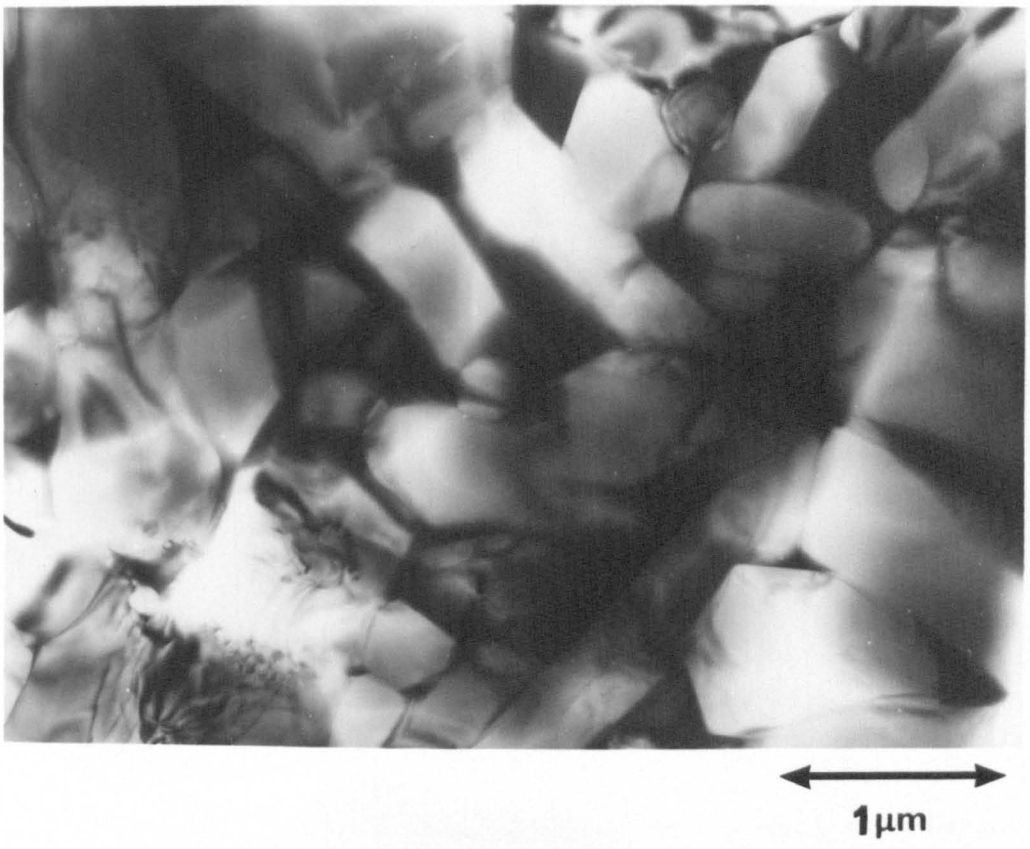

(d)

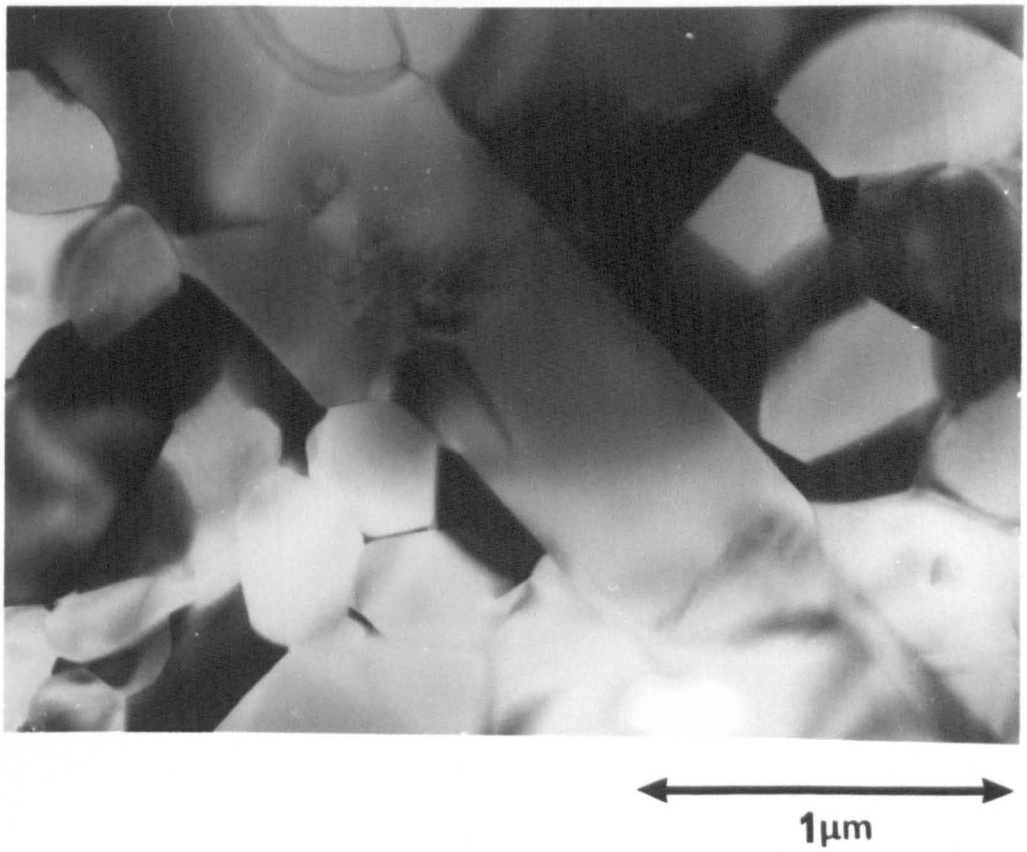

Although an increase in the sintering liquid viscosity, as indicated by slower β' grain growth, implies reduced kinetics of densification, these ceramics were found to have densities approaching theoretical, little residual porosity being evident. This is consistent with the whole series of ceramics, which all have densities approaching theoretical (ie >99.9%), an indication that the sintering route and composition has been refined to a level where dense ceramics may be obtained.

As expected with this high polytpoid ceramic, the residual glass phase volume is low. This may be attributed to three factors, (i) reduction in Al_2O_3 level, (ii) high polytypoid level and (iii) high α' content which reduces both ytrrium and aluminium still further. However, XRD and EDX analysis, figure 4.9 showed the matrix itself to be multi-phased, comprising of a glass phase of near eutectic composition, and a substantial amount of N-α-wollastonite. This is in contrast to the 201/8 ceramic where XRD results show the crystallisation of only small amounts of N-α-Wollastonite ($Y_3Si_3O_6N_3$), during sintering. The appearance of this phase may be explained as follows; large amounts of α' formation due to excessive levels of nitrogen, coupled with the low aluminium levels due to the removal of Al_2O_3, shift the liquid composition from the β'-glass phase field into a phase field where crystallisation of N-Wollastonite becomes stable. The appearance of significant quantities of the quaternary phases in the Si_3N_4-SiO_2-Y_2O_3 is of extreme concern. The significance of the presence of these phases on the high temperature stability will be discussed in Chapter 5.

4.2 Microstructure of the billet surface

The requirement to produce ceramic components to near final shape, precluding the need for expensive diamond machining, and the

Figure 4.9 X-ray diffraction spectra of sintered 201/0 fabricated with 0% Al_2O_3 addition. This is compared with one after crystallisation treatment (see section 4.3.3).

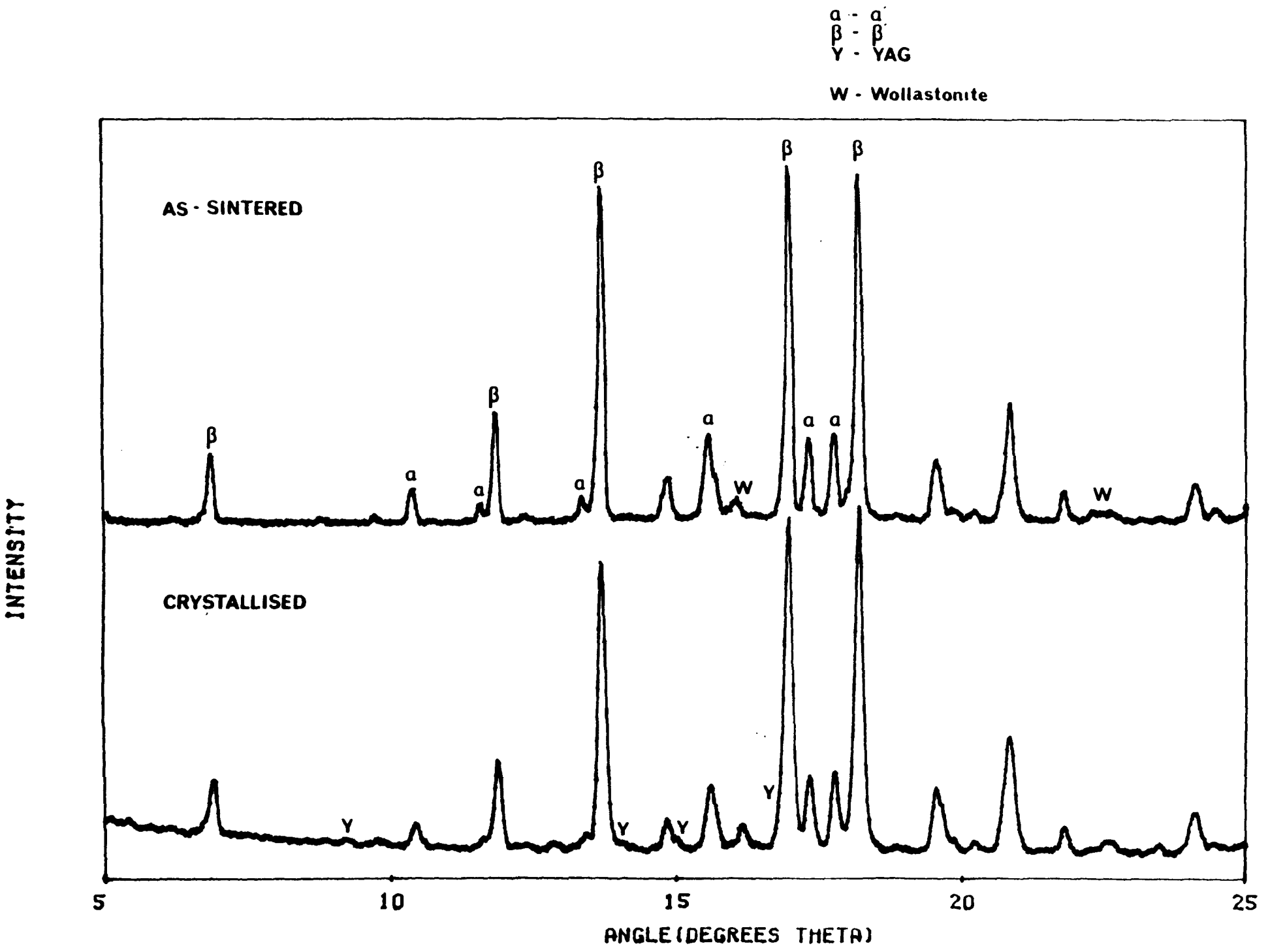
α - α
β - β
Y - YAG
W - Wollastonite
AS - SINTERED
CRYSTALLISED
INTENSITY
ANGLE (DEGREES THETA)
5
10
15
20
25

susceptibility to oxidation and corrosion of β'/YAG surfaces at temperatures in excess of 1300°C has stimulated interest into the microstructural development of the near surface regions during sintering. The second point is of particular interest since the reduction of the YAG reversion reaction may provide a means of extending the high temperature limit beyond 1350°C.

The near surface, or billet surface microstructure as it shall be referred to, varied considerably with increasing polytypoid level, and at high levels differed considerably from the bulk microstructure. The 201 ceramic best demonstrates the differences between the 'surface' and 'bulk' structures, figure 4.10. The billet surface microstructure was found to consist of a layer approximately 40 μm thick of large α' crystals. The grain size in this region is up to 20 μm in the basal plane, and 40 μm along the c-axis. This is far greater grain size than found in the bulk of the material, section. 4.1.1. XRD analysis of the billet surface indicates the α' in the surface region to be orientated in the <102> crystal direction. This indicates nucleation and growth from the surface. Near to the billet surface, just under the α' layer, large α' crystals of random orientation are seen to have nucleated and growth.

The growth of the α' layer may be as a result of increased nitrogen levels during sintering. During this process, due to the low oxygen potential at the surface, SiO may be evolved, increasing the local nitrogen levels, moving the liquid composition into a phase field where α' is precipitated in preference to β', a similar mechanism to that described in section 4.1.3 for the increased nitrogen levels when Al_2O_3 is removed from the composition. The nitrogen level in this surface region would also be enhanced by some absorption from the atmosphere, although the extent this occurs could not be determined. The dependence of the formation of the α' billet

Figure 4.10 Backscattered electron micrograph of the billet surface microstructure of sintered LCS 201.

Fig 4.10

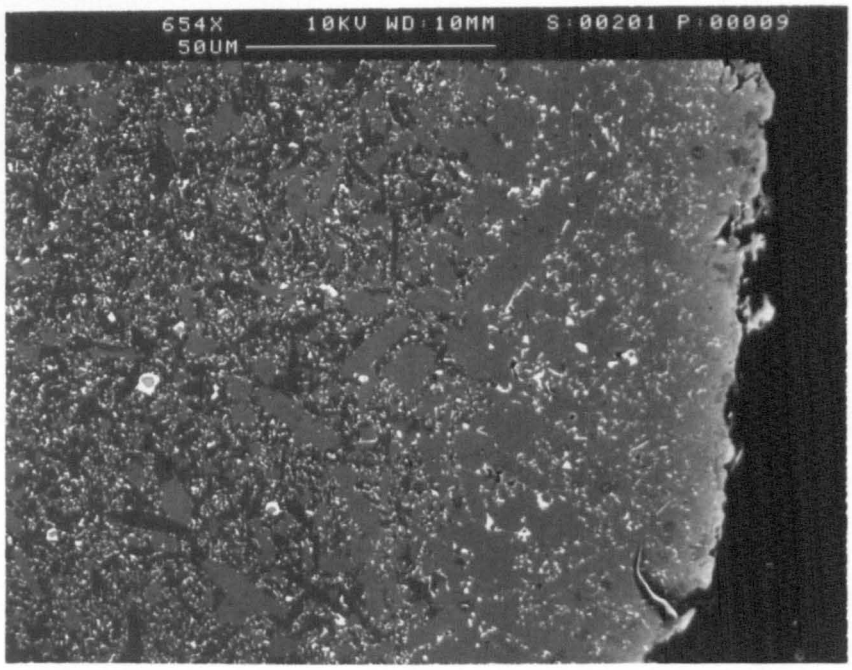

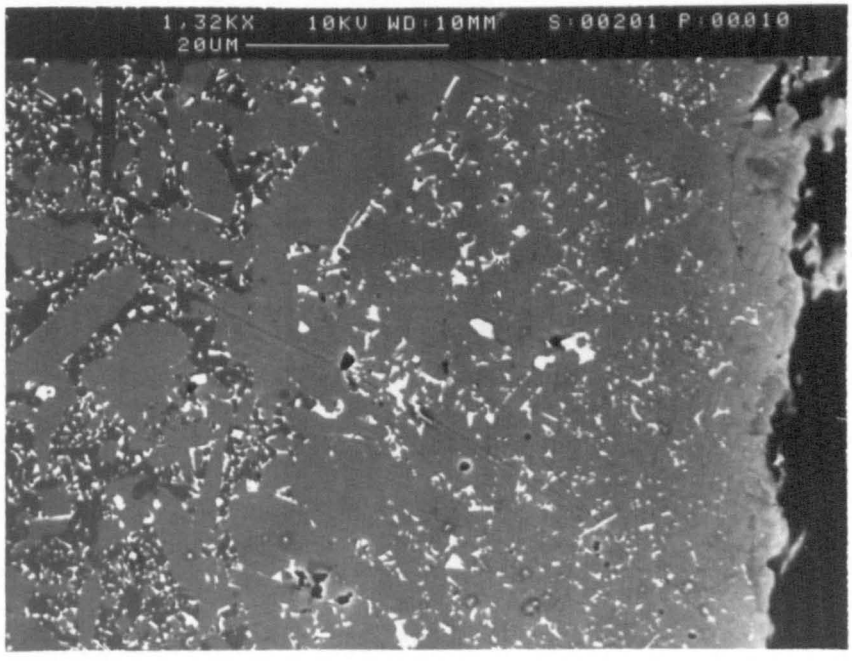

α′ layer

surface layer on the local nitrogen level is clearly shown by examination of the surface regions in ceramics with alternative polytypoid additions. Low additive ceramics, show no α' layer on the billet surface, the microstructure in this region being essentially unchanged from the bulk. The α' layer, as seen in the 8% polytypoid, does not form until the polytypoid addition reaches 6%. The 0% Al_2O_3 material showed a similar α' formation.

Backscattered imaging, figure 4.10, show little matrix phase present in the α' layer. Any observed matrix was analysed to be mainly iron silicide, $FeSi_2$, being insoluble in the α' crystals during sintering. The absorption of aluminium and yttrium by the growing α' crystal during precipitation, coupled with SiO losses from the surface as already discussed above would account for the small volume of residual glass in this region. Small volumes of residual glass at triple junctions were observed, the billet surface having a similar morphology to single phase Si_3N_4 based ceramics (40,170). The α' crystals in the billet surface show little difference in the composition to those found in the bulk of the material, indicating the narrow band of compositional stability that α' has. The imaging of the billet surface also shows β' crystals enclosed by the larger α' crystals figure 4.10. These β' crystals nucleating from the liquid during sintering have been enveloped by the faster growing α' crystals from the billet surface. TEM imaging of these areas show no residual glass phase present at the grain boundary, any being either rejected by the growing α' crystal front, or absorbed into the growing α'. After envelopment, the only reaction between the two is conversion of β' to α' via a solid state diffusion process, indicated by the rounding off of the grain edges, compared with the prismatic growth in the bulk as a result of unhindered growth from the liquid phase.

4.3 Microstructural characterisation of heat-treated ceramics containing crystalline matrices

The operating criteria for ceramics in advanced gas turbine engines require use at temperatures in excess of 1200°C. At these temperatures all ceramics of this type undergo crystallisation of the residual glass phase, though the exact kinetics are critical on the composition.

4.3.1 Matrix Crystallisation of LCS 201

Much previous work (171) has shown that single stage heat treatments tend to cause the devitrification of large oriented crystals throughout the matrix. This has degrading effects upon the properties of the ceramic; the large crystals may cause strength anisotropy of the ceramic, and pore networks may be associated with the crystallisation front. The latter may act as critical defects resulting in premature failure of the ceramic. Therefore, a classical glass-ceramic nucleation/growth heat-treatment has been adopted to crystallise the residual intergranular glass. This would ensure high nucleation densities in addition to maximal crystallisation of the residual glass. The heat-treatment chosen for the LCS 201 was a nucleation treatment of 1250°C for 7 hours, followed by a growth step of 1400°C for 5 hours.

Figure 4.11 shows a typical microstructure exhibited upon the above heat-treatment showing extensive crystallisation of the matrix glass. The major crystallising phase was identified as yttrogarnet (YAG, $Y_3Al_5O_{12}$). The crystallisation in this case is a major feature resulting from successful control of the residual glass composition and volume, in this range of ceramics, by the use of polytypoid additions. Figure 4.2 shows the Janecke prism representation of compositional relationships in the Y-Si-Al-O-N system. Addition of

Figure 4.11 a) and b) Backscattered electron micrograph of crystallised LCS 201 with EDX spectra of β', α' and YAG intergranular phase.

c) and d) Transmission electron micrograph of crystallised LCS 201, bright field (top) and dark field (bottom).

Fig 4.11

(a)

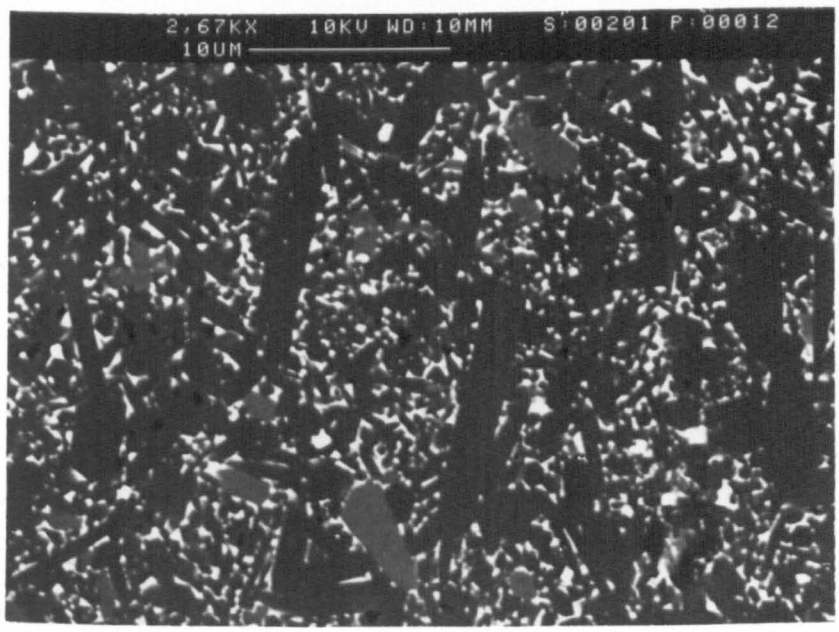
2,67KX 10KV WD:10MM S:00201 P:00012
10UM

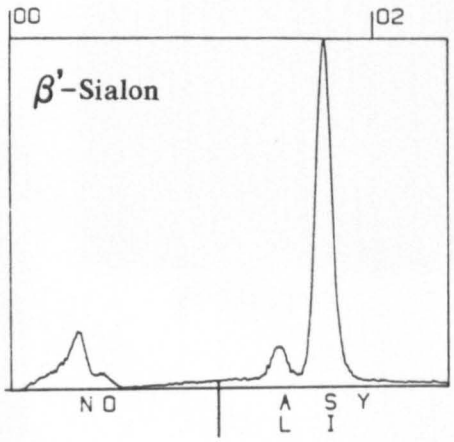
00
02
β'-Sialon
NO
ALSI
Y

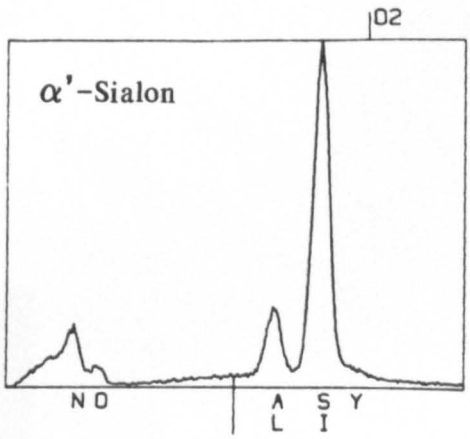
02
α'-Sialon
NO
ALSI
Y

(b)

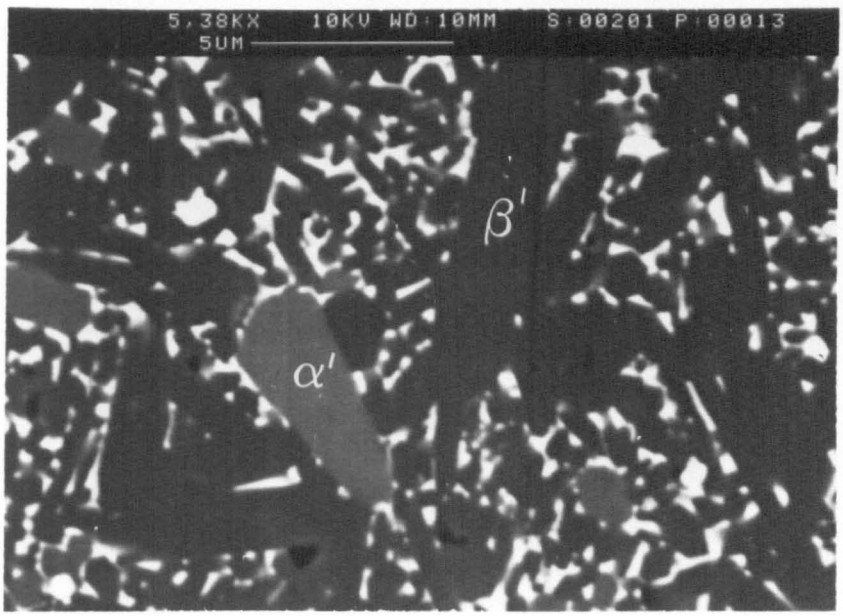
5,38KX 10KV WD:10MM S:00201 P:00013
5UM
β'
α'

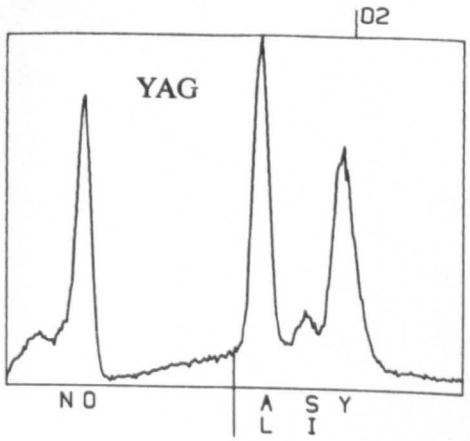
02
YAG
NO
ALSI
Y

Fig 4.11

(c)

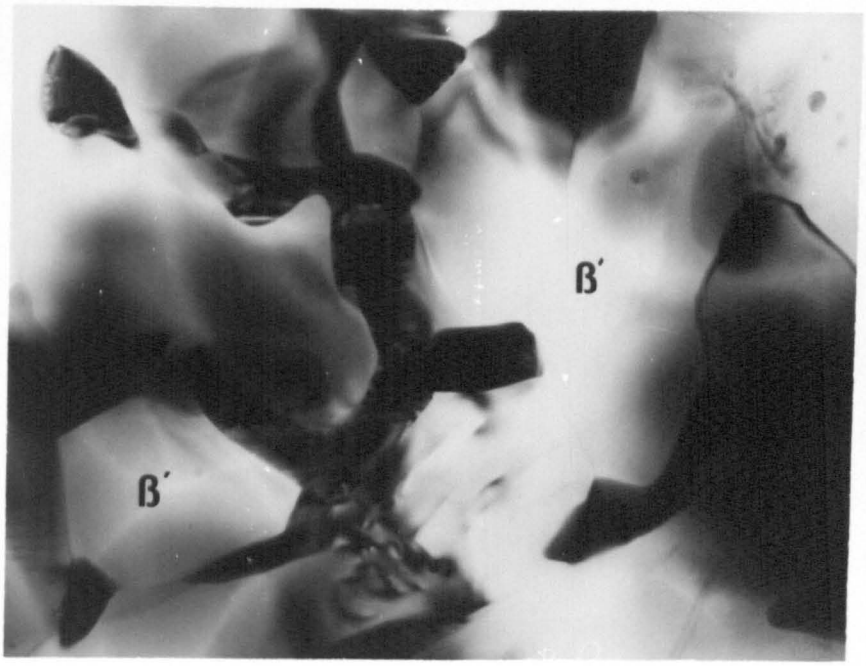

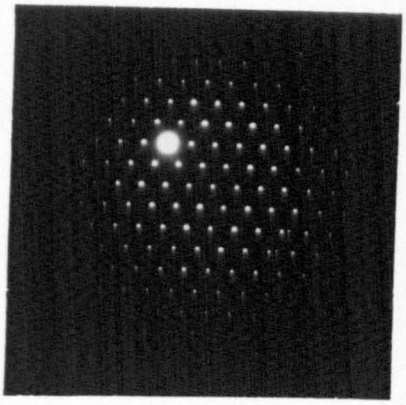

ß' [0001]

1 μm

(d)

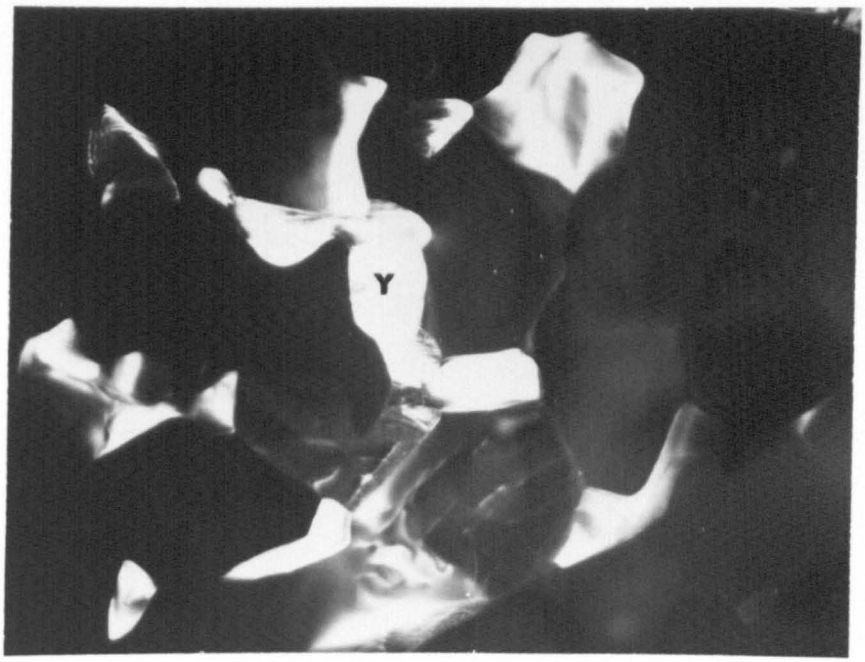

1 μm

the polytypoid phase is assumed to shift the residual glass composition to more nitrogen rich levels, approaching the YAG-Si_2N_2O tie line. Associated work on Y-Si-Al-O-N bulk glasses (163), of similar Si/Al/Y ratio's but of varying nitrogen levels has shown that as one approaches the tie line, crystallisation of the glass tends to be more complete, forming nearly complete two phase YAG-Si_2N_2O composites at maximum possible nitrogen solubility (~30 equivalent percent). In the sialon ceramics, crystallisation of this type does not produce significant crystallisation of silicon oxynitride, this is absorbed into the β' crystals by solid state diffusion. EDS and electron diffraction studies of the β' shows no significant change in aluminium substitution level. This is not unexpected because if the level rule is applied to the phase relations in the Y-Si-Al-O-N system, enhanced nitrogen levels shift the average composition nearer to the β' compositional line. Using the point of average composition as a locus, any change in composition from a near eutectic liquid to YAG will result in only a small shift in β' composition, assuming that overall composition is conserved, which may not be true as some SiO evolution is observed during these crystallising treatments. The predicted change in β' composition by the application of the lever rule easily falls within the scatter produced by the experimental methods measuring it. Winder (173) also found in similar systems that variations in β' aluminium substitution level were insignificant after crystallisation treatments. Significant changes in the substitution level was only observed after extending heat-treatments.

The crystalline YAG matrix in this material is found to have nucleated heterogeneously in the bulk of the material. The nucleation density of the YAG was found to be high, with constantly oriented crystal not extending more than a grain diameter in most cases. Careful observations of these areas at high resolution shows little

evidence for residual glass at triple junctions. In this range of ceramics, two compositional modifications can be attributed to the completeness of crystallisation observed. Firstly, the increase in the nitrogen level of the glass residue by addition of the AlN polytypoid phase, as already discussed, and secondly, the reduction of impurity levels avoid segregation during crystallisation which form stable regions of glass in the three grain junctions, particularly calcium and fluorine derived from the milling and acid washing of the powders. It is well established that calcium inhibits complete crystallisation (42), but it has been recently shown that only small additions of fluorine can inhibit crystallisation drastically (163), and is thought to be a major factor influencing the incomplete crystallisation of the intergranular glass of comparable ceramics fabricated with silicon nitride powders supplied by H.C. Starck.

This is of particular importance when considering the high temperature mechanical properties of these materials. Residual glass in the intergranular regions is responsible for such effects as sub-critical crack growth and cavitation during creep. These effects will be discussed with relevance to the crystallisation in these materials in Chapter 6.

4.3.2 Optimisation of matrix crystallisation in high nitrogen ceramics

The crystallisation treatment given to the LCS 201 as described in the previous section was essentially derived from a study of the crystallisation kinetics of earlier development sialon ceramics (172,173). In this material it was found that it was difficult to (i) avoid large cellular growth of the crystallising intergranular phase and (ii) fully crystallise the glass phase. Therefore the two stage glass-ceramic nucleation/growth heat-treatment was used, and was found to be optimal although not completely satisfactory at 1250°C/7hrs followed by 1400/5hrs. This was carried through with the development

of the LCS 201 ceramics, although it was not known whether or not it was an optimal treatment for the composition of the glass phase in this case. Therefore a study of the crystallisation kinetics at different nucleation/growth temperatures, shown in figure 4.12.

All heat-treatments showed YAG crystallisation. Single stage treatments showed that below 1250°C crystallisation was incomplete, with visible residual glass figure 4.13(a). At 1250°C-1300°C, YAG crystallisation was almost complete with a high nucleation density as observed in the previous section. Above 1300°C, the crystallisation of the YAG became more coarse and cellular, optically shown in Fig. 4.13(b). TEM sections of these areas show constantly orientated YAG crystals growing from a nucleus at the centre of the sphere. Dye penetrant tests of these surfaces (174) have indicated that the crystallisation of this nature results in a zone of microporosity at the outer extreme of the YAG spherite. Examination of these surfaces could not distinguish either the YAG spherical crystallisation regions, or the microporosity associated with it. The cause of this alleged porosity would be due to small volume changes occurring during crystallisation. As the YAG crystal grows from the nucleus, the porosity is "pushed" outwards ahead of the crystallisation front. Although over the range of crystallisation treatments investigated observable changes in the behaviour were seen, under no conditions was surface nucleation of YAG observed. All crystallisation, to varying degrees was found to be heterogeneous throughout the bulk.

The single stage heat-treatments indicated that annealing at temperatures between 1250°C and 1300°C results in high nucleation density of YAG, but a final growth treatment was necessary to finalise crystallisation. The treatment of 1400°C for 5 hours was found to crystallise completely, and longer growth times to this were found to

Figure 4.12 The heat-treatment cycles used to optimise crystallisation of the intergranular YAG phase.

Figure 4.12 Crystallisation treatments for sintered LCS 201

Temperature (°C)	Time (hrs)	Comments
1100	50	Partial YAG crystallisation
1200	50	YAG crystallisation
1250	50	YAG crystallisation
1300	50	Full YAG crystallisation "cellular growth"
1100	5	Full YAG crystallisation
+ 1400	7	
1250	5	Full YAG crystallisation
+ 1400	7	
1300	5	YAG crystallisation-
+ 1400	7	"cellular growth"

Figure 4.13 Light micrographs of LCS 201 after (a) 1100°C/50 hours and (b) 1400°C/50 hours, the two extremes used for crystallisation of the intergranular phase.

Inset - transmission electron micrograph of partial YAG crystallisation after 1100°C heat-treatment.

Fig 4.13

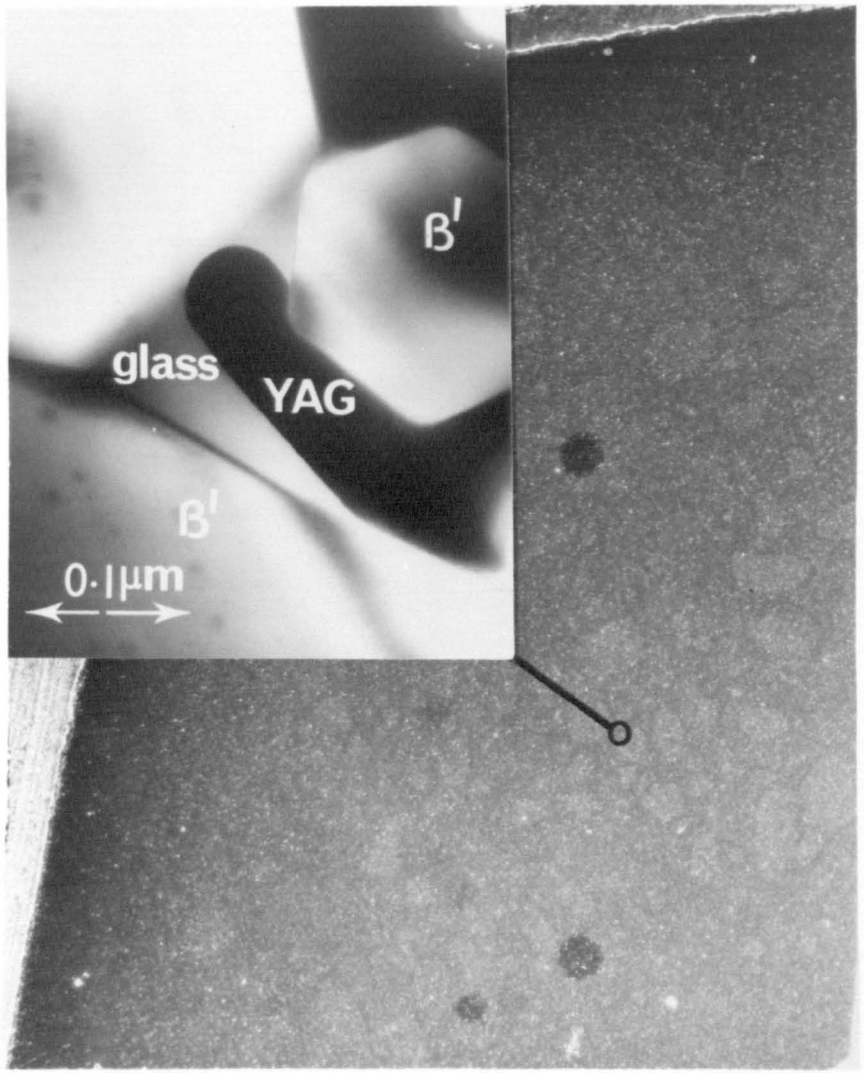

cause little change at all. Therefore, it is concluded that the use of the longer growth treatments would benefit little, and would be an economic hinderance.

In conclusion, the use of the nucleation/growth treatment of 1250°C/7hrs followed by 1400°C/5hrs developed for other Y-Si-Al-O-N ceramics suits the crystallisation behaviour of LCS 201. Care should be taken however, as deviation from these temperatures either results in incomplete crystallisaion, or large spherites of YAG forming. Therefore the window for optimal crystallisation is very narrow.

4.3.3 Effect of polytypoid additions on the kinetics of crystallisation

The effects of increasing polytypoid additions on matrix crystallisation were quite marked. Analysis of the annealed ceramics, having been given the standard heat-treatment of 1250°C/7hrs followed by 1400°C/5hrs, indicated YAG ($Y_3Al_5O_{12}$) as the only crystallisation product. Figure 4.14 shows optical micrographs of the annealed ceramics, increasing in polytypoid content from 2% to 8%, figure 3.1, the latter being the 201 microstructure. The lowest polytypoid ceramic LCS 201/2, figure 4.14(a) shows extensive surface nucleation, with large columnar growth of the crystals into the bulk of the specimen (zone 1). This front stops short of complete crystallisation, forming a higher central core (zone 2). Sectioning through these zones show that in zone 1, highly orientated zones of YAG are observed, with a large degree of crystallisation. Zone 2 shows evidence for incomplete heterogeneous YAG crystallisation, with significant volumes of residual glass in the intergrannular regions.

Increasing the polytypoid content results in a dramatic change in the crystallisation behaviour. Figure 4.14(b) shows the crystallistaion of the 4% polytypoid addition, LCS 201/4. The increase

Figure 4.14 Light micrographs showing crystallisation behaviour with varying polytypoid additions.

a) 201/2 - 2% polytypoid

b) 201/4 - 4% polytypoid

c) 201/6 - 6% polytypoid

Fig 4.14

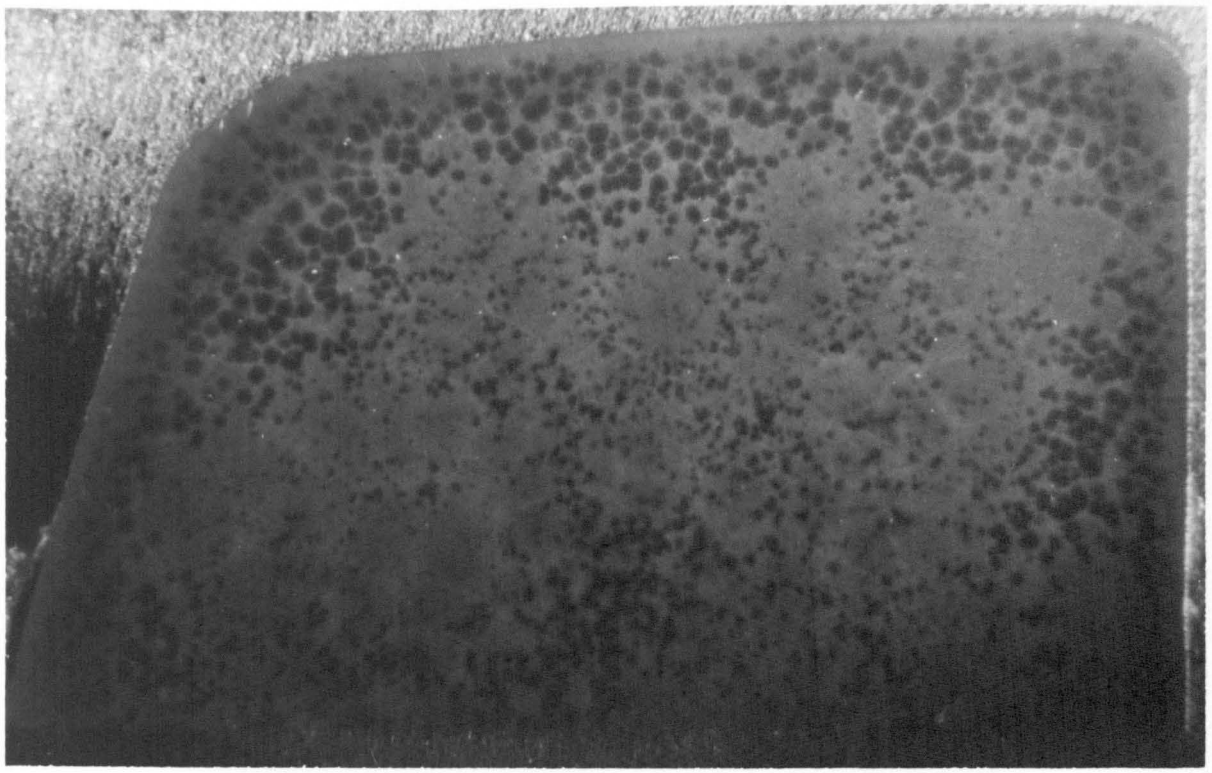

(b)

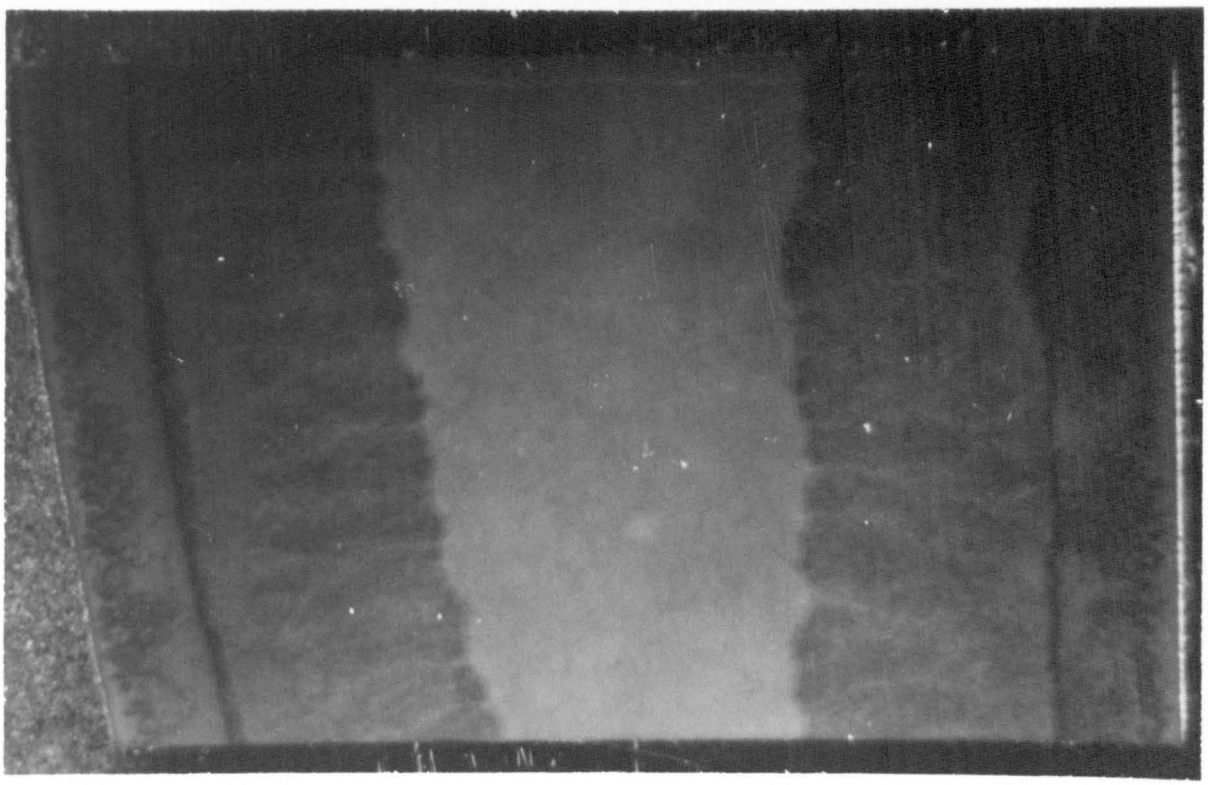

(a)

Fig 4.14

(c)

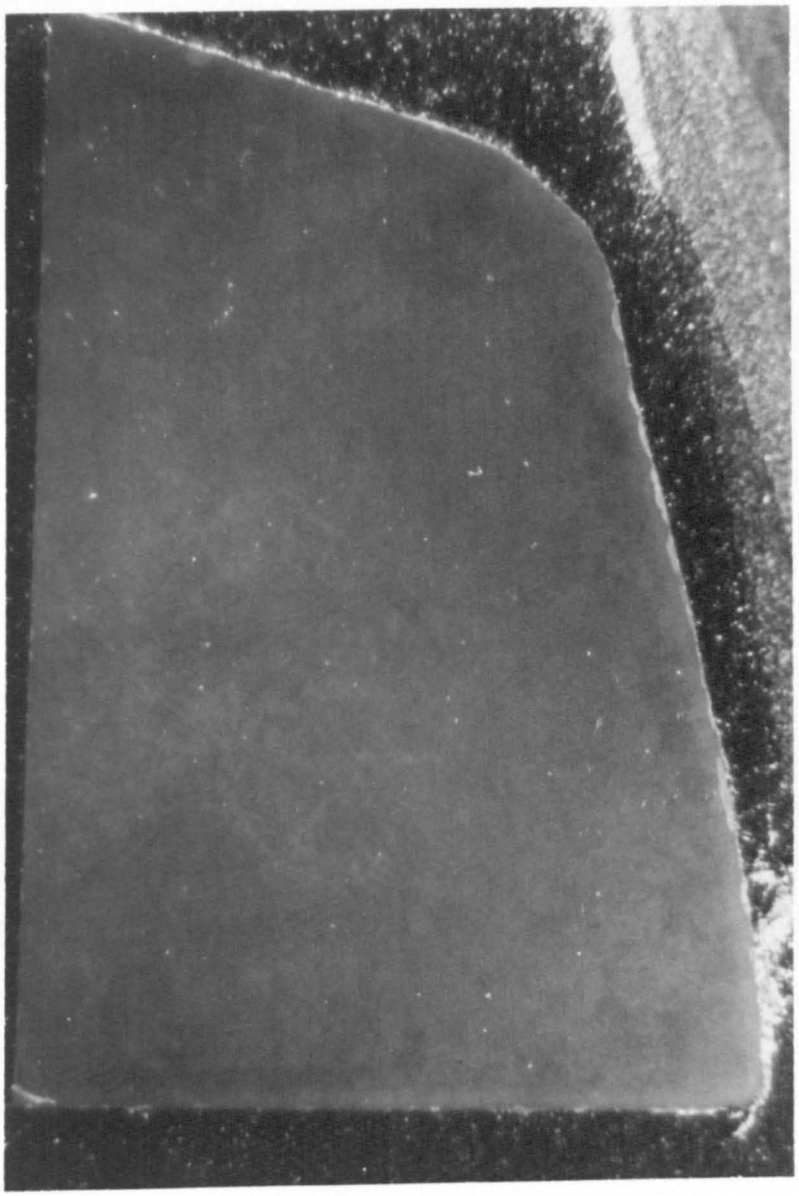

in nitrogen changes the crystallisation from surface dominated to bulk dominated. However, the kinetics are yet to be sufficiently high to ensure full crystallinity. Dark field optical microscopy shows dark circular areas corresponding to spherically nucleated YAG growth from a point at the centre. As with the previous case, these areas show orientated YAG growth with little glass residue, whereas the lighter regions shows incomplete crystallisation with large areas of glass residue.

Increasing the nitrogen level still further, increases the uniformity and completeness of crystallisation. The 6% polytypoid addition LCS 201/6 shows complete crystallisation similar to that found in the LCS 201/8 ceramic, the commercially produced ceramic. The crystallisation in these cases is heterogeneous, with little residues evident and with a high nucleation density, avoiding the problems associated with large columna growth of the crystals found in the lower polytypoid additive materials.

4.4 Microstructural development during post-sintering hot isostatic pressing

Hot isostatic pressing (HIP) is an technique for the densification of ceramics to near-net shapes. Therefore a microstructural survey of a HIP'ed version of the 0% Al_2O_3 based ceramic designated LCS 201/0. The ceramic was sintered as shown in figure 3.1, attaining a dense microstructure with a high proportion of α'-sialon and α-Wollastonite as described in Section 4.1.3. This material was then HIP'ed at 1750°C for 1 hour at 15000 psi, followed by the standard heat-treatment to crystallise the residual intergranular glass.

Figures 4.15 and 4.16 shows the microstructure and XRD analysis of the HIP'ed material. The basic structure is similar to that in the crystallised material, the microstructure consisting of β' grains, a high proportion of α' grains (~25%) in a matrix of α-Wollastonite and YAG. The first obvious difference in the structure is the formation of zone of increased matrix volume throughout the specimen. At low magnification these areas are randomly orientated, vein-like in structure. Analysis of these areas indicate that these areas are of the same composition as the matrix in the un-HIP'ed state. The origin of this veining is unclear. Pressure is isostatically applied during the HIP'ing procedures, therefore pressure gradients across the specimen are not expected, variation of which may be a possible driving force for mass transport from one region to another. It is possible that during the HIP'ing, the α-Wollastonite present, known to form during the sintering process, continues to grow forming large crystals within the bulk, relatively unhindered due to the reversion by some of the material to the liquid state. These regions (figure 4.16(b)) have similar composition to the crystalline matrix found in the sintered and crystallised ceramic. Analysis of a number of regions showed little variation in the composition, possibly vindicating the argument of single crystal growth. However, no substantial microscopical evidence could be attained because of selectivity of the areas observed.

The second major microstructural change observed as a direct consequence of the isostatic pressing was observed in the near surface region of the sample. The sintered ceramic contains a high proportion of α' within the structure, up to 25% by volume of the major crystalline phase. After the isostatic pressing, a surface zone completely devoid of α' was formed, approximately 1 mm in depth. In addition, the α' billet surface layer had also been removed.

Figure 4.15 Backscattered electron of 201/0 after hot isostatic pressing

Fig 4.15

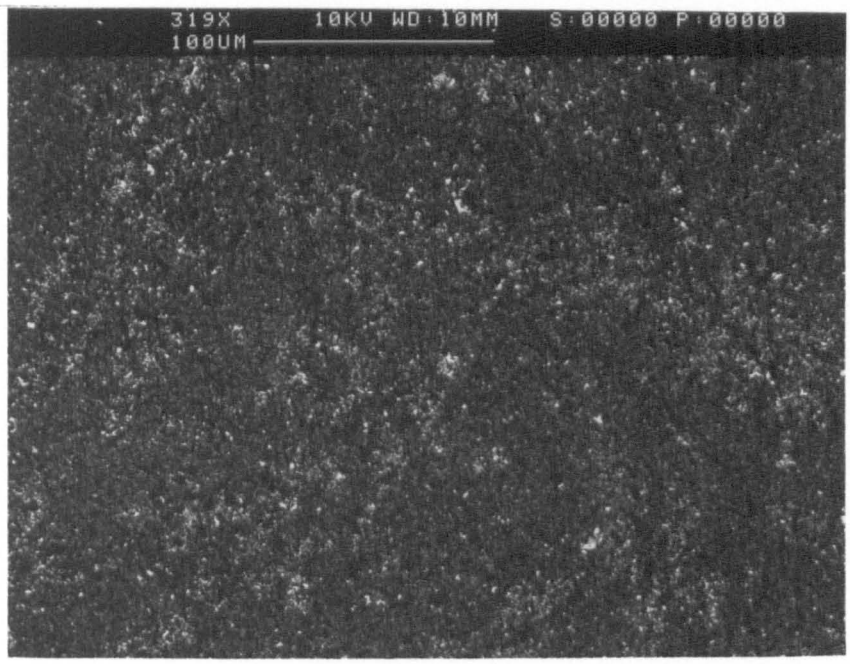
319X
100UM
10KV WD:10MM
S:00000 P:00000

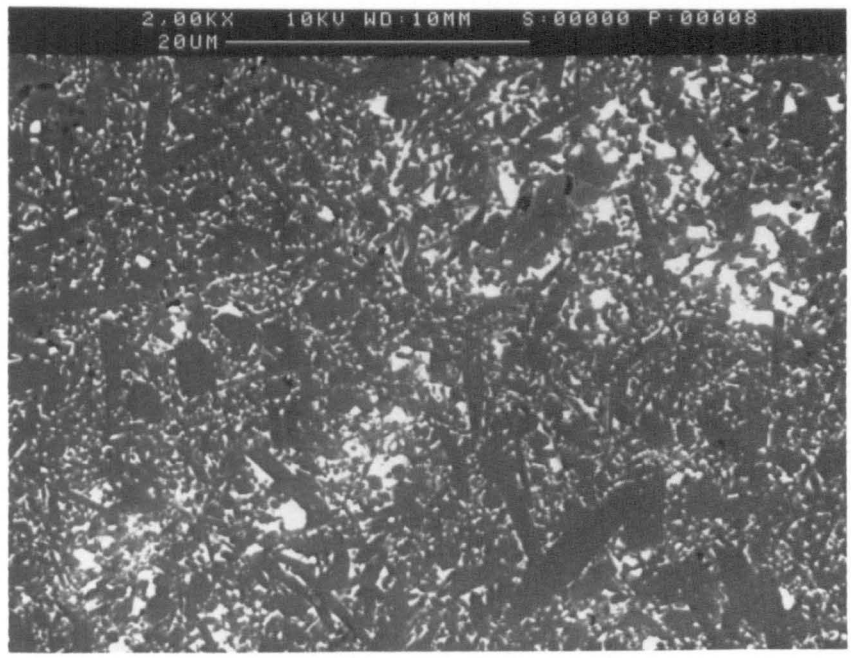
2,00KX
20UM
10KV WD:10MM
S:00000 P:00008

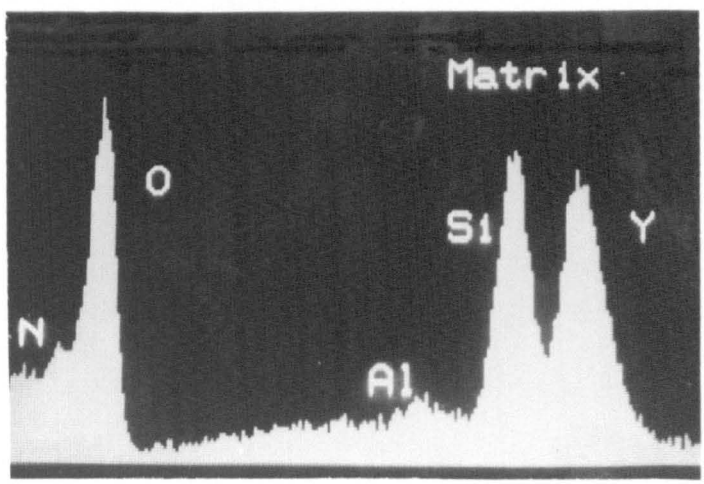
Matrix
O
Si
Y
N
Al

Figure 4.16 X-ray diffraction spectra of 201/0 after hot isostatic pressing. This is compared with the spectra obtained prior to HIP'ing.

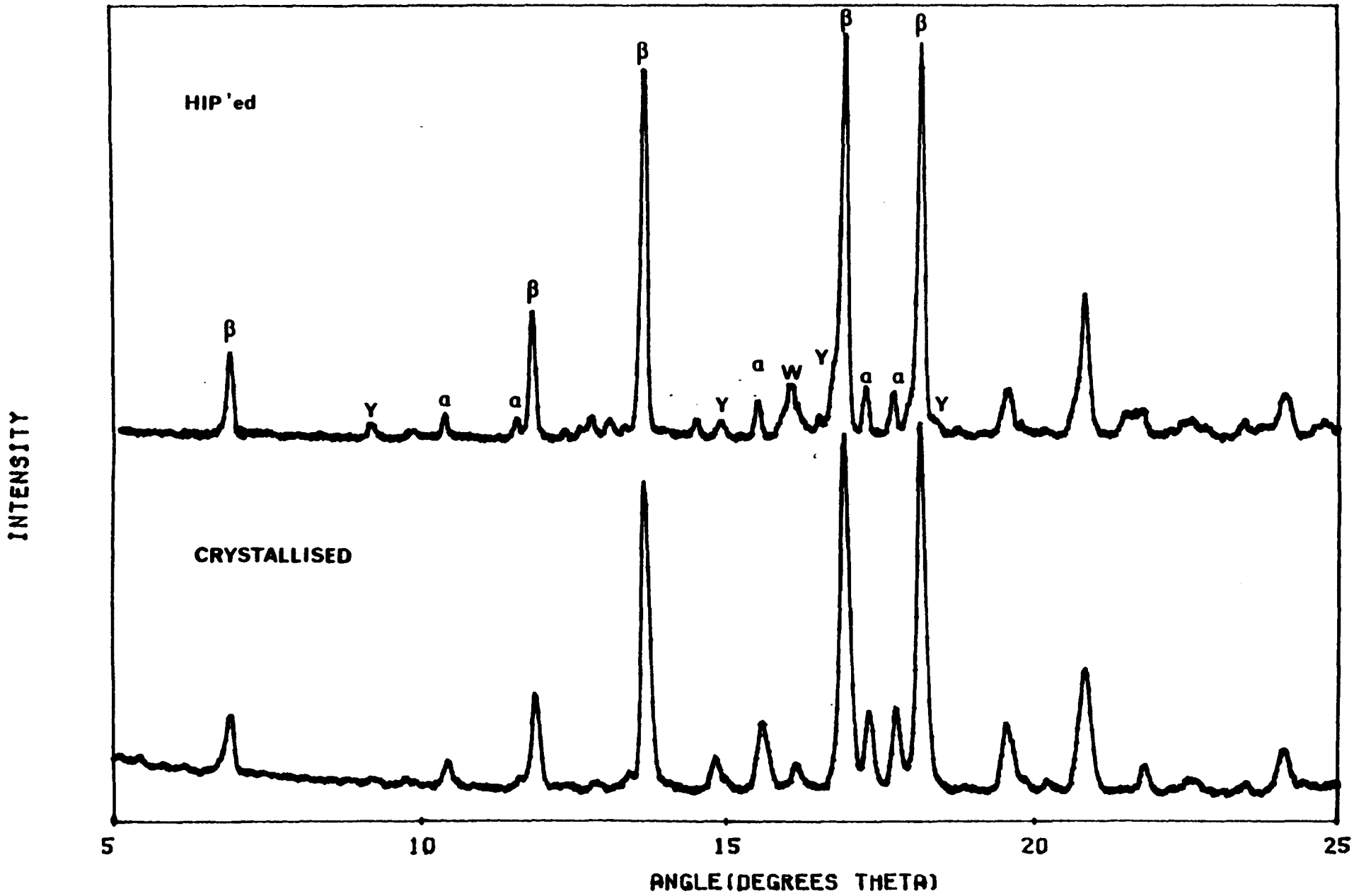
HIP 'ed
CRYSTALLISED
β
γ
α
W
INTENSITY
5
10
15
20
25
ANGLE (DEGREES THETA)

This effect appears to contradict all other observations on the formation of α' growth in these ceramics. It has been assumed that the major cause of α' growth is a shift of the nitrogen level to such an extent that it passes from a β'+glass phase field to a α'+β'+glass field. This mechanism was substantiated by observations of ceramics with increasing polytypoid level. Increasing this to a critical level, ~6^{w}/o, caused the formation of α' in the bulk. At the billet surface, the α' layer growth is further aided by absorption of nitrogen from the gaseous atmosphere and loss of SiO. From these deductions it would be expected that the application of a high pressure nitrogen atmosphere would further cause absorption of nitrogen causing even greater formation of α' in the surface. The formation of a layer completely depleted of α' contradicts this hypothesis. The cause cannot purely be due to the application of pressure as the whole specimen would be transformed. The only possible explanation for this is a chemical shift away from the α' phase field, such that even at high nitrogen levels, only β' is formed.

It must be noted that the effects observed may not be typical, as only a limited amount of material was available for analysis.

4.5 Conclusion

The refinement of the LCS 201 ceramics by use of "balanced" compositions has had significant effects on the microstructure as compared with previous development ceramics. The most significant observations may be summarised;

1) The addition of the AlN polytypoid has marked effects upon the sintered microstructure;

   (i) causes the overall volume of residual glass phase to be reduced.

(ii) increases the nitrogen content of the glass. This will move the composition nearer to the YAG-Si_2N_2O tie line, a factor desirable with respect to devitrification.

(iii) nitrogen saturation of the sintering liquid causes the formation of the yttrium stabilised α'-sialon in addition to the β' form.

(iv) the high nitrogen levels also results in the crystallisation of N-α-Wollastonite ($Y_2Si_2O_4N_2$), in small quantities, which may be detrimental to the ceramics properties at medium temperatures (~1000°C).

(v) the increased nitrogen level as specified in (ii) causes a greater degree of crystallisation to YAG on subsequent heat treatment. The ease of crystallisation diminishes rapidly with reductions in the polytypoid levels.

2. Reduction in the impurity levels, particularly calcium reduces elemental segregation during devitrification allowing a greater degree of crystallisation of the grain boundary glass.

3. The addition of high levels of AlN polytypoid causes the formation of α'-Sialon at the billet surface. The formation of this layer is critically dependent on the overall nitrogen level, and provides a possible means of protection at high temperatures.

4. Post-sintering hot isostatic pressing (HIP) may alter both surface and bulk microstructure radically. The reason for this is unknown. The process also removes the presence of α'-sialon from the near-surface regions.

Chapter 5 HIGH TEMPERATURE ENVIRONMENTAL STABILITY AND SURFACE TRANSFORMATIONS

This chapter will discuss the high temperature environmental stability and surface transformations observed in LCS 201 type ceramics. The short term oxidation kinetics and mechanisms will be presented, and a study of the microstructural effects that this and longer term oxidation has. Finally a study of the effect that various controlled surface transformations have on both the microstructure and oxidation kinetics will be made.

5.1 Environmental stability below 1300°C

The identification of the yttrium N-α-wollastonite phase ($Y_2Si_2O_4N_2$) in the LCS 201 sintered material, is similar to that reported by Lange (96) which has been shown to exhibit instability at temperatures around 1000°C. Therefore a study was undertaken of the stability of this range of ceramics at medium temperatures where this effect would become apparent if at all.

5.1.1 Oxidation studies

Specimens of sintered and crystallised LCS 201 and the high nitrogen, high α-wollastonite containing material were oxidised at 1000°C and 1200°C for times up to 100 hours. Figures 5.1 and 5.2 show the effects of oxidation at 1000°C to be minor, the oxide layer forming as a thin discontinuous silica (SiO_2) layer on the surface of the specimen. Little yttrium or aluminium ion diffusion into the oxide layer was observed, the YAG phase being stable at this temperature. Hence, no detectable degradation of the sub-surface was observed.

Figure 5.1 Oxide surface of LCS 201 after oxidation at 1000°C for 100 hours.

Fig 5.1

(a)

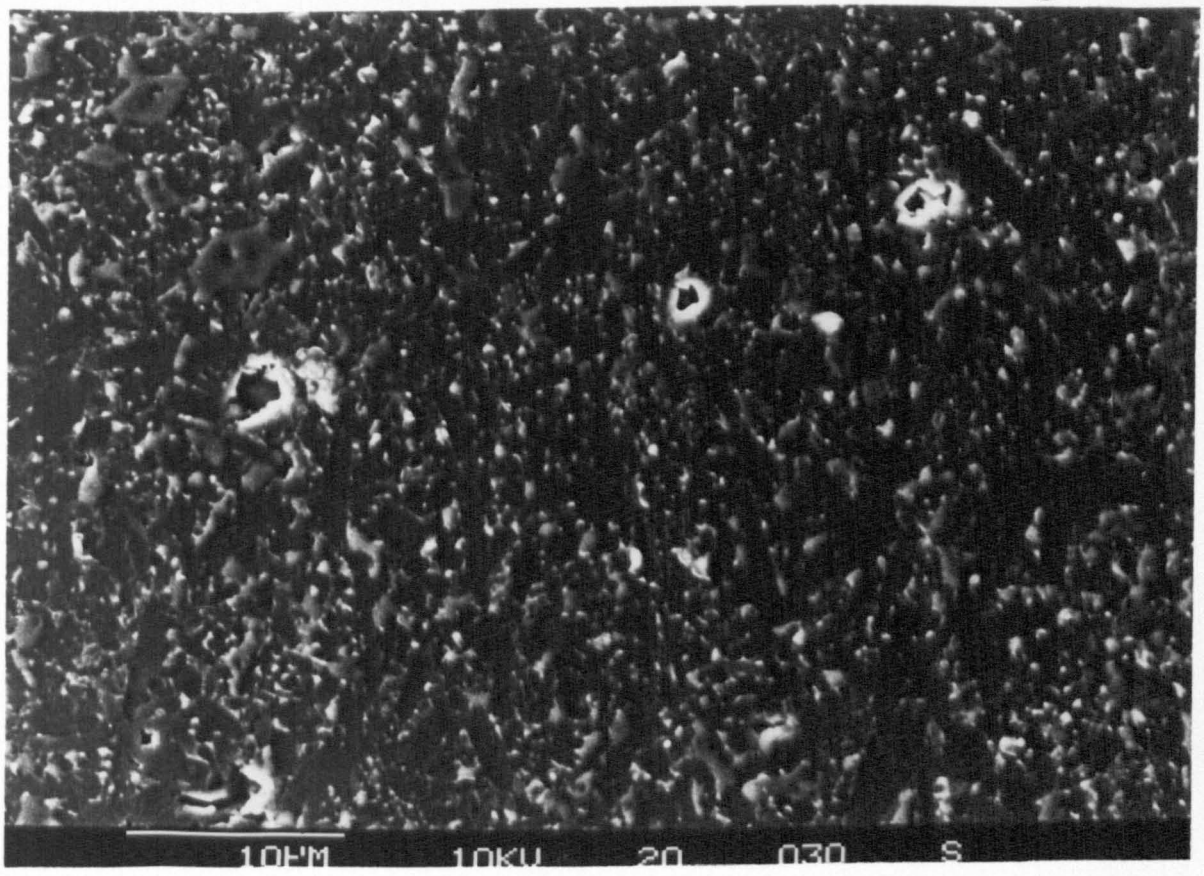

(b)

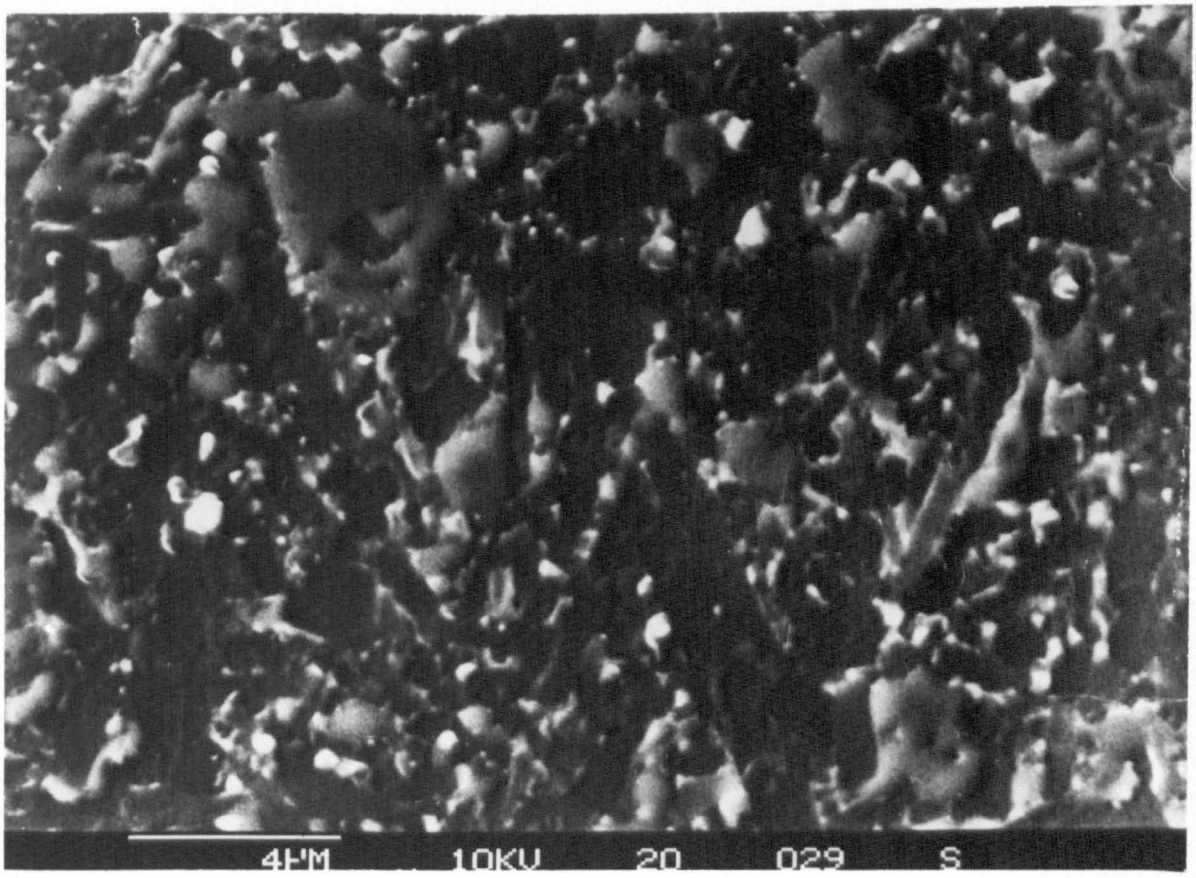

Figure 5.2 Oxide and sub-oxide development after oxidation at 1000°C for 100 hours.

Fig 5.2

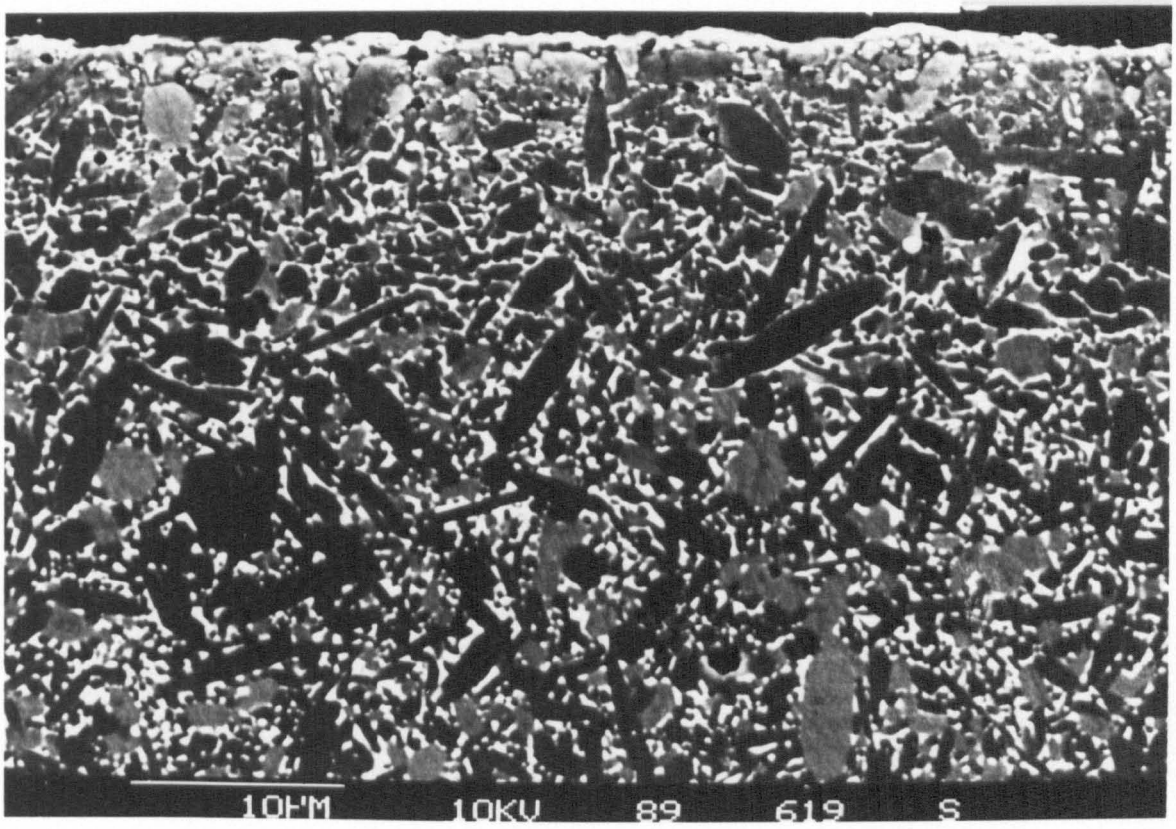

In the LCS 201 with a YAG intergranular phase, the Y-N-α-wollastonite levels are low, being only detectable as trace amounts by X-ray diffraction. The materials studied by Lange (96) contained large volumes of the oxynitride phase, and the oxidative instability occurred rapidly, due to new surfaces being created continuously by the cracking associated with the volume expansion. In the LCS 201 ceramic, catastrophic oxidation does not occur in this manner as the α-wollastonite is dispersed discontinuously within the larger volume of crystalline YAG. Hence the effects of this instability is confined to the extreme outer surface.

Similar oxidation experiments were performed on LCS 201 with a glassy intergranular phase. Oxidation occurred in a similar fashion to that observed in the previous case. However, a zone of increased matrix volume (~10μm) was found to have formed during the treatment, (figure 5.2). This is due to diffusion of components of glass towards the surface as a result of oxidation. These effects would be inhibited by the crystallisation of the glass to YAG, stabilising the matrix to the effects of oxidation at this temperature.

In addition, the same heat-treatments were performed on the 0% Al_2O_3 containing, increased α-wollastonite ceramic, in sintered, crystallised and HIP'ed/crystallised states. Oxide layer and sub-surface development was observed to be essential the same as observed in the LCS 201 material. No microcracking was observed in these materials either.

At 1200°C oxide layer development in the LCS 201 ceramic changes dramatically. At this temperature the oxide layer is found to be mainly glassy with small crystals of β-$Y_2Si_2O_7$ (ASTM 22-1103). At short oxidation times these crystals were found to form as small needles, but after prolonged heat-treatment were found to lose their

Figure 5.3 Oxide surface of LCS 201 after oxidation at 1200°C for 100 hours (a + b) and (c) EDX spectra of $Y_2Si_2O_7$ crystals.

(a)

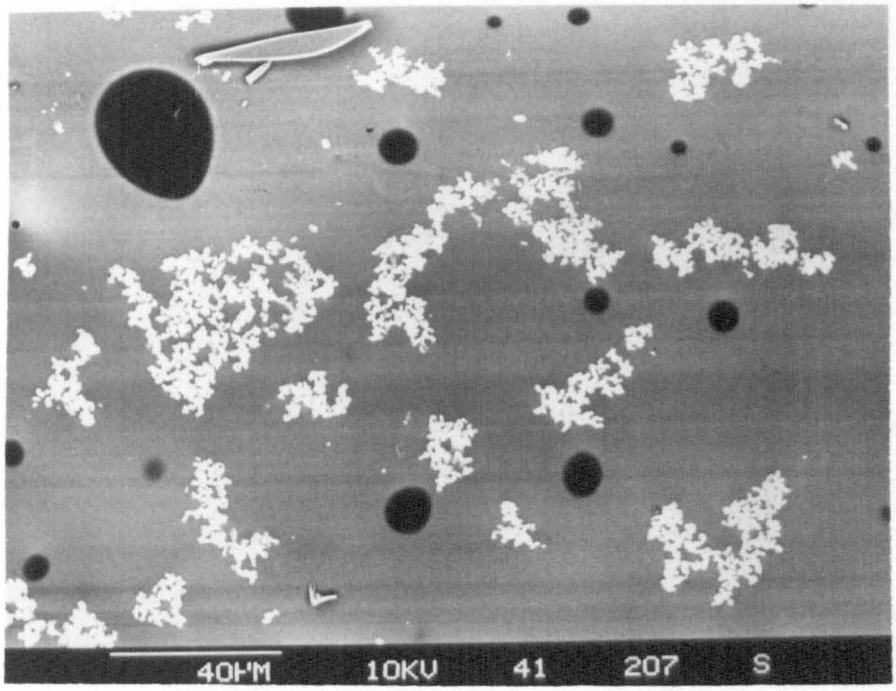

Fig 5.3

(b)

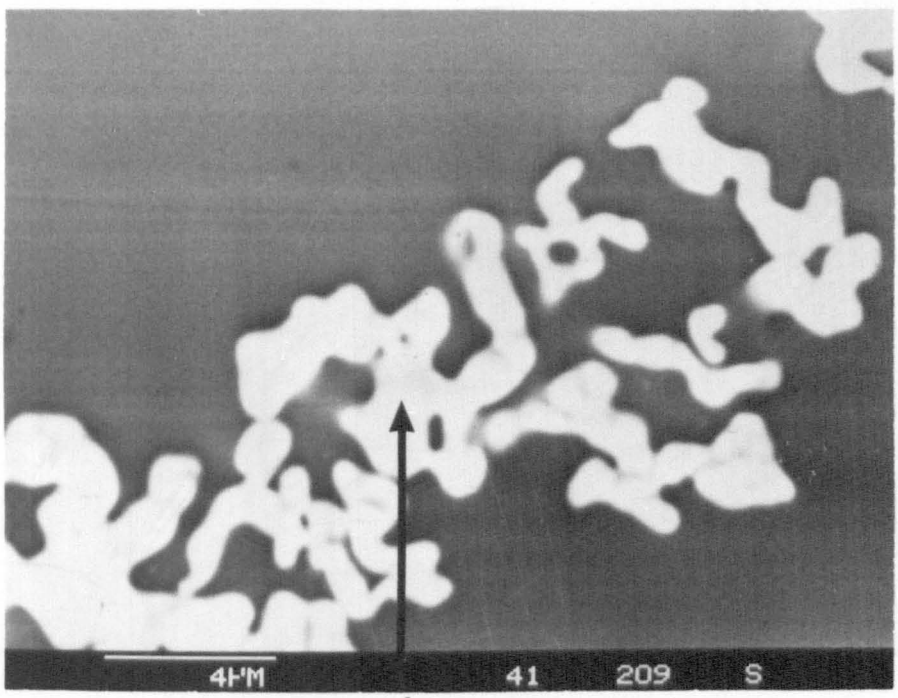

(c)

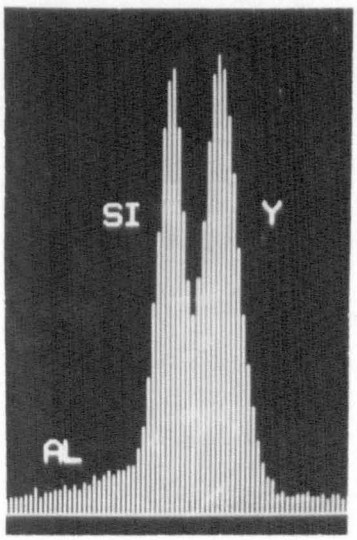

distinct prismatic morphology, becoming more rounded and broken (figure 5.3).

In cross-section, figure 5.4, the oxide layer is thin (~1-2μm), being difficult to observe due to unavoidable rounding off of the specimen edge during preparation. The oxide layer wets the surface with little evidence of nitrogen gas evolution by oxidation of β' to silica. The oxide layer was found to be silicon rich with only small concentrations of yttrium and aluminium present, having diffused from the matrix. Little sub-surface YAG reversion was observed, any being confined to within the first 5μm. This small reaction zone accounts for the small levels of yttrium and aluminium detected in the oxide glass.

5.1.2 Modulus of rupture for oxidised materials

The possible instability around 1000°C due to the transformation of α-Wollastonite to yttrium disilicate ($Y_2Si_2O_7$) with an associated volume expansion prompted the need to examine if any strength degradation occurred in the absence of any associated severe microstructural changes. If the α-Wollastonite phase transforms during oxidation, the volume change would exert an overall tensile stress at the surface. Should an external tensile stress be then applied, such as in 4pt or 3pt bend testing, the measured failure strength would be reduced by the superposition of the two stress fields, resulting in a measured strength much less than obtained at room temperature.

In order to assess whether the α-Wollastonite phase would have the above effects on the material strength, room temperature 3 point bend tests were performed on twenty specimens. Essentially no change

Figure 5.4 Oxide and sub-oxide development of LCS 201 after oxidation at 1200°C for 100 hours.

Cristobalite

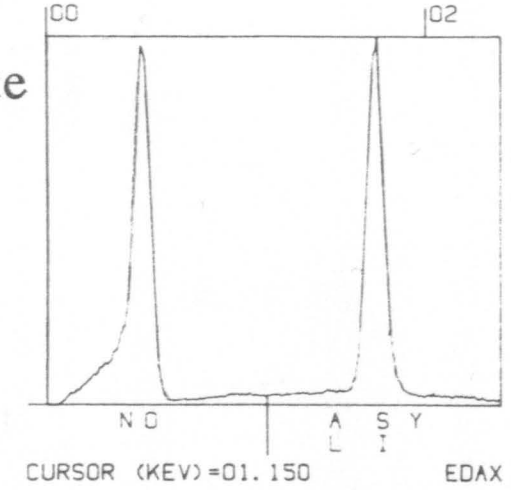

Oxide glass

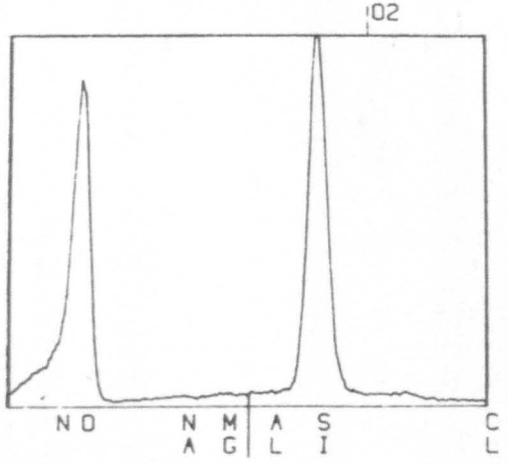

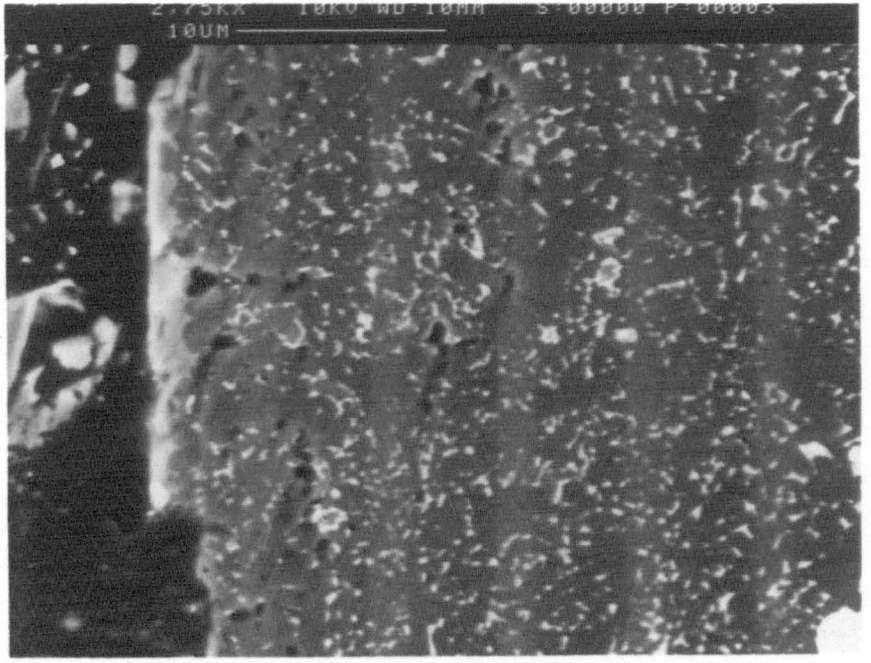

Fig 5.4

in both the Weibull modulus (m~17), and the average MOR (σ) of 880MPa was observed. SEM studies of the fracture surfaces showed no significant differences between the oxidised ceramic and those given no heat-treatment.

The strength data obtained in this section supports the evidence from the previous section that although the unstable α-Wollastonite does exist in LCS 201 in small quantities, it does not affect the mechanical strength either in the value of the MOR or by increasing the flaw population, ie an effective decrease in the measured Weibull modulus (m).

5.2 High temperature oxidation of LCS 201

Upon increasing the temperature to 1300°C and above, the oxidation characteristics differ considerably from those observed at the lower temperatures. This section will detail observations of the effects of oxidation in the range 1300°C to 1400°C predominantly for the β'-YAG LCS 201 material.

5.2.1 Oxide layer observations

Below 1300°C oxide layer development was found to consist of small needle-like yttrium disilicate crystals in a thin continuous glassy layer. At 1300°C and above, a morphological transition occurs, with the distinct $Y_2Si_2O_7$ needle-like growth being replaced by a more equiaxed tablet like morphology. This is as a result of increased nucleation and growth rates in a reduced viscosity oxide layer at the higher temperatures.

Oxide layer development at 1300°C and 1350°C is shown in figure 5.6. At short times, yttrium disilicate is the only crystalline

Figure 5.6

a) Oxide surface development at 1300°C for (i) 3 hours, (ii) 100 hours and 1350°C for (iii) 3 hours, (iv) 100 hours.

b) Typical EDX spectra of α-cristabolite, oxide glass and mullite ($3Al_2O_3.SiO_2$)

Fig 5.6(a)

(i)

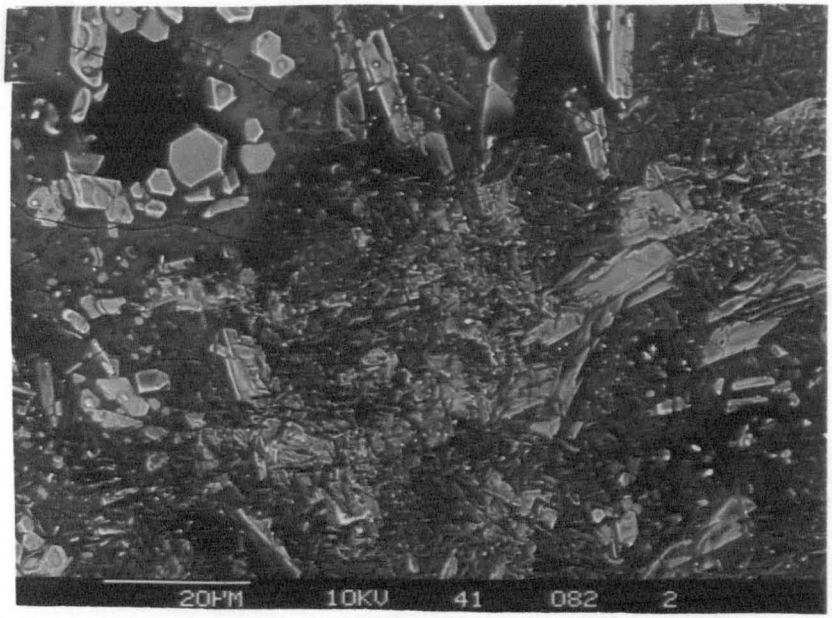

(iii)

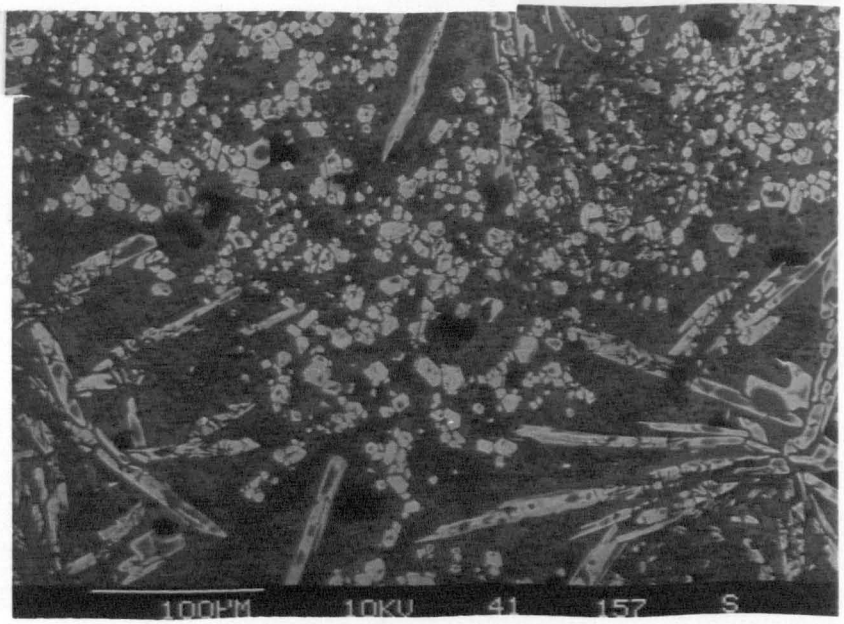

(ii)

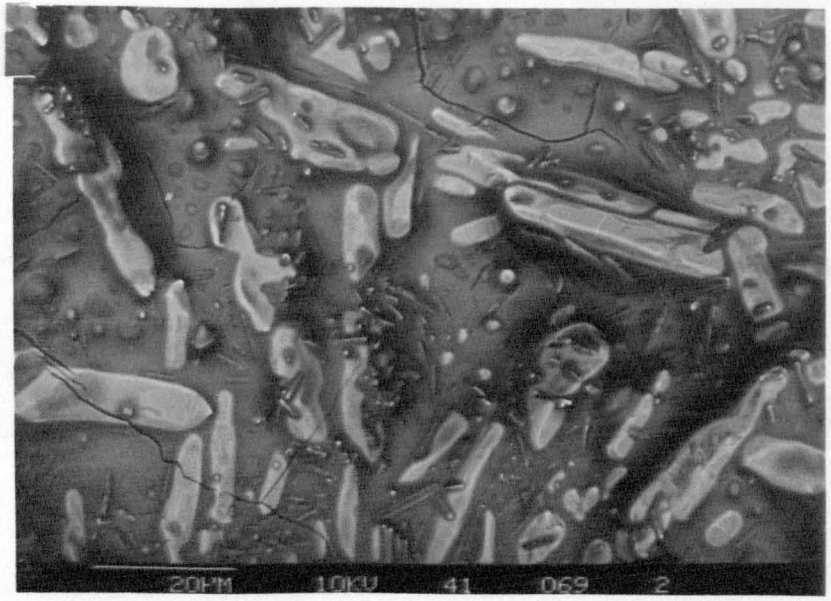

(iv)

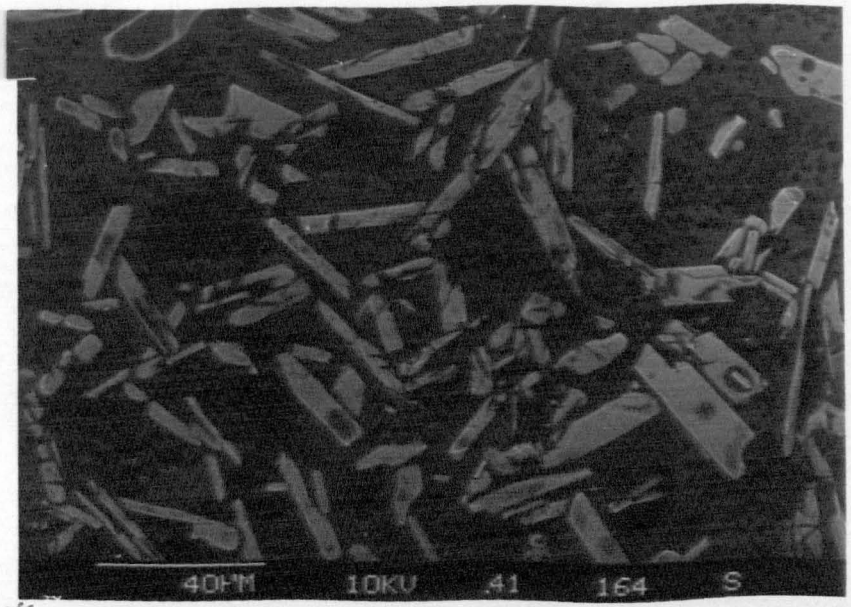

Fig 5.6(b)

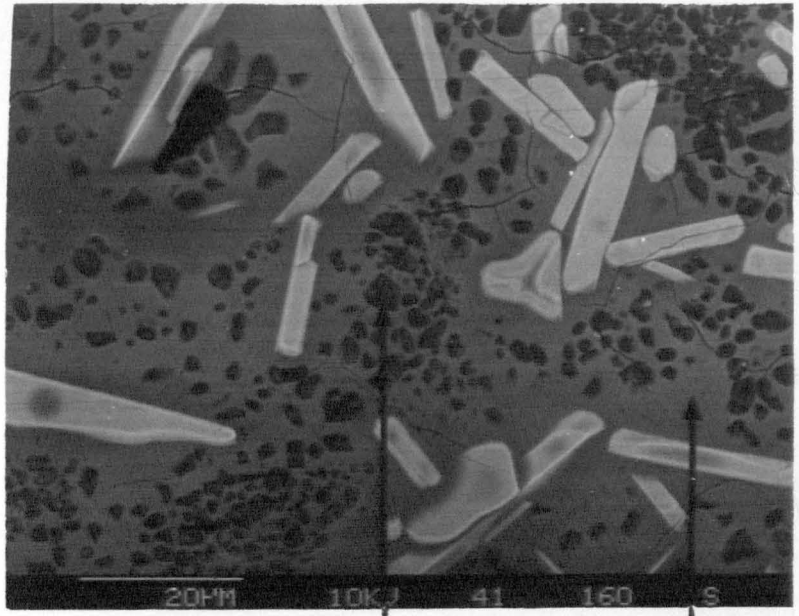

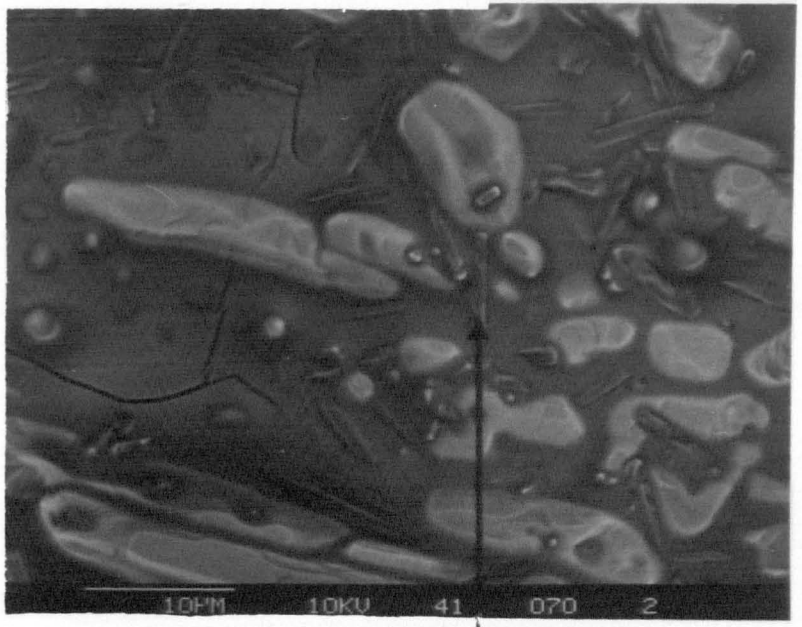

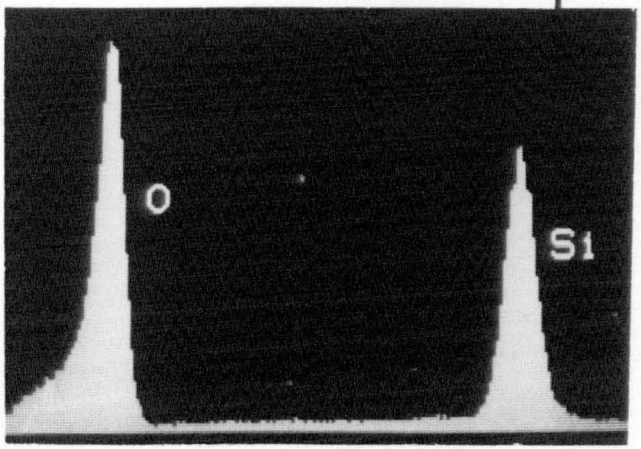

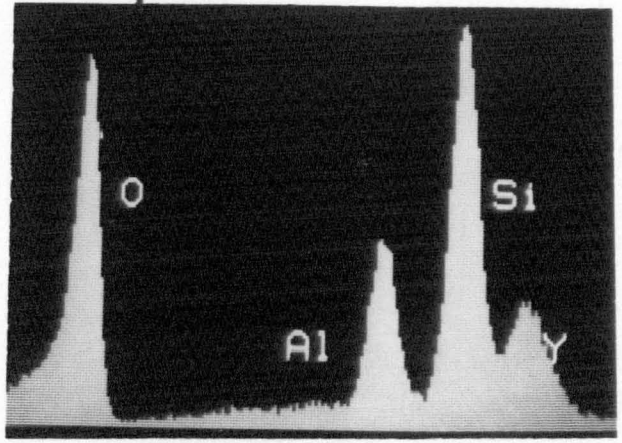

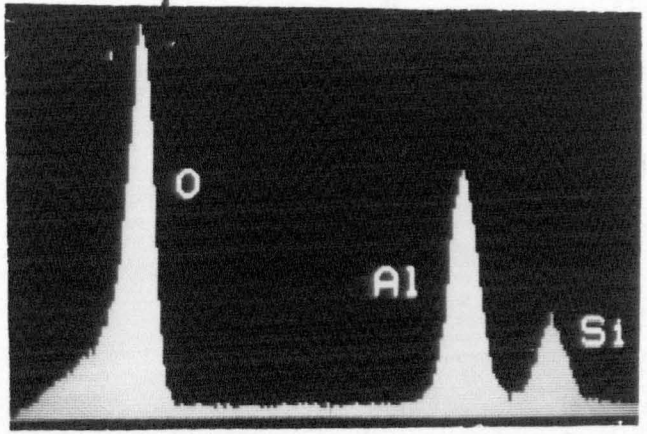

species forming in the oxide layer glass. The distinct needle-like morphology is replaced with a large increase in small tablet-like $Y_2Si_2O_7$ crystals (~ 1-2μm), evenly covering the surface. Increasing time resulted in the growth of these, and the nucleation of small needle-like mullite crystals, $3Al_2O_3.2SiO_2$ (ASTM No. 15-776). The yttrium disilicate crystals are much larger and irregularly shaped, growth being controlled by the merger and envelopment of adjacent grains, and the dynamic solution into the oxide layer glass.

At 1350°C, the reduced viscosity of the oxide layer results in increased crystallisation. Large yttrium disilicate crystals form (>100μm), with significant amounts of α-cristobalite and mullite crystals. Also evident are pores associated with penetration of nitrogen gas through the oxide layer as a result of increased kinetics.

5.2.2 Oxidation kinetics, surface and sub-surface reactions

Oxidation kinetics in all materials at temperatures of 1300°C and above were determined from oxide film thickness measurements of sectioned samples with increasing time. Chemical reactions and sub-surface microstructural changes were also monitored by this method at all stages of testing.

Figure 5.7 shows plots of oxide layer thickness versus time for oxidation of LCS 201 at 1300°C and 1350°C. Oxidation at both temperatures approximated to parabolic kinetics, consistent with previous observations by Lewis et al (97) and Babini et al (90). It can be seen that although the oxidation kinetics remain parabolic, the rate increases dramatically over the small temperature range 1300°C to 1350°C. At the lower temperature, the oxide layer increases in thickness continuously with time, obeying a parabolic rate law.

Figure 5.7 Oxidation kinetics for LCS 201 derived from oxide layer thickness measurements at

a) 1300°C

b) 1350°C

Fig 5.7

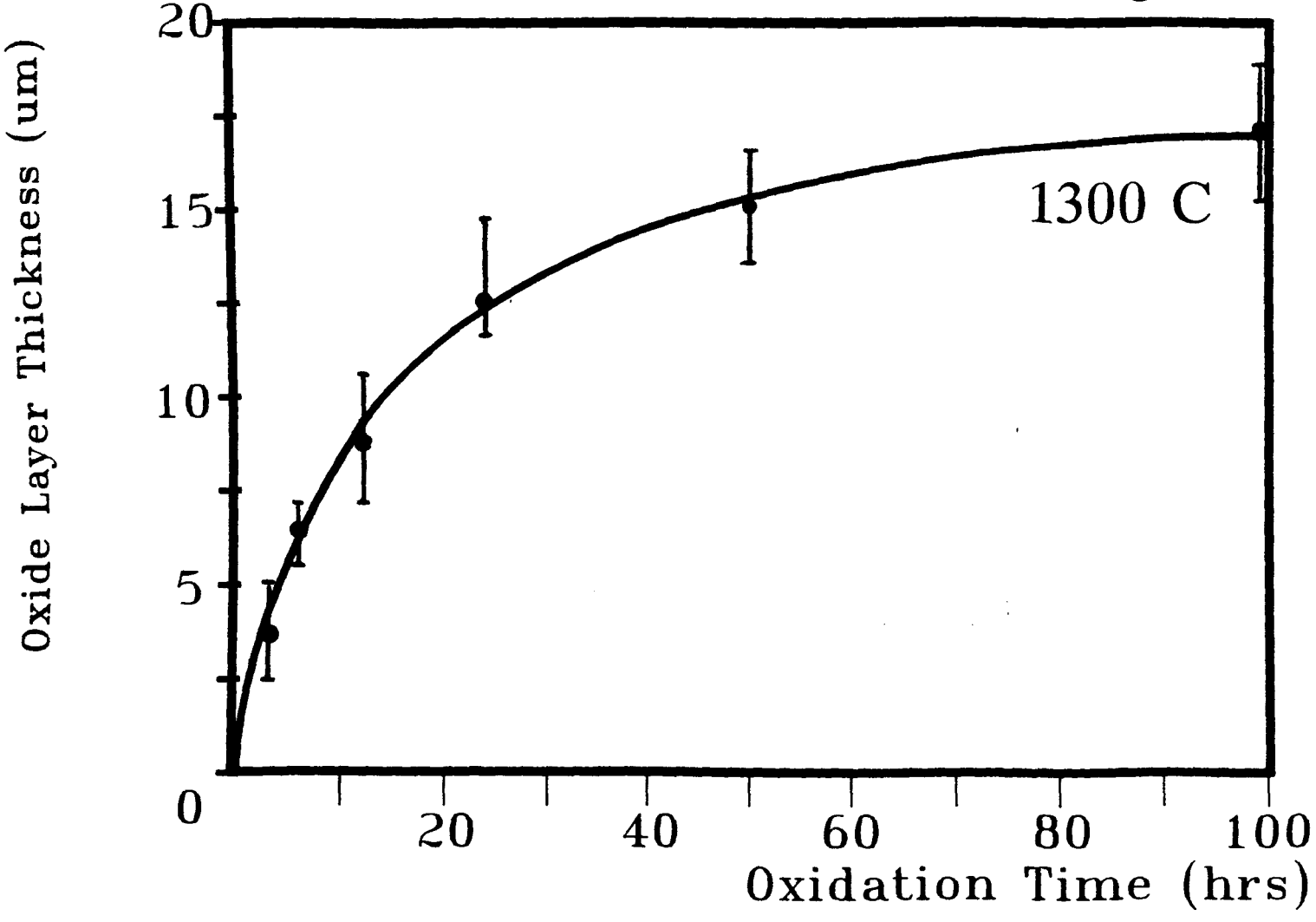
Oxide Layer Thickness (um)
20
15
10
5
0
1300 C
20
40
60
80
100
Oxidation Time (hrs)

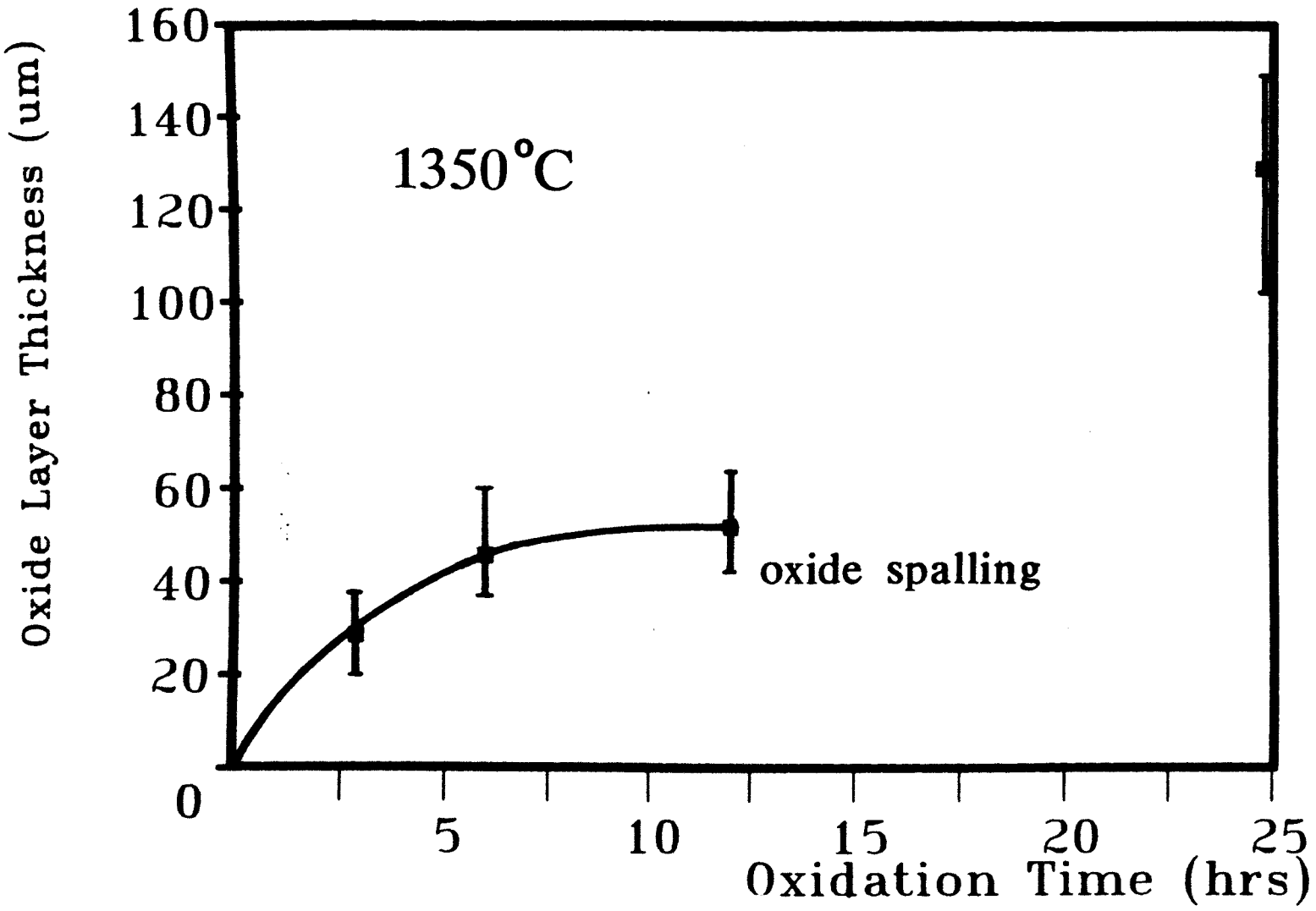
Oxide Layer Thickness (um)
160
140
120
100
80
60
40
20
0
1350°C
oxide spalling
5
10
15
20
25
Oxidation Time (hrs)

However, at 1350°C, although the general form of the oxidation behaviour remains parabolic, a discontinuity is observed after approximately 12 hours. This effect was explained from observations of the cross-section of the oxidised sample.

Below 1300°C, oxide layer development was found to be so slow that oxide film thickness could not be measured. Above 1350°C, severe spalling and disruption of the oxide scale caused extreme variations in the measured oxide layer thickness. Therefore calculated errors from these effect precluded meaningful plots of the oxidation kinetics above 1350°C for the β'/YAG materials.

Figure 5.8 shows the oxide and sub-oxide layer development for the LCS 201 β'-YAG ceramic at temperatures between 1300°C and 1400°C. At 1300°C, the oxide layer is predominantly glassy with some crystallisation of β-$Y_2Si_2O_7$ and α-cristobalite, with some large bubbles as a result of nitrogen gas evolution at or near to the oxide/substrate interface. Marked microstructural changes were observed even after short periods of exposure.

Sectioned specimens were observed to have developed a zone below the oxide scale depleted of yttrium and aluminium from the intergranular regions with increased porosity. This is due to the reversion of YAG to a eutectic liquid by direct reaction with the oxide layer. The formation of this liquid results in rapid cation diffusion away from the reaction front, driven by a chemical potential derived from the compositional difference between the oxide layer and the reaction front, shown schematically in figure 5.9, in order to equilibriate the overall composition. This rapid cation out-diffusion has two effects. Firstly, compositional modification of the oxide layer reduces the viscosity and causes the observed crystallisation of species such as yttrium disilicate and mullite. The lower viscosity

Figure 5.8

a) ⟶c) Oxide layer development with time at 1300°C

d) EDX analysis of oxide glass, $Y_2Si_2O_7$ and α-cristabolite

e) Backscattered electron micrograph of sub-oxide YAG reversion zone after oxidation at 1300°C, and transmission electron micrograph of β' dissolution.

f) ⟶h) Oxide layer development with time at 1350°C

i) ⟶k) Oxide layer development with time at 1400°C

(a)

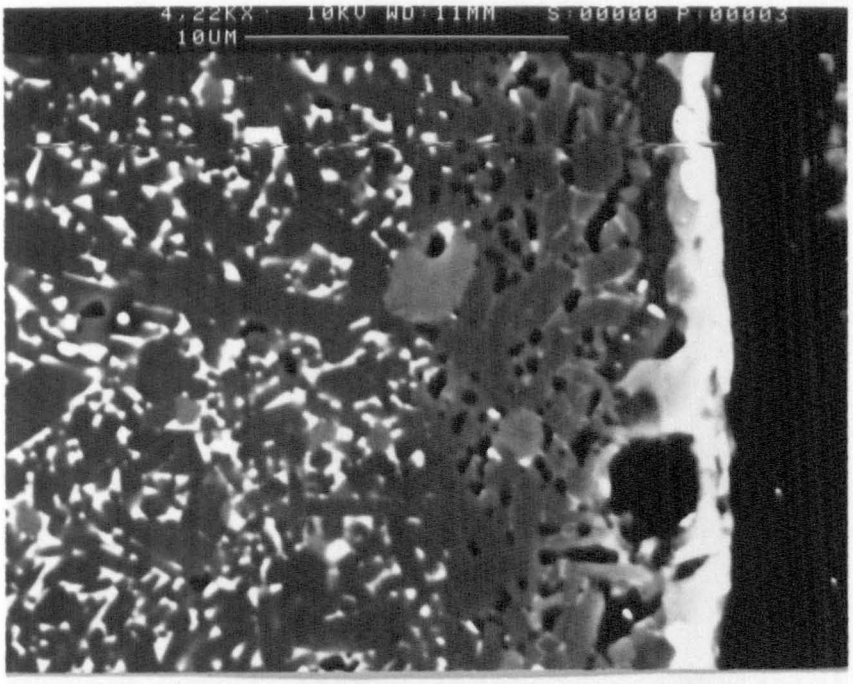
4,22KX 10KV WD 11MM S 00000 P 00003
10UM

Fig 5.8

(b)

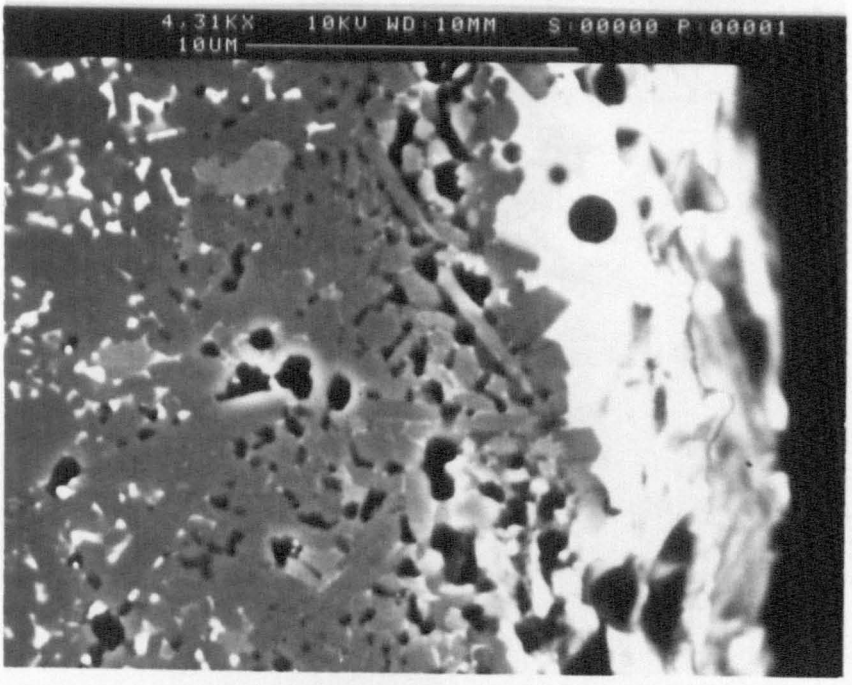
4,31KX 10KV WD 10MM S 00000 P 00001
10UM

(c)

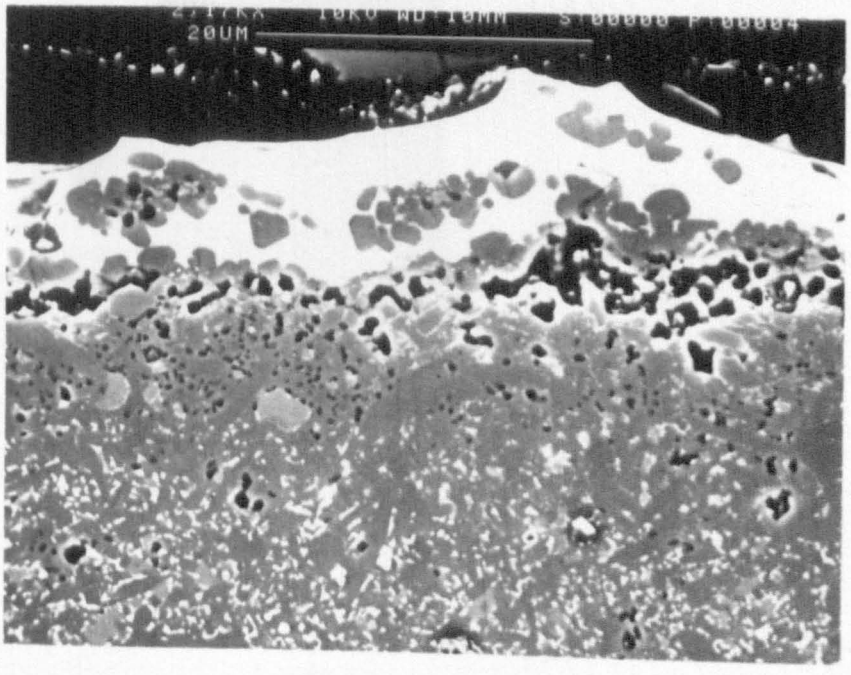
20UM

Fig 5.8

(d)

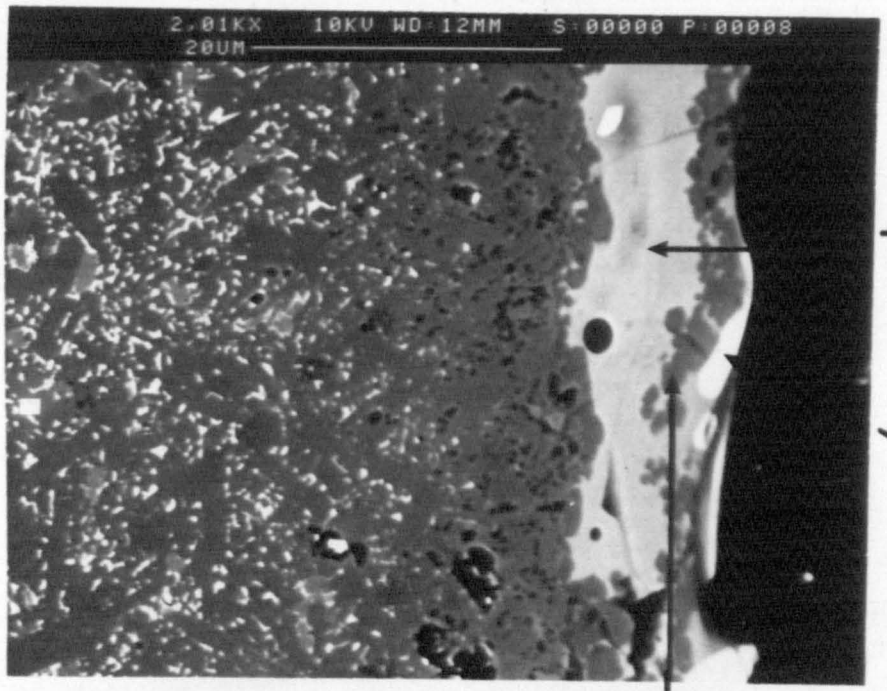
2.01KX 10KV WD 12MM S:00000 P:00008
20UM

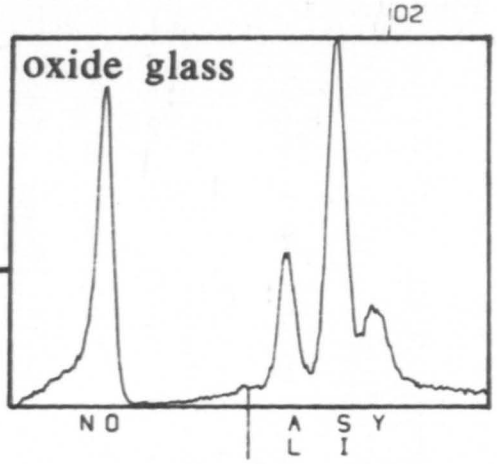
oxide glass
102
NO
ALLY

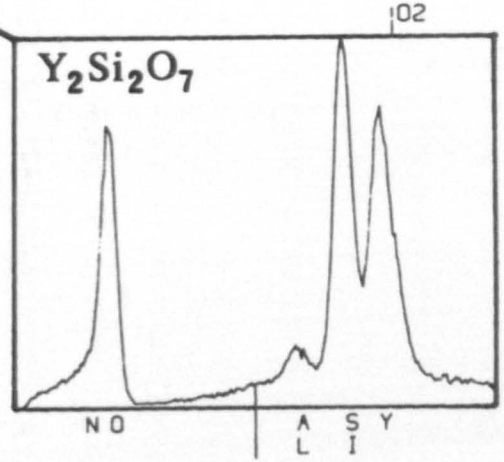
$Y_2Si_2O_7$
102
NO
ALLY

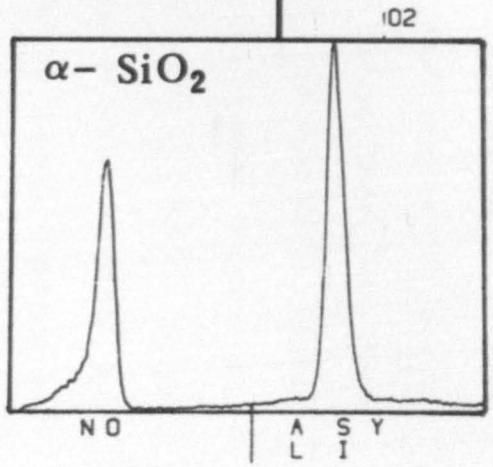
α– SiO_2
102
NO
ALLY

results in more rapid inter-diffusion of oxygen to the reaction front, hence causing an increase in the oxidation rate. The second effect of the rapid out-diffusion from the reaction interface is that the now Si^{4+} and O^{2-} enriched liquid readily reacts with YAG at the interface resulting in continued rapid reversion.

The source of silicon ions in this layer is further enhanced by the dissolution of the β' grains by the silicate liquid within this region, figure 5.8(e). This effect is consistent with observations of oxidation of earlier development sialon ceramics (172).

At 1350°C, the dramatic increase in the oxidation kinetics is associated with a rapid increase in the sub-surface reversion zone, due to increased out-diffusion of metallic cations into the oxide layer, figure 5.8(f to h). This is associated with an increase in porosity within this zone. At this temperature, the YAG matrix readily reacts with the oxide layer forming a low temperature liquid (melting temperature T≈1320°C). This results in the rapid out-diffusion of metallic cations, due to the lower viscosity reverted liquid at this temperature. Large scale crystallisation of yttrium disilicate and α-cristobalite within the oxide layer was also observed, being due to the reduced viscocity of the oxide layer. Hence the oxide layer assumes a more crusty, uneven morphology, compared with the predominantly glass layer observed at 1300°C. After approximately 12 hours exposure, it was observed that nitrogen gas evolution caused severe blistering of the oxide layer, leading to spalling. Oxidation kinetics were observed to increase at this point due to the oxide layer now being non-protective.

Increasing the oxidation temperature to 1400°C shows the susceptibility of these type of materials to catastrophic oxidation, figure 5.8(i to k). At this temperature, extensive oxide layer development was observed, with large scale crystallisation within the

Fig 5.8

(e)

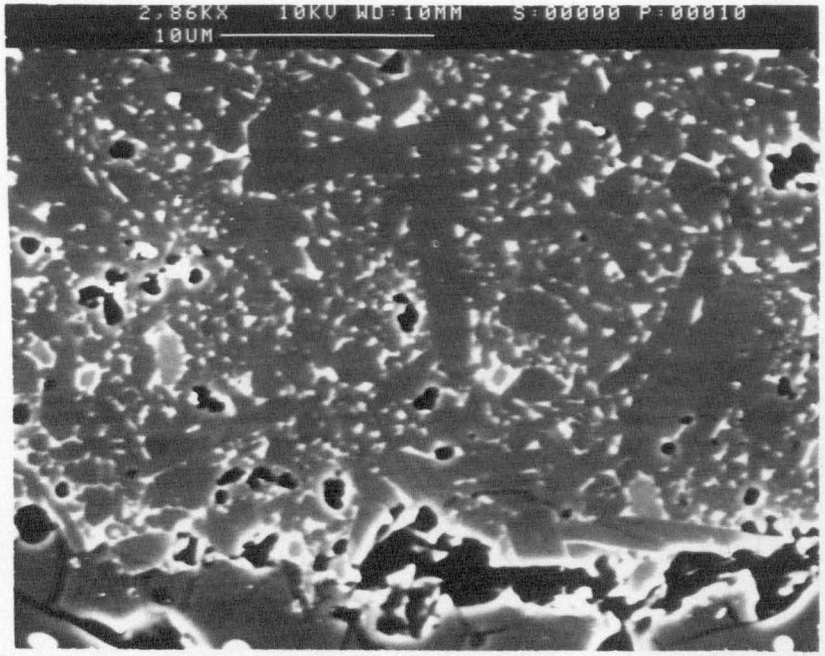

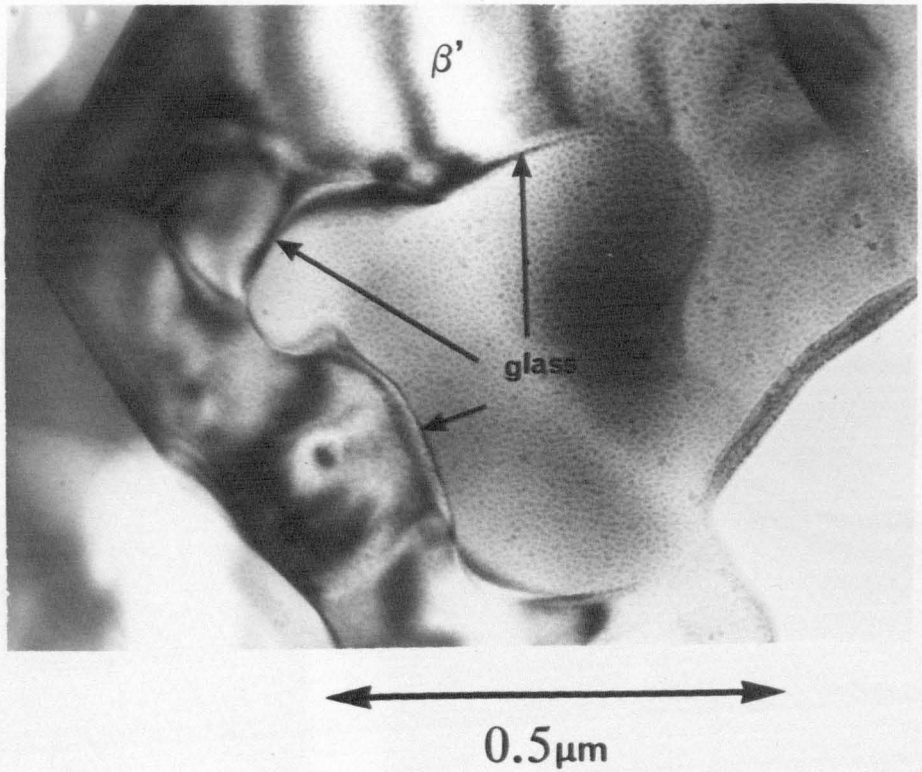

(f)

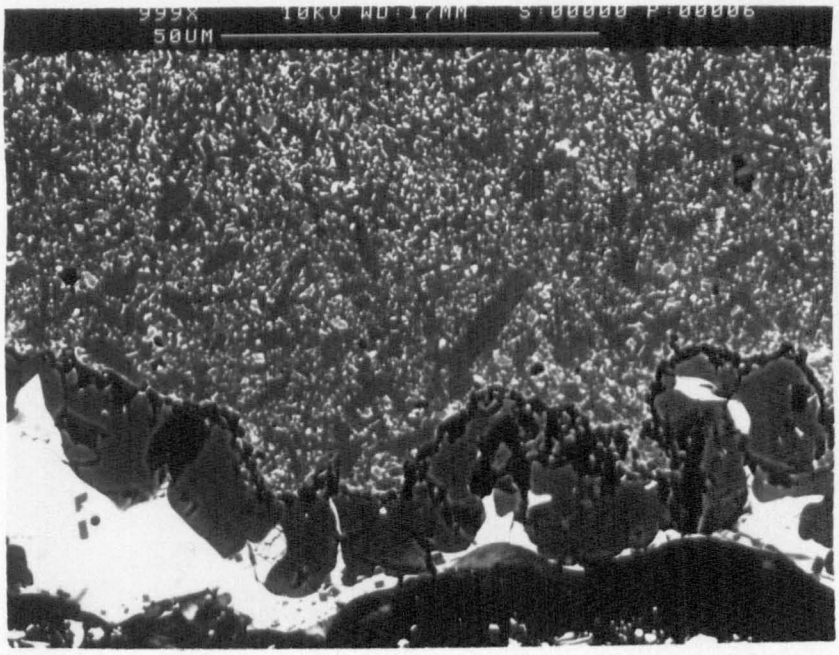
999X 10KV WD:17MM S:00000 P:00006
50UM

Fig 5.8

(g)

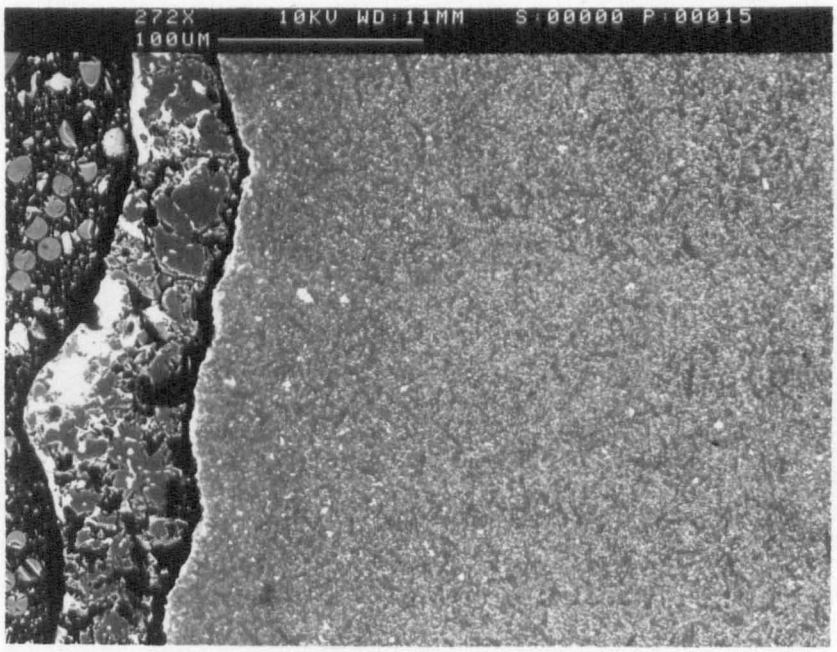
272X 10KV WD:11MM S:00000 P:00015
100UM

(h)

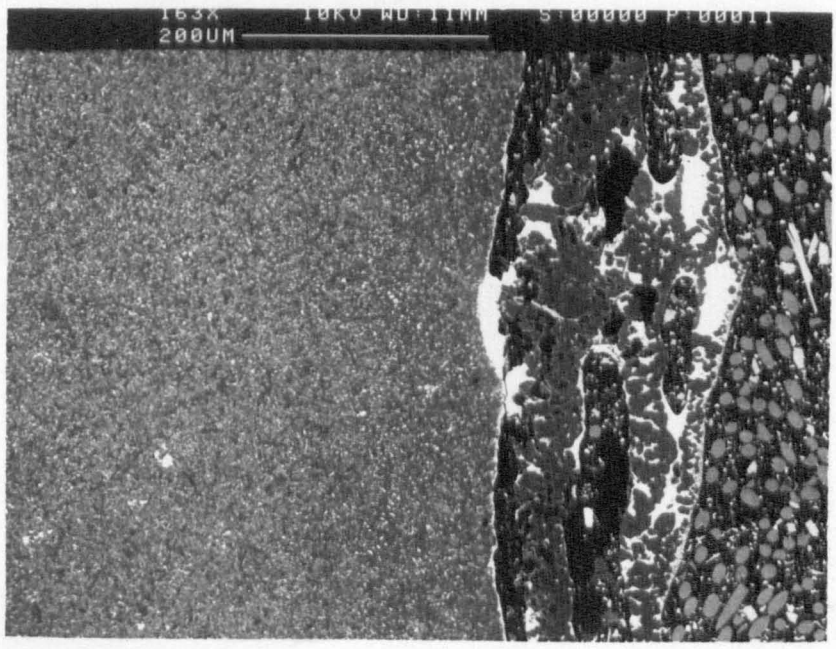
163X 10KV WD:11MM S:00000 P:00011
200UM

(i)

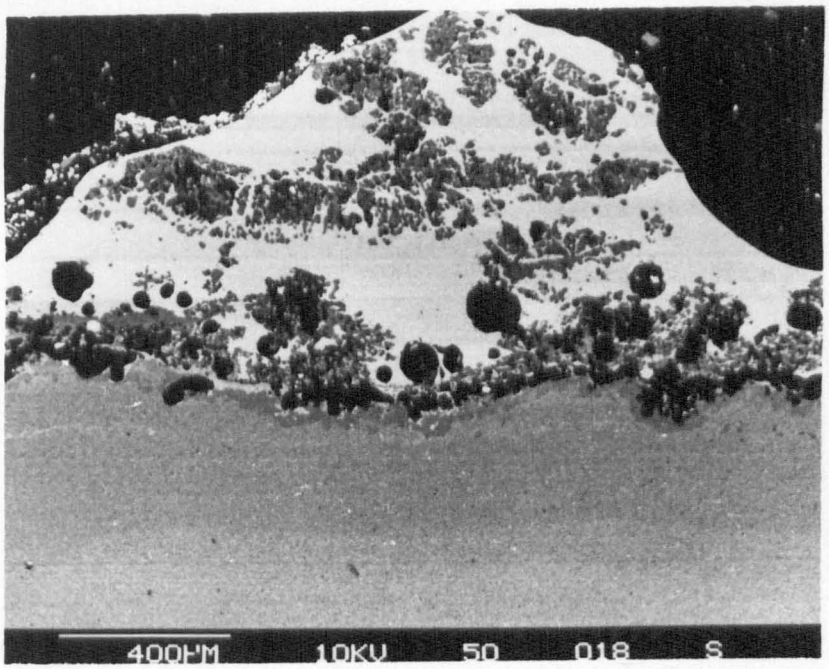

Fig 5.8

(j)

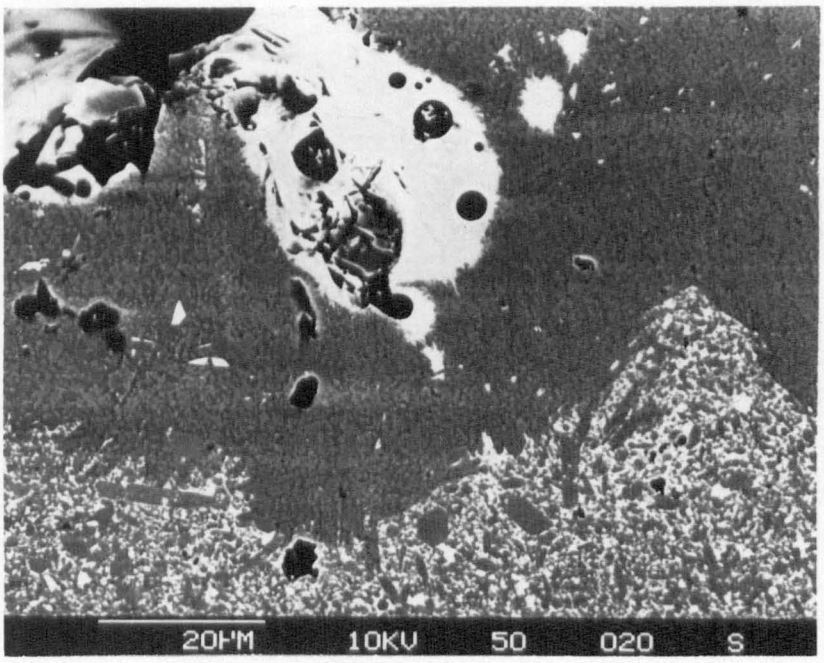

(k)

Figure 5.9 Schematic representation of oxidation in LCS 201 β' - YAG materials.

Fig 5.9

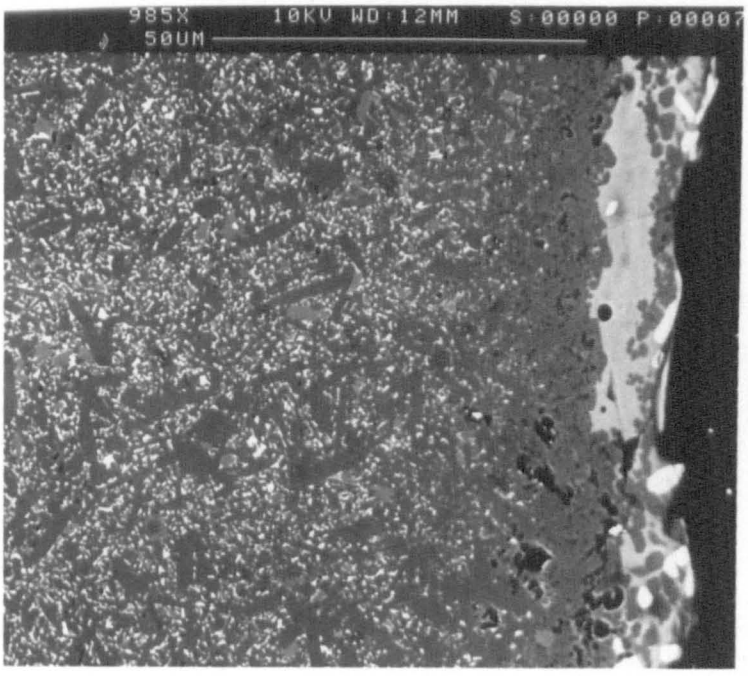
985X 10KV WD:12MM S:00000 P:0000
50UM

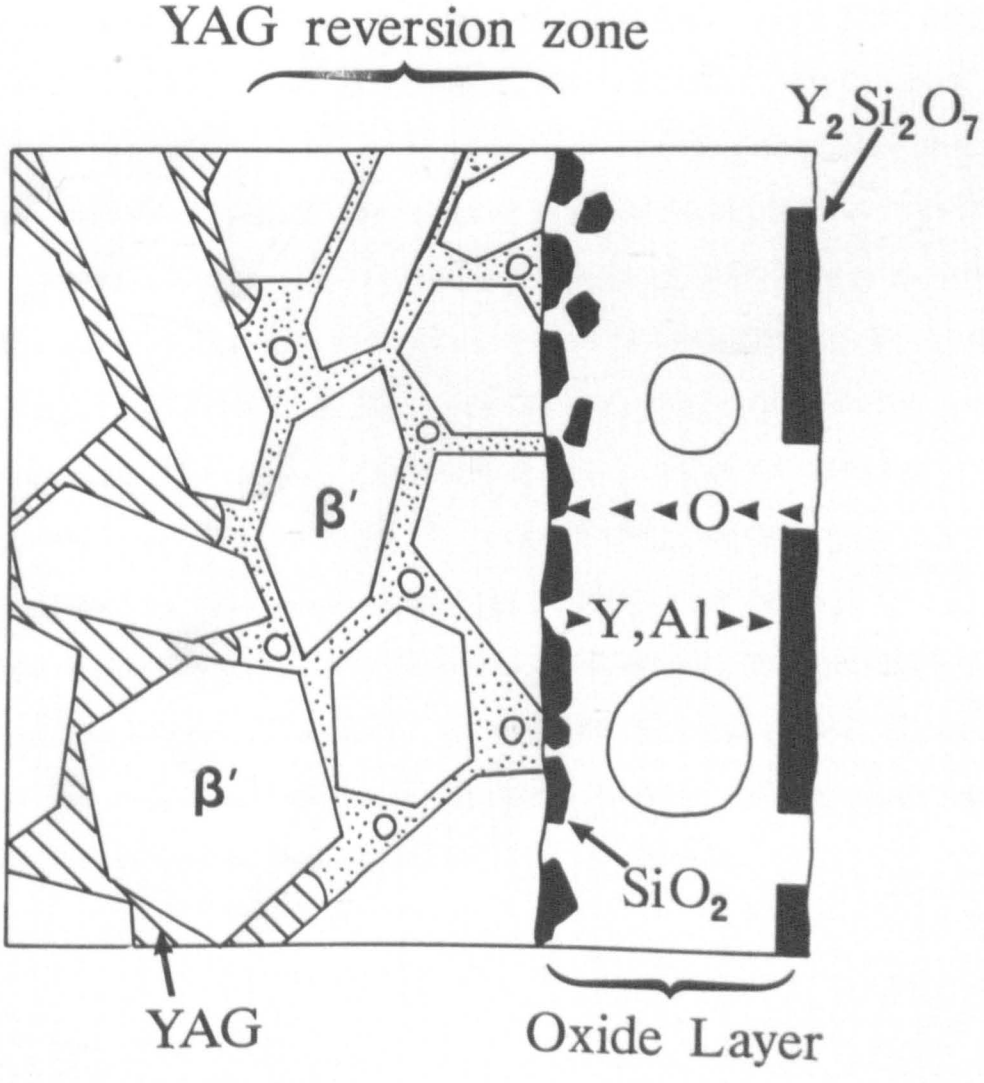
YAG reversion zone
$Y_2Si_2O_7$
β′
β′
O
Y, Al
SiO_2
YAG
Oxide Layer

layer, and significant YAG reversion taking place in the sub-surface as described at the previous temperatures but increased.

5.2.3 Discussion of the mechanism for oxidation

The mechanism for oxidation for sialon ceramics containing YAG matrices may be concluded to follow this general form.

(i) At all temperatures initial oxidation of the β' grains occurs by the reaction;

$$Si_{3-x}Al_xO_xN_{4-x}\ (s) + (3 - \frac{3x}{4})\ O_2\ (g) \rightarrow (3-x)SiO_2\ (\ell) + \frac{x}{2}\ Al_2O_3\ (\ell) + \frac{(4-x)}{2}\ N_2(g) \qquad (5.1)$$

This forms a continuous aluminium containing oxide layer at the surface.

(ii) A chemical gradient is set up between the oxide layer and intergranular phase, and the need to equilibrate the composition provides the required driving force for cation (Y,Al, + impurities such as calcium and iron) outdiffusion to the oxide layer. This equilibrium is rarely established due to the dynamic nature of the oxidation reaction. Firstly, continued reversion of YAG at the reaction interface provides a source of cations. Secondly, direct dissolution of β' grains within the reversion zone provides a source of silicon ions, reducing the (Y+Al) concentration. This is coupled with surface crystallisation of yttrium disilicate which further reduces the cation concentration in the oxide layer.

(iii) The oxidation rate is determined by elemental diffusion through the amorphous oxide layer to the YAG interface, and reversion of YAG. This is controlled by the viscosity of the glass which is determined by the concentration of cations.

The oxidation properties observed in this range of materials was found to be generally consistent with that observed for a range of related silicon nitride based materials (92,93,172). The viscosity modification due to diffusion of metallic cations from the reaction interface to the oxide layer is totally dependent on the nature of the grain boundary phase. The choice of matrix phase is therefore an essential one, especially if the material is to be used at high temperatures. Ideally it is undesirable to choose a second phase which during oxidation forms a third product which, in the case of YAG, is the sole cause of the observed catastrophic degradation. In general, it is undesirable to have a matrix product lying on the Y_2O_3-Al_2O_3 side of the ternary phase diagram (figure 4.2). Compositions which lie close to SiO_2 in the SiO_2-Y_2O_3 system have been shown to exhibit superior oxidation resistance. These systems generally have a higher temperature binary eutectic, resulting in an increase in the oxidation resistance. This effect has clearly been shown in materials with $Y_2Si_2O_7$ matrix phases which show marked improvement in oxidation resistance compared to those with YAG intergranular phases.

Factors such as the effect that crystallisation of α-cristobalite and oxide layer spalling have not been quantified with respect to the overall oxidation rate. Hence, oxidation is not a single reaction, but the sum of a number of contributing factors, the most dominant one being cited as the rate-controlling factor, though it is recognised that the interdependence of these is not well understood.

5.3 The development of oxidation resistant surface layers

5.3.1 The development of α' layers

Post-sintering thermal treatments at 1800°C were performed on the sintered β'/glass LCS 201 ceramic. One sample was heat-treated in a nitrogen atmosphere in a boron nitride powder bed, the other was given an identical thermal cycle, but a thin AlN/21R coating was applied before the treatment (section 3.3.3).

(a) Uncoated specimen: Figure 5.11 shows the microstructure after heat-treatment. The bulk of the material was not found to be significantly changed from the structure of the original material, apart from two aspects.

Firstly, the amount of α' was observed to have increased after heat-treatment, being attributed directly due to SiO losses moving the overall composition more nitrogen rich and into a phase field where α' formation is more preferred. Secondly the composition of the intergranular phase had moved from its original near ternary eutectic composition to one depleted of aluminium with a composition close to yttrium disilicate if plotted on the oxide face of the Y_2O-SiO_2-Al_2O_3 ternary phase diagram, though the intergranular phase after heat-treatment remained glassy.

The shift in the composition of the intergranular phase is attributed to the increases in the α' level, which is receptive to finite volumes of aluminium and to a lesser extent yttrium. The shift in residual glass composition will critically effect the crystallisation behaviour, both in the product and extent of crystallisation.

An α' layer approximately 20-40μm thick was found to have formed at the β'-glass free surfaces after treatment (figure 5.11(d)).

Figure 5.11 Typical microstructure obtained after heat-treatment at 1800°C.

(a) bulk microstructure

(b) new α' layer formed at free surfaces

(c) original α' layer

(d) zone below original α' layer

Fig 5.11

(a)

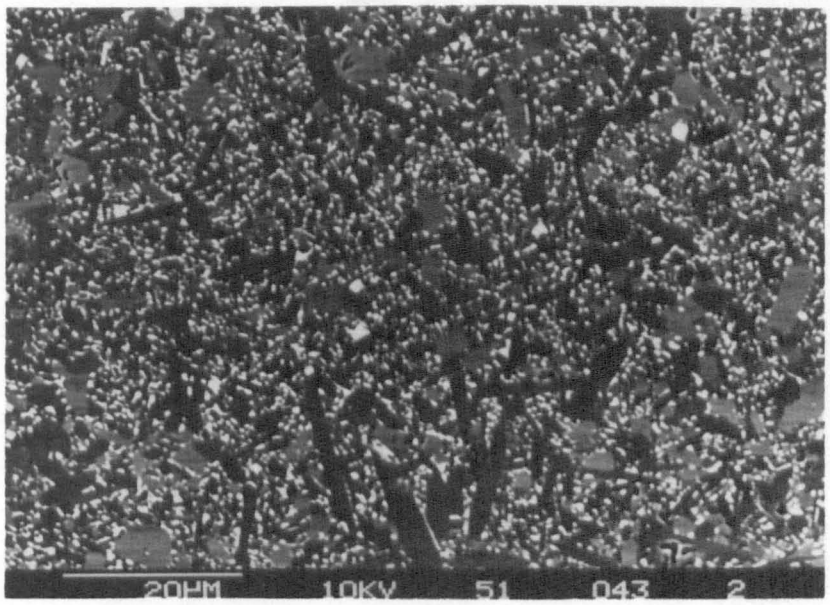

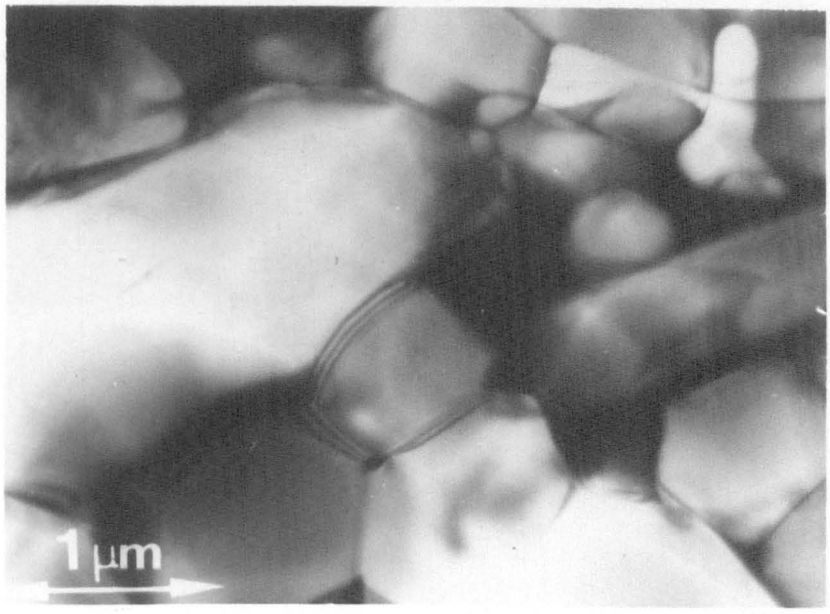

Fig 5.11

(b)

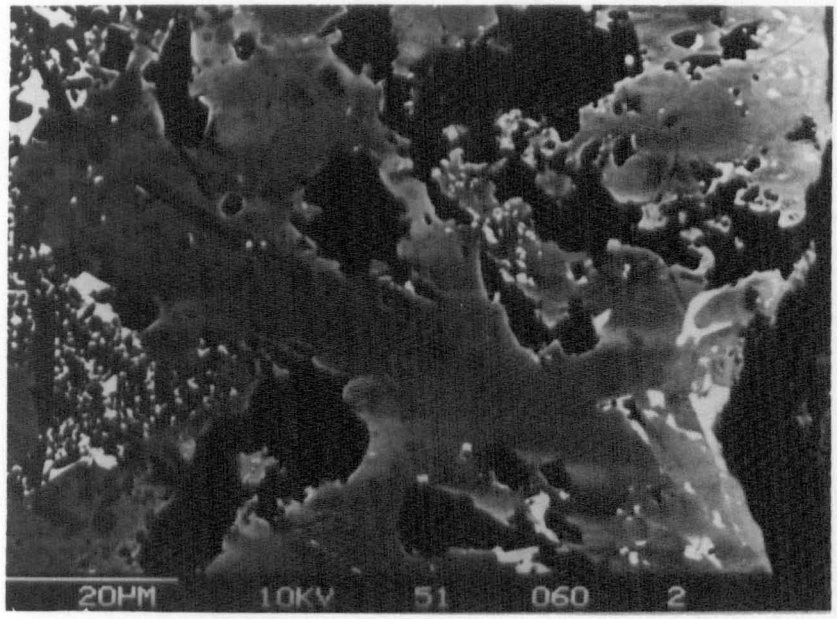
20HM 10KV 51 060 2

(c)

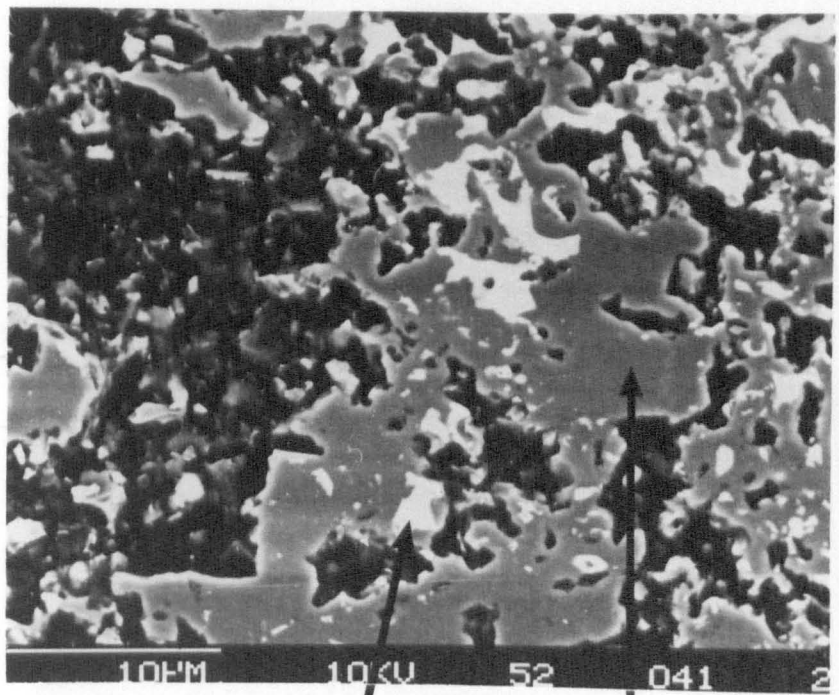
10HM 10KV 52 041 2

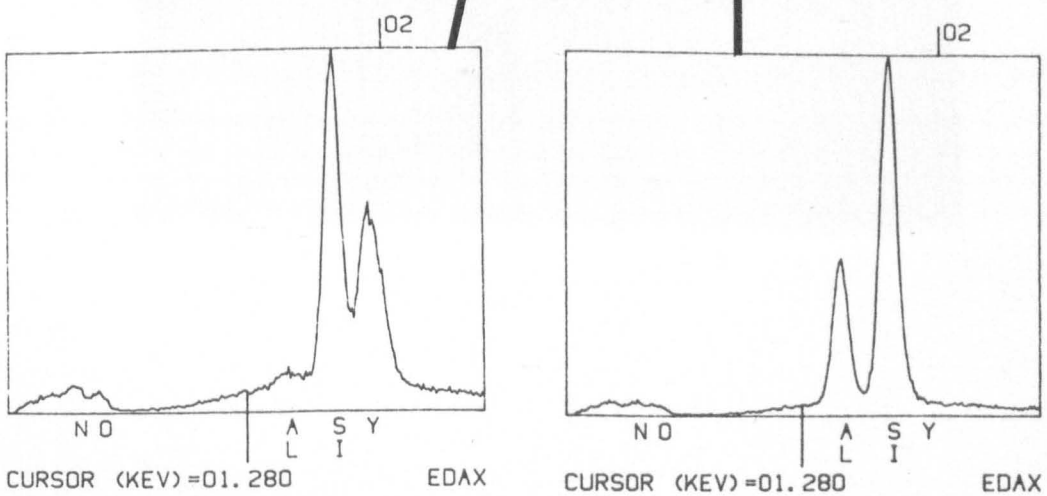
02
NO
ALSI
CURSOR (KEV)=01.280
EDAX
02
NO
ALSI
CURSOR (KEV)=01.280
EDAX

Fig 5.11

(d)

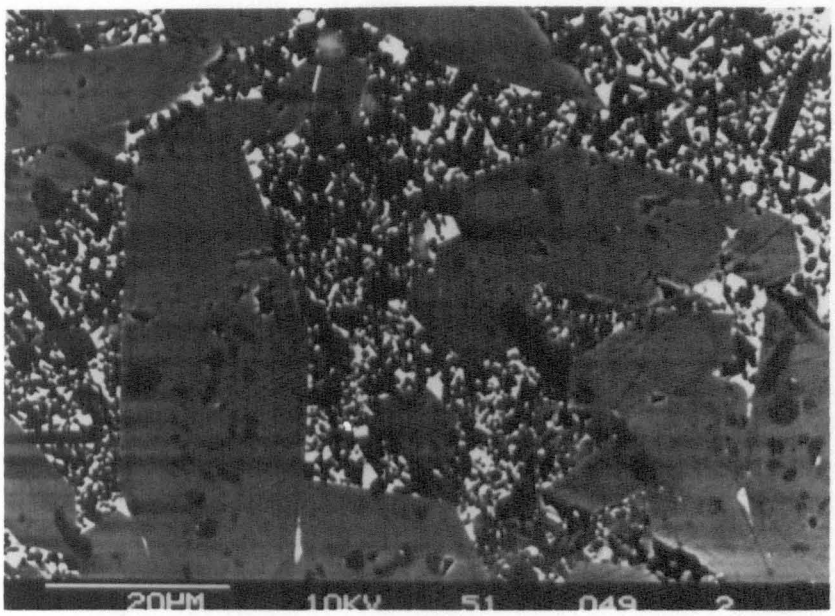

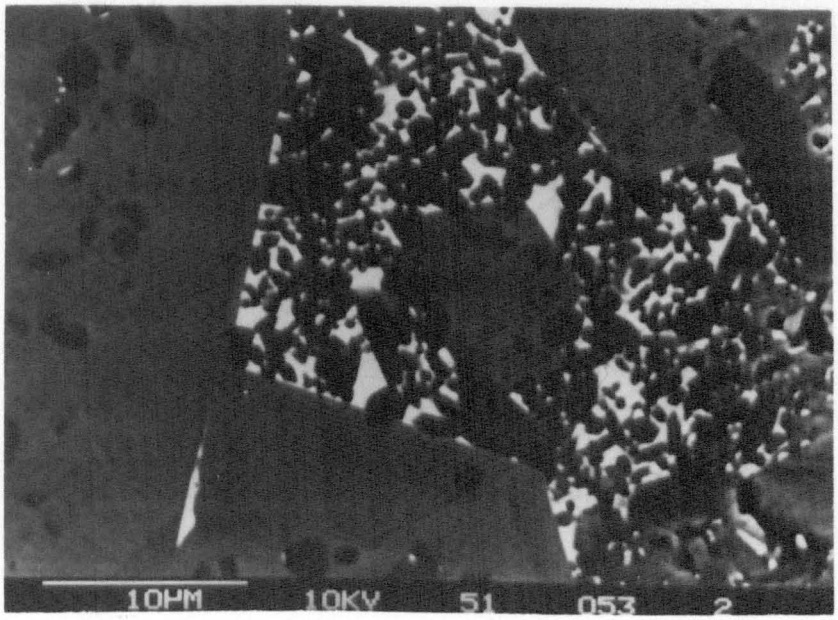

Formation of this layer occurred by the same mechanism as during the sintering process; SiO losses producing a locally nitrogen rich zone. As in the case of the sintered material the α' layer was found to be irregular and disrupted by gas evolution.

The original α' surface layer was found to have reduced to a course two phase structure consisting of β'-sialon (x~1) of composition;

$$\beta' - Si_2Al\ O\ N_3 \qquad (5.2)$$

and a yttrium rich phase with composition near to the Y_2O_3-SiO_2 binary eutectic (figure 5.11(b)). Beneath this, large α' crystals had formed, enveloping smaller β' grains as a result of local high nitrogen levels (figure 5.11(c)).

(b) Specimen coated with AlN/21R: this coating was used in an attempt to reduce the gaseous losses during heat-treatment and to promote the β'-α' transformation by increasing the nitrogen level in the surface region.

Figure 5.12 illustrates the typical microstructures observed. Generally similar microstructural changes were observed to those seen previously. Increased α' levels and an aluminium depleted matrix phase were found in the bulk. Large areas were found to have degraded to the high substitution β'(x~1), a glass of similar composition to that observed into the bulk, and a large amount of porosity. Below this, as in the previous case was a zone where large α' crystals were found to have formed.

α' was found to have formed at the free surfaces, as before, but with a greater volume of residual glass present. The layer was also less disrupted than the previous case, the AlN/21R coating restricting SiO losses from the surface, acting in a similar fashion to a powder bed, and as a source of aluminium during growth of α'.

Figure 5.12 Typical microstructure obtained from the AlN/21R coated ceramic after heat-treatment at 1800°C.

(a) bulk

(b) original α' layer

(c) new α' layer formed at free surfaces

Fig 5.12 (a)

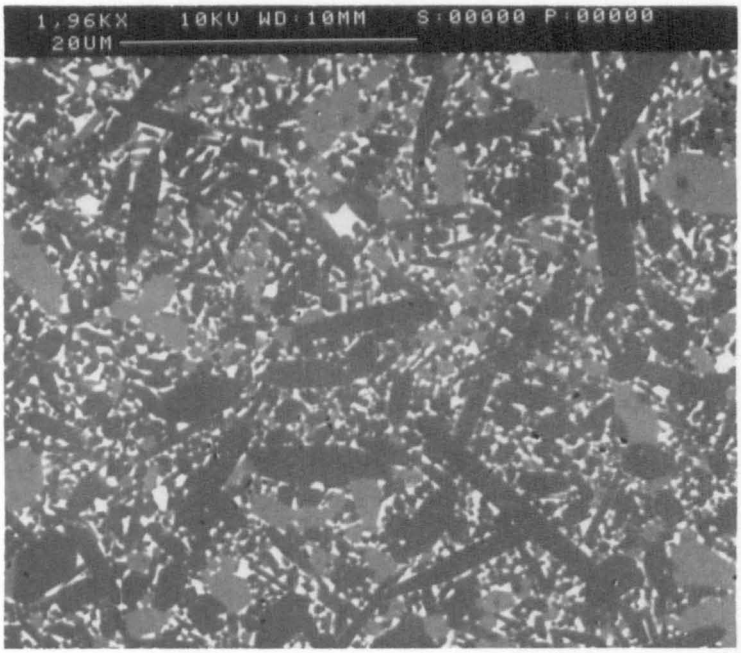
1,96KX 10KV WD:10MM S:00000 P:00000
20UM

(b)

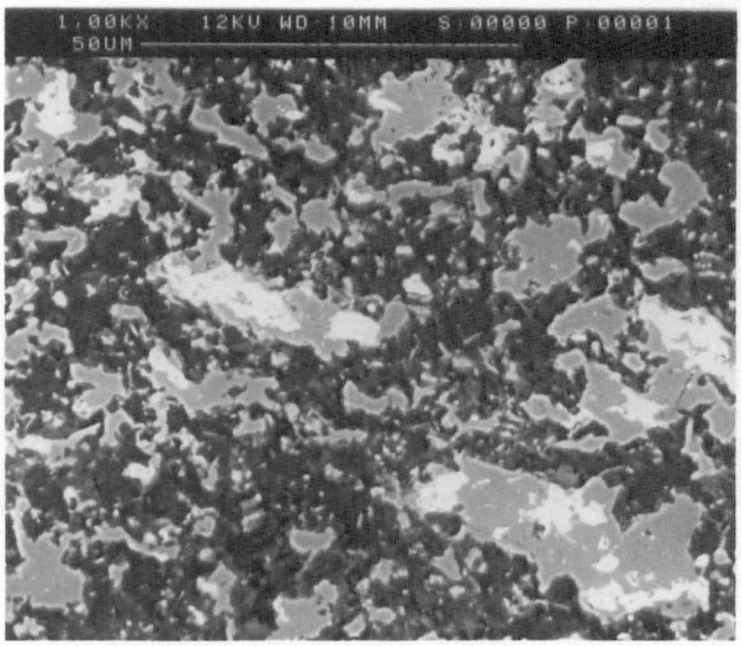
1,00KX 12KV WD:10MM S:00000 P:00001
50UM

(c)

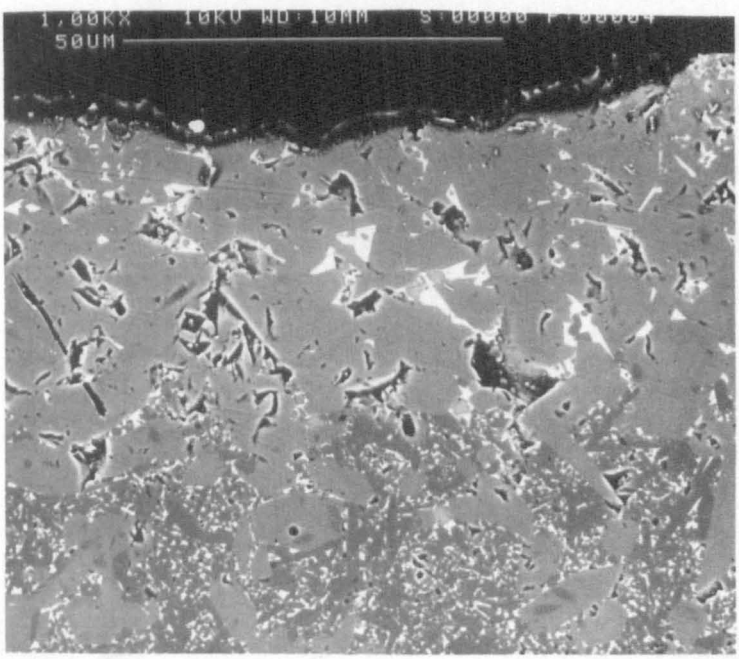
1,00KX 10KV WD:10MM
50UM

However, it must be noted that although an improvement in the α' layer was obtained, substantial disruption of the surface still occurred.

5.3.2 Oxidation of the "billet" surface

The ideal of near net shape processing within the ceramic industry has generated interest in the environmental stability of natural surfaces. In section 4.2 of this study it was shown that in the case of this LCS 201 type of ceramic that the surface microstructure after sintering differed markedly from the bulk microstructure. The presence of nearly single phase α' in this region produced the possibility of increased resistance to oxidation, as YAG reversion would not be a significant factor, at least in the short time.

Oxidation was studied at temperatures of 1300°C and 1350°C for times up to 25 hours. However, determination of kinetics via oxide layer thickness measurement in a similar way to that used in the previous section was not possible due to the irregular nature of the α' layer. This surface could be not be polished because there would be a high probability of perforating the α' layer during this process. Therefore the assessment of the oxidation resistance was only done by direct examination of the sample cross-sections after oxidation.

Figure 5.10 shows typical examples of oxide layer development at the billet surface. At 1300°C, oxide layer development occurs in a similar fashion to that observed at β'/YAG surfaces, i.e. the formation of a glassy silicate layer by direct reaction with the α' crystals with modification by metallic cations (Y,Al) which diffuse from the major crystal phase into the oxide layer, effectively determining the oxidation rate.

At 1350°C, the oxide layer was found to increase dramatically, as in the case of the β'/YAG matrices, with more extensive

Figure 5.10 Oxide layer development at the billet surface

a) 1300°C - 24 hours

b) 1350°C - 3 hours

c) 1350°C - 24 hours where the α' layer has been completely removed as a result of oxidation.

Fig 5.10

(a)

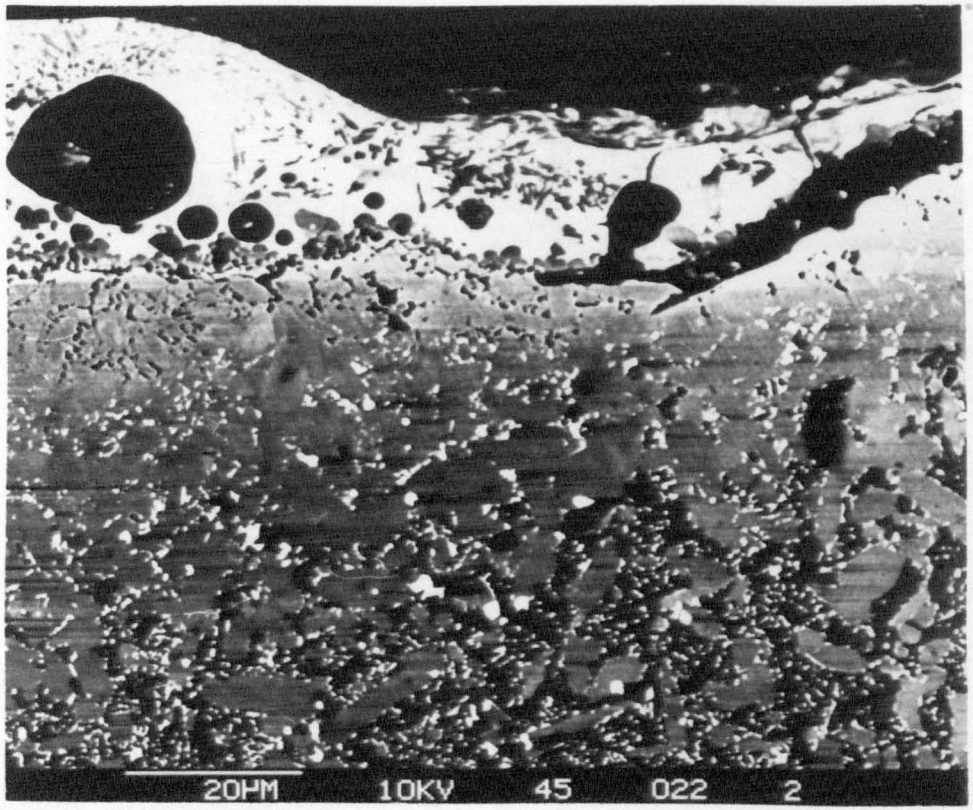

(b)

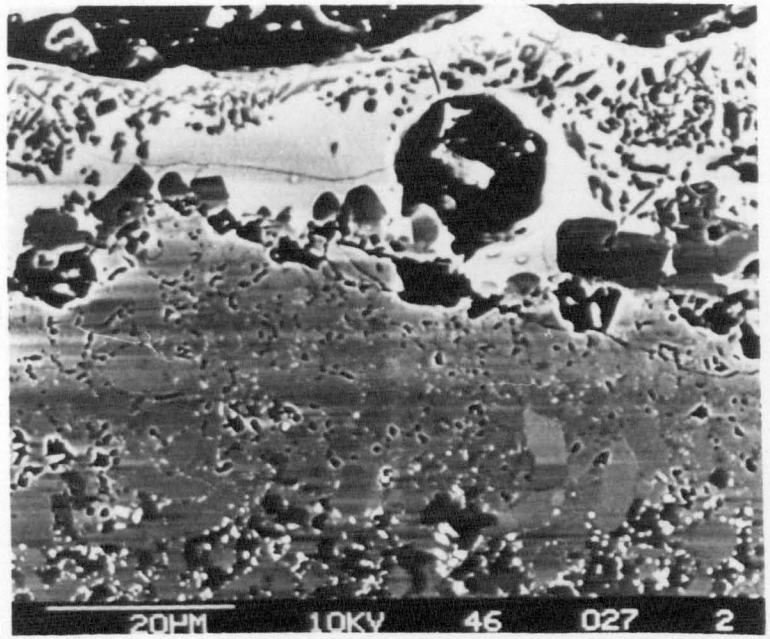

(c)

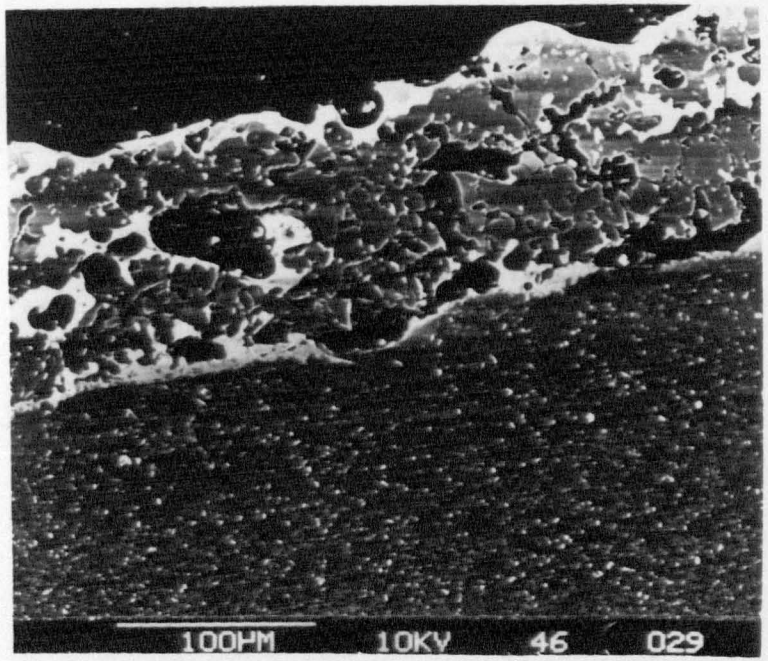

crystallisation within the oxide layer due to the reduced viscosity at this temperature. In several cases the α' layer appeared to have been removed, with continued oxidation occurring at exposed β'/YAG surfaces, with typical effects at this temperature.

The subsurface microstructure remained stable at 1300°C, the α' layer protecting the underlying YAG matrix from reversion by reaction with the oxide layer. The only observable effect was the formation of small amounts of porosity in the vicinity of the oxide-substrate interface caused by the out diffusion of the small amounts of glass and iron silicide impurities into the oxide layer.

It is unclear whether the α' layer produces any significant increase in the oxidation resistance. Clearly, the evidence raises some questions regarding the overall stability of α' in oxidising atmospheres, with the complete removal of some of the α' layer observed at temperatures above 1300°C.

5.3.3 The development of β'/O' oxidation resistant layers

Protective β'/O' layers were formed by two distinct routes. The first being the formation as a result of extended oxidation at elevated temperatures, and the second by formation controllably in much shorter times.

(1) β'/O' layers were observed to form in specimens oxidised for extended periods (>100 hours and up to 1000 hours) at 1300°C, the first observation being in creep specimens after testing. Figure 5.13 shows a typical β'/O' layer formation after such treatment. The β'/O' layer was generally found to be 10 to 15μm in thickness existing directly below the oxide layer. This layer is depleted of YAG, being two phase, the original β' major phase with O' formed in the intergranular regions, replacing any residual reverted YAG.

Figure 5.13 The formation of β'/O' layers by long term oxidation

a) YAG reversion zone after short oxidation times

b) The formation of β'/O' layer after extended treatment.

c) Backscattered electron micrographs of β'/O' layer

d) and e) transmission electron micrographs, bright and dark field, and typical EDX analysis.

(a)

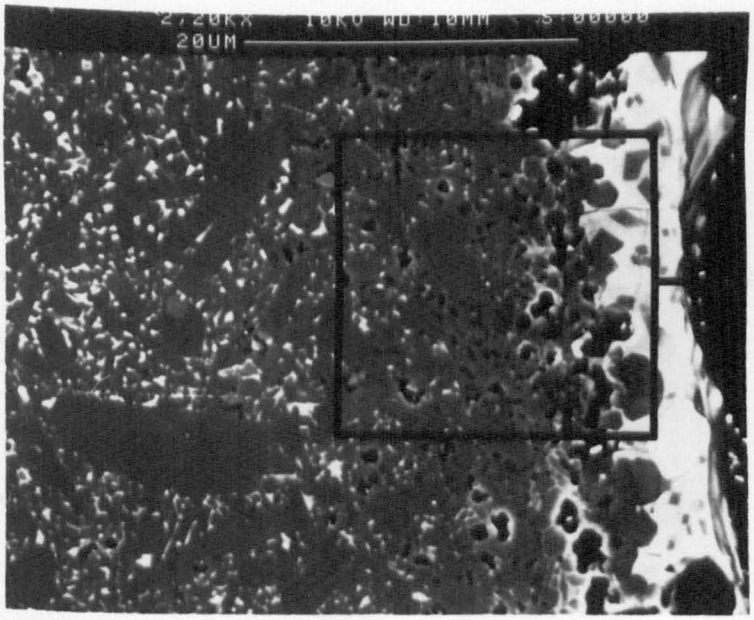

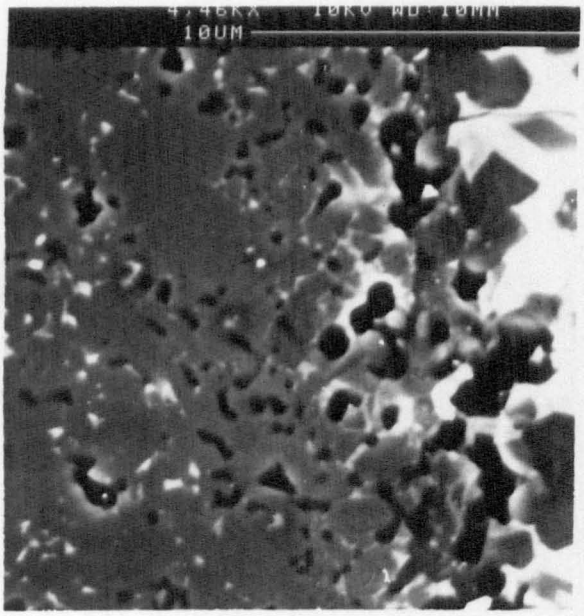

β′+glass

oxidation

β′ + O′

(b)

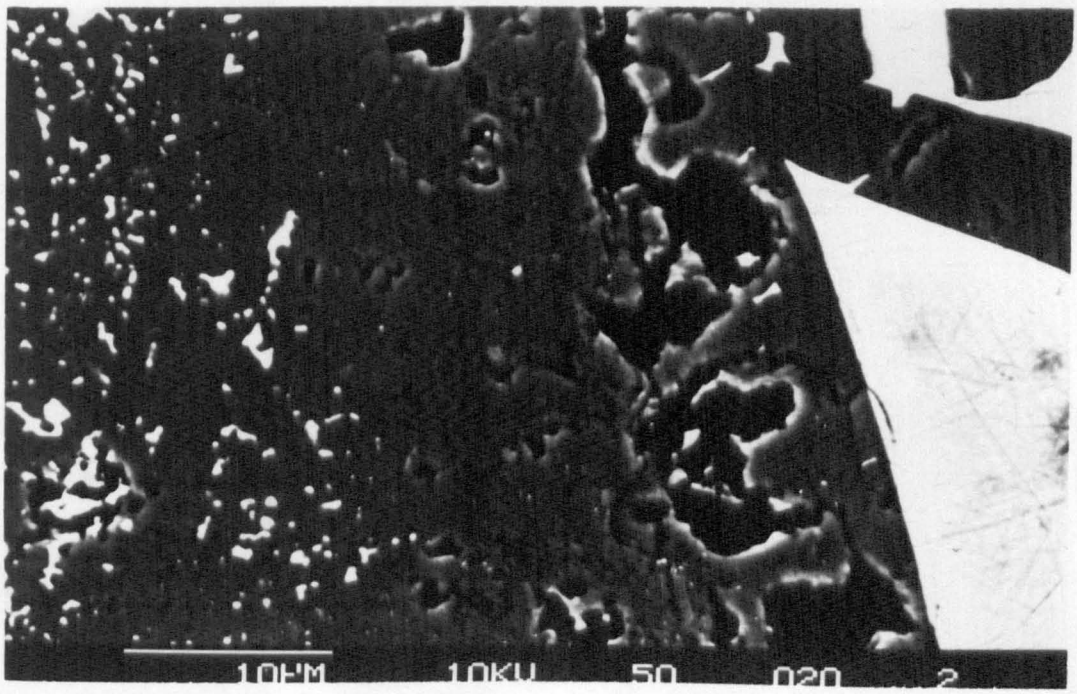

Fig 5.13

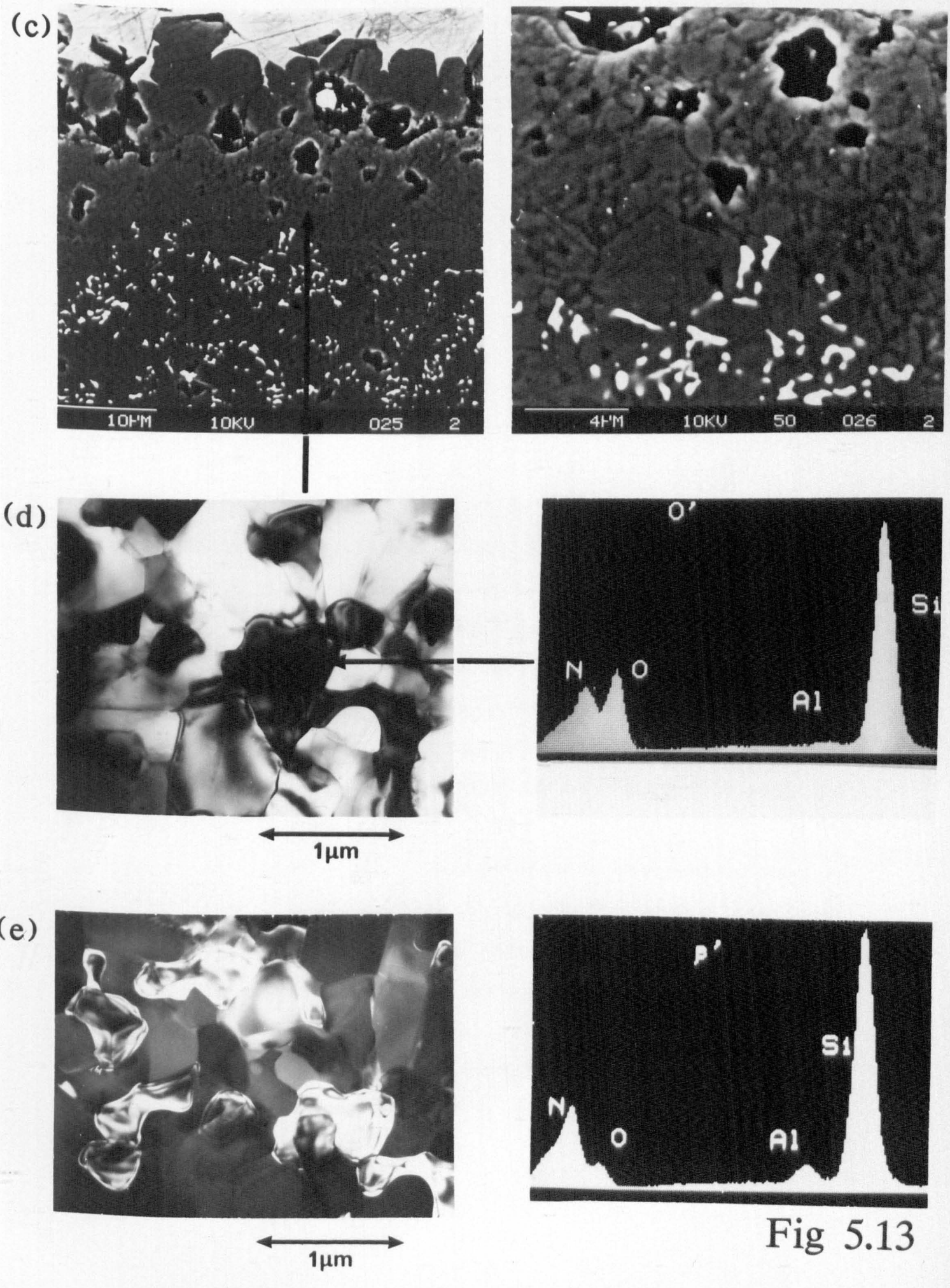

Fig 5.13

The aluminium substitution level Z as defined by the equation;

$$Si_{2-Z}\ Al_Z\ N_{2-Z}\ O_Z \quad \text{where } Z \leq 0.4 \qquad (5.3)$$

was measured to be approximately 0.05. This is in general agreement with other observations of O' ceramics notably Lewis et al (74), and Jack (63). Unlike the case of β-Si_3N_4, aluminium substitution in silicon oxynitride is very low.

O' growth occurs from the liquid phase by direct reaction between the β' and oxygen enriched, cation (Y,Al) depleted, reverted intergranular glass. However, insufficient oxygen is present to form α-cristobalite as observed at the surface, so O' is formed by the simplified reaction;

$$Si_3N_4 + SiO_2 \rightarrow 2Si_2N_2O \qquad (5.4)$$

After complete removal of the liquid phase by growth of O', further growth may only occur by solid state reaction with β'. This is slow, and only constitutes a minor part in the overall reaction.

Even after several thousand hours' exposure at 1300°C it was observed that the β'/O' layer did not exceed 10-15μm in thickness. This is in sharp contrast to a previous report (172) where β'/O' layers of up to 40μm were observed in similar materials under comparable conditions. Several compositional and morphological differences were identified between the material in this study and that of the previous study;

(a) the volume of grain boundary phase is significantly lower in the LCS 201 material compared with the earlier development material ceramic. This results in there being greater proportions of two β'/β' grain junctions, which restricts the O' growth from the surface.

(b) The intergranular phase in LCS 201 has been shown to be fully crystalline YAG. The rate of reversion will be a factor

dictating the growth of O'. Little reverted YAG was found below the β'/O' layer. This has been shown to be connected with the reaction with the oxide layer. The formation of the β'/O' surface layer effectively causes this reaction to cease. Subsequently, the YAG reversion zone does not increase significantly with time thereafter.

(c) Continued growth of O' from the surface therefore is limited to the extent of the reversion layer in the sub-surface. In addition, the growth of O' will reject species such as yttrium, aluminium and some nitrogen at the growth front. This will cause the glass to move away from the oxygen/silicon rich composition seen within the zone during oxidation, to one nearer the original eutectic composition.

5.3.4 Environmental stability of β'/O' layers

Oxidation kinetics for nominally β'/O' layers were measured at 1350°C and 1400°C for up to 100 hours duration. As with the case in section 5.2.2, oxidation kinetics were determined by measurement of the oxide layer thickness as a function of time. Specimens with suitable β'/O' layers were fabricated by heat-treating β'/YAG containing LCS 201 for 600 hours at 1300°C, to form a 10-15μm β'/O' layer. The oxide layer was then removed by gentle grinding until the β'/O' layer was exposed. The surface was then given a final 6μm polish prior to being subject to heat-treatment. XRD was used to confirm that the surface was indeed β'/O'.

Oxide layer thickness as a function of time is shown in figure 5.14. The oxidation kinetics for the β'/YAG surface at 1350°C is shown in figure 5.16 for comparison. Oxidation of the β'/O' surface shows a considerable improvement over the β'/YAG surface. The

Figure 5.14 Oxidation kinetics for LCS 201 with transformed β'/O' layer at 1350°C and 1400°C, determined by oxide layer thickness measurement.

Fig 5.14

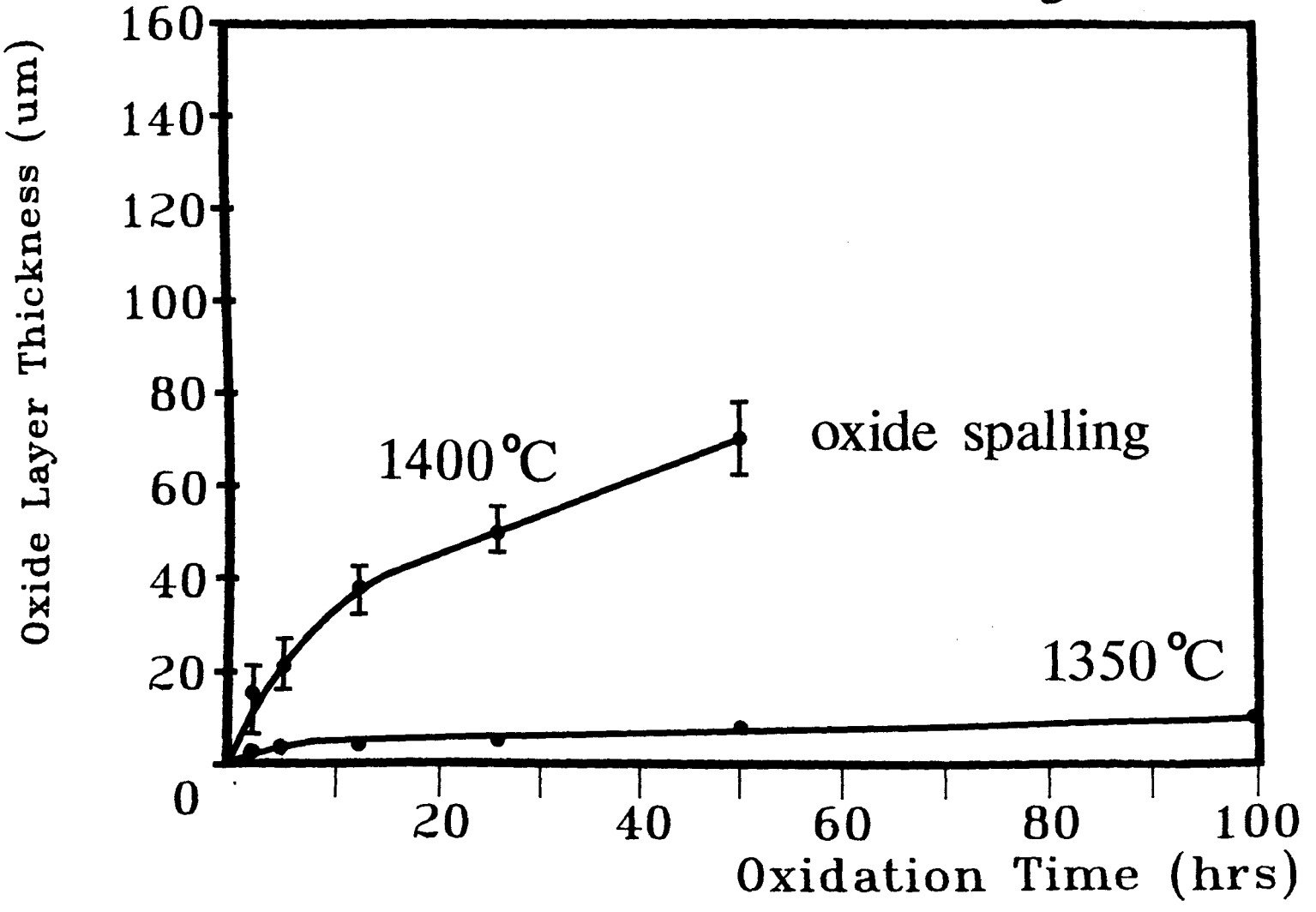
Oxide Layer Thickness (um)
160
140
120
100
80
60
40
20
0
1400°C
oxide spalling
1350°C
20
40
60
80
100
Oxidation Time (hrs)

kinetics were found to be so low that there was difficulty in determining whether behaviour was parabolic or linear, although by its nature parabolic kinetics are assumed.

At 1350°C and 1400°C, the oxide layer is mainly glassy with some crystallisation of $Y_2Si_2O_7$ and SiO_2 (figure 5.15). Little cation diffusion into the oxide layer was observed, the β'/O' layer being an effective barrier to the diffusion couple set up between the YAG and oxide layer. Hence oxidation only proceeds by reaction with the β' and O' at a very reduced rate. Oxidation only takes place by reaction of the extreme surface, the rate being controlled by the rate of oxygen transport through the viscous silicate oxide layer to the surface. Without the liquid phase to enhance transport, cation outdiffusion rates are very low, being controlled by diffusion along β'-β' and β'-O' grain boundaries.

A comparison of oxidation rates for various Y-Si-Al-O-N matrices figure 5.16 demonstrates the wide range of oxidation kinetics which may be obtained by simply altering the matrix chemistry. Careful selection of this enables oxidation resistant materials to be produced, and further improvements may be obtained by the ability to choose an optimum matrix for the best mechanical properties, and by further transformation produce the oxidation resistant layer. This will produce a "composite" material with optimal thermo-mechanical properties not attainable with a single matrix.

The matrix transformations discussed in this section result from extended periods of heat-treatment. The practical use of such mechanisms to enhance high temperature properties is dependent on the layer being formed easily and controllably. This will be discussed in the next section.

Figure 5.15 Oxide layer development with time for LCS 201 with transformed β'/α' layer at

a) 1350°C

b) 1400°C

Fig 5.15(a)

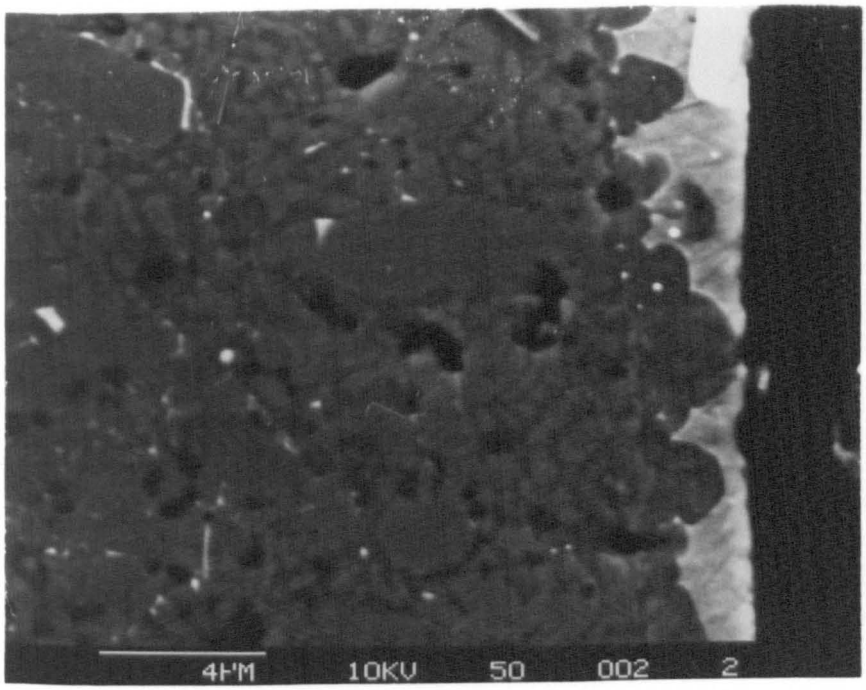

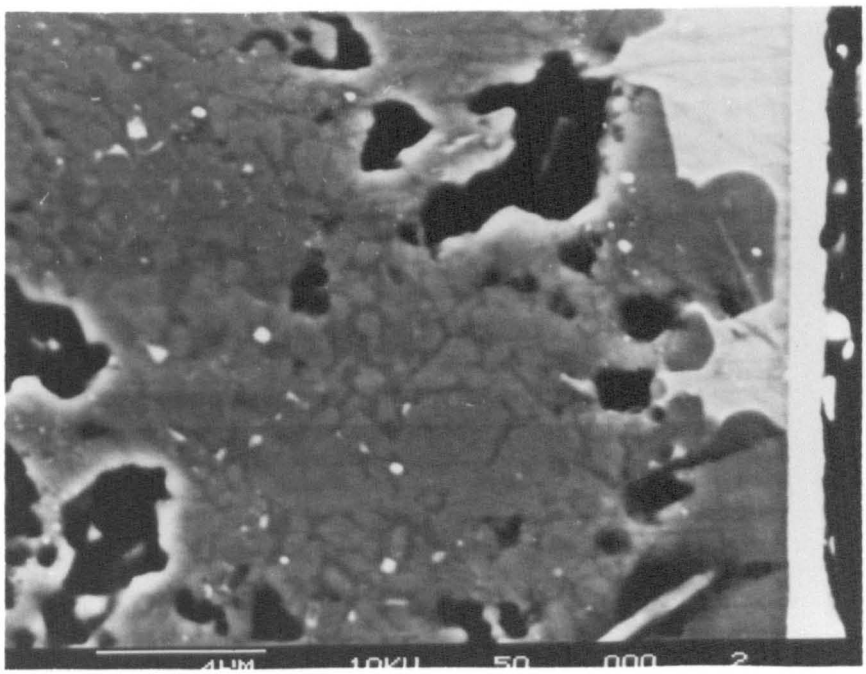

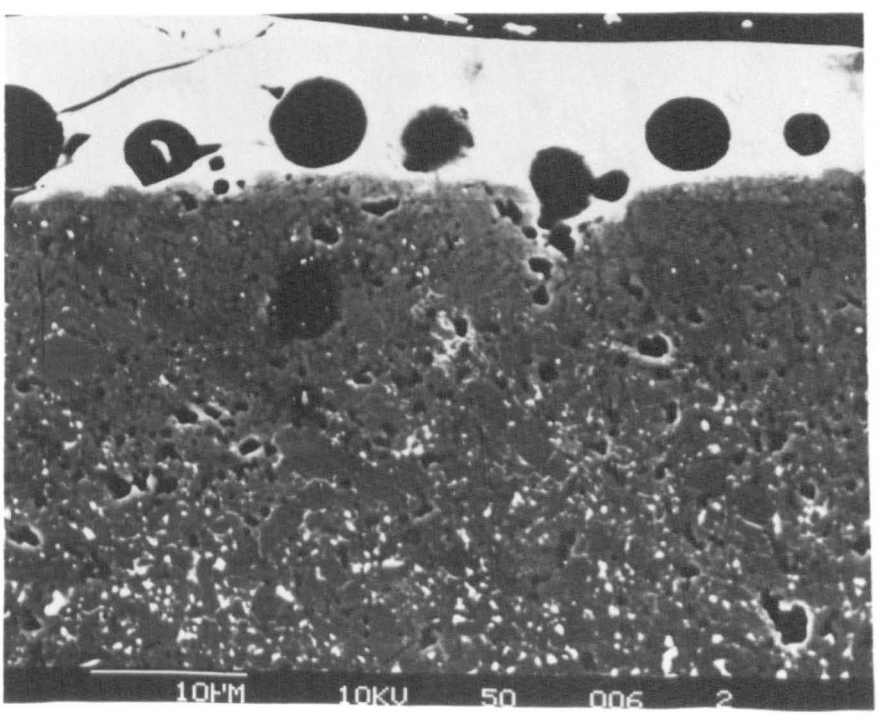

Fig 5.15(b)

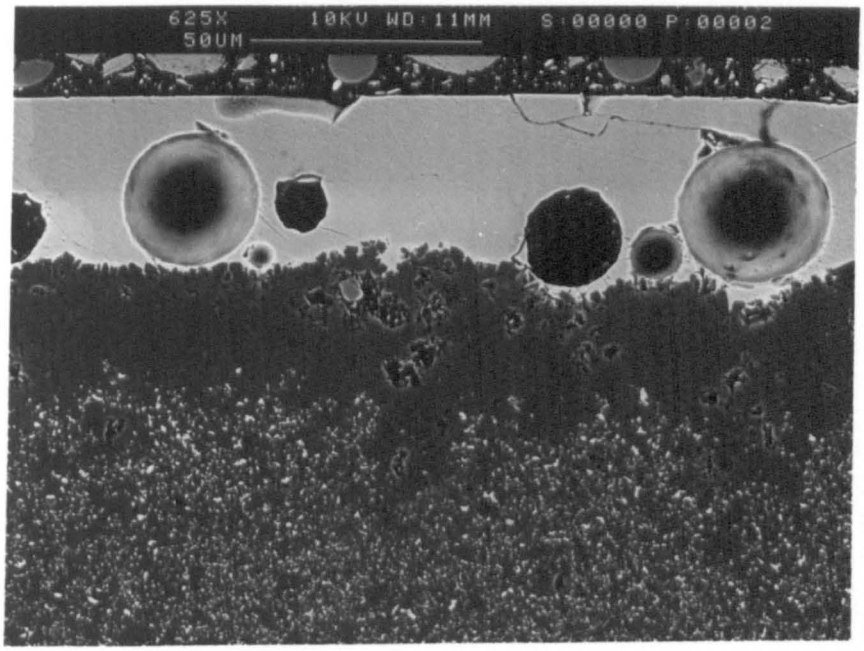
625X 10KV WD:11MM S:00000 P:00002
50UM

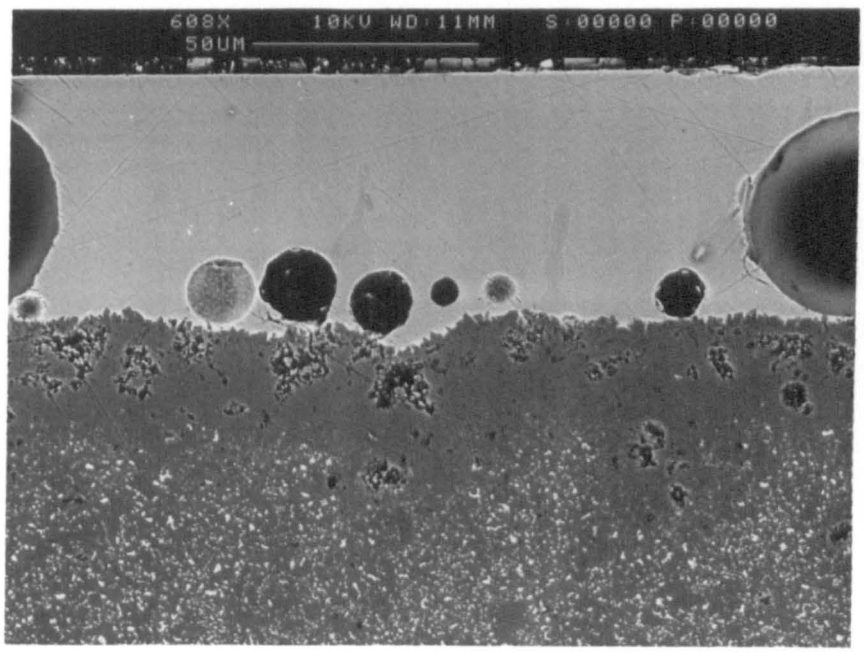
608X 10KV WD:11MM S:00000 P:00000
50UM

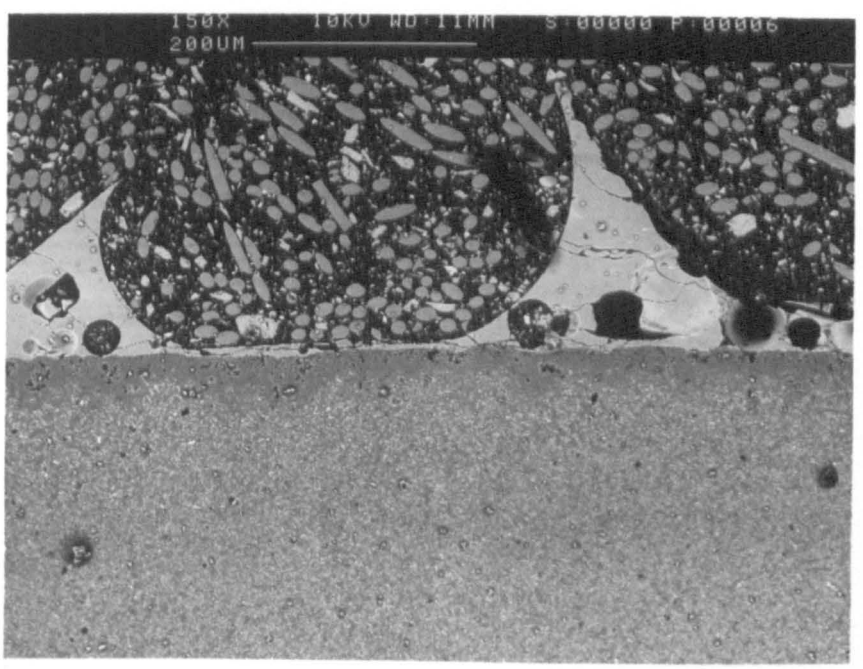
150X 10KV WD:11MM S:00000 P:00006
200UM

Figure 5.16 Comparison of oxidation kinetics for β'-sialon materials with different intergranular matrices.

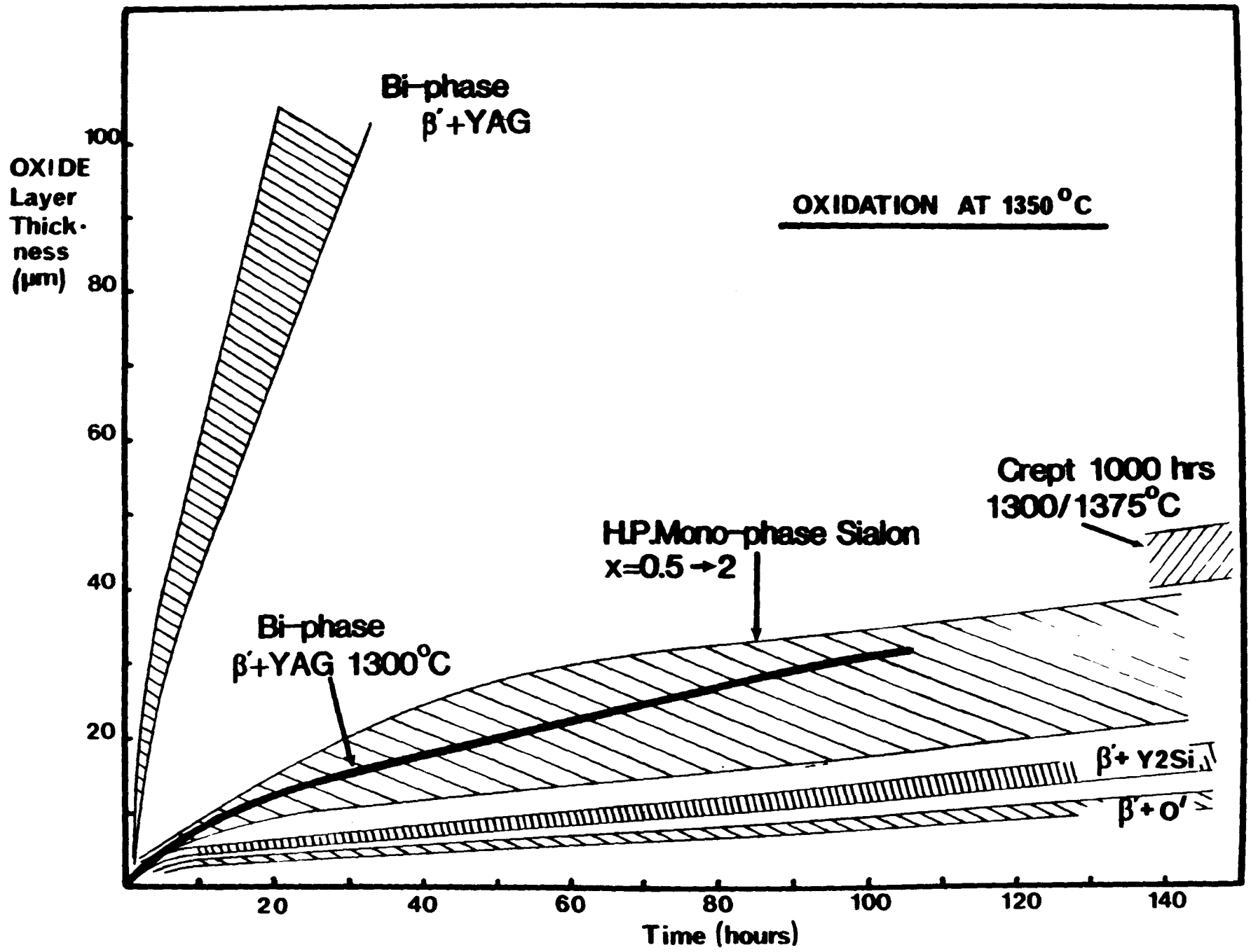
Bi-phase
β'+YAG
OXIDATION AT 1350°C
OXIDE
Layer
Thick-
ness
(μm)
100
80
60
40
20
Crept 1000 hrs
1300/1375°C
H.P.Mono-phase Sialon
x=0.5→2
Bi-phase
β'+YAG 1300°C
β'+ Y2Si2O7
β'+ O'
20
40
60
80
100
120
140
Time (hours)

5.3.5 Controlled development of β'/O' layers

It has been seen in the previous section that β'/O' may to some degree be formed by extensive oxidation over long periods at 1300°C. This route has several drawbacks if it is to be used to the benefit of the material;

(i) the oxidation reaction causes both YAG reversion and some degradation of the surface. Surface degradation has been repeatedly shown to be a cause of strength loss at high temperature due to critical flaw generation (153).

(ii) The formation of the β'/O' layer by this method takes a very long time at high temperatures. This would be highly uneconomical if applied in a commercial situation. Therefore, a more convenient route for the production of the layer was sought.

Initially, variations of producing β'/O' by atmospheric oxidation were used. It has been established that the growth of O' at the surface is dependent on the YAG reversion zone at the surface, where significant outdiffusion of metallic cations was found to have occurred. Therefore, a process akin to a glass ceramic nucleation/growth crystallisation treatment was given. Careful consideration was first given to the temperatures at which this was to be attempted. Referring to the oxidation characteristics observed in section 5.2.2, treatments below 1300°C would be of little use as YAG reversion does not occur on a significant scale. At 1350°C and above it was seen that degradation the surface was severe, likely to be unacceptable in real applications. Therefore, the choice for heat-treatment temperatures was limited by these considerations. An initial treatment of 1300°C was therefore chosen to form a YAG reversion zone followed by a longer higher temperature treatment to form the O' layer. Measurement of the sub-surface layer thickness as

a function of time in previous sections indicated that little appreciable growth was observed after 25 hours. Therefore this was used for the 'nucleation' step of the process. Varying times and temperatures were then used to try to produce the O' layer, combinations of 1350°C, 1400°C and 1450°C for 75 hours, an example shown in figure 5.17. In this case the O' layer was found only to be approximately 10μm thick but with significant levels of porosity and surface degradation.

The fact that a coherent O' layer could only be formed by oxidation in air over very long periods prompted the investigation of the use of heat treatments in an inert atmosphere.

Heat-treatments were performed at 1500°C for 150 hours in a powder bed of SiO_2. Figure 5.18 shows the microstructure obtained. All specimens were found to have formed significant O' layers (~40μm) at the surface, although there was evidence of severe degradation. In addition, severe sub-surface modifications were observed, summarised in figure 5.18(a).

(i) 1st layer - β'/O', figure 5.18(a,b). The outer surface of this layer, in direct contact with the SiO_2 frit was completely converted to O' to a depth of 40μm. Large O' crystals were found to have grown in from the surface enveloping existing β' crystals, producing a two phase β'/O' layer. Once enveloped, further reaction could only occur via a solid state process, resulting in irregular β' morphology.

It must be noted that a uniform β'/O' layer was not formed, generally being highly irregular and in some instances non-existent.

(ii) 2nd layer - β'/glass, figure 5.18(c). Directly below the β'/O' layer a zone of YAG → glass reversion was observed, 800-850μm in thickness. This layer is as a result of reaction between the YAG and the SiO_2 frit in a similar way to that observed during oxidation.

Figure 5.17 Backscattered electron micrograph of β'/O' layer growth obtained from two stage 'nucleation - growth' type treatment at 1300°C/25 hours and 1400°C/75 hours. Although O' growth was obtained, significant porosity and surface disruption is evident.

Fig 5.17

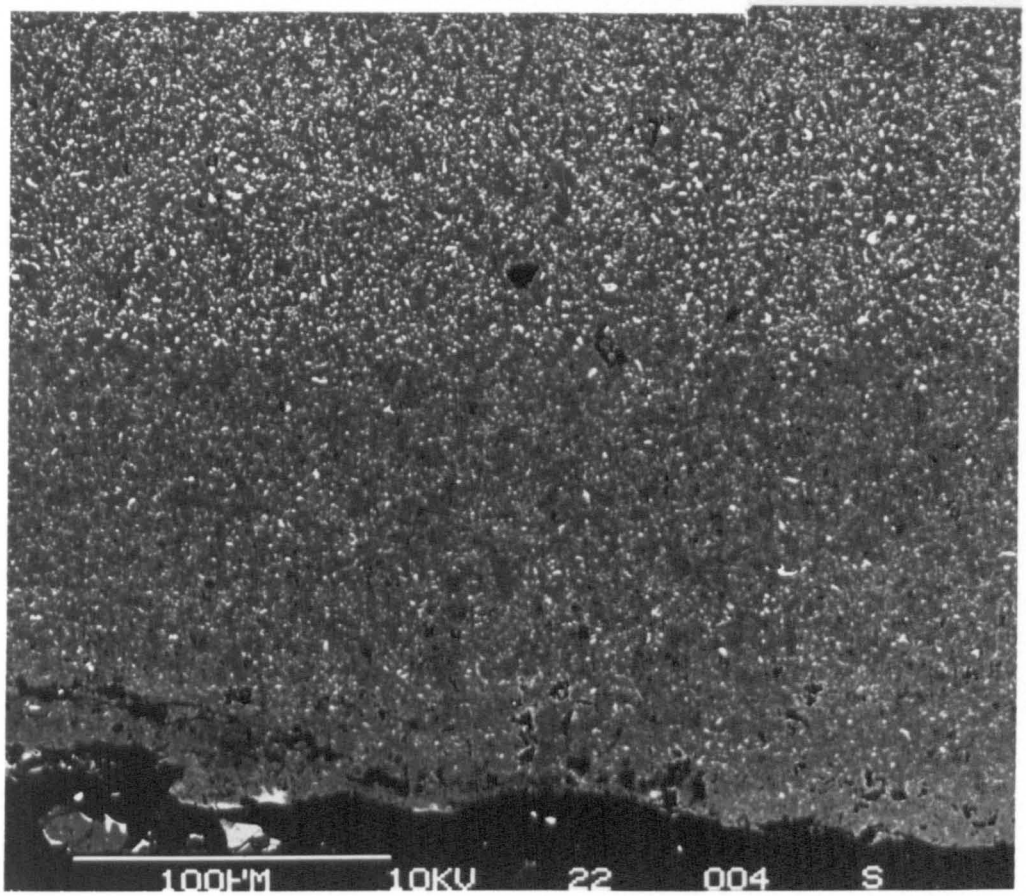

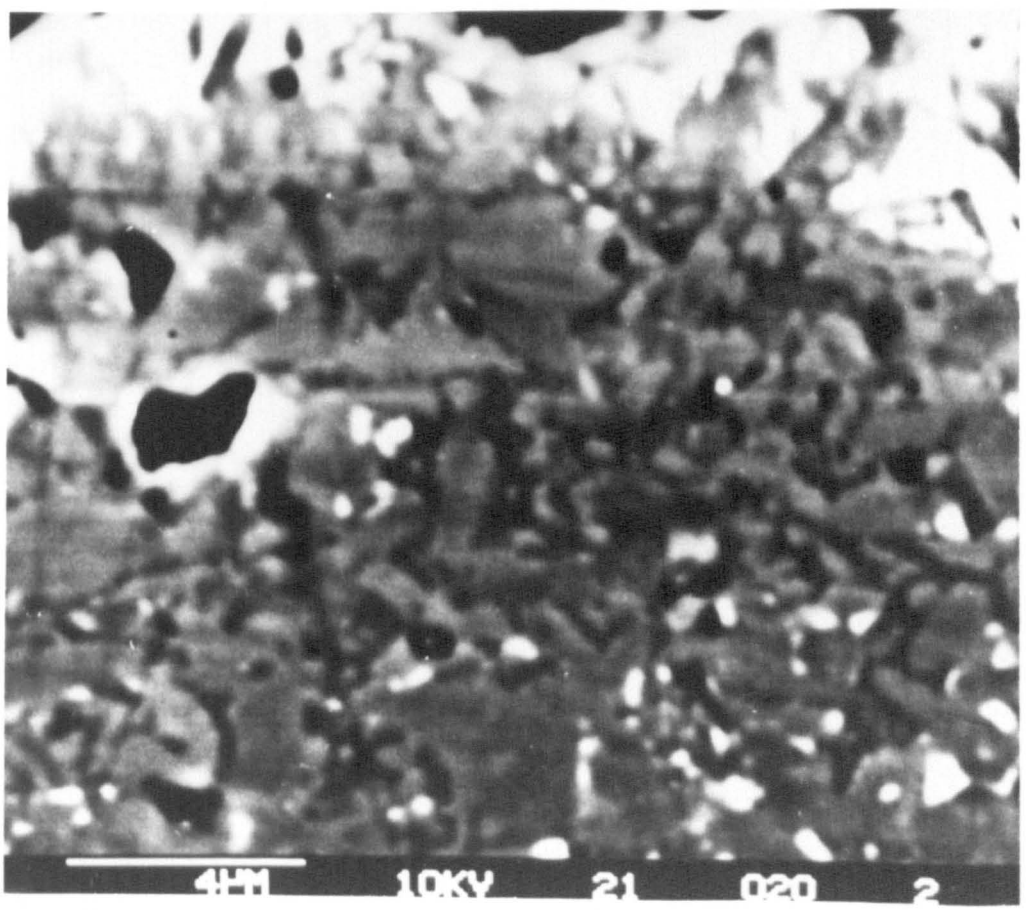

Figure 5.18 Backscattered electron micrographs of β'/O' layer growth and sub-surface microstructure from LCS 201 heat-treated at 1500°C.

a) Surface - residual SiO_2 and transformed β'/O' zone.

b) β'/O' zone extending 40 m into the bulk, with typical EDX analyses of β' and O' (top). Microstructure directly below β'/O' layer (bottom).

c) β'/glass layer directly below β'/O' layer with typical EDX analysis of β' and intergranular phase.

	Matrix (at %)	Eutectic (at %)
Si	49.4 ± 5.4	52.1
Al	24.1 ± 2.6	27.6
Y	26.2 ± 3.1	20.3
Fe	0.3 ± 0.3	-

d) YAG to glass reversion front.

e) β'/YAG layer in which all α' has been transformed to β'. This layer effectively defines the extent of the reaction.

(a)

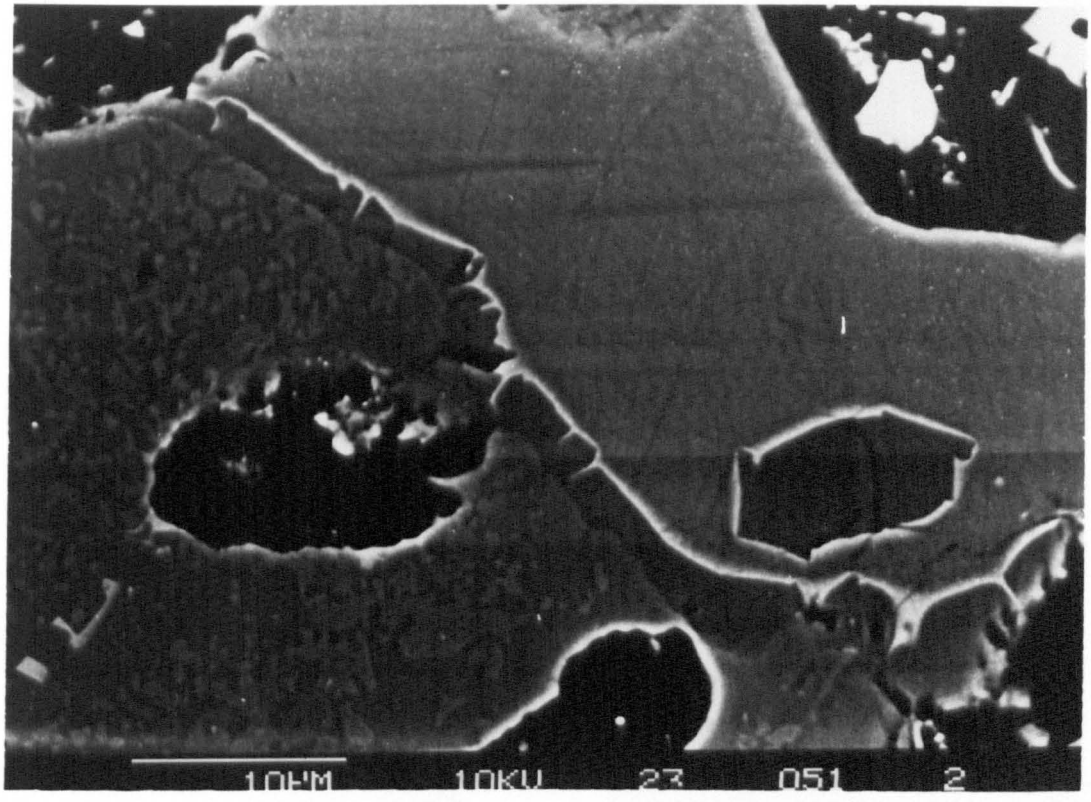

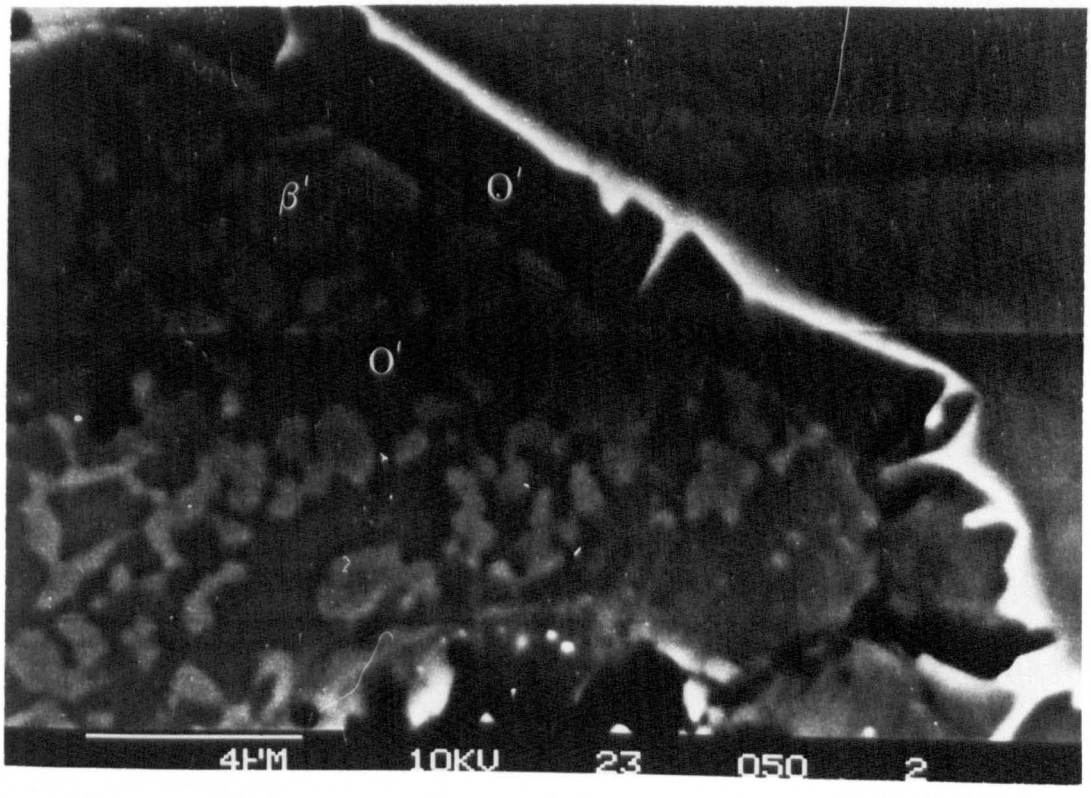

Fig 5.18

(b)

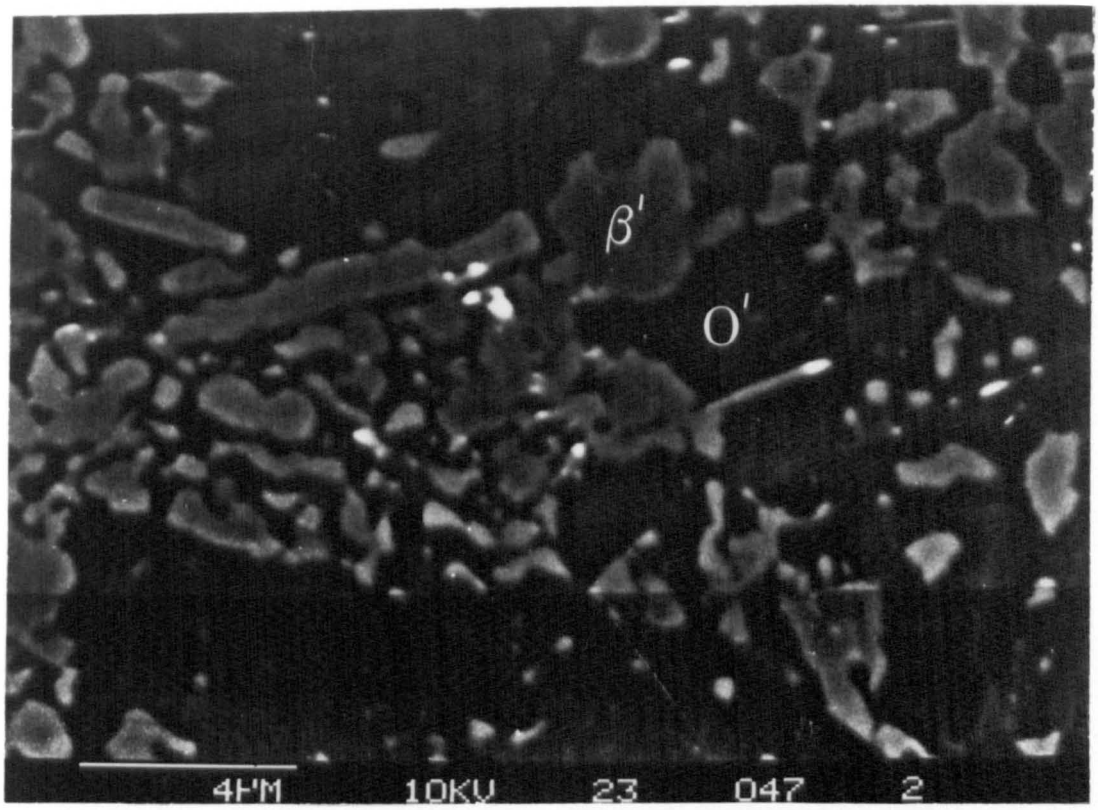
β′
O′
4μM 10KV 23 047 2

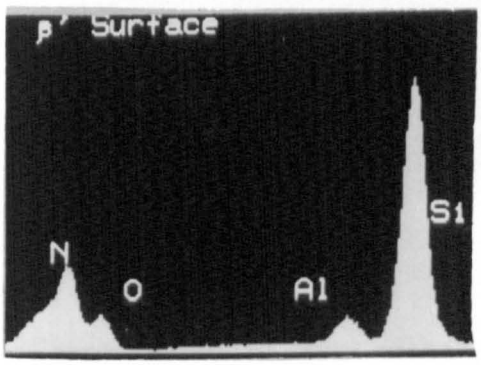
β′ Surface
N
O
Al
Si

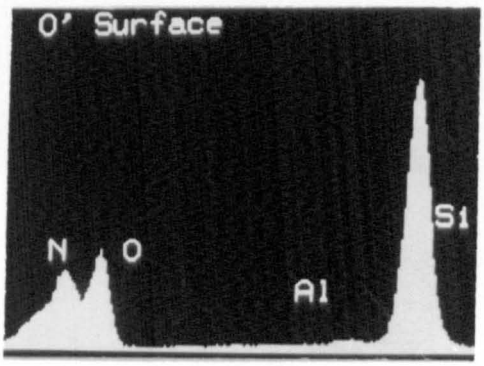
O′ Surface
N
O
Al
Si

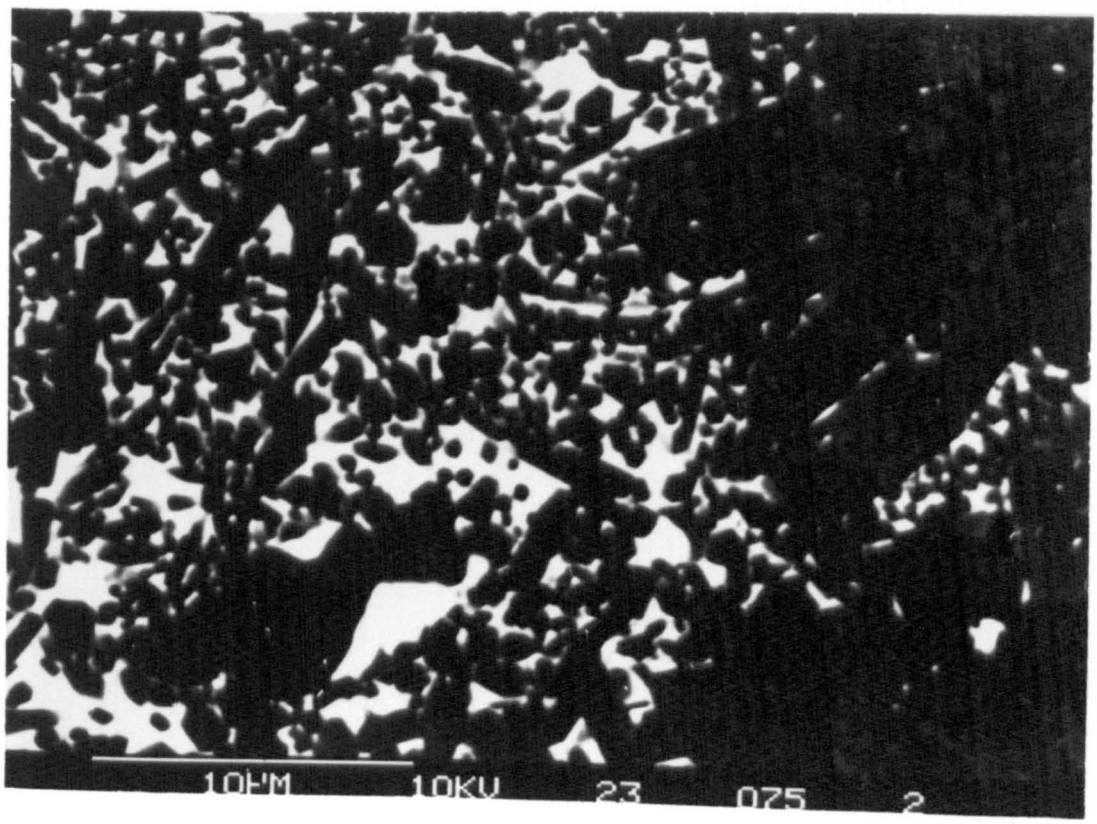
10μM 10KV 23 075 2

Fig 5.18

Fig 5.18

(c)

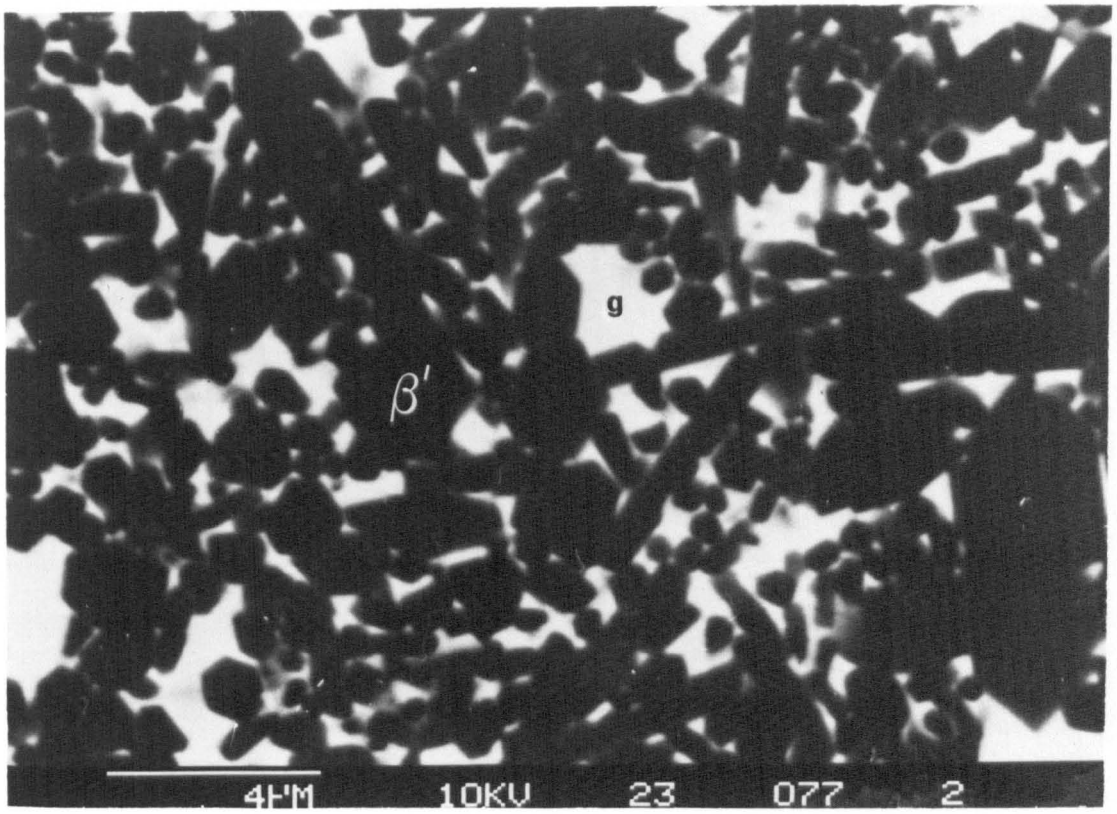
g
β′
4μM
10KV
23
077
2

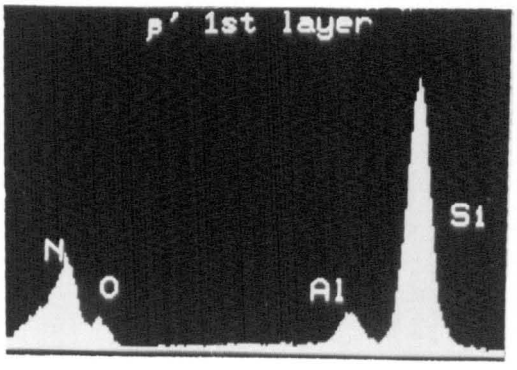
β′ 1st layer
N
O
Al
Si

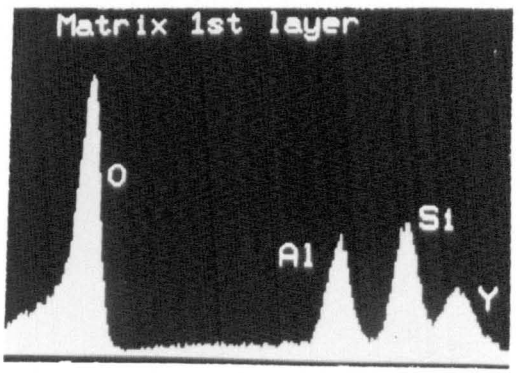
Matrix 1st layer
O
Al
Si
Y

(d)

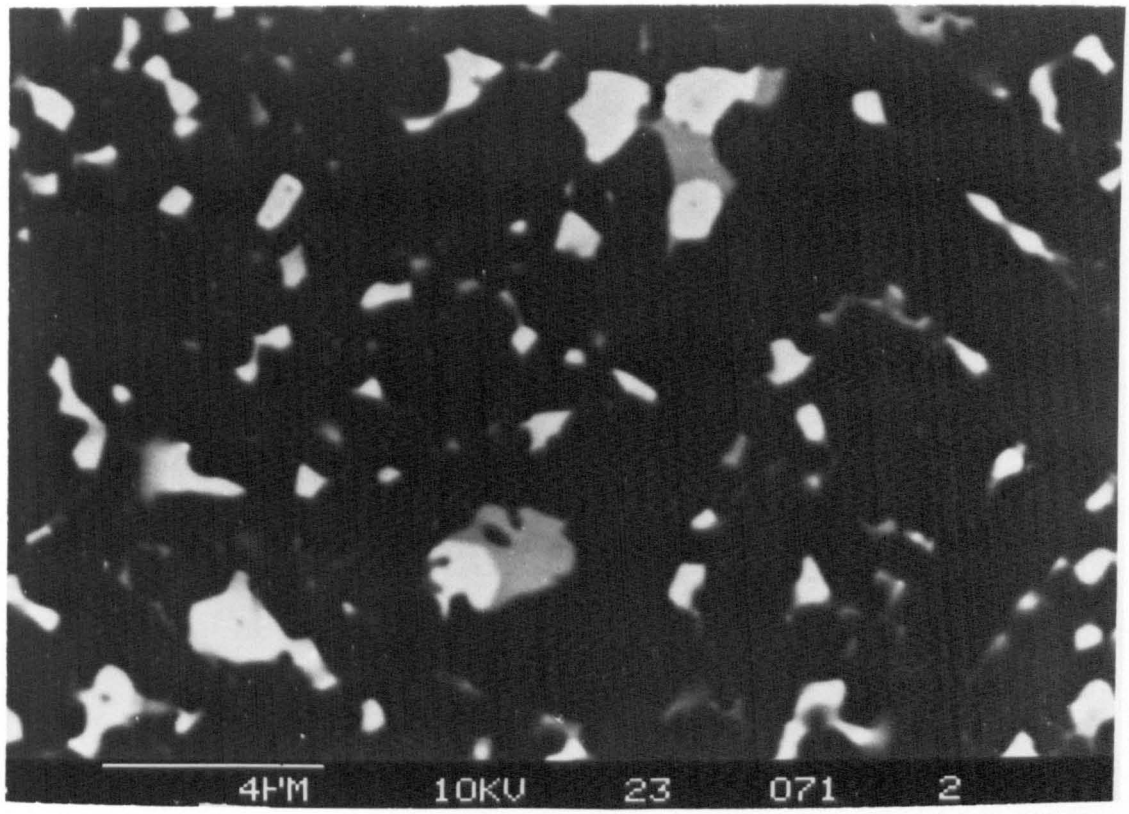

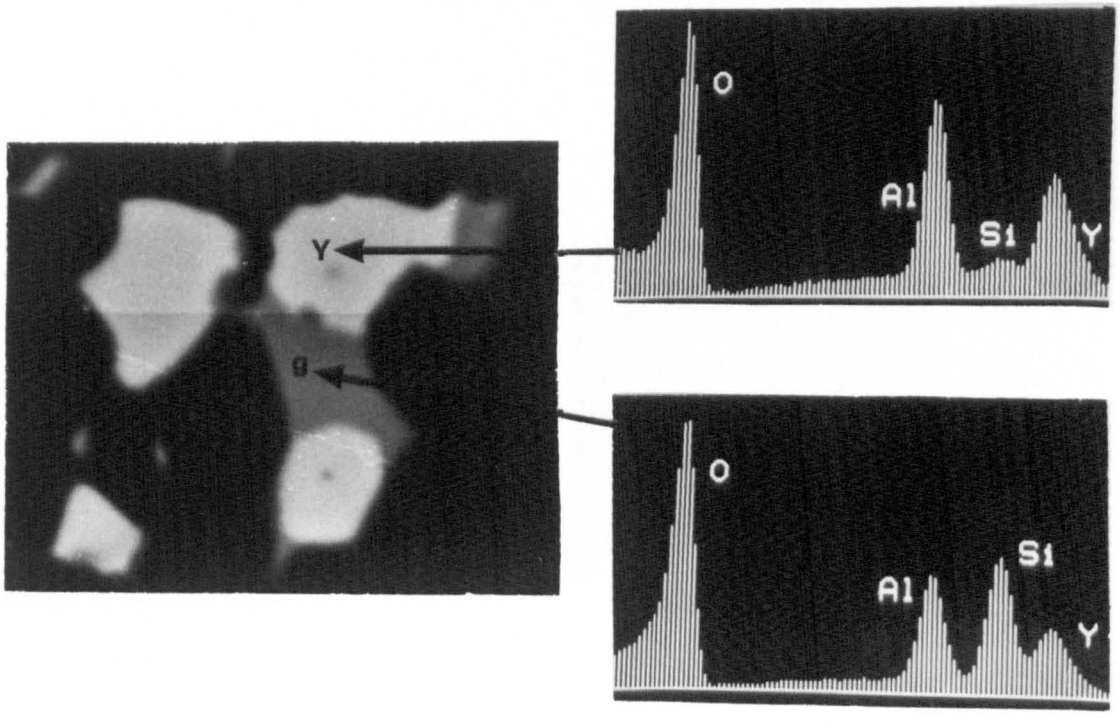

Fig 5.18

(e)

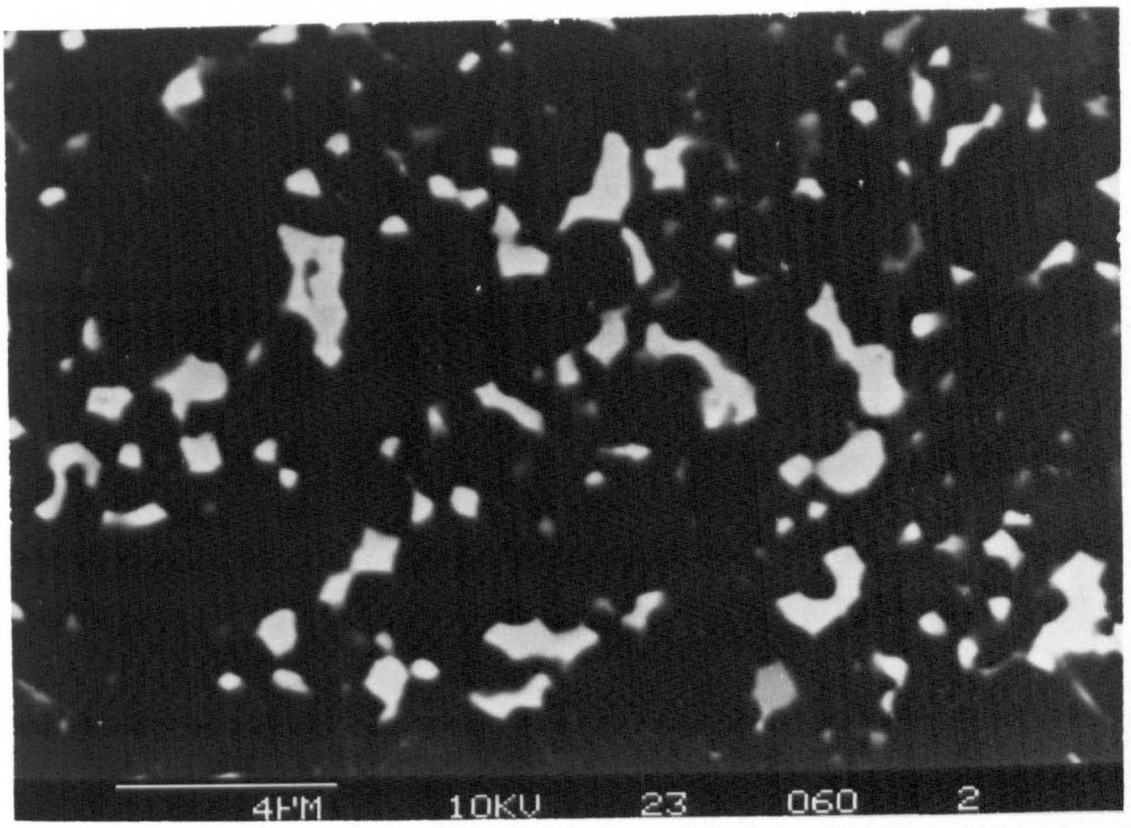

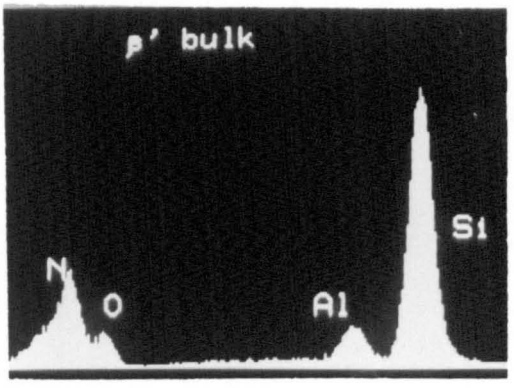

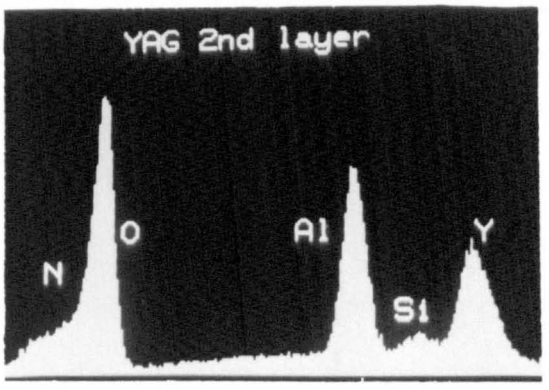

Fig 5.18

(iii) 3rd layer - β'/YAG/glass, figure 5.18(d). This zone was thin, ~20μm, and constituted the reaction front for YAG reversion. Clear areas of partial YAG dissolution was observed.

(iv) 4th layer - β'/YAG, figure 5.18(e). This zone extended some 450μm from the YAG reversion front, and exhibited a typical LCS 201 type morphology devoid of all α'. This is similar to those observed during atmospheric oxidation, the α' having transformed to β'. This has been discussed in section 5.2.2.

(v) 5th layer - β'/YAG+α'. This effectively defines the limit of reaction, being some 1.3 mm from the surface.

5.3.6 Discussion

The philosophy of using the inherent chemistry of the material, has on the face of it, several advantages over other possible methods (eg coatings). Primarily, these layers form as an integral part of the structure such that cohesion between the layers is not a problem. Also in the case of β'/O' layers, the layer is produced naturally as a result of oxidation, within the regime of intended use of this type of material.

However, as has been shown, the production of these layers generally causes severe degradation of the surface in an uncontrolled manner. In addition the formed layer is not thick enough to allow subsequent machining to remove the generated flaws. Probably of greater significance is that severe sub-surface reaction results, both the generation of porosity and of YAG reversion. Attempts to increase β'/O' and α' growth both resulted in the increase in the subsurface reactions.

The LCS 201 materials greatest attribute is the fully crystalline grain boundary phase, which results in the good thermo-mechanical properties. However, the scale of reversion seen would be expected to seriously affect these. Therefore it is concluded that the use of "in-situ" chemically derived protective coatings is of limited use, and that further developments of methods of formation of them would also be limited.

5.4 Conclusions

The conclusions regarding the environmental stability and transformation properties of LCS 201 based materials are summarised as follows:-

(i) The stability of the YAG matrix is good up to 1300°C. Little reaction occurs at or below the surface. The presence of small amounts of yttrium α-wollastonite ($Y_2Si_2O_4N_2$) did not cause any degradation of properties, both thermal and mechanical, at temperatures around 1000°C. This was also valid for materials based upon the LCS 201 but with significantly higher $Y_2Si_2O_4N_2$ levels.

(ii) The mechanism for oxidation in the LCS 201 type materials at temperatures above 1300°C is a YAG-SiO_2 reaction which produces a ternary eutectic liquid. This reaction allows rapid atom transport, and hence the catastrophic oxidation kinetics above 1300°C.

(iii) The α' billet surface layer was found not to significantly improve the oxidation resistance even though it was found to be nearly single phase.

(iv) Surface transformations were used in an attempt to improve the oxidation resistance. The use of β'/O' layers in particular were found to significantly improve the oxidation resistance, exhibiting minimal oxidation up to 1400°C. However, the growth of such layers was extremely problematic.

(v) The controlled growth of both α' and O' layers met with significant difficulties. Both uniformity of layer and control of the sub-surface structure were difficult to control. The practical use of protective layers appears to be confined to those which develop in-situ during use. The forced growth of these layers is generally unreliable and hence is not seen as a method of attaining surface protection.

Chapter 6 HIGH TEMPERATURE MECHANICAL PROPERTIES OF LCS 201 CERAMICS

This chapter details the high temperature mechanical properties of the LCS 201 type of material, specifically the β'/YAG material. Short term fracture properties were observed in both the sintered, β'/glass, materials and the crystallised, β'/YAG, materials up to 1500°C in vacuum. The long term high temperature creep and creep rupture properties are studied with particular emphasis being placed upon the role that the fully crystallised YAG matrix has on the creep resistance, and the long term environmental protection afforded by the formation of a β'/O' surface layer.

6.1 High temperature fracture - K_{IC}-T results

This section will detail the effect of the microstructure on the fracture mechanism. The effects that oxidation up to 1000°C on room temperature MOR has been investigated in Chapter 5 and will not be reiterated.

6.1.1. Determination of K_{IC}-T relation for LCS 201 ceramics

The K_{IC}-T relationship for the LCS 201 ceramic in both sintered (β'+glass matrix) and crystallised (β'+YAG matrix) forms are shown in figure 6.1(a and b). K_{IC} levels were determined in both vacuum and in air over a range of temperatures from room temperature to 1500°C, although vacuum testing was not performed on specimens at temperatures below 800°C.

The variation of K_{IC} with temperature, is similar for both the glass containing and YAG containing materials up to 1000°C. Little variation between the tests in air and vacuum was observed although the average value for the YAG containing material was slightly lower

Figure 6.1 K_{Ic}-T relationships determined for

a) sintered LCS 201 - β'/glass material

b) crystallised LCS 201 - β'/YAG material

Fig 6.1 (a)

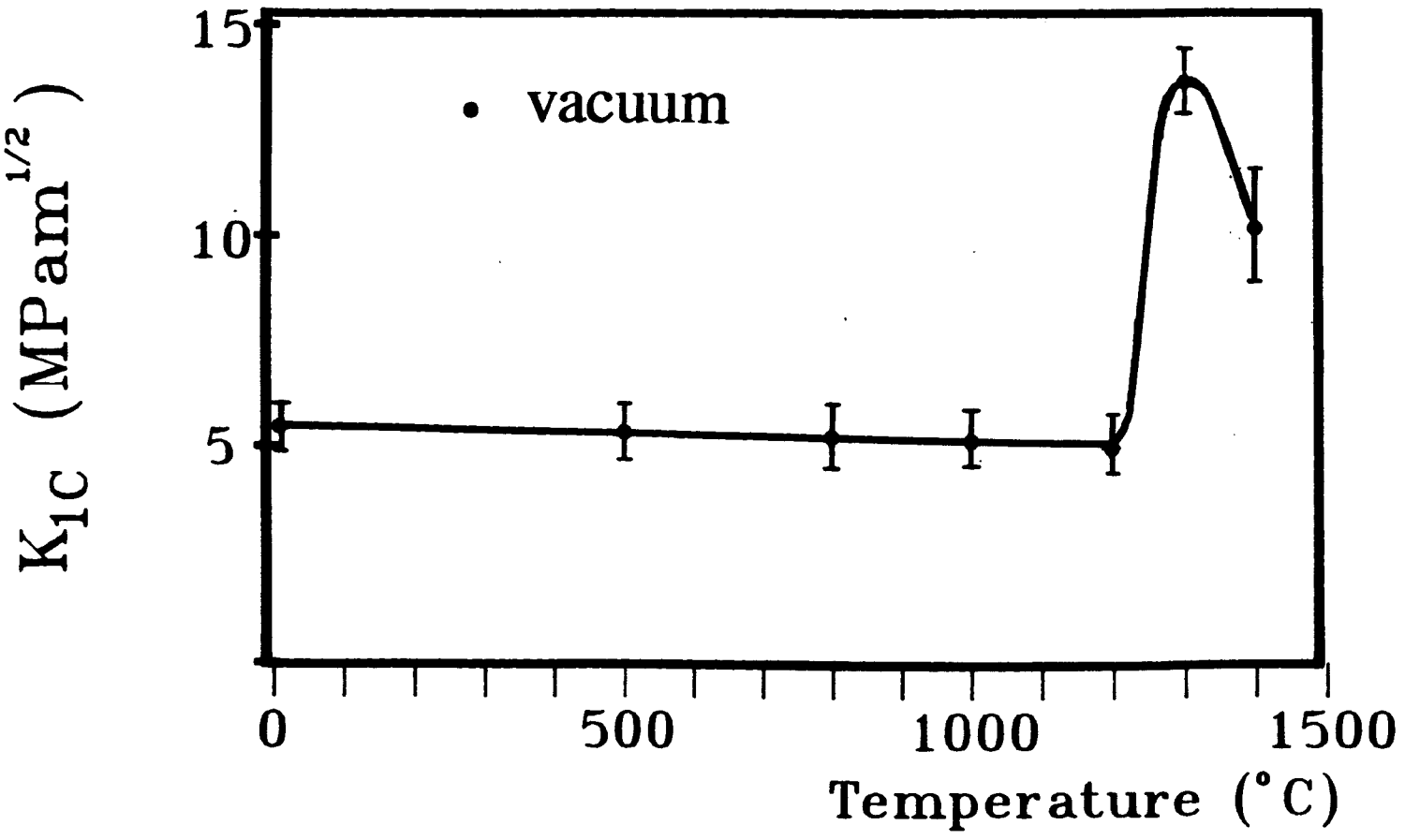

Fig 6.1(b)

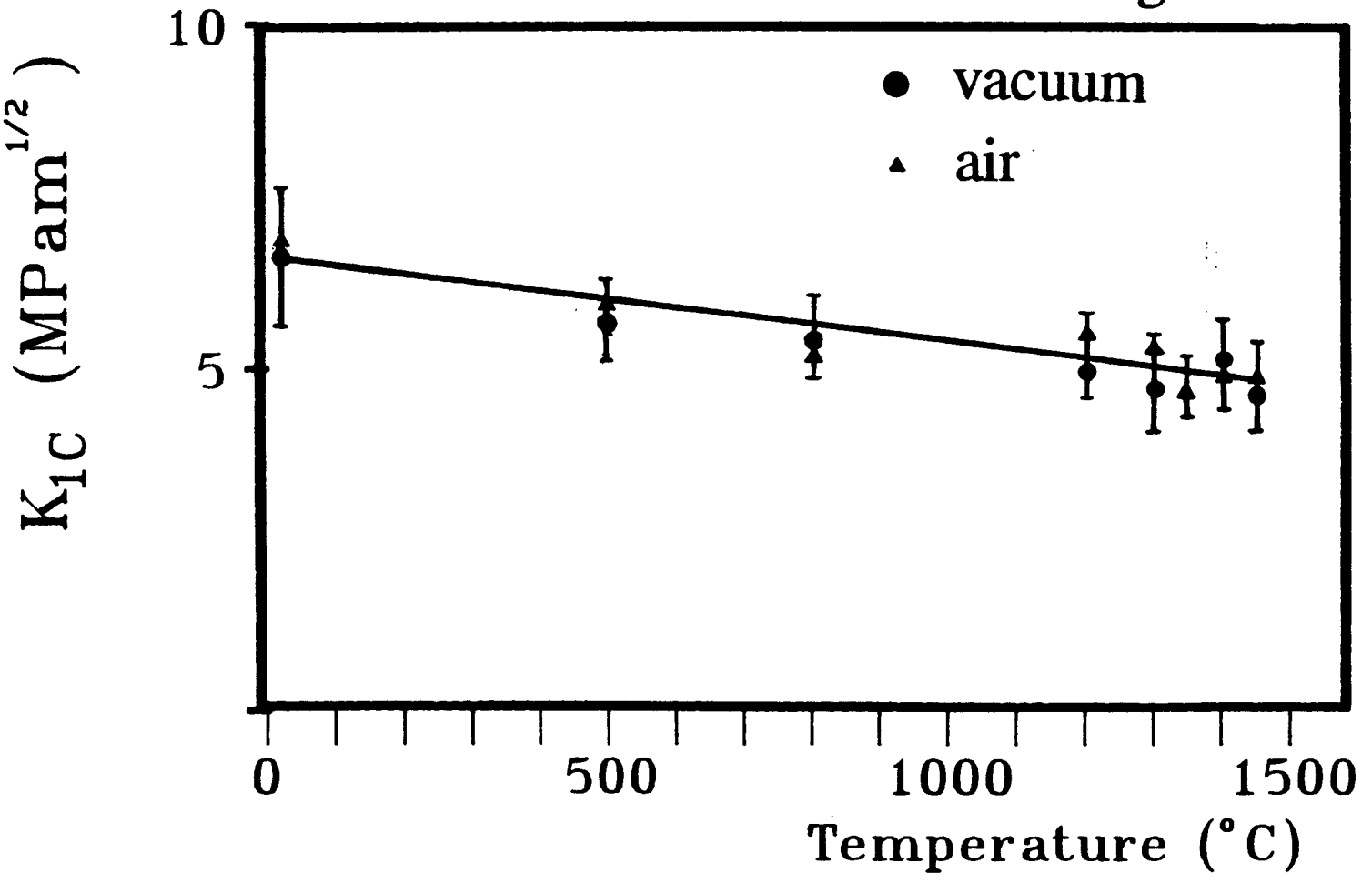

than in the glass material. This is expected as at these temperatures, environmental effects are negligible.

Analysis of the fracture surfaces in the SEM showed that at very low temperatures fracture is almost exclusively transgranular in nature, with no evidence of any sub-critical crack growth. Increasing the temperature caused no change in the fracture mode, failure being still catastrophic ie. load-displacement curve remaining linear. However, analysis of the fracture surface reveals that crack propagation was a mixture of transgranular and intergranular. This may be due to decohesion at the grain boundary very near to the crack tip resulting in some grain pullout of smaller grains. Grain boundaries constitute the weak link in the structure, and may, under high stresses at or near the crack tip during failure, slight deviation via separation of the grain boundary rather than transgranular fracture.

The slight reduction in the average K_{IC} level in the β'/YAG materials is probably due to residual stresses in the material. The source of this is unclear, but may be due to factors such as volume change due to crystallistion or thermal expansion mismatch between β' and YAG. It has been reported that the type of matrix crystallisation affects the value of the fracture toughness. K_{IC} has been shown to increase upon crystallisation of the residual glass phase to yttrium disilicate ($Y_2Si_2O_7$), but decrease for crystallisation to YAG. This criteria follows for the K_{IC} values measured in these materials. The mechanism by which the reduction in K_{IC} level as a result of the matrix crystallisation is not very well understood. Heath (172) explained it by the loss of plasticity at or near to the crack tip due to the removal of the intergranular glass.

Increasing the temperature above 1000°C reveals a marked difference in the fracture behaviour between the sintered and

crystallised ceramics. The sintered β'+glass material exhibited essentially brittle fracture up to 1250°C. As at lower temperatures, fracture is a mixture of transgranular fracture and grain pullout. The amount of grain pullout would be expected to be greater as decohesion of grains is more likely as the temperature tends towards the glass softening point.

However, at 1300°C the fracture behaviour alters dramatically, departing from the linear stress-strain behaviour observed at lower temperatures. This is associated with the appearance of a zone of modified reflectivity (figure 6.3), corresponding to the onset of subcritical crack growth (S.C.G.) resulting in the apparent increase in the value of K_{IC}. This is an artificial phenomena, resulting not in a true increase in the fracture resistance but as a result of the method of calculation. K_{IC} levels were determined by taking the sum of crack length (a) as the sawn notch length and the length of subcritical zone. The zone of subcritical crack growth was found to increase with temperature and cross-head speed. Hence, a constant cross-head speed was used in all tests.

The fracture behaviour at high temperatures for the crystallised β'/YAG material is markedly different to that observed in the β'+glass case. Above 1000°C, the level of K_{IC} stayed relatively constant, decreasing only slightly over the temperature range. At 1300°C and above, the K_{IC} level continues to drop, with little evidence of subcritical crack growth as seen in the case of the β'+glass material. Analysis of the fracture surface revealed the fracture mode to be still predominantly transgranular, crack propagation remaining catastrophic (ie. linear stress-strain behaviour). A significant amount of grain pullout, similar to that observed at temperatures below 1000°C, was also observed. This again

Figure 6.3 Light micrograph of fracture surface of β'-glass material which has undergone sub-critical crack growth.

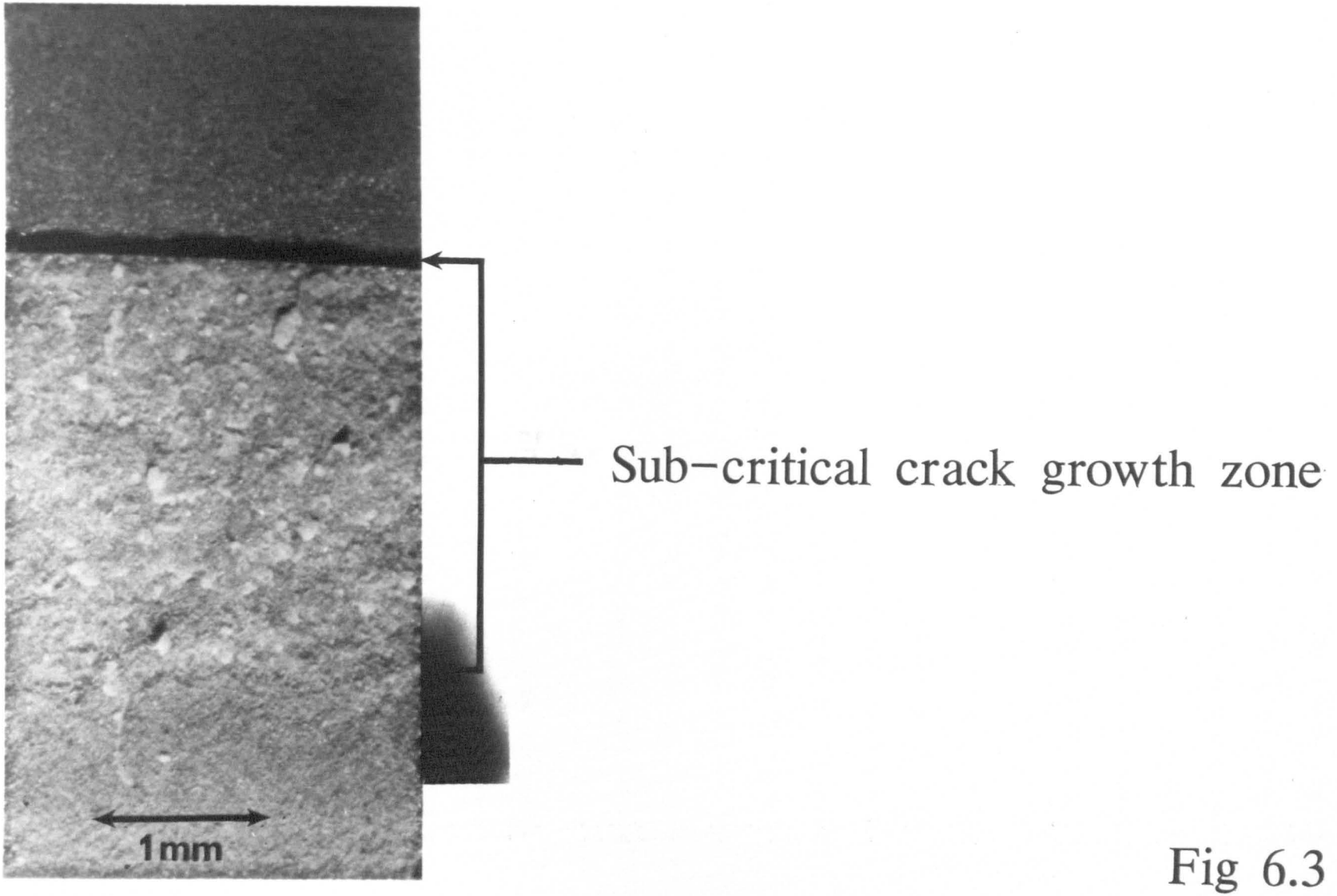

Fig 6.3

is caused by decohesion at the grain boundaries in some cases, though due to the higher temperatures, grain pullout is more frequent. An increase in the temperature from 1300°C to 1450°C results in a continued decrease in the level of K_{IC}. No evidence of subcritical crack growth was observed from the load-displacement curve, though analysis of the fracture surface does reveal significant amounts of grain pullout.

At 1500°C, no fracture was observed under normal strains. Instead, the specimen was found to deform significantly under load, creep mechanisms having become dominant at these high temperatures. High creep rates ($\sim 10^{-4}$ s^{-1} minimum) cause stress relief at the crack tip during loading, resulting in no crack extension. Due to the high creep rates, it is assumed that ultimate failure results from the formation and coalescence of cavities. The crack will slowly propagate by cavity linkage, an order of magnitude slower than a sub-critical crack.

Analysis of the fracture surface, figure 6.5, shows the crack to have propogated in an intergranular fashion accompanied by some β' decomposition. The fracture surface was found to be covered with fine yttrium containing glass filaments, which tend to follow the direction of crack propagation. These could be formed in several ways. Firstly, at 1500°C, YAG reversion to a liquid becomes possible. As the fracture surfaces are pulled apart at the crack tip, the small areas of liquid (reverted YAG) are pulled into filaments and deposited over the surface. An alternative explanation is that small amounts of oxygen present during testing caused some oxidation induced YAG reversion at or near to the crack tip. Both mechanisms are equally applicable, and are likely to be competing processes.

Figure 6.5 SEM micrographs of fracture surfaces

a) transgranular fracture

b) intergranular fracture

c) crack growth at 1500°C

Fig 6.5 (a)

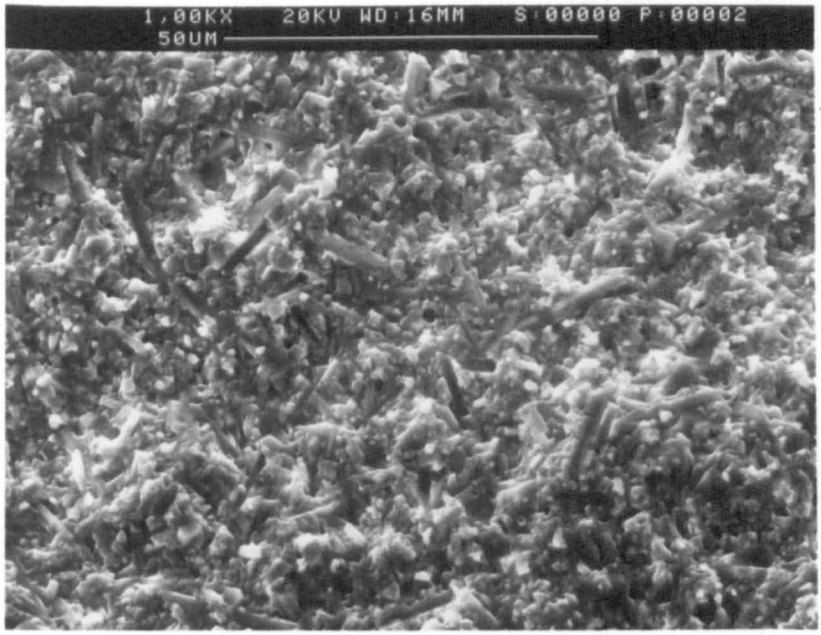
1,00KX 20KV WD:16MM S:00000 P:00002
50UM

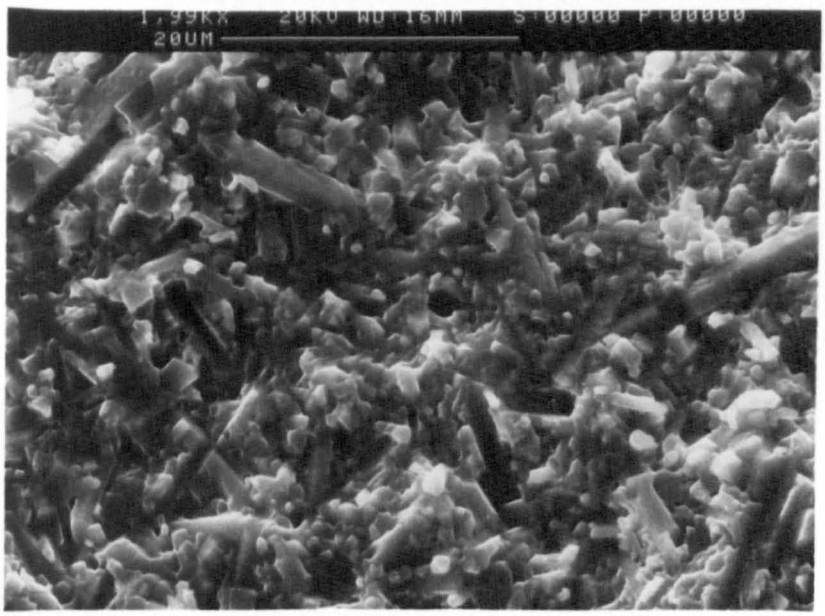
1,99KX 20KV WD:16MM S:00000 P:00000
20UM

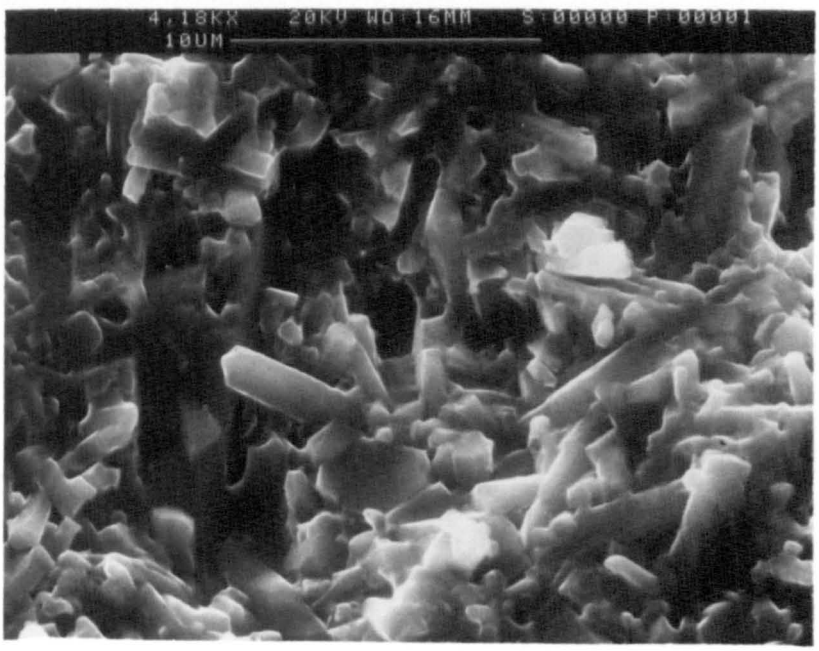
4,18KX 20KV WD:16MM S:00000 P:00001
10UM

Fig 6.5

(b)

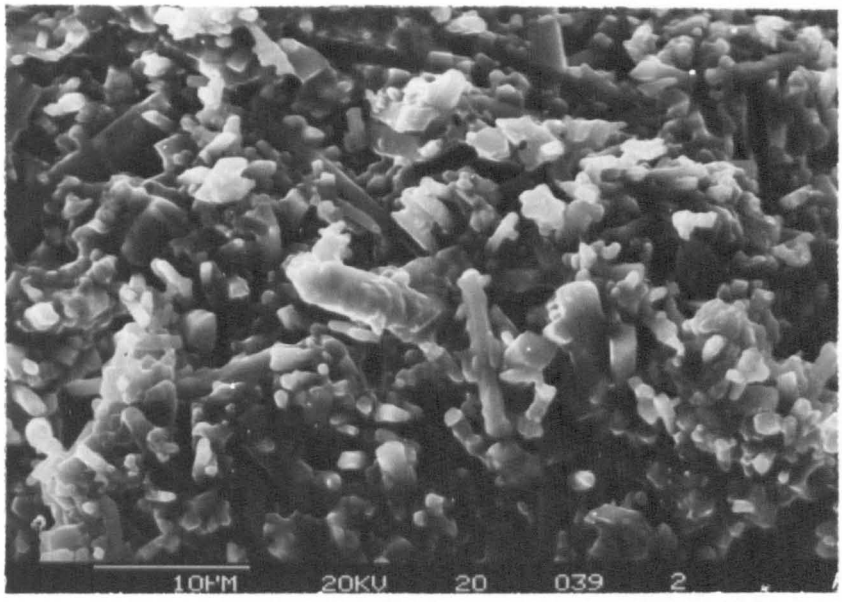

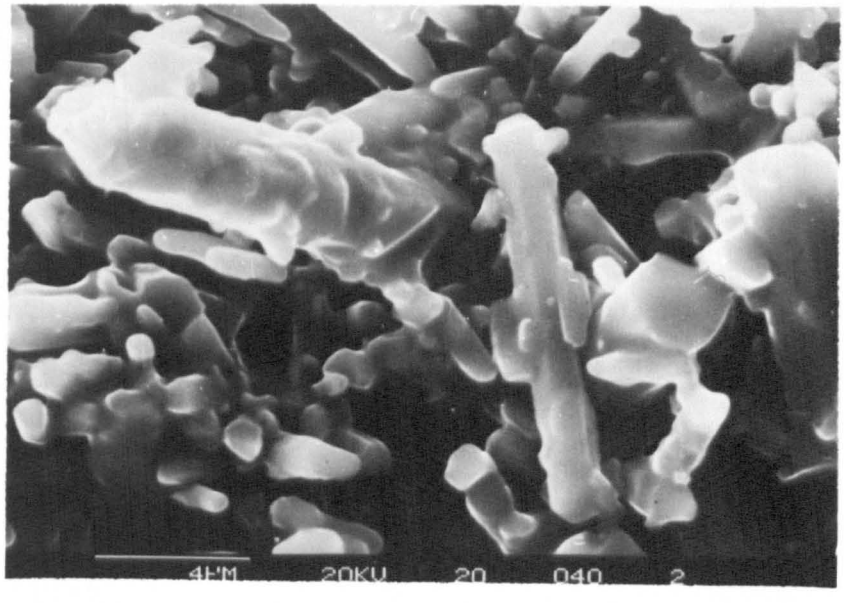

Fig 6.5(c)

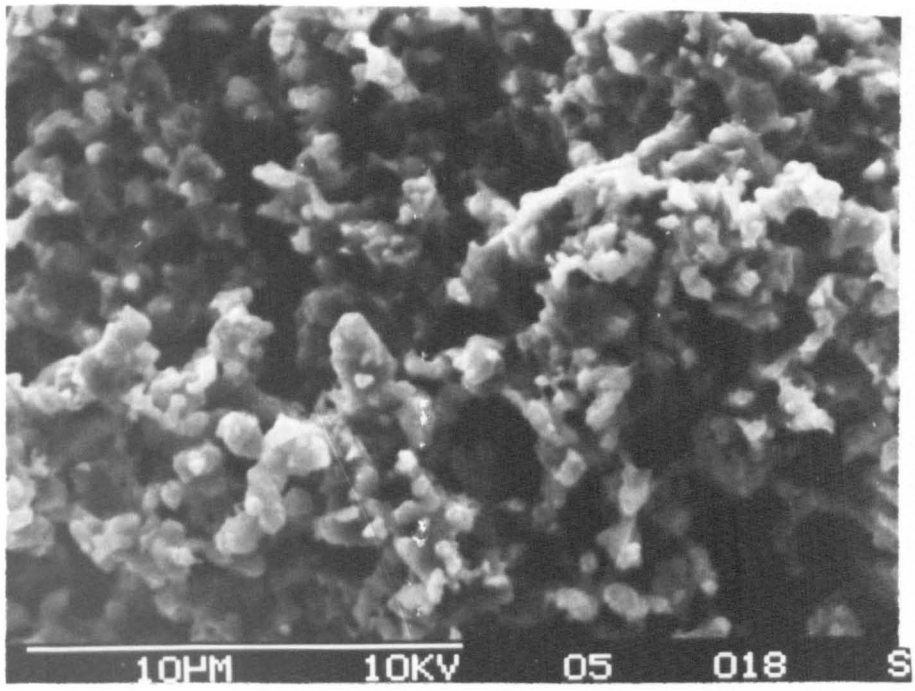

(1)

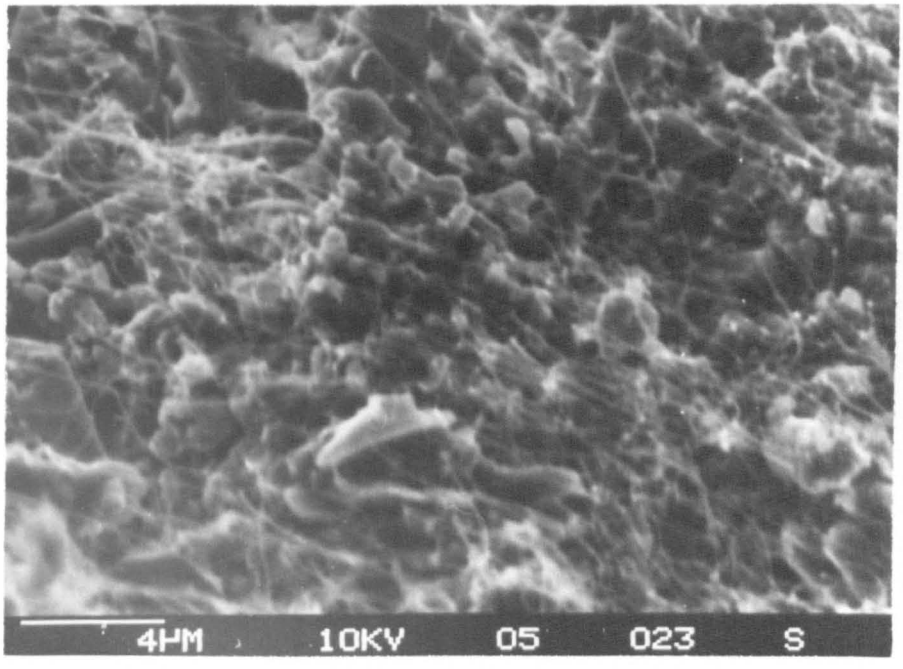

(2)

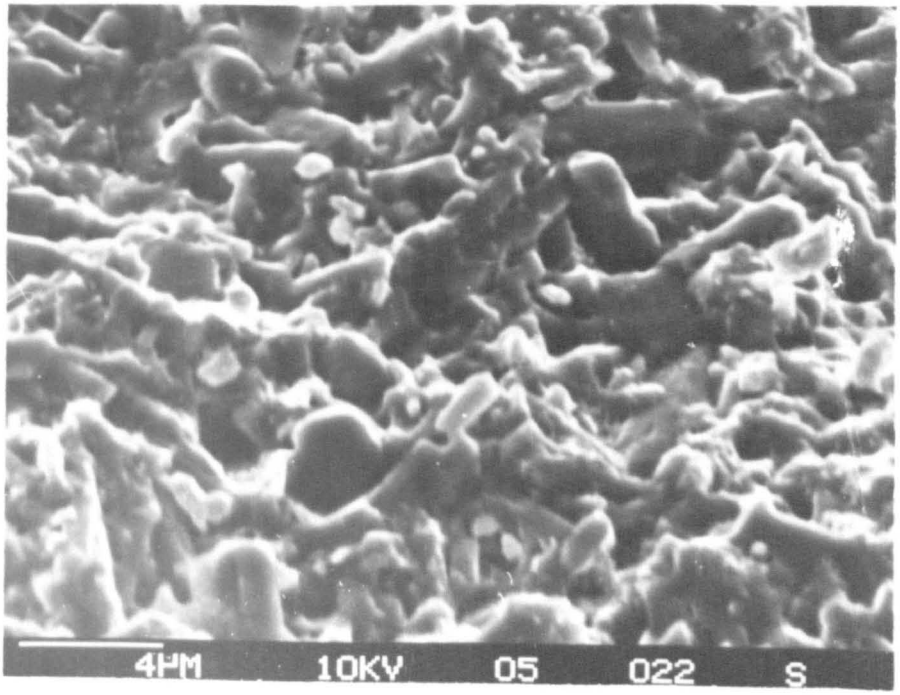

(3)

Subsequent tests using an atmosphere of high purity argon showed that the fracture reverted to that of one dominated by subcritical crack growth. The existence of subcritical crack growth at only extreme temperatures indicates that the primary cause is not the existence of a glass phase. If this was the case, the transition to subcritical crack growth from catastrophic failure would occur in a similar regime to that observed in the β'-glass containing ceramic ie around 1300°C. Rather at these temperatures the primary mechanism must be thermally activated decohesion of the grain boundaries. The cause of decohesion could be due to decomposition of the phases at the grain boundaries.

All microstructural analyses of fracture surfaces were performed using specimens broken under vacuum. Parallel experiments were performed on all specimens in ambient air to assess whether any environmental factors affected the K_{IC} levels and fracture modes. Little effect was observed until 1300°C where the decrease in K_{IC} was greater, though only marginally, for samples fractured in air. Analysis of fracture surfaces at these temperatures was impossible due to rapid oxidation producing a uniform glassy layer on the fracture surface. The reduction in K_{IC} can readily be explained by considering oxidation effects at the crack tip or notch root. The specimen was allowed to soak at temperature for 30 minutes after the indicated test temperature was attained. This was common to all fracture experiments. It has been shown in Chapter 5, that at temperatures above 1300°C even at short exposure times, significant YAG reversion occurs at the free surface, to depths of several microns. The effects of oxidation have been shown to have severe effects on the strength of LCS 201 by Reed (176) by the rapid generation of critical flaws which interact with the stress field during testing, causing a reduction in strength. It is proposed that oxidation causes an increase in the flaw size at the root of the notch, by the direct chemical

modification of the near surface, causing a slight reduction in the level of measured K_{IC}.

6.1.2 Discussion

The variation of the K_{IC} results for LCS 201 clearly demonstrates the effect that the nature of the intergranular phase has on the mode of fracture. The fracture behaviour of these materials becomes far more complicated at high temperatures than at low temperatures (176). At low temperatures the strength is governed by catastrophic crack extension from pre-existing or generated flaws. This is seen to be the case in these materials, fracture on the whole not being microscopically controlled by slight variations in microstructure. Factors such as crystallisation are essentially second order.

At high temperature however, the processes which affect failure are more numerous, including cavity nucleation and linkage in the zone around the crack tip. The mechanism of failure is now controlled by the small variations in the microstructure, particularly as illustrated in the previous section the nature of the grain boundaries.

The general behaviour of the materials is consistent with many other findings (178,180) - the presence of glassy residues at the grain boundaries causes the onset of subcritical crack growth. Unlike many other commercial ceramics however, crystallisation of the grain boundary phase is complete, eliminating the mechanism for subcritical crack growth. This is achieved in these materials by satisfying two main conditions. Firstly, by balancing the overall composition during fabrication, resulting in the composition of the residual phase lying near to the YAG-Si_2N_2O the line, complete crystallisation may be attained. Secondly, reduction in the impurity levels, particularly fluorine and calcium, which have been shown to inhibit crystallisation

(173), results in the reduction in stable residual phases which inhibit complete crystallisation. Previous work (172) on the fracture of glass matrix and partially crystallised materials has shown that it is temperature-viscosity relationship rather than the volume fraction which is the dominant influence on the subcritical crack growth threshold. It was shown that partially crystallising the grain boundary phase had little effect on the crack growth characteristics, until the crystallisation was complete, whence subcritical crack growth was eliminated. However, the results found with the high glass viscosity LCS 201 prior to crystallisation were found to be consistent with many other findings. The threshold temperature for subcritical crack growth was found to have increased for these high viscosity, high nitrogen glass when compared with the low viscosity LCS 101 glass of similar composition.

Therefore in summary, matrix crystallisation if taken to completion offers great benefits over its glass matrix parent with regard to the elimination of subcritical crack growth at elevated temperatures. However, although good strength retention at elevated temperatures is maintained as a result of matrix crystallisation, levels of toughness have not been increased by the greater process and compositional control.

6.2 High temperature creep

6.2.1 Creep properties of sintered LCS 201

Isothermal creep experiments were performed on the crystallised β'+YAG LCS 201 at temperatures between 1300°C and 1375°C at 25°C intervals. Tests were performed in both compressive and four point bend modes at stresses in the range of 50-500 MNm^{-2}. These experiments permit both analytical determination of the stress

exponent, n, and the activation energy, Q. A knowledge of the stress exponent and activation energy allows some mechanistic interpretation of the processes governing creep in the steady state regime.

The creep data obtained are shown in figures 6.6 and 6.7 for compressive and four-point bend modes respectively. These show the ultimate secondary creep rates determined 100 hours after initial loading at each stress. Comparative data for alternative silicon nitride and sialon materials, under steady state conditions, is given in figure 2.5.

At 1300°C, the creep behaviour is uniform up to nearly 500 MNm^{-2} in both compressive and four point bend modes. Creep behaviour in four point bend was not determined to extreme stress levels (>400 MPa), as at these stresses the fracture behaviour becomes the limiting factor.

The stress exponent, n, is calculated from these tests to lie within the range 0.8 to 1.1. This indicates that the creep process is dominated by grain boundary diffusion. Increasing the temperature incrementally up to 1375°C, shows that although the creep rate increases with temperature, the gradient, and hence the stress exponent does not change, indicating that the overall steady-state creep process does not change appreciably.

Microstructural investigations of the crept samples indicated that the dominant creep mechanism is indeed grain boundary diffusion. Figure 6.9 shows a typical microstructure of a crept specimen. No evidence was found for any cavity formation at the grain boundaries, even after extreme deformation of 2-3% at 1375°C.

All creep experiments were undertaken after a long initial heat soak to ensure that the temperature for testing was constant. Hence no information could be generated regarding the behaviour of the

Figure 6.6 Isothermal creep plots for LCS 201 in compression.

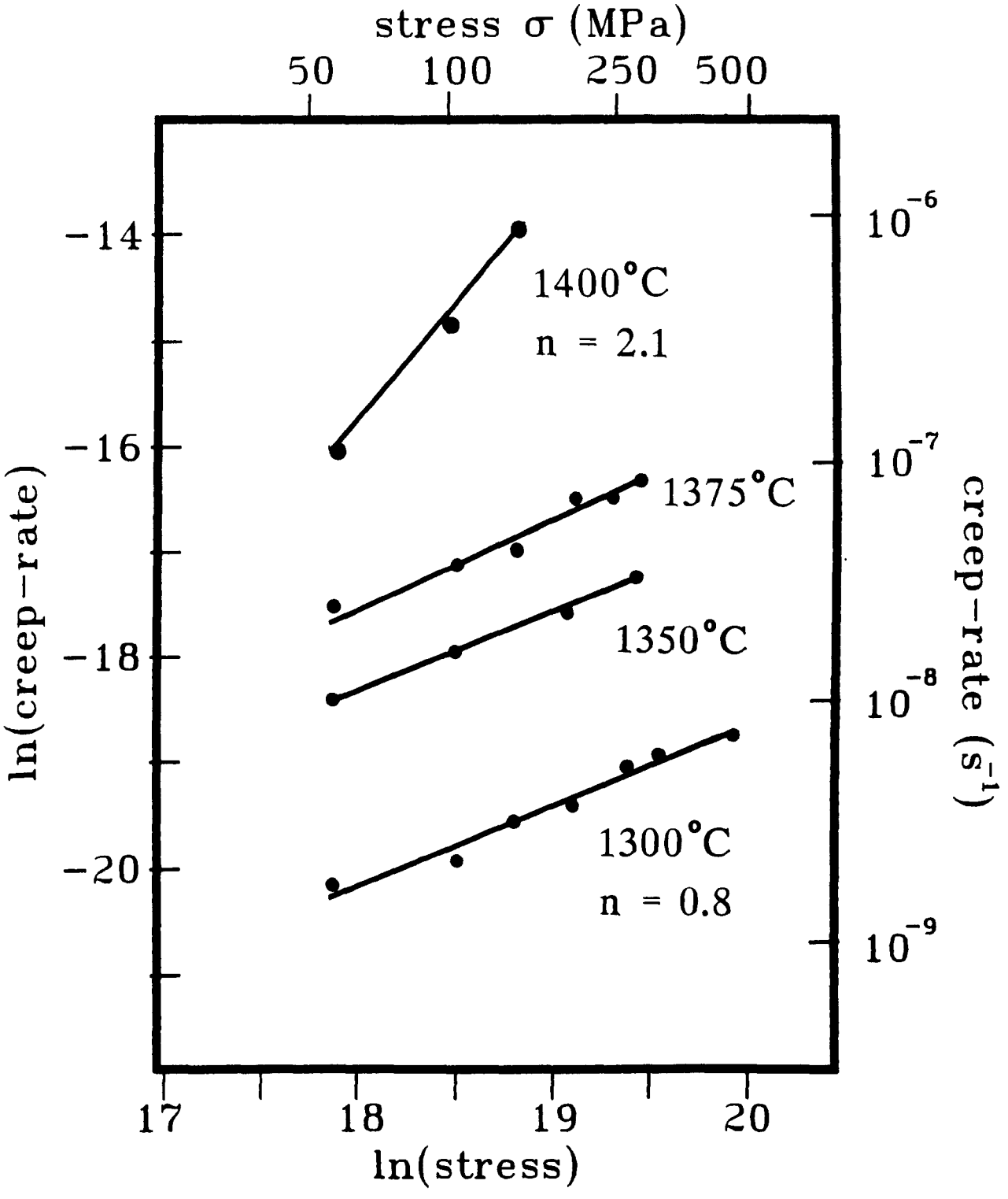

Fig 6.6 201/3 Compressive Creep

Figure 6.7 Isothermal creep plots for LCS 201 in four - point bend mode.

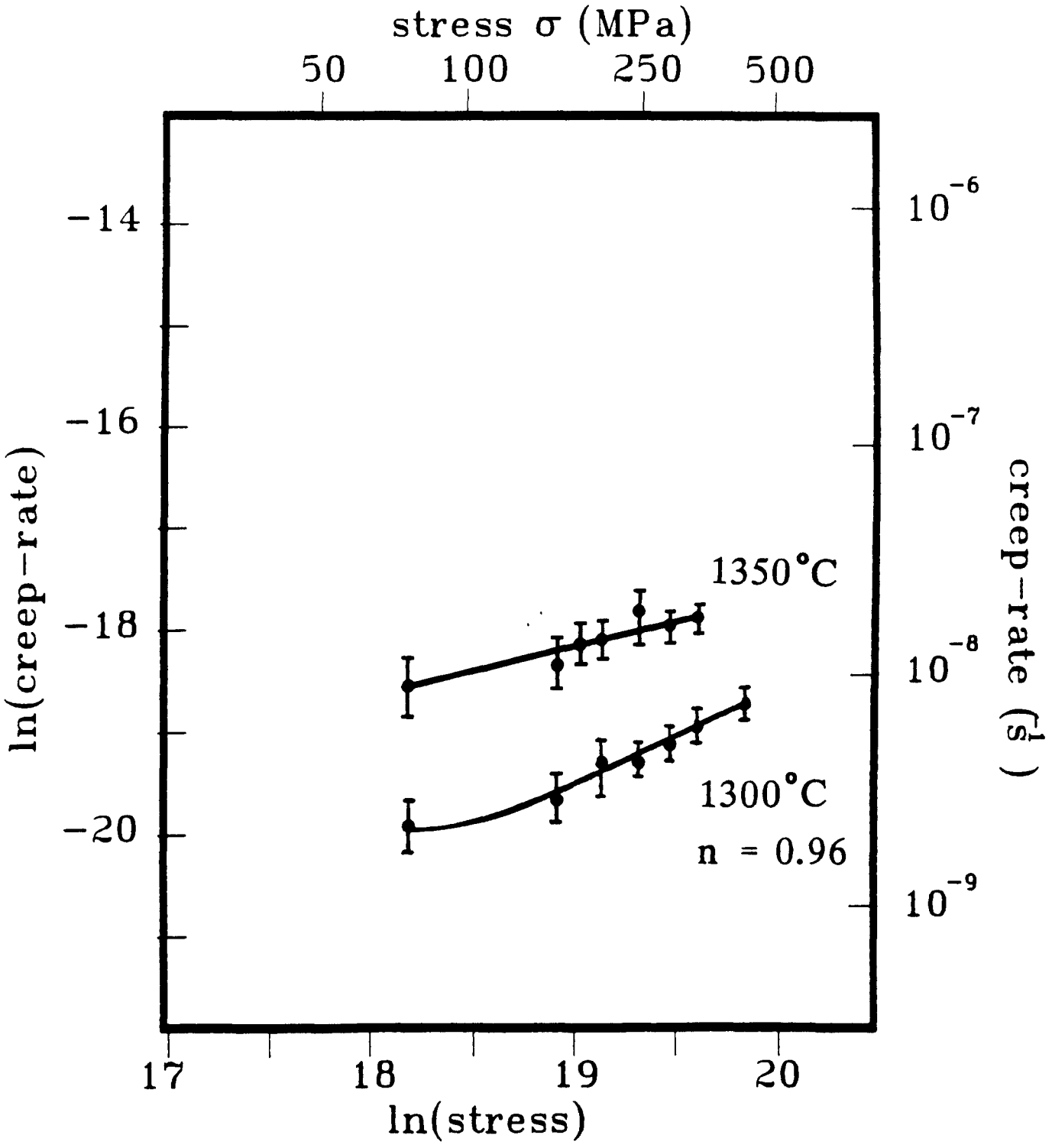
stress σ (MPa)
50
100
250
500
−14
−16
−18
−20
ln(creep-rate)
10^{-6}
10^{-7}
10^{-8}
10^{-9}
creep-rate (s^{-1})
1350°C
1300°C
n = 0.96
17
18
19
20
ln(stress)

Fig 6.7

as-crystallised material, it having had a substantial heat-treatment during stabilisation of the furnace. However, a comparison of the relative creep rates of an as-crystallised material, ie that only give the standard 1250°C/7 hours plus 1400°C/5 hours crystallisation treatment, and a similar material subjected to an additional 1200 hours heat-treatment at 1300°C was undertaken.

The results are plotted in figure 6.8, in the form of the log-log plot, with data points plotted at 25, 50, 100 and 200 ksec to illustrate the decay of the primary creep, and the domination of the secondary creep. In the case of the untreated specimen, this is significant, the large primary component of creep decays over a lengthy period of time, and it can be seen that the true secondary creep is not achieved until a long time after loading.

However, after heat-treatment, secondary creep was attained at a far greater rate, indicating that the primary creep component in this case is substantially less significant. Microscopic analysis of the structures, has shown that even in the untreated state, the as-received LCS 201, that residual glass zones are not detectable, hence it is assumed that crystallisation is complete. However, these experiments suggest that there exist small amounts of residual glass phase, possibly at two grain junctions, resulting in the large primary component of creep. Only extended heat-treatment causes complete devitrification of the residual glass phase, reducing the primary component of creep.

6.2.2 Environmental stability at high temperatures and stresses

Chapter 5 described the effects of high temperature exposure of LCS 201 in oxidising atmospheres. Long term creep tests at elevated

Figure 6.8 Comparison of decay of primary creep rates before and after extended heat-treatment.

Fig 6.8

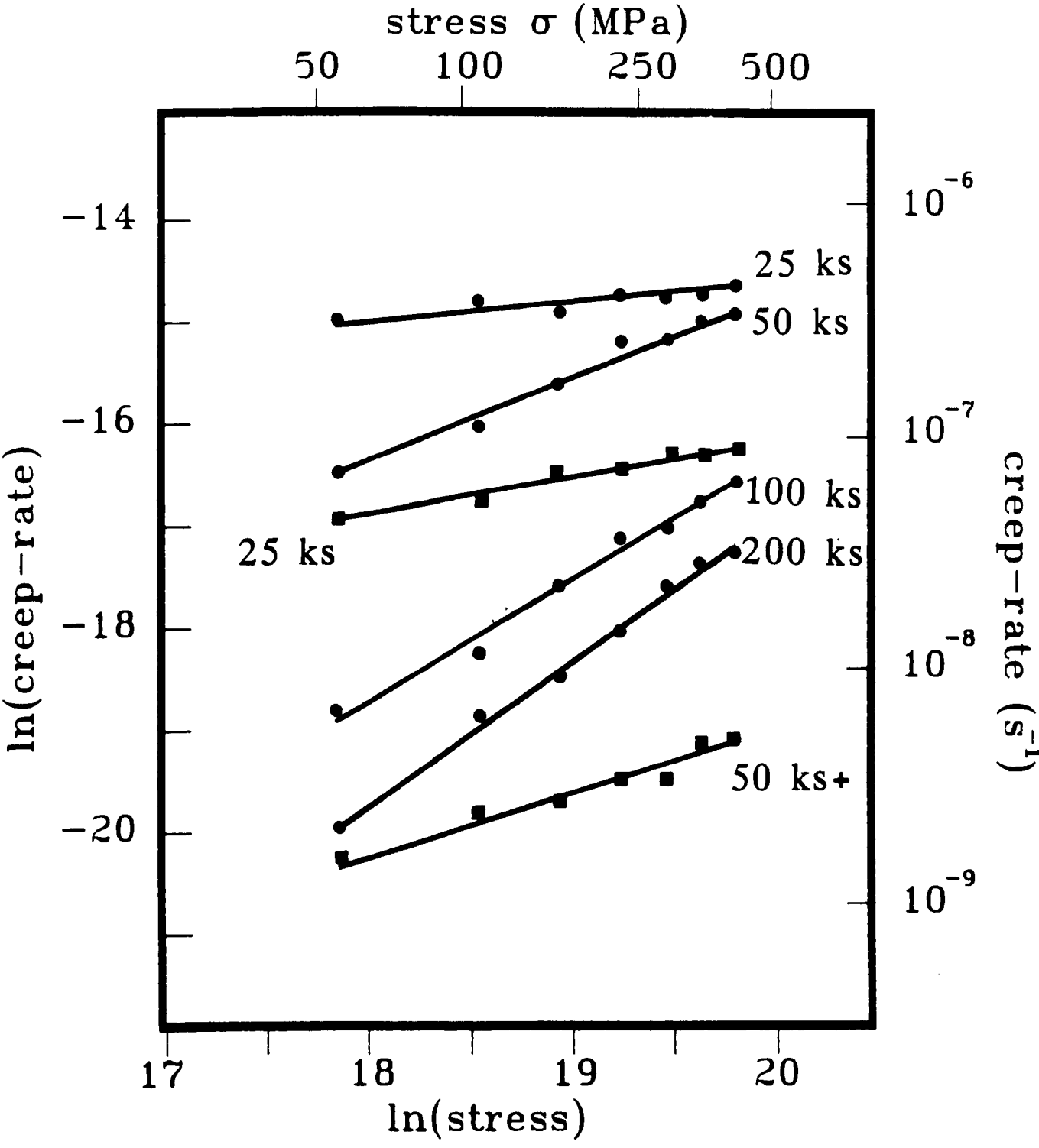

• as−received

▪ heat−treated 624 hrs at 1300 C

temperatures would be expected to cause similar effects that were observed during static oxidation.

Examination of creep specimens after testing shows that significant oxidation had taken place at the surface, forming a white oxide scale. The morphology of the oxide layer is a simple extension of what was observed during the shorter term static oxidations tests. Creep specimens subjected to long dwells at 1300°C were found to have a continuous glassy layer on the surface. Analysis of the cross-section, figure 6.9, shows that extensive exposure at 1300°C causes more extensive growth of α-cristabolite, to such a degree that it has grown throughout the oxide layer. The formation of a large volume of α-cristabolite at the oxide-substrate interface does not appear to be continuous and protective due to extensive porosity and cracking.

However, a β'/O' zone approximately 20μm thick in the immediate sub-surface, was formed offering the environmental protection at temperatures above 1300°C. Specimens which were not subjected to extended heat-treatment at 1300°C to form a continuous β'/O' layer, suffered extensive and catastrophic oxidation, resulting in the ultimate failure during testing (see section 6.3). The β'/O' layer protects the bulk of the material from the extreme degrading effects of oxidation at temperatures above 1300°C. The dependence on the protection afforded by the β'/O' layer is demonstrated by heat treating a specimen at 1300°C to form the layer under static air conditions. This formed an oxide layer similar to that observed for the creep specimens. This was then removed by careful grinding to expose the β'/O' layer, and the specimen creep tested at 1350°C and 1375°C. Post-test examination indicated that the oxide layer formed was thin and glassy, with little evidence of extensive cation out-diffusion.

Figure 6.9 Microstructure of crept LCS 201

a) backscatter electron micrographs of oxidised surface and bulk showing β'/O' layer.

b) transmission electron micrograph showing isolated YAG with no cavitation.

Fig 6.9

(a)

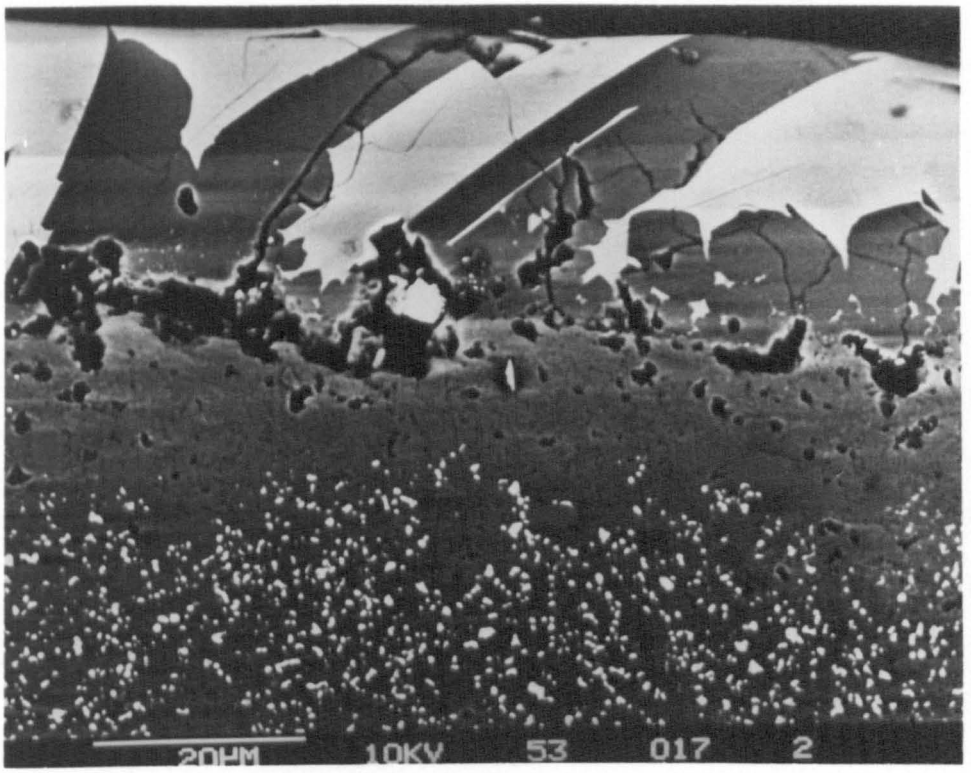

(b)

1μm

The protection afforded by the formation of the β'/O' layer is however limited. As in the case of static oxidation, it was observed that above 1375°C, the protective layer broke down, and severe oxidation ensued. This effect was also observed for specimens under stressed conditions. The secondary creep rate at this temperature was found to be significantly higher, as shown in figure 6.6. However, examination of the specimen after testing showed severe oxidation effects. In fact the specimen was almost totally oxidised, the β'/O' layer offering little protection at this temperature, direct oxidisation of the β' and O' removed the thin protective layer in a short time. The secondary creep rate $\dot{\varepsilon}_S$ was found to increase with time at constant load. This effect was put down to the effects of oxidation, and the resulting oxide scale spalling, reducing the effective cross-section that the stress was acting upon, thus increasing the stress in turn.

Microscopic examination of the sub-surface region below the β'/O' layer revealed a substantial zone (~0.5mm) where no α' existed, the structure being β' + isolated YAG. This is consistent with earlier findings where it is presumed that the presence of oxygen diffusing via the grain boundaries causes instability of the α' resulting in reversion to β'.

The outdiffusion of the metallic cations, and the subsequent growth of the O' at the surface resulted in some residual porosity in this region. These were not found to cause unexpected failure by acting as critical flaws, particularly at high stresses (~450 MPa). It has been concluded that surfaces compressive stresses due to oxidative phase changes, particularly the formation of oxynitride phases (178). This effectively reduces the resolved stress on the outer fibre, leading to an apparent increase in strength, and a resistance to the nucleation of critical flaws.

The protection afforded by the formation of the β'/O' layer is however limited. As in the case of static oxidation, it was observed that above 1375°C, the protective layer broke down, and severe oxidation ensued. This effect was also observed for specimens under stressed conditions. The secondary creep rate at this temperature was found to be significantly higher, as shown in figure 6.6. However, examination of the specimen after testing showed severe oxidation effects. In fact the specimen was almost totally oxidised, the β'/O' layer offering little protection at this temperature, direct oxidisation of the β' and O' removed the thin protective layer in a short time. The secondary creep rate $\dot{\varepsilon}_S$ was found to increase with time at constant load. This effect was put down to the effects of oxidation, and the resulting oxide scale spalling, reducing the effective cross-section that the stress was acting upon, thus increasing the stress in turn.

Microscopic examination of the sub-surface region below the β'/O' layer revealed a substantial zone (~0.5mm) where no α' existed, the structure being β' + isolated YAG. This is consistent with earlier findings where it is presumed that the presence of oxygen diffusing via the grain boundaries causes instability of the α' resulting in reversion to β'.

The outdiffusion of the metallic cations, and the subsequent growth of the O' at the surface resulted in some residual porosity in this region. These were not found to cause unexpected failure by acting as critical flaws, particularly at high stresses (~450 MPa). It has been concluded that surfaces compressive stresses due to oxidative phase changes, particularly the formation of oxynitride phases (178). This effectively reduces the resolved stress on the outer fibre, leading to an apparent increase in strength, and a resistance to the nucleation of critical flaws.

Figure 6.10 Activation energy plot for LCS 201 at constant stress.

Fig 6.10

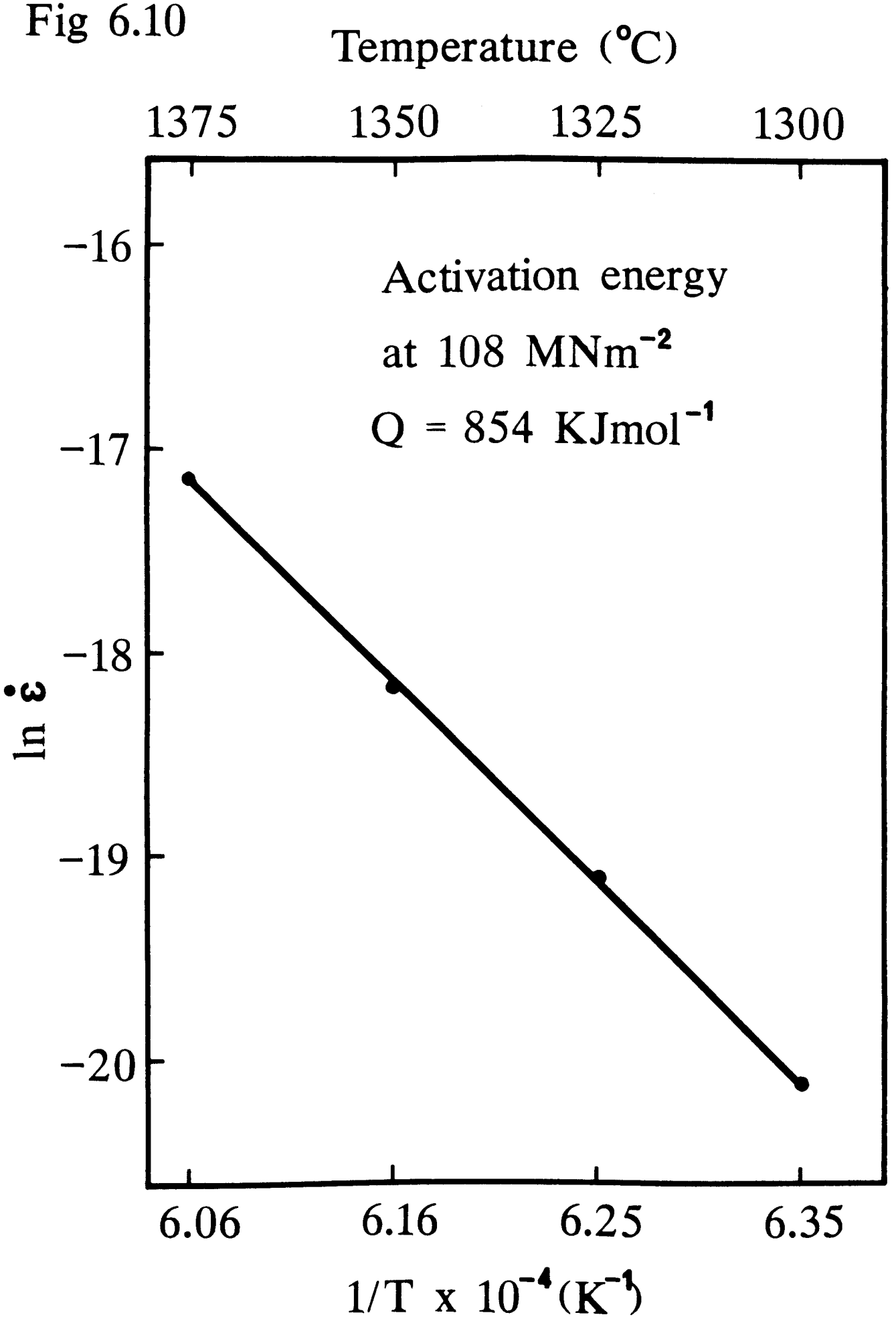
Temperature (°C)
1375
1350
1325
1300
−16
−17
−18
−19
−20
Activation energy
at 108 MNm^{-2}
Q = 854 KJmol^{-1}
ln $\dot{\varepsilon}$
6.06
6.16
6.25
6.35
1/T x 10^{-4}(K^{-1})

6.2.3 Creep properties of ceramics with varying polytypoid additions

The variation in the level of polytypoid addition from the basic LCS 201 composition has been shown in section 4.1.2 to have observable effects on the microstructure. The reduction in the overall nitrogen level results in incomplete crystallisation of the intergranular glass phase.

Compressive creep behaviour for the compositions with 2,4,6% added polytypoid addition are shown in figure 6.11. The measured secondary creep rates for the range of these materials was found to be significantly higher than for the fully crystallised LCS 201 ceramic. In addition the calculated values for the stress exponent, n, at 1300°C were in the range of 1.4 to 1.6. The non-integral stress exponent, n, indicates that in these materials the creep mechanism may be characterised by intergranular cavitation. This is as a direct result of the presence of significant amounts of residual glass phase at the grain boundaries, which unlike the high nitrogen containing LCS 201 does not fully crystallise to YAG even after extended heat treatment (see section 4.3.2).

Although the amount of crystallisation of the intergranular phase in these materials increased with increasing polytypoid addition, only the high polytypoid level material, effectively LCS 201 ceramic exhibited diffusional creep behaviour rather than a cavitational controlled mechanism. Even extended thermal treatments during the creep trials were not significant to nucleate and fully crystallised the intergranular YAG phase. Therefore, creep rates were found to be dominated by the presence of the glassy phase.

Subsurface transformations, the formation of the β'/O' layer again occurred as a result of the extended thermal treatments in oxidising environments. This factor, a result of initial yttrium

Figure 6.11 Isothermal creep plots for ceramics fabricated with varying polytypoid additions in compression.

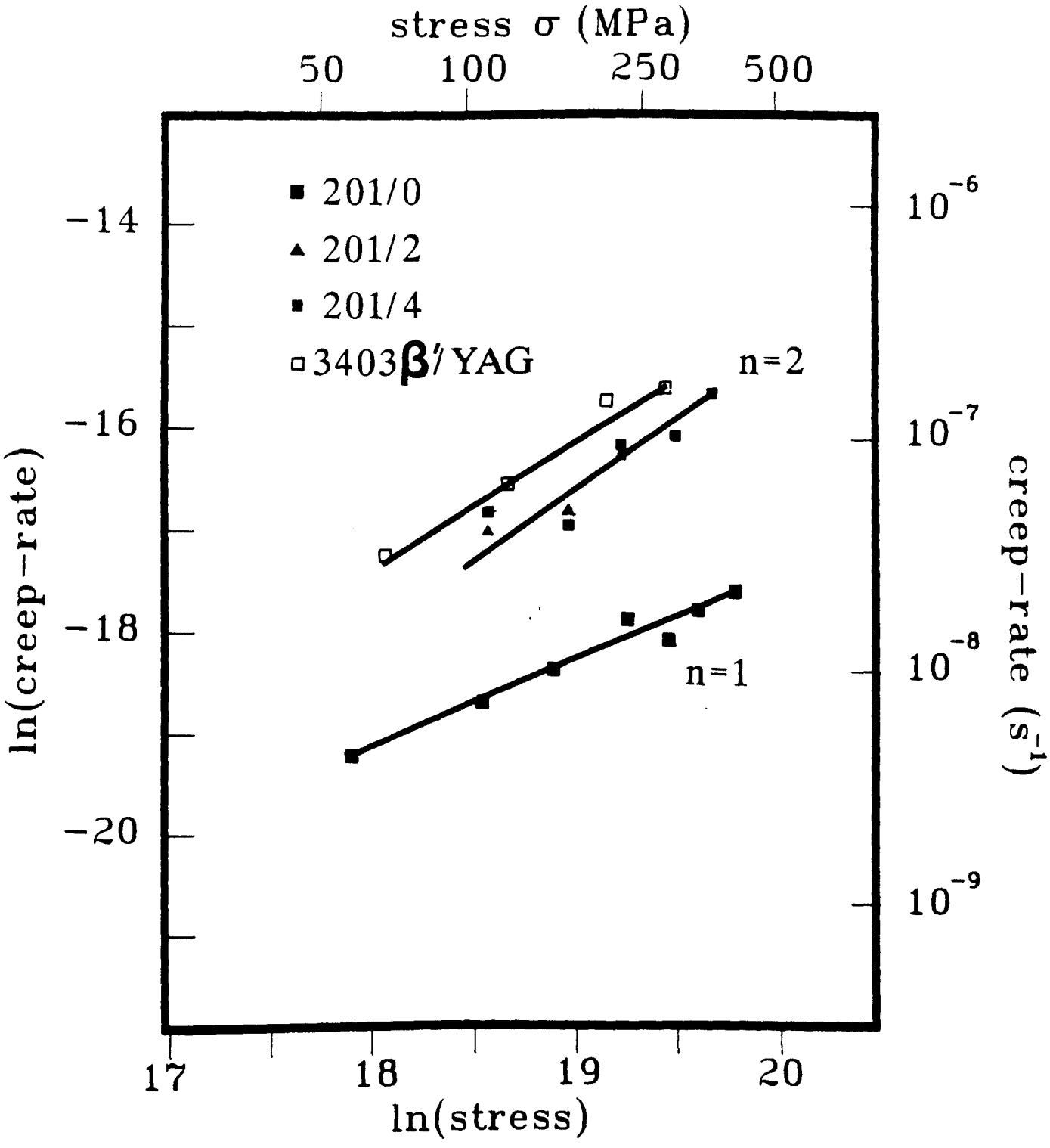

Compressive Creep 1300°C

outdiffusion from the near surface regions, effectively in the long term causes the reduction of further outdiffusion to any great extent preserving the overall composition of the bulk of the material. The amount of β'/O' produced as a result of the transformation is still therefore small compared with the bulk of the material, and thus the creep properties of the bulk were still found to dominate.

6.2.4 Discussion

The most significant factor affecting the creep properties is the removal of residual glass at the intergranular sites by crystallisation. This results in diffusion controlled (n=1) creep even at high stresses (~400 MPa). Comparing this with the creep behaviour with other silicon nitride ceramics shows the importance of residual grain boundary phases. In many other systems, residual glass is observed at triple junctions (138). This is directly attributed to the cavitational behaviour observed. This was demonstrated in this study with a comparative creep test of a Syalon ceramic of similar composition, but fabricated with a different source Si_3N_4 powder. The α-Si_3N_4 powder for this ceramic was provided by H.C. Stark Ltd, and has been shown to contain measurable amounts of fluorine (173), derived from the leeching of the Si_3N_4 powder to remove impurities, mainly iron (Fe). It has been shown that even small quantities of fluorine (~1^{ω}/o) in Y-Si-Al-O-N glasses can alter the properties significantly (163) by reducing the viscosity by up to 3 orders of magnitude. During crystallisation, these impurities are segregated and concentrate in regions of stable glass formation at triple junctions, resulting in incomplete crystallisation.

Secondary creep rates for this material are plotted in comparison with LCS 201 in figure 6.6. It can immediately be seen that the absolute creep rates and the stress exponent (n=3) are

significantly higher than the LCS 201. This may be directly attributed to the residual glass phase, the low viscosity glass being the cause of the high creep rates at high temperatures, and the cavitational dominated creep mechanism (n>1) as a result of the stable residual glass in intergranular regions.

The calculated activation energies, Q, for creep correspond to, and are consistent with similar materials where grain boundary diffusional creep was found to be dominant (33), and higher than those calculated for cavitating ceramics (125). These materials were single phase β'-sialon where the rate-determining step for creep was atom mobility along β'-β' grain boundaries. As the measured activation energy for the studied materials are comparable to the single phase materials β'-β' grain boundaries are thought to represent the rate-determining step rather than β'-YAG grain boundaries.

It can therefore be seen that the creep resistance is enhanced greatly by the elimination of residual glass at intergranular sites. This may be attained by the reduction in the impurity levels, as shown above. In addition, careful compositional control results in a greater degree of crystallisation of the glass. The presence of some iron in the LCS 201 in the form of iron silicide does not appear to affect the creep rate significantly as on the whole it is finely distributed in well defined, discreet intergranular sites, and not found continuously throughout the structure.

The formation of the β'/O' sub-surface layer is as a result of YAG reversion due to oxidation (section 5.3.3). The reverted zone in the sub-surface was subjected to gross cation out-diffusion at temperatures above 1300°C, resulting in a silica-rich reversion zone from which the β'/O' layer forms. Directly below the β'/O' layer, no reversion is apparent, the structure essentially is β'/YAG. The microstructure, protected by the β'/O' layer, remains a stable β'/YAG

structure, and creep is determined by diffusion along β'/β' and β'/YAG boundaries rather than diffusion via a glassy phase.

6.3 High temperature stress rupture of LCS 201

Creep rupture tests, or time-to-failure at constant load were performed at temperatures of 1300°C and 1350°C and are shown in figure 6.12. As little degradation in properties was observed below 1300°C, it was concluded that no extra information would be obtained by testing at temperatures below 1300°C.

The stress-rupture behaviour at 1300°C indicates a good resistance to stress rupture. At high stresses (~450MPa), failure was observed to be either instantaneous or within the first few minutes of loading. Failure in this regime occurred by the catastrophic extension of surface or near surface flaws upon loading. The applied stress, 450 MPa, is approximately 80% of the measured fast fracture strength, such that any surface or sub-surface flaw such as an agglomerate or pore for instance which has the effect of intensifying the stress locally has a high probability of causing failure. Short but finite failure times (usually less than 3 minutes) were considered to be directly as a result of oxidation effects, the extension of a flaw by environmental attack to a critical level resulting in catastrophic failure. At lower stresses (<400 MPa), specimens were found to survive for times in excess of 1000 hours under stress. This illustrates the resistance to any form of subcritical crack growth at this temperature, primarily as a result of the extent of crystallisation of the intergranular phase, and as a result of the retention of diffusional controlled creep properties.

The long term environmental effects also appear not to have a significant degrading effect on the properties either. Degradation of the surface by pitting and increased porosity as a result of oxidation

Figure 6.12 Creep rupture behaviour of LCS 201 at 1300°C and 1350°C.

Fig 6.12

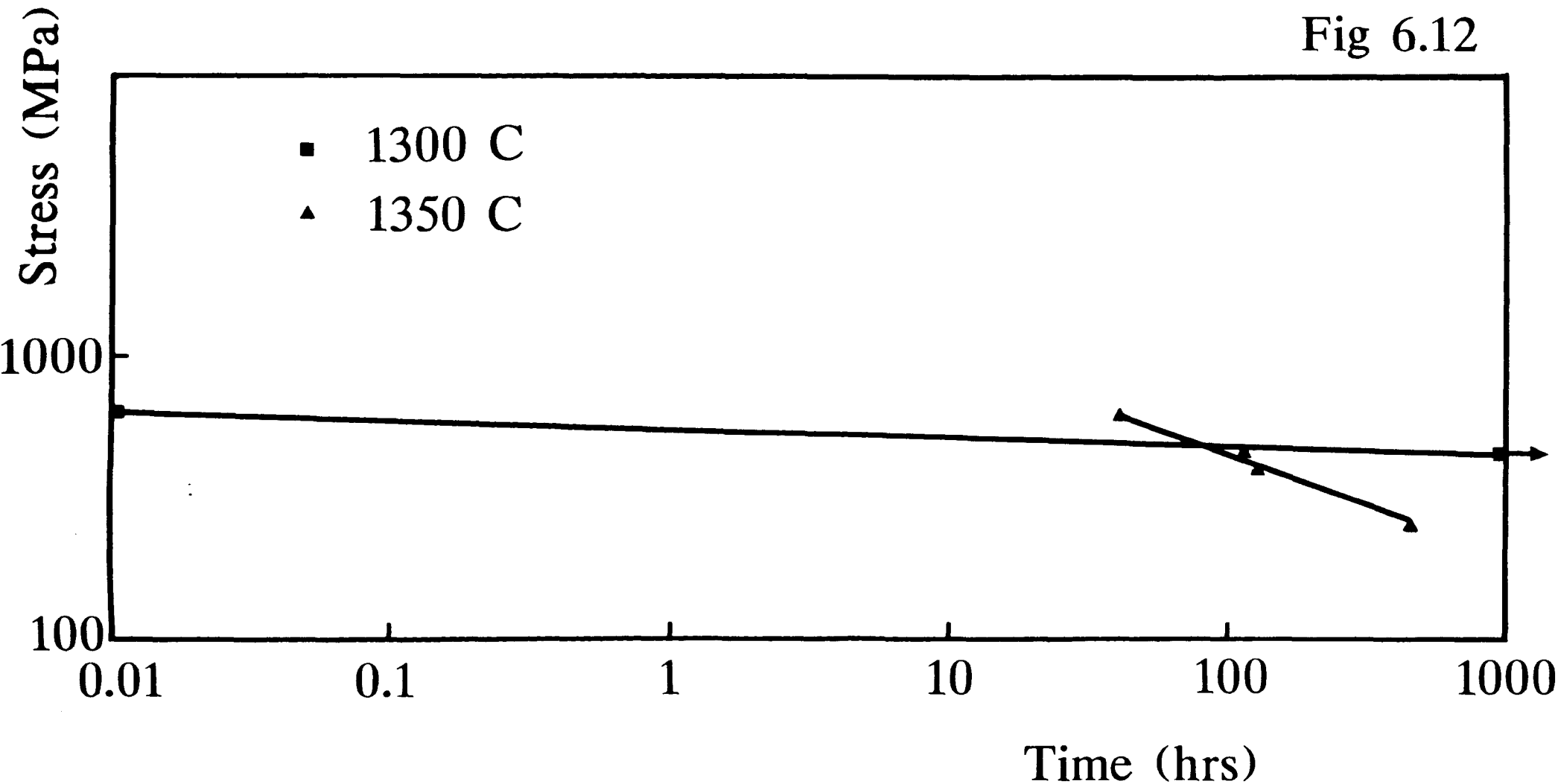

do not at these stresses cause catastrophic failure as seen at the marginally higher stresses. The formation of a protective β'/O' surface layer, in addition to the effect of reducing the oxidation kinetics also may cause stress relief at the tensile face. The formation of the O' has reported by Lange (178) to be the cause of surface compressive stresses. This would effectively reduce the stress on the tensile face, thus reducing the probability of failure as a result of catastrophic extension of a critical flaw.

At 1350°C a marked transition occurs in the stress rupture behaviour. Marked time dependent behaviour occurred over the stress regime, even at high stresses (400 MPa). The long term secondary creep rates measured at 1350°C in section 6.2.1 indicated a diffusional controlled creep mechanism, hence one would expect no time dependent failure as a result of the intrinsic creep mechanism, like, for instance, what would be expected from NC 132 at temperatures in excess of 1000°C (148). As a result it is proposed that the time dependent failure mechanism is one induced by environmental attack. A subcritical crack is formed as a direct result of YAG reversion to a low viscosity glass by oxidation at the tensile face. Extension of the crack is achieved by continuous YAG reversion at the crack tip. Again catastrophic failure occurs when the subcritical crack reaches the critical flaw size, depending on the applied stress level.

The stress rupture results indicate yet again the limitation that the basic chemistry of this system has on the high temperature properties. Although compositional balancing and crystallisation of the grain boundary phase results in the retention of properties at elevated temperatures, the mere fact that the grain boundary phase is YAG becomes the limiting factor, and this dictates the high temperature limit of the material. It is clear however, that the elimination of factors such as pores, residual glass from much

previous work has beneficial effects on the stress rupture life (148). These results substantiate this basic premise, and that it can be inferred that in the case of residual glass phase, if present is either dimensionally small or isolated.

None of these experiments were performed on specimens with a protective β'/O' layer. Long term exposure at 1300°C at the lower stresses where failure did not occur showed the predictable development of the β'/O' layer. At 1350°C, no such development was observed, the lifetimes measured do not account for such layer formation. Thus the stress rupture behaviour does not reflect this aspect of microstructural evolution of the β'/YAG type materials at elevated temperatures.

6.4 Conclusion

Compositional balance and full crystallisation of the intergranular YAG phase has resulted in the improvement in observed high temperature mechanical properties. This has been demonstrated in short term fracture modes where subcritical crack growth is eliminated at elevated temperatures (up to 1400°C) simply by the crystallisation of the intergranular glass phase. This behaviour is also reflected in the long term mechanical stability, where improved creep resistance was observed over previous pressurelessly sintered sialon ceramics (173) directly as a result of the grain boundary crystallisation.

The factor which was found to limit the high temperature use of the β'/YAG LCS 201 was oxidation induced YAG reversion, which at temperatures in excess of 1300°C was found to be the cause of time dependent creep rupture behaviour. The use of protective β'/O' layers produced by extended thermal treatments at 1300°C were shown to protect specimens from the effects of catastrophic oxidation at

temperatures up to 1375°C. However, the effect that this would have on the stress rupture life was not investigated.

Although the β'/O' layer has been shown to give good oxidation protection upto 1375°C, the development of the use of surface transformations as a method of protection in real applications is dependent on the ease at which it can be formed, and its life at maximum target temperatures. It has been shown in Chapter 5 that the development of β'/O' layers is very difficult to control, and rapid development causes severe surface and sub-surface degradation. It has also been shown in this chapter that the effective protection is limited to 1375°C, beyond that catastrophic oxidation occurs.

Therefore in order to address these problems, the use of coatings applied to the surface of the ceramic will be investigated in the next chapter. These offer potentially several benefits over oxidation induced surface layers; they can be formed in short times at temperatures which will not induce significant microstructural changes in the substrate, and the composition can more easily be tailored to suit the application.

CHAPTER 7 - CERAMIC COATINGS - MICROSTRUCTURE AND INFLUENCE ON PROPERTIES

In this chapter, the use of protective coatings based upon chemical vapour deposited (CVD) silicon nitride and silicon carbide will be investigated. A study has been made of the microstructure of the as-coated layers, their stability, and effect on the long term mechanical properties. Finally an assessment of the suitability of the concept of ceramic coating as a method for high temperature protection will be made.

7.1 Introduction

The use of thermal barrier ceramic coatings on metallic components as a method of increasing the high temperature limit is now well established. The surface temperatures of the metal are lowered by 50 to 300°C by relatively thin ceramic coatings (<1mm) (181). In addition to thermal protection, ceramic coatings offer reduced oxidation, corrosion, erosion and wear, thereby increasing overall efficiency of the component. A broad range of coating materials (oxide, nitride, boride and carbides) and processes are now available as shown in figure 7.1.

Although coating of metals with ceramics is now common, the coating of ceramics in a similar fashion is less well known. The need for this arises from the stability of dense ceramics. The use of metal oxide additives eg. Y_2O_3, has been shown in the previous chapters to be the limiting factors for high temperature stability, below target levels of 1375°C to 1400°C for Si_3N_4 based materials. Much of the degradation is due to environmental reactions with the grain boundary phases, leading to the onset of sub-critical crack growth and stress rupture. The application of a ceramic coating may provide a barrier against diffusion, and thus the savage effects

Figure 7.1 Summary of coating processes.

Figure 7.1 Coating deposition techniques

Atomistic deposition	Particulate deposition	Bulk coatings	Surface Modification
Electrolytic environment	**Thermal spraying**	**Wetting processes**	**Chemical conversion**
Electroplating	Plasma spraying	Painting	Electrolytic anodization (Oxide)
Electroless plating	D-Gun	Dip coating	Fused salts
Chemical displacement	Flame spraying		
Vacuum environment	**Fusion coatings**	**Electrostatic spraying**	**Chemical-liquid**
Vacuum evaporation	Thick film ink	Printing	**Chemical vapour**
Ion beam deposition	Enameling	Spin coating	
Molecular beam epitaxy	Electrophoretic		Thermal
		Cladding	Plasma
Plasma environment	**Impact plating**	Explosive	**Leaching**
		Roll bonding	
Sputter deposition		**Overlaying**	**Mechanical**
Activated reactive evaporation			Shot peening
Plasma polymerization		Weld coating	
Ion plating			**Thermal**
Chemical vapor environment			**Surface enrichment**
Chemical vapor deposition			Diffusion from bulk
Reduction			
Decomposition			**Sputtering**
Plasma enhanced			
Spray pyrolysis			**Ion implantation**
Liquid phase epitaxy			

of the environment at elevated temperatures would be reduced. Hence an increase in the operating temperature may be attained.

The criteria for such a coating would be that it should have superior oxidation resistance to the substrate, that it be dense, and most importantly have a similar thermal expansion coefficient to the substrate. The latter is of critical importance due to large stresses which occur at the coating-substrate interface as a result of differences in thermal expansion, which could lead to spalling of the coating. Considering these factors, it is believed that coatings based upon silicon nitride and silicon carbide would be suitable for adequately protecting the sialon type materials.

The process which has been found to easily form dense, refractory coatings is chemical vapour deposition (CVD). This process may be defined as the deposition of a solid onto a heated substrate as a result of chemical reactions in the gas phase, which often occur at or near to the substrate surface.

Silicon nitride coatings have been prepared from a number of silicon sources - SiH_4 (182), SiF_4 (183), SiF_2 (184), SiH_3F (185), but most commonly, $SiCl_4$ (186,189). Other silane sources have been investigated, but to a lesser extent.

In the CVD process, the layer is formed by a nucleation-growth process, the structure being highly dependent on the coating conditions such as temperature, pressure, reactant concentration, gas flow, pressure and dynamics. Therefore this method of coating is highly controllable, allowing amorphous, polycrystalline or even single crystal coatings to be deposited. The deposition rate, and uniformity of coating depend on the rate of mass transfer of reactants to the substrate and the rate of reaction at the substrate surface. At atmospheric pressure, these rates are found to be of the same order of magnitude. However, at low pressure, the lower reactant gas

pressure increases the mass transfer rate resulting in more uniform denser deposition.

As stated previously, the structure of the coating is dependent on the conditions of deposition. Oda et al (190) studied the effects of deposition temperature on structure obtained. β-Si_3N_4 coatings were obtained at 1300°C, while $\alpha+\beta$ and α-Si_3N_4 coatings were obtained at 1250°C and 1150°C respectively. The formation of the β-phase was attributed to impurity concentrations such as SiO, CaO, MgO, whose presence even in small amounts accelerates the rate of β formation markedly. Further studies by Motojima et al (191) over a wider parameter range showed that at low temperatures the coating was amorphous. Increasing the temperature of deposition, >1100°C, resulted in increased crystallinity of the layer. The morphology of the crystalline layer was found to be columnar (55), with good adherence to the substrate, while amorphous layers showed some globular structure on the surface. The Si_3N_4 layer deposited by this method has been shown to be nearly stoichiometric with a density greater than 97% theoretical.

Due to high purity of CVD Si_3N_4, the oxidation resistance has been shown to approach that of pure single crystal silicon nitride (192,86), being superior to that of sintered silicon nitride ceramics. Oxidation, for dense CVD materials, is parabolic in nature, the rate being determined by the formation of a SiO_2 oxidation product on the surface.

7.2 Experimental techniques

The ceramic substrates were in the form of 3mmx3mmx70mm bars polished to 1µm on all surfaces. The bars were coated at Archer

Technicoat Ltd., High Wycombe, under the conditions shown in figure 7.2 by the reactions

$$3SiCl_4(g) + 4NH_3(g) \rightarrow Si_3N_4(s) + 12HCl(g) \quad (7.1)$$

$$2Si(CH_3)Cl_3(g) + H_2(g) \rightarrow 2SiC(s) + HCl(g) \quad (7.2)$$

Figure 7.2

Coating	Temp	P_{N_2}(mbar)	Reactant gases	Coating Form
Si_3N_4	1400°C	80	$SiCl_4 + NH_3$	α-Si_3N_4
SiC	1100°C	80	$Si(CH_3)Cl_3+H_2$	Amorphous

Selected samples of both Si_3N_4 and SiC coated ceramics were exposed to static air oxidation in the temperature range 1100° to 1400°C for periods up to 100 hours. The structural development of the amorphous SiC layer was studied following controlled heat treatment in inert (Ar) gas atmosphere. In addition, both types of coated samples were deformed at high temperature both in compressive and four point flexure, to assess the effect that the coatings have on the time dependent creep rupture behaviour of LCS201 at 1350°C, and the effectiveness of these coatings at high stresses.

7.3 Microstructure of CVD ceramic coatings

7.3.1 Microstructure of Si_3N_4 CVD coatings

The coating was deposited onto the substrate in the form of the the crystalline α-Si_3N_4 phase, to a thickness of 40-60μm uniformly on all faces of the specimen (figure 7.3). The coating was essentially

Figure 7.3 Microstructure of CVD Si_3N_4 coating deposited at 1400°C.

a) Backscattered electron micrograph with typical EDX analysis.

b) Transmission electron micrograph

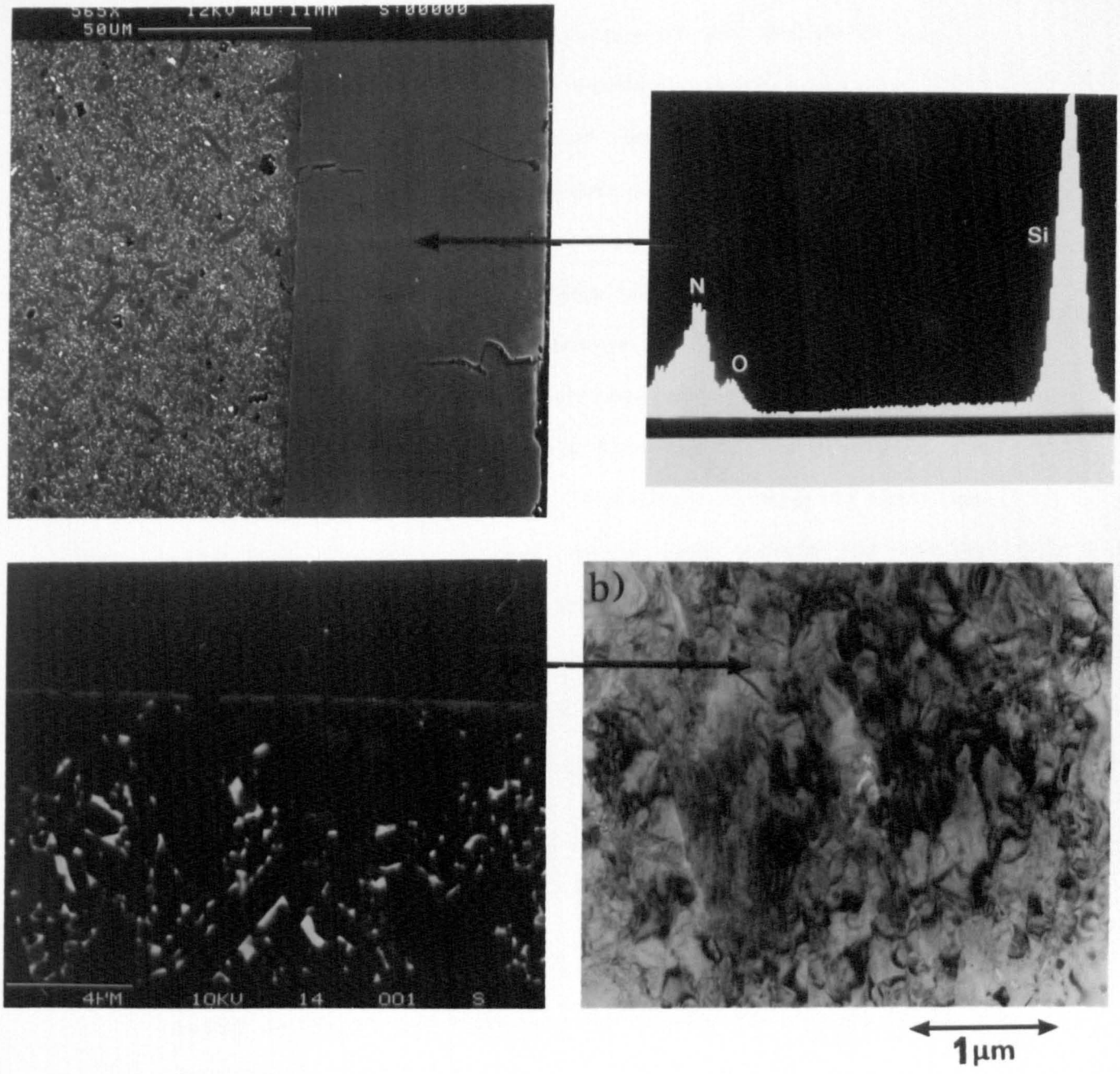
565X 12KV WD:11MM S:00000
50UM
Si
N
O
4UM 10KV 14 001 S
b)
1μm
[001]
[2̄10]
0.2 μm

Fig 7.3

single phase, consisting of large crystals of the α-form of Si_3N_4. XRD analysis of the coating indicates oriented growth along the (102) plane. TEM imaging of the layer shows the large grain size of the coating as compared with the substrate, very few grain boundaries being observed. In addition to this, there existed significant bend contrast due to residual stresses within the coating. These are due to microscopic hetrogenities in structure and chemistry during the epitaxial growth of the layer. There was no evidence of residual glass, a feature which would be solely dictated by the purity of the reactant gases. The only indication of accidental impurity additions were in the form of the occasional 'black spot' within the α-Si_3N_4 crystal. EDX analysis of this phase indicated a high concentration of barium and sulphur species. The origin of this is unknown, and can only be assumed to be derived from the reaction vessel itself.

EDX analysis of the CVD layer indicates that the coating contains a measurable amount of oxygen, thus making the structure non-stoichiometric. This impurity may be derived from two possible sources;

(i) Oxygen is derived as an impurity from the gaseous reactants, being incorporated into the structure as the coating is deposited.

(ii) outdiffusion from the substrate.

The latter is thought unlikely for a number of reasons. Firstly, no other species having diffused out of the substrate eg. yttrium. Secondly, the oxygen content is uniform over the layer, from the outside surface to substrate interface, and finally at 1400°C diffusion out of the substrate is thought to be unlikely in a non-oxidising atmosphere as atom mobility in the β'/YAG materials is low under these conditions. Therefore the first option explains the presence of oxygen most satisfactorily.

Analysis of the interfacial region shows a small (<5μm) depletion zone in the substrate, with some yttrium having diffused into the interfacial region to form a thin layer <0.1μm between substrate and coating (figure 7.3), being due to a diffusion gradient being set up across the interface. The source of the yttrium may be small amounts of glassy phase left at the grain boundaries after the crystallising heat-treatment. This is also assumed to be responsible for the decaying viscoelastic creep component observed in section 6.2.1 in the previous chapter. There is no evidence for any long range chemical reaction between coating and substrate.

Evident within the small depletion layer at the coating-substrate interface, are α' crystals (light grey contrast as compared with black in figure 7.3) where the prismatic hexagonal faceting has been rounded off. This is caused by destabilisation of the α' structure by diffusion of yttrium out of the crystal. The driving force for this would only come from the diffusion gradient across the interface. α'-Sialon requires yttrium to stabilise the structure, removal of which causes a crystallographic change to the β' form. This effect is similar to that observed in specimens which had undergone medium to long term oxidation, the mechanism of transformation being similar.

7.3.2 Microstructure of SiC CVD coatings

The coating was deposited at a lower temperature than the Si_3N_4 coating in the previous section, the temperature being 1100°C. As a result of this, the coating was deposited in the amorphous state. Figure 7.4 shows the coating in the as deposited state, being a dense layer ~30 μm in thickness, uniformly on all sides of the bar.

The layer shows a lack of structure to the coating, evidence of the amorphous state of the layer. Selected area diffraction supports this, the only diffraction contrast being that of a very diffuse ring. High resolution dark field imaging showed some evidence of microcrystallinity, though it could not be ascertained whether this was a true observation or simply an artifact of the ion-beaming preparation process. The amorphous nature of the coating allowed more stress relaxation during the deposition process. Unlike the Si_3N_4 case, the effects of residual stresses are not as apparent, the amorphous coating being less sensitive to hetrogenities caused by the deposition process.

Analysis of the layer indicates that silicon carbide is the only phase present throughout the coating. Again measureable oxygen content was observed. This again can only be attributed to small amounts of oxygen being present in the reactant gases. Due to absorption difficulties of the light elements, it was again not possible to measure the oxygen content quantitatively. Backscattered imaging through the layer shows some contrast through the layer. Analysis of these regions indicate no chemical variation through the layer. Therefore the contrast observed in the backscattered images can only be as a result of a variation in the structure of the coating. However, no transmission sections of these regions could be obtained due to the close proximity of the surface.

It may, however, be as a result of some crystallisation of the coating during deposition, although with no microscopical evidence this is mostly conjecture. If this is indeed the case, it shows the versatility of this method not only for observing compositional changes, but for structural changes. However, it does pose intrinsic problems with interpretation of observed features.

Figure 7.4 Microstructure of CVD SiC coating deposited at 1100°C

a) Backscattered electron micrograph with typical EDX analysis

b) Transmission electron micrograph (bright and dark field).

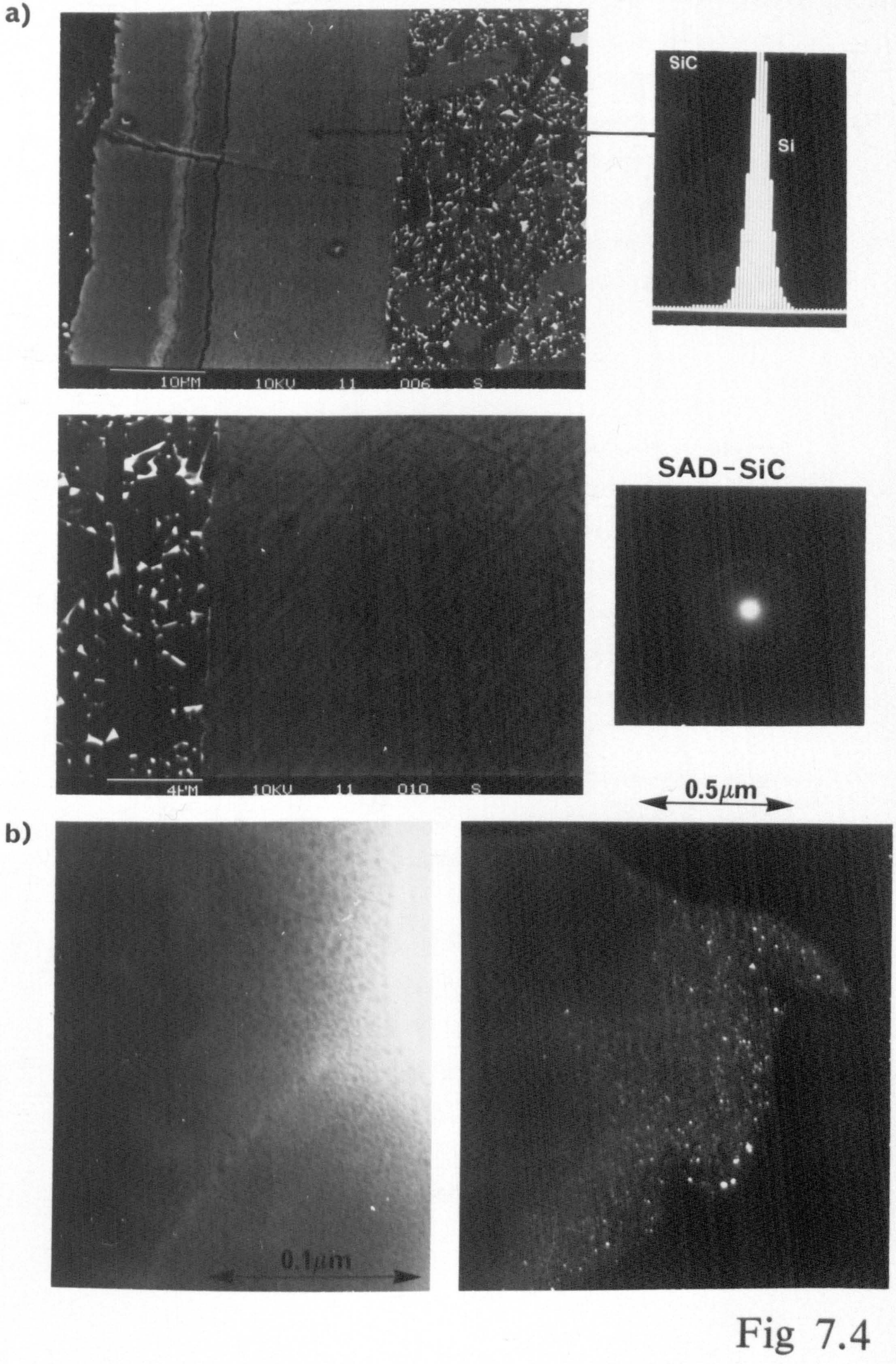

Fig 7.4

The substrate microstructure remained essentially unchanged as a result of the coating procedure, even at the interface. This is to be expected as the deposition temperature in this case is 1100°C. At these temperatures it has been shown that the fully crystallised β'/YAG material is stable (Chapter 5). Therefore, with almost no atom motion, even for glassy residues at this temperature, no diffusion across the interface is now possible such as observed in the coating with Si_3N_4 in the previous section.

7.3.3 Crystallisation of the CVD-SiC coating

The temperatures in which these SiC coatings would be expected to operate is in the region of 1300°C to 1400°C. The coating as-deposited in the amorphous state would be expected to be metastable with respect to crystallisation at these temperatures. As a consequence, the coated ceramic was subjected to thermal treatments in this temperature range to assess the microstructural development. Treatments were conducted in inert (N_2) atmospheres at 1300°C and 1400°C for 100 hours respectively.

Figure 7.5 shows the development of the CVD layer as a result of the thermal treatments. Backscattered imaging shows a layer of brighter contrast on the extreme outer edge of the coating, though no compositional differences where found. Analysis reveal highly oriented growth in the surface region compared with the underlying coating material. The thermal treatment causes surface nucleation of the 3C cubic silicon carbide polytype (ASTM No. 29-1128) which grows into the coating in a columnar style with similar morphology to that observed in the case of the silicon nitride coating. Often it was the case that this region was found to be detached from the underlying coating. This is caused by the impingement of the surface nucleated oriented SiC crystal and heterogeneously nucleated SiC within the

Figure 7.5 Microstructure of CVD SiC coating after heat-treatment at 1400°C.

a) Backscattered electron micrograph

b) to d) Transmission electron micrographs. Selected area diffraction patterns show coarsening of the SiC coating with heat-treatment.

(a)

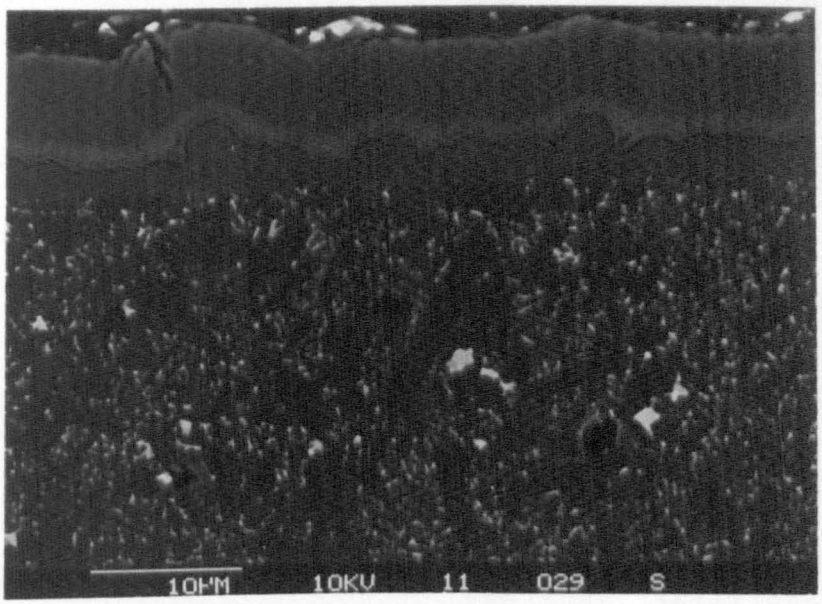

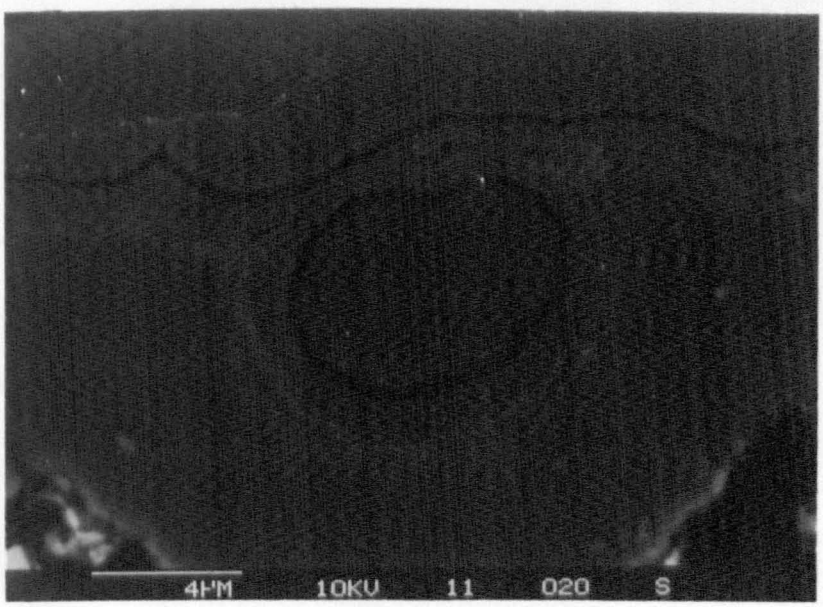

Fig 7.5

(b)

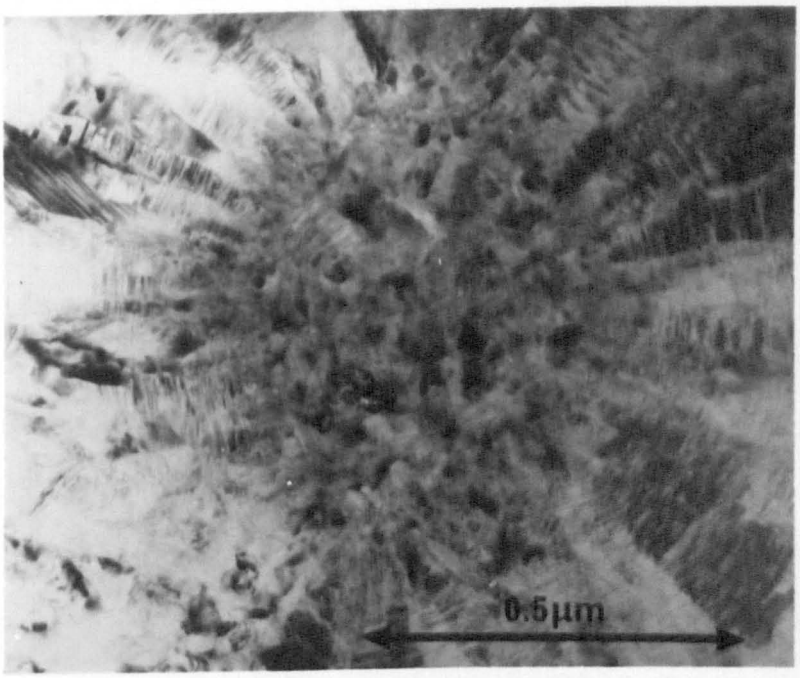

(c)

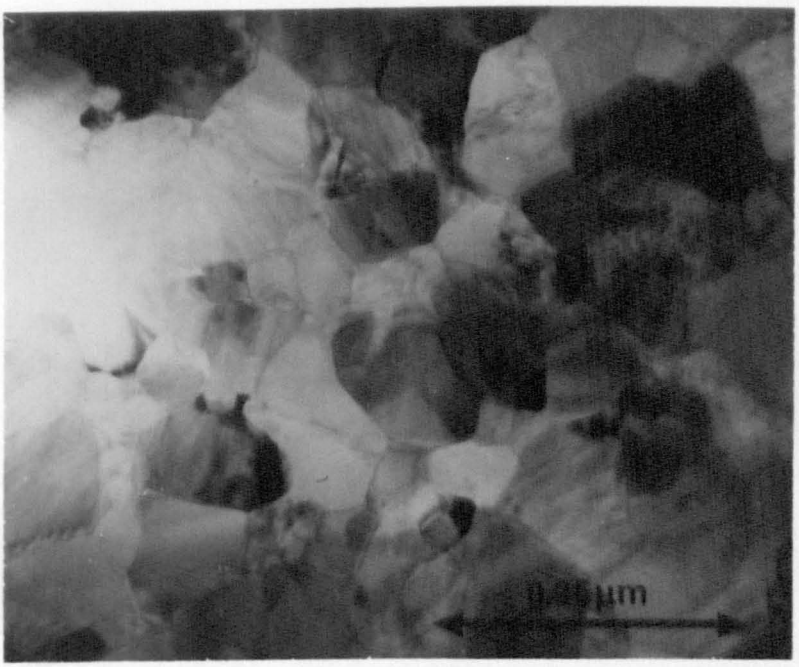

(d)

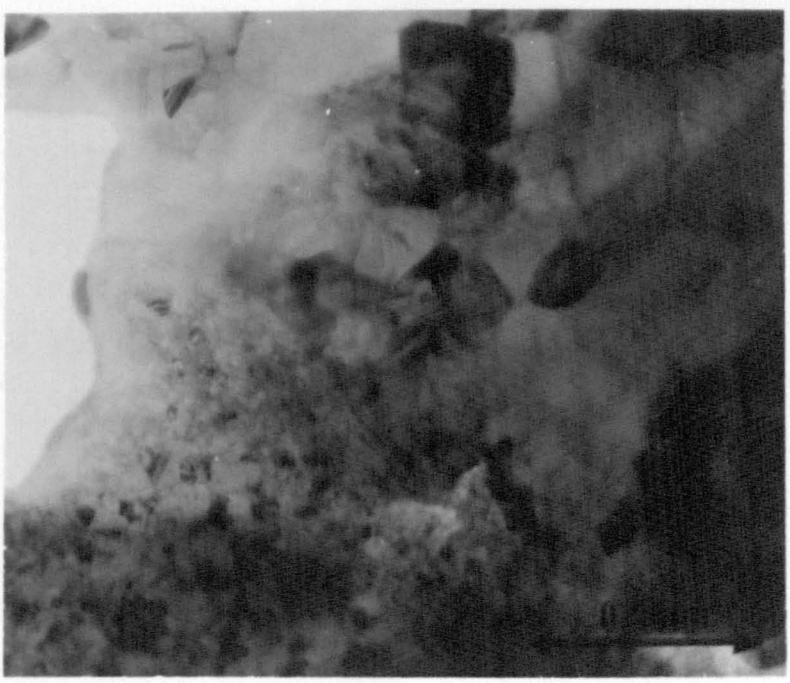

SAD - SiC

Fig 7.5

underlying coating and may be due to either thermal expansion mismatch between the two, or as a result of impurity segregation due to the columnar growth. Poor adhesion of these causes separation on cooling from the temperatures at which the thermal treatments were undertaken. As this extreme layer has become detached it does not provide an effective diffusion barrier this part of the layer will not be analysed in any further detail. The surface crystallisation effect is caused by a thermal treatment which was not optimised. Such optimisation may result in the application of traditional glass-ceramic nucleation/growth type of treatment which has been shown on a number of systems to control crystallisation such that the desired microstructure was attained.

Figure 7.5 shows the crystallised coating to be predominantly crystalline, the grain size generally being very small, <0.1 μm. Selected area diffraction indicates that grain size varies considerably from region to region. Regions of small grains show typical ring patterns indicating the growth of small randomly orientated SiC crystals. Analysis indicates the phase is the 3C cubic polytype SiC.

Crystal development in the layer at both temperatures was found to be essentially the same. Crystallisation is predominantly caused by spherical growth about a central nucleus of small randomly oriented SiC crystals. The average diameter of these is 1-2 μm, comprising of a central nucleus of a large number of small cubic 3C-SiC crystals, the area approximately 0.5 μm in diameter with larger (1-2μm) crystals growing radially from the central nucleus. In the regions between these spheralites random cubic SiC crystallisation has taken place independent of the spherical growth. This may be due to coarsening of the microcrystalline as-coated structure.

The controlled crytallisation of the CVD coating is necessary to maximise the protection afforded. Deposition of crystalline coatings often results in oriented columnar growth, and amorphous coatings require subsequent heat-treatment to optimise the structure. The working environment of these coatings will naturally cause crystallistion but optimisation would require specific heat treatments.

7.4 High temperature oxidation of CVD coated LCS 201

In this section the oxidation behaviour of both Si_3N_4 and SiC coated LCS 201 will be discussed relative to the behaviour observed in Chapter 5. Conclusions to the effectiveness of these coatings as diffusion barriers will be drawn.

7.4.1 Oxidation of Si_3N_4 CVD coatings

The oxide layer development of silicon nitride coated LCS 201 was observed in the temperature range 1100°C to 1400°C for time periods up to 150 hours.

At temperatures of 1100°C and 1200°C, oxide layer development was slow, with only a thin amorphous silicate layer forming, barely detectable in SEM cross-section. Oxidation at these temperatures cause no other observable microstructural changes in both the coating, interface and substrate microstructure. This was expected for two reasons. Firstly, it has been shown (81,86) that pure Si_3N_4, such as CVD-Si_3N_4 or reaction-bonded Si_3N_4 (RBSN), that the oxidation kinetics are very low at these temperatures, mainly due to the lack of grain boundary phase derived either from additive or impurity. Secondly, the LCS 201 material has been shown in Chapter 5 to exhibit good oxidation resistance at temperatures below 1300°C, due to the stability of the YAG matrix at these temperatures. Therefore, the

coating of the material would not be expected to provide any benefit.

Oxidation kinetics were determined at 1300°C, 1350°C and 1400°C and are plotted in figure 7.6. At 1300°C and 1350°C the addition of the CVD coating dramatically decreases the oxidation rate compared with the uncoated ceramic. At these temperatures a uniform silicate oxide layer forms on the surface as a result of direct reaction between the atmosphere and the Si_3N_4 coating ie

$$Si_3N_4 + 3O_2 \rightarrow 3SiO_2 + 2N_2 \qquad (7.3)$$

The Si_3N_4 coating was relatively unaffected, the effects of oxidation being confined to the exposed surfaces. Some YAG reversion as a result of oxygen diffusion through the layer was observed in the substrate near the interface. This was associated with some cation diffusion into the CVD layer, but compared with reversion effects observed in the uncoated ceramic, these were minor.

At 1400°C, the oxidation kinetics were found to increase dramatically, associated with an increase in YAG reversion and outdiffusion of cations into the oxide layer. The oxide layer therefore has departed from the purely glassy morphology to one more typical of the uncoated ceramic, with extensive crystallisation of α-cristobalite and yttrium disilicate. Differential thermal expansion coefficients ($3x10^{-6}$ K^{-1} for Si_3N_4 compared with $0.5x10^{-6}K^{-1}$ for SiO_2) had caused significant spalling of the oxide layer from the CVD coating.

Although the CVD coating remained intact after oxidation, substantial silicon oxynitride formation was observed throughout the layer. It appears to have formed in the cracks and grain boundaries of the coating, the result of a reaction between the Si_3N_4 layer and the silicate oxide layer. O' growth however was not observed in the substrate where a much larger volume of intergranular phase was present.

Figure 7.6 Oxidation kinetics of CVD Si_3N_4 coated LCS 201 as determined by oxide layer thickness measurements.

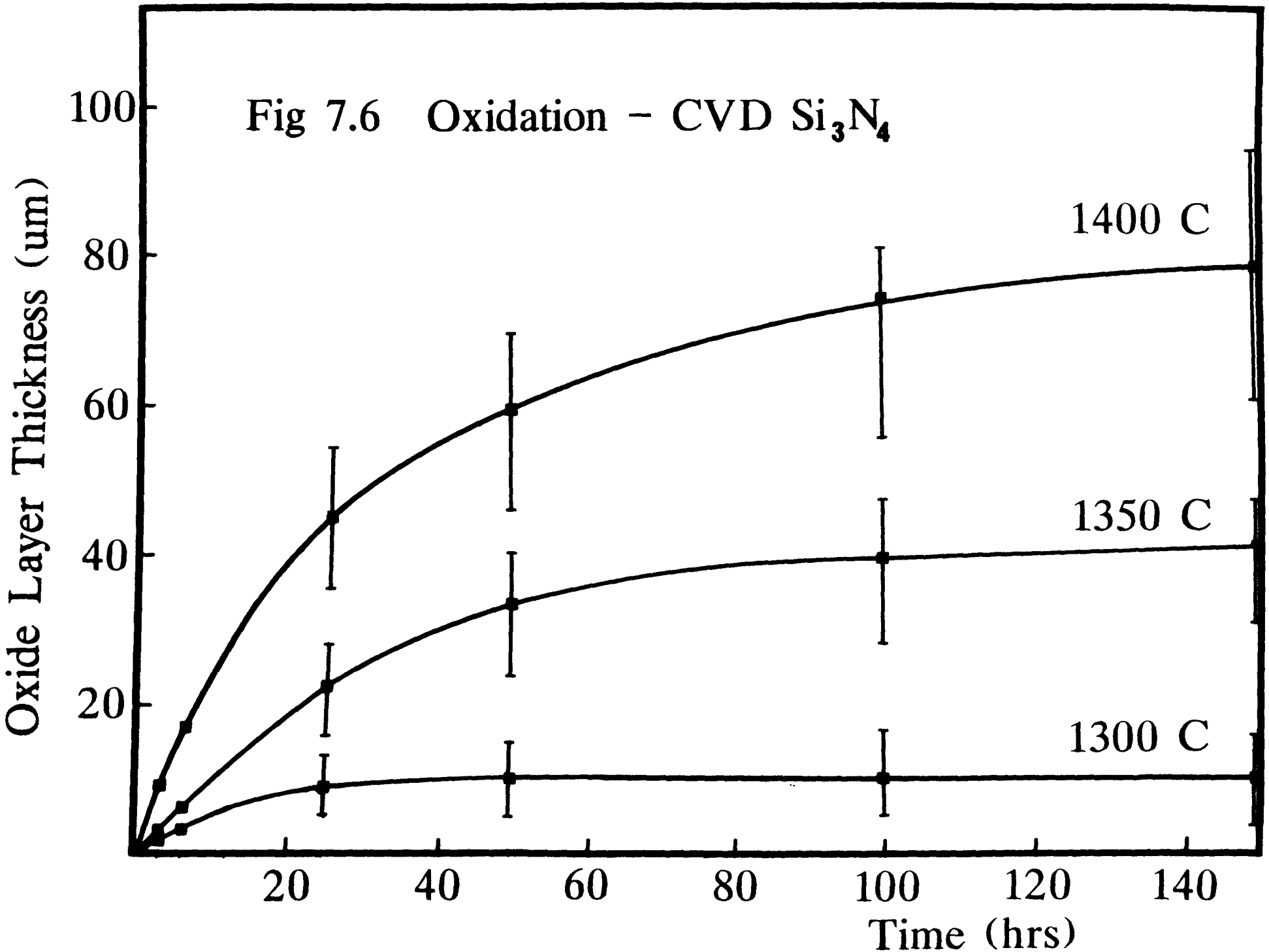
Fig 7.6 Oxidation – CVD Si_3N_4
Oxide Layer Thickness (um)
100
80
60
40
20
1400 C
1350 C
1300 C
20
40
60
80
100
120
140
Time (hrs)

Figure 7.7 Oxide layer development with time

a) 1300°C

b) 1350°C

c) 1400°C

Fig 7.7

(a)

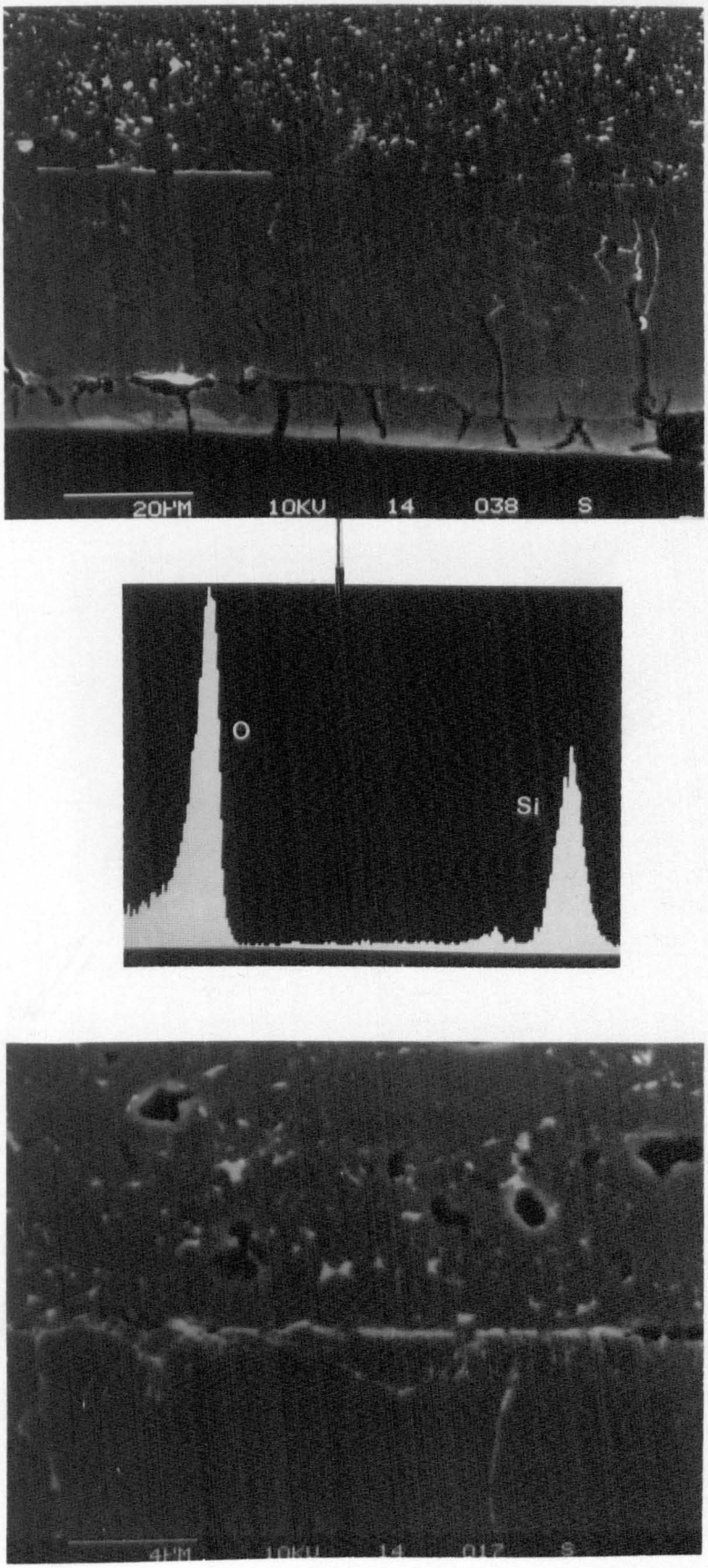

Fig 7.7

(b)

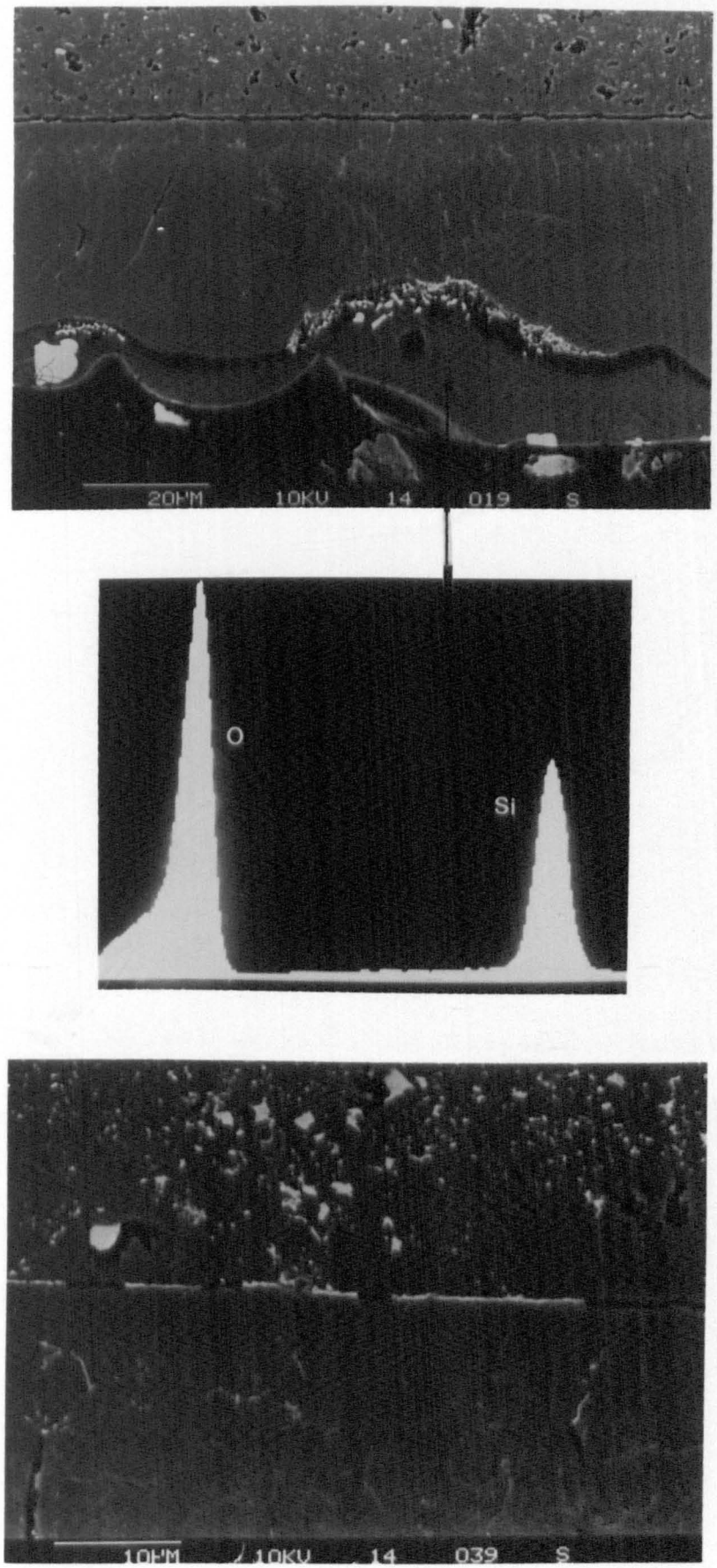

Fig 7.7

(c)

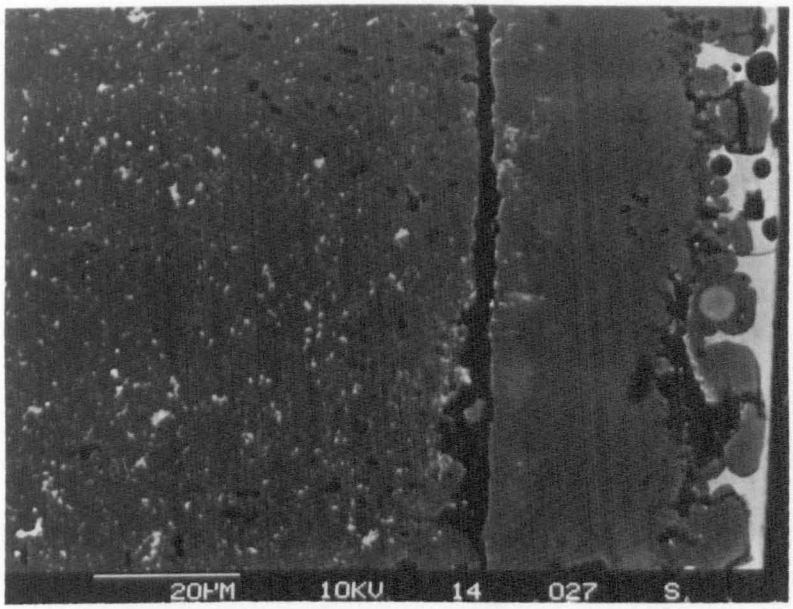

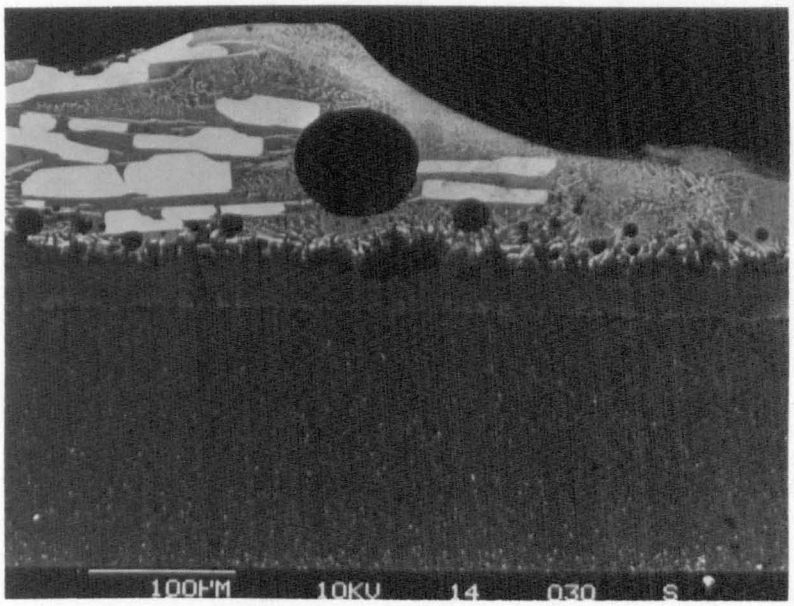

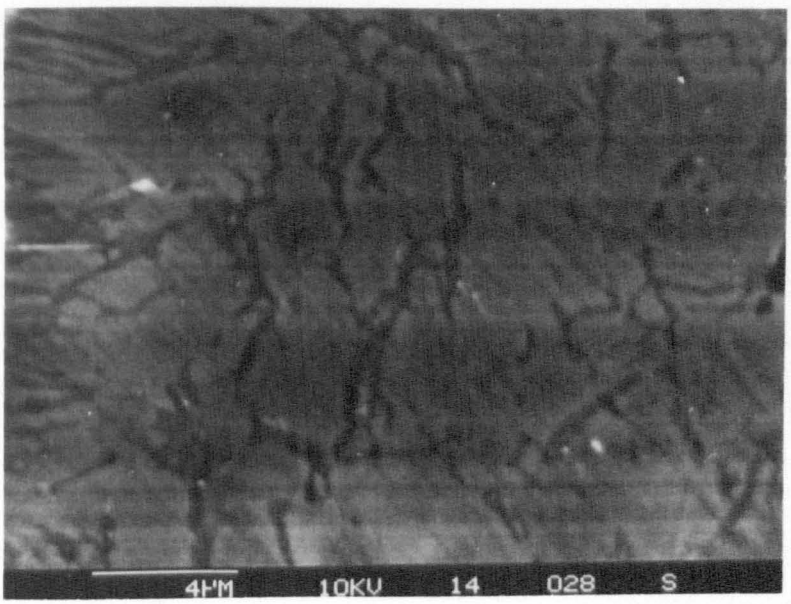

The formation of the silicon oxynitride does not, however, increase the oxidation resistant. It has already been shown that above 1375°C, β'/O' layers do not offer adequate protection against oxidation.

Overall, the application of the silicon nitride CVD layer resulted in a diffusion barrier between the oxide layer and the YAG phase. This resulted in significantly less YAG reversion and hence cation outdiffusion. The viscosity modifying effects of the cations result in an increase in oxygen diffusion through the oxide layer and hence determine oxidation kinetics. This method has proved effective up to 1350°C, but beyond that reversion effects again become significant, and catastrophic oxidation ensues in spite of the presence of the CVD layer.

7.4.2 Oxidation of SiC CVD coatings

The oxide layer development for silicon carbide CVD coated LCS 201 was determined at temperatures between 1100°C and 1350°C for time periods up to 150 hours.

The oxide layer development at temperatures below 1300°C was similar to that observed for the Si_3N_4 CVD coated material. Only a thin amorphous silica layer formed even after prolonged oxidation, barely detectable in SEM cross-section. The oxidation at these temperatures causes no observable changes in both the CVD layer and the substrate microstructure. This is expected as silicon carbide has been shown to exhibit good oxidation resistance at these temperatures, comparable to silicon nitride.

As with the previous case, oxidation kinetics were determined by measurement of the oxide layer versus time. Figure 7.8 shows oxide layer thickness development for the silicon carbide coated material at temperatures of 1300°C to 1350°C. As with all the previous cases, the

Figure 7.8 Oxidation kinetics of CVD SiC coated LCS 201 as determined by oxide layer thickness measurement.

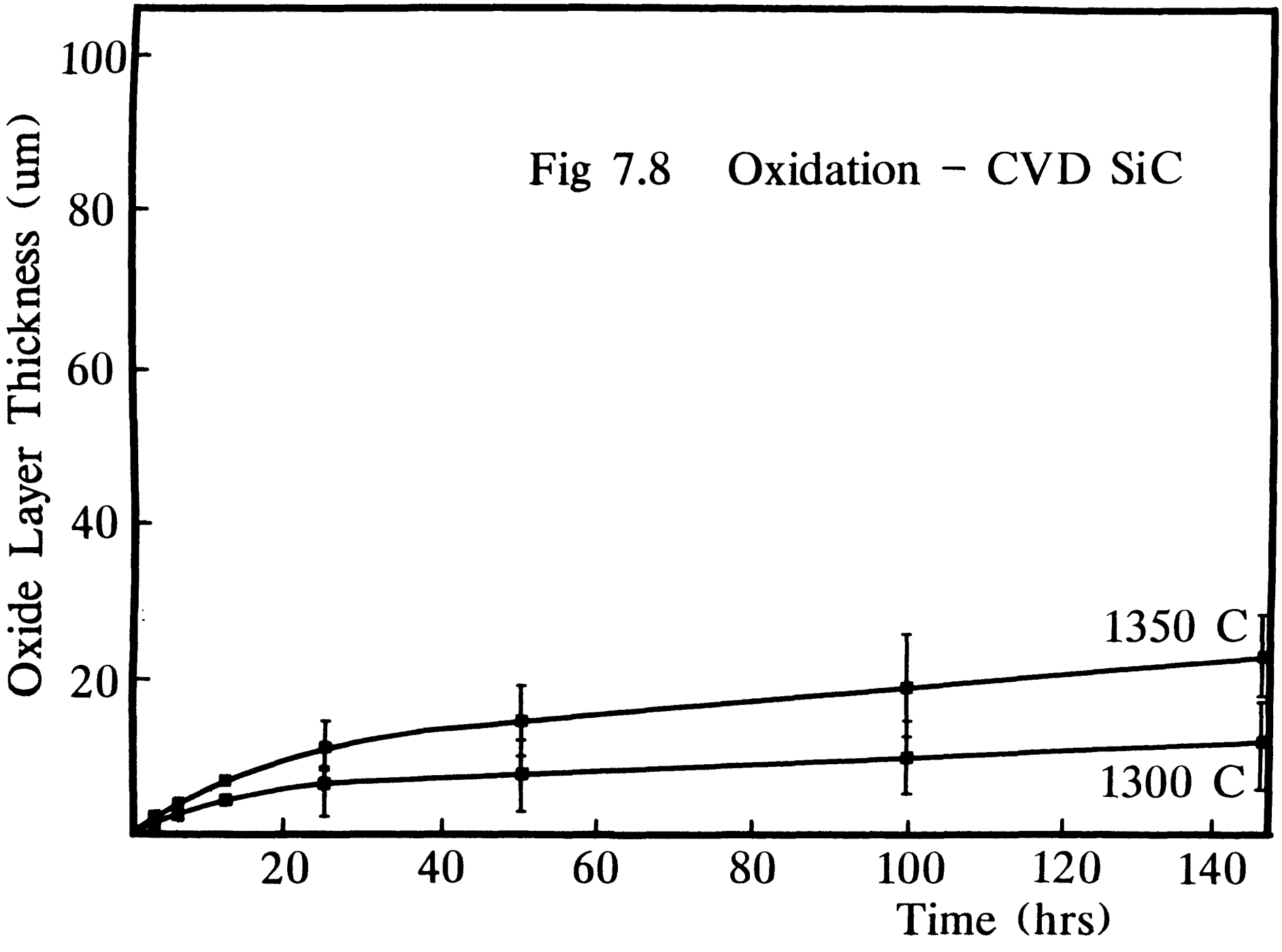
Fig 7.8 Oxidation - CVD SiC
Oxide Layer Thickness (um)
100
80
60
40
20
1350 C
1300 C
20
40
60
80
100
120
140
Time (hrs)

oxidation kinetics are parabolic, similar to those observed for the silicon nitride coating. Indeed, at 1300°C oxide layer development is almost identical to those observed for the silicon nitride coating, being only 10μm in thickness after 150 hours. Imaging of the oxide layer is shown in figure 7.9. The oxide layer is seen to wet the CVD layer being mainly amorphous SiO_2. This is derived from the direct reaction between oxygen and the CVD layer via the reaction:

$$SiC(s) + 2O_2(g) \rightarrow SiO_2 + CO_2. \qquad (7.5)$$

At 1300°C, little degradation of the CVD coating and substrate is observed. No evidence of any YAG reversion and subsequent diffusion through the CVD layer to the oxide layer was observed.

At 1350°C, oxidation kinetics remain parabolic but increased. Imaging the cross-section indicates that the oxide layer remains glassy and wets the surface of the coating well. EDX analysis shows that the oxide layer remains essentially silica, with little evidence of large amounts of yttrium out-diffusion. No YAG reversion was observed on a large scale in the substrate, the original β'/YAG microstructure being retained beyond 5μm from the interface. The only evidence of macroscopic diffusion from the substrate to the oxide layer was in the coating near the interface where some yttrium was found to have diffused. This is derived from diffusion from the near interface region of the substrate into the coating.

7.4.3 Conclusion

The application of the CVD coating to the ceramic, both silicon nitride and silicon carbide has been shown to dramatically increase the oxidation resistance by providing a diffusion barrier at temperatures above 1300°C by providing an effective barrier against the mechanism by which the oxidation process is rapidly accelerate ie. that of glass reversion via reaction between SiO_2 and the YAG matrix

Figure 7.9 Oxide layer development with time

a) 1300°C

(i) 3 hours

(ii) 100 hours

b) 1350°C

(i) 3 hours

(ii) 50 hours

(iii) 100 hours

Fig 7.9(a)

(i)

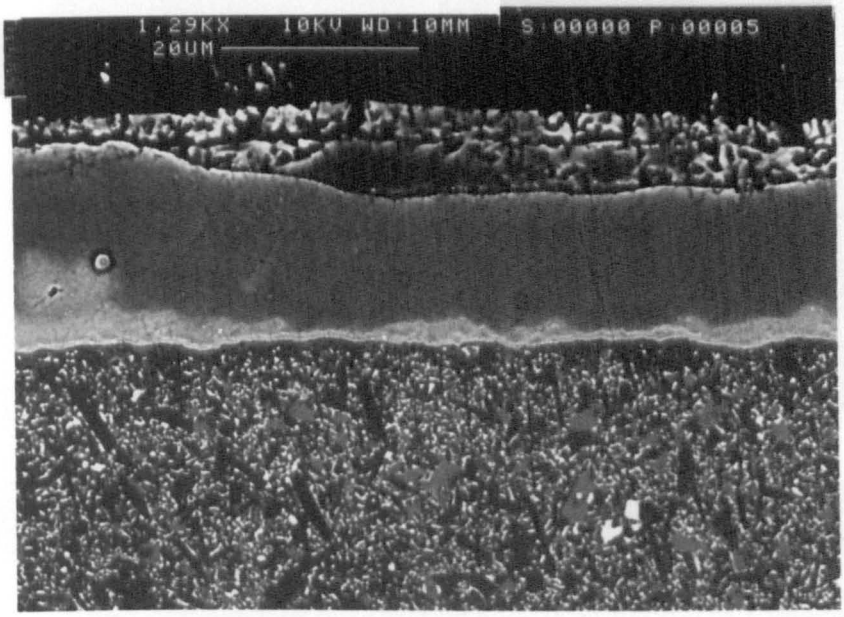

(ii)

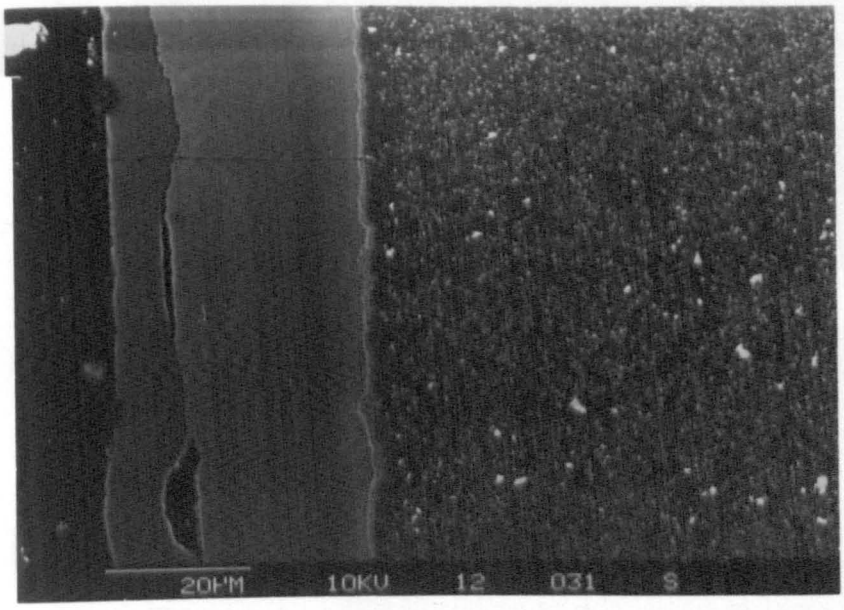

Fig 7.9(b)

(i)

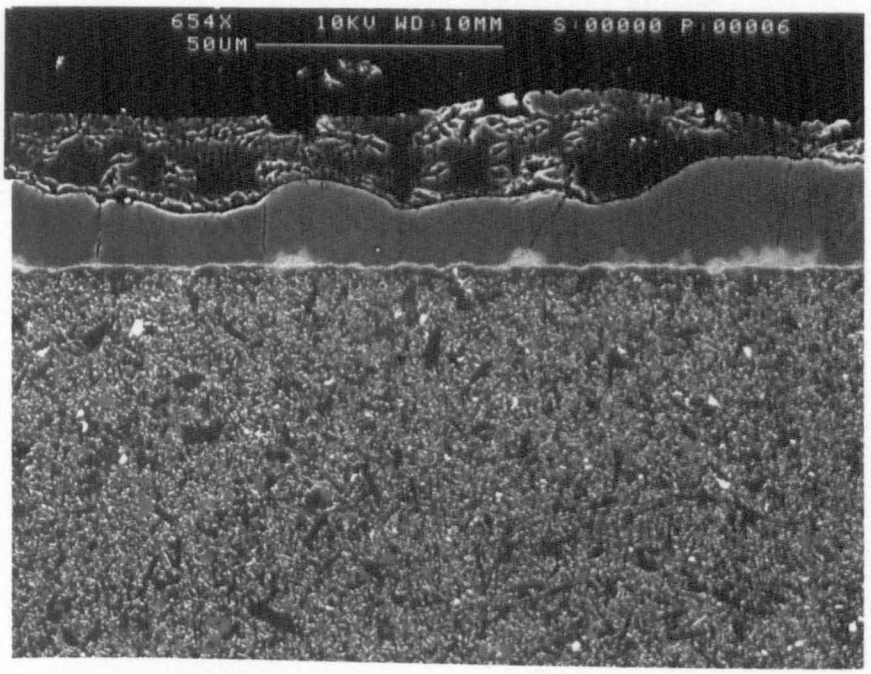

(ii)

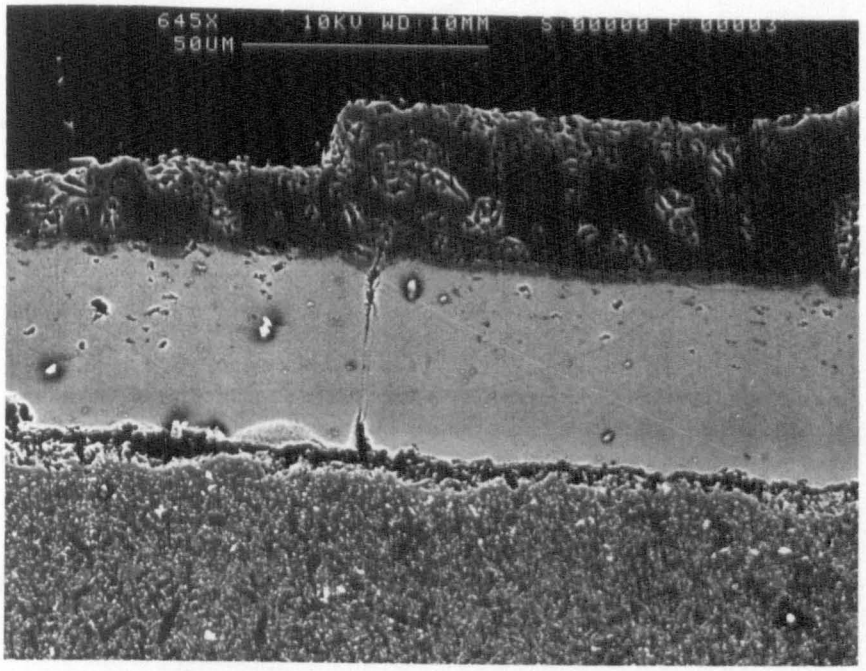

(iii)

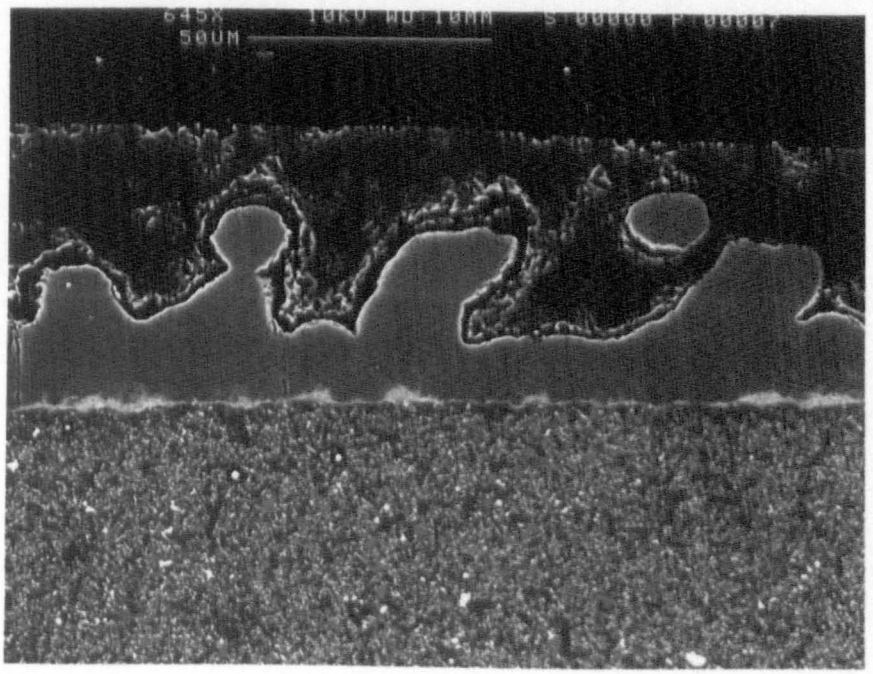

phase. Reduction of this reaction eliminates the degrading effects of oxidation seen in Chapter 5, that of surface degradation and increased porosity.

Oxidation of these materials after coating is dominated by the properties of the coating, and this is reflected in the measured oxidation kinetics. The generally superior oxidation resistance exhibited by silicon carbide ceramics is carried through the coatings up to a limit where diffusion through the CVD becomes significant enough to once again introduce intergranular phase into the overall reaction. It is this aspect which limits the use of coatings at high temperatures, ie to 1350°C.

7.5 Degradation of CVD coated ceramics in corrosive environments

7.5.1 Introduction

The degradation of a range of Syalon ceramics has been investigated by Reed (176) in corrosive atmospheres at 1200°C. Investigations showed that after exposure for 100 hours, specimens had formed a significantly thicker reaction layer compared with the case of static oxidation. The cause of the dramatic increase in kinetics was found to be due to the effects that the injected ions have on the viscosity of the silica layer derived from the oxidation of the β' grains. The presence of the sodium ions not only significantly reduced the viscosity of the oxide layer, but was found to drastically increase the dissolution rate of the β' grains. Thus for exposure in corrosive environments, the addition of another modifying cation increases the diffusion rate through the oxide layer. This causes serious material loss problems in the near surface regions, resulting in the formation of large flaws leading to serious loss in mechanical strength. Figure 7.10 shows the degrading effects that brine

injection has on the surface microstructure. The associate strength reduction is shown in figure 7.10 illustrating the generation of critical flaws as a direct result of corrosion.

A possible solution to the degrading effects is to use CVD layers to reduce modified oxide layer/matrix reactions.

7.5.2 Experimental

Corrosion studies were performed using a kerosene burner test-rig situated at Rolls-Royce plc, Leavesden. The conditions used were the same as those used by C.J. Reed in investigation into the hot corrosion of mono- and bi-phase ceramics eg. LCS201. The injection of brine was maintained at 10ml/hour for 100 hours of testing at a temperature of 1200°C.

The ceramic test pieces were in the form of Si_3N_4-CVD coated 3mm x 3mm x 50mm bars mounted on a rotating carousel situated in the burner rig hot zone. Comparative analysis using SEM/EDX was subsequently performed.

7.5.3 Corrosion of Si_3N_4 CVD coatings

The effects of hot corrosion at 1200°C for 100 hours are shown in figure 7.11. The formation of a thin oxide layer on the surface of the CVD coating is clearly evident. The coating uniformly wets the surface, the cracking through the layer being due to cooling effects. Little solution of sodium ions within the layer although this was the major impurity ion, but some measurable amounts of magnesium ions were detectable. A minor crystalline phase was detected, showing as slightly brighter contrast at the extreme surface of the oxide film.

Little evidence was also found of nitrogen gas evolution causing spalling of the oxide layer, revealing new surfaces available

Figure 7.10 Effect of brine injection on the oxidation behaviour at 1200°C.

Figure 7.11 Oxide layer development for CVD Si_3N_4 coated LCS 201 at 1200°C with brine injection. EDX analysis shows typical oxide layer composition.

Fig 7.10

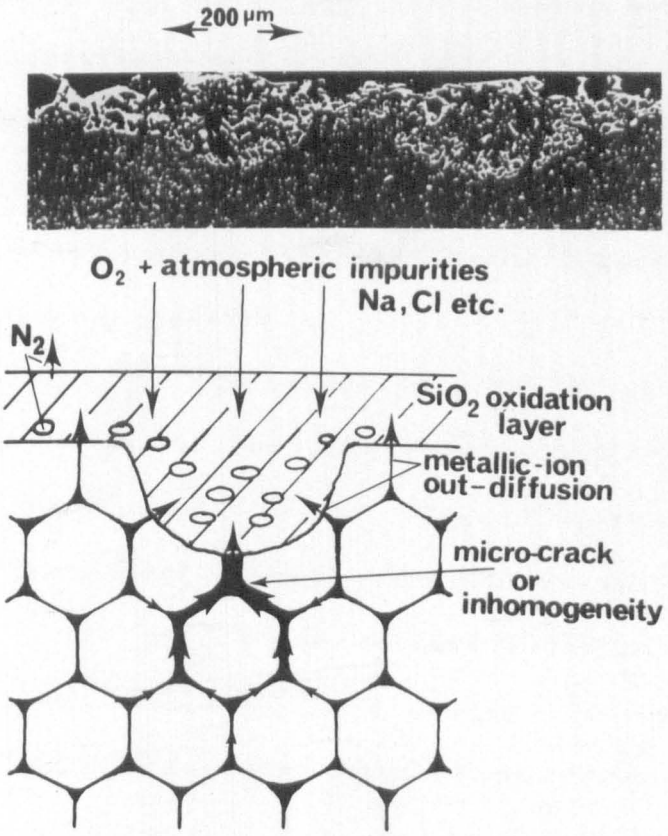

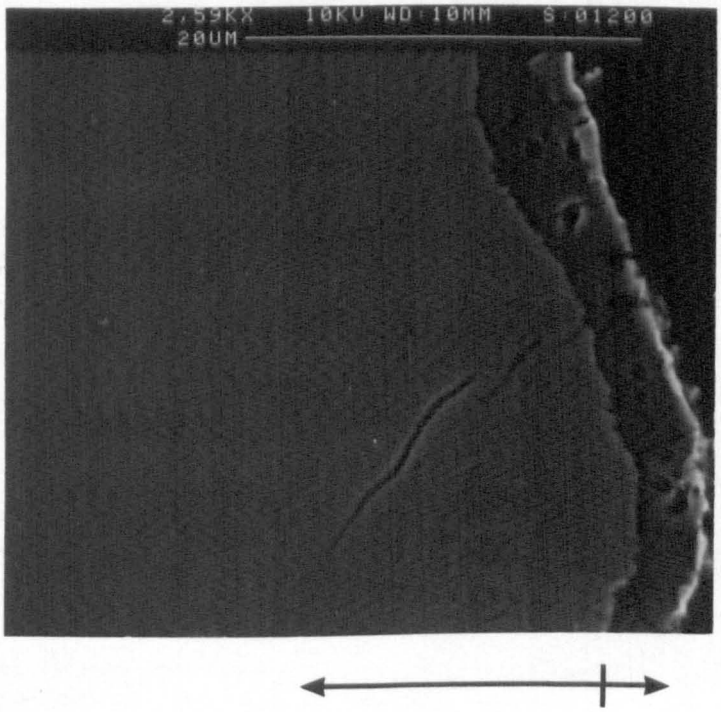

Fig 7.11

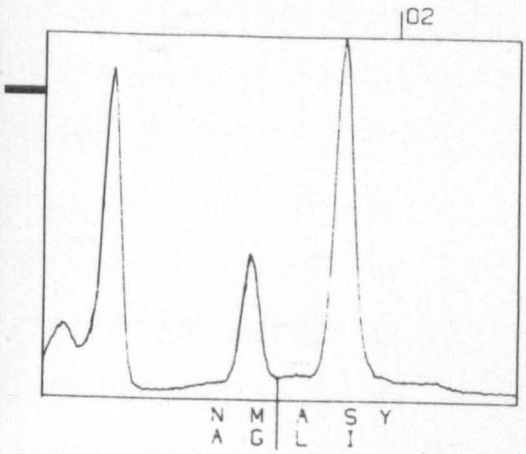

CVD Si_3N_4 Oxide Layer

for oxidation. Some minor regions of porosity within the oxide layer were observed, although this was minor when compared with that observed in the corrosion studies by C.J. Reed.

The coating and substrate exhibited negligible degradation as a result of impurity in-diffusion. In fact, as with static oxidation of the coated ceramics at temperatures below 1300°C, no degradation of both coating or substrate was observed.

The slight increase in the oxidation kinetics at 1200°C resulting from the action of the impurities derived from the brine injection modifying the viscosity of the layer is expected when comparing with the effects found by Reed. However, the accelerated critical flaw growth by the formation by macro hemispherical flaws observed in the LCS 201 was eliminated by the coating. The mechanism by which these are formed, oxidation/dissolution of both the major and matrix phases possibly preferentially at sites high in concentrations of impurity levels catalysed by the presence of sodium (Na^+) ions is inhibited by the coating. This leads to the conclusion that the dramatic loss in strength observed in 3 point bend MOR testing will be significantly reduced if not unobserved at all as a consequence of the CVD coating. The success of the coating is totally dependent on the integrity, ie, a dense coating is essential as the reaction is activated via a gaseous route, therefore inhibition of this is essential to provide adequate corrosion protection.

The degradation in properties observed by Reed when compared with static oxidation is reduced by the formation of a dense CVD layer. The major role of this layer is to primarily inhibit the reaction between the corrosive atmosphere and the YAG matrix. It is therefore thought that it will reduce the degrading effects observed as a direct result of atmospheric corrosion, providing a significant increase in temperature limit for the ceramic in real gas turbine environments.

7.6 High temperature deformation of CVD coated LCS 201

The base creep rate observed for the ceramic remained unaltered as the total volume was small compared with the volume of the substrate.

Isothermal creep rupture tests at 1350°C for the CVD-Si_3N_4 coated LCS 201 ceramic are shown in figure 7.12 for a temperature of 1350°C. At high stresses, ~600MPa, failure occurred either instantaneously or within 3 minutes of loading. At lower stresses ~450 MPa, no failure was observed, the run was terminated after 1200 hours at 1350°C. This contrasts significantly with the creep-rupture behaviour of the uncoated ceramic shown in Chapter 6, where clear time dependent failure was observed.

Imaging of the crept specimen showed little difference to the structure observed after creep at 1350°C to that of specimens subjected to static oxidation at the same temperature. There was no evidence for the large scale YAG reversion reaction within the substrate due to oxidation, presumed to be the factor responsible for the time dependent behaviour observed in the uncoated ceramic.

The oxide layer was found to remain glassy and predominantly silica even after severe deformation at 1350°C, being less than 50 μm on average. In addition, the CVD layer was also intact after severe deformation, showing that the coating adhesion does not degrade with time. At higher temperatures, degradation of the coating becomes more severe, as seen in the case of static oxidation. At 1400°C, some degradation of the coating occurs, though no more severe then that seen in the case of static oxidation, indicating that stress plays a minor role in the oxidation behaviour of these materials. At 1500°C, oxidation rates are catastrophic, with the coating offering little protection even at moderate stress levels. It must be noted that at this temperature creep rates were so high $\dot{\varepsilon} \sim 10^{-3}\ s^{-1}$, that the CVD layer may have formed extensive cracks in the early stages allowing

Figure 7.12 Creep rupture behaviour of CVD Si_3N_4 coated LCS 201 at 1350°C.

Fig 7.12

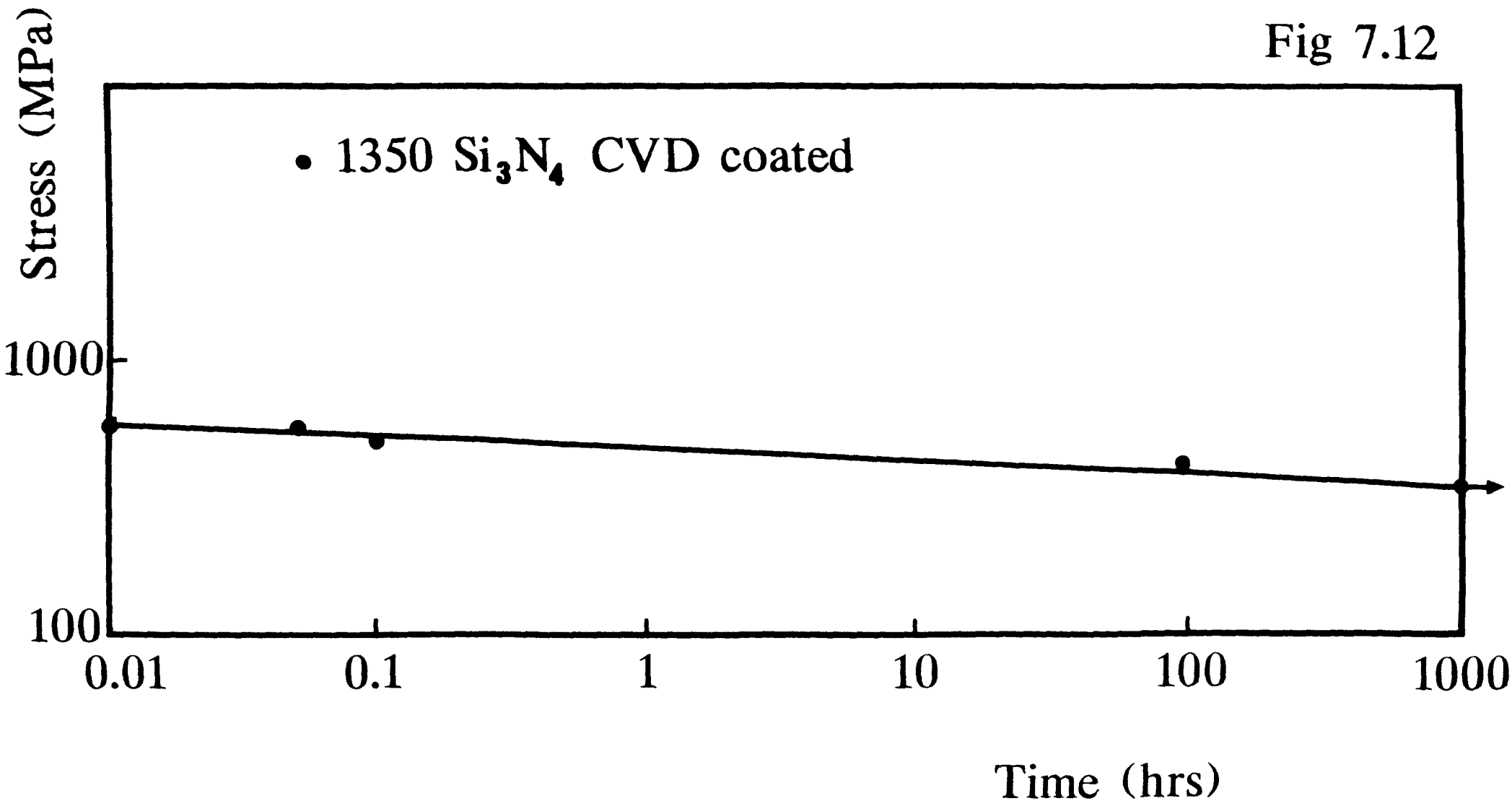
Stress (MPa)
• 1350 Si_3N_4 CVD coated
1000
100
0.01
0.1
1
10
100
1000
Time (hrs)

access of oxygen to the substrate, leading to catastrophic oxidation and spalling of the CVD layer being the result.

The application of the CVD coating has been shown to protect the LCS 201 ceramic against its primary weakness, that of the oxidation problem above 1300°C. The base creep rate of the material has been shown to be intrinsically good even at temperatures above 1300°C, showing non-cavitating behaviour with the rate controlling mechanism being that grain boundary sliding accommodated by grain boundary diffusion. Above 1300°C, the stress-rupture testing showed clear time dependent behaviour, being directly attributed to crack extension under stress as a result of the environmental effects as discussed in Chapter 6. The use of a coating as a simple diffusion barrier allows the possibility of using ceramics with optimised matrices which allow the highest strength and creep properties, with a coating acting as a diffusion barrier protecting against environmental effects which may cause degradation.

Tailoring of the chemical vapour deposition process can produce coatings which optimise the microstructure, the oriented large crystal growth with large residual stresses not being optimised in any form, which may be resisted at even higher temperatures. Process control may also allow the deposition of coating with high surface finish quality.

7.7 Conclusion

The use of chemical vapour deposited coatings as an alternative to the earlier discussed surface transformations offers several advantages, namely those relating to control of structure and thickness. The ability to deposit various types of coating both

different chemically eg. SiC, Si_3N_4, and structurally, eg. amorphous, crystalline allows greater flexibility than the surface transformation route does, including the benefit that little degradation to the subsurface occurs which may be the problem with transformation processes. Further work is required in optimising the coating conditions to further enhance the effectiveness as a diffusion barrier for both materials.

CHAPTER 8 - OVERVIEW AND FUTURE WORK

This chapter will draw together the main conclusions of the work presented in this thesis. A summary of the effects that the continued development of the syalon ceramics on microstructure, crystallisation and high temperature mechanical properties will be made. Finally, suggestions regarding future ceramic developments will be made.

8.1 Overview

The broad objectives of this thesis was towards a greater understanding of the effect that improved processing has on the structure, and in particular the high temperature properties of a syalon ceramic currently under development by Lucas-Cookson-Syalon. This has involved the reduction of impurity levels by the use of high purity starting powders, particularly α-Si_3N_4, the use of "balanced" compositions to control and improve the crystallisation of the intergranular residual glass phase, and the use of optimised nucleation/growth post-sintering heat-treatments to control and optimise the kinetics of crystallisation. The removal of residual glass by these methods was generally seen to be essential to attain the required mechanical and thermal properties demanded by many proposed applications for these types of materials.

The thesis investigates the effects that the improved processing has on the microstructure, and how this influences the oxidation kinetics and mechanical properties (short term fracture and long term creep/creep rupture). A high temperature limit of the material was observed, and a significant proportion of the thesis is dedicated to an investigation of methods to extend this limit by the use of induced surface transformations and coatings and their effect on the high temperature properties.

The major conclusions drawn from this thesis are;

(a) A fully crystallised sialon ceramic with a YAG matrix has been produced. This has been achieved by improvements in the purity of the starting powders, particularly the silicon nitride. Some impurities, such as calcium or fluorine have been shown to segregate upon crystallisation of the intergranular glass phase, concentrating at the triple junctions between grains. The high concentration of impurity ions in these regions inhibit further crystallisation, forming pockets of stable glass, which at elevated temperatures are the sources of mechanical degradation.

In addition full crystallisation of the intergranular glass phase has been achieved by the use of "balanced" compositions. This may be achieved by tailoring the glass composition to lie on the tie line between two crystalline species. Fully crystalline YAG was produced by increasing the nitrogen level by the addition of AlN polytypoid. The increased nitrogen levels were established directly by EELS and windowless EDX techniques, and indirectly by the observation of the α' phase and N-α-Wollastonite at high polytypoid (nitrogen) levels.

The importance of nitrogen was illustrated by the crystallisation behaviour of materials based upon the LCS 201 composition but with the nitrogen level varied by the addition of different amounts of AlN polytypoid. This resulted in incomplete crystallistaion at low polytypoid levels, as a result of the composition moving away from the YAG-Si_2N_2O tie line. This has been supported by other studies on the crystallisation behaviour of Y-Si-Al-O-N bulk glasses. Variability in the O/N ratio showed that full crystallisation to YAG + Si_2N_2O was only attained at high nitrogen levels.

Further, the increased nitrogen content of the glass raises the glass transition temperature, which increases the temperature at which the onset of sub-critical crack growth was observed (1300°C for LCS 201 compared with 1150°C for low nitrogen containing sialon ceramics).

(b) In oxidising environments above 1000°C, the low ion mobilities as a result of grain boundary crystallisation to YAG reduced oxidation kinetics to levels similar to monophase sialons. This behaviour was retained up to 1300°C. However, above this temperature the YAG matrix was found to react with the oxide layer forming a near eutectic liquid. This was found to subsequently increase the oxidation kinetics, catastrophically at temperatures of 1350°C and above. Studies of the sub-oxide layer silicon oxynitride (O') was identified in the matrix, the result of reaction between the β'grains and the yttrium depleted intergranular glass.

(c) Oxidation studies were performed to determine the effectiveness of the β'/O' layer as a mode of surface protection. Oxidation kinetics at temperatures above 1300°C were found to be significantly reduced, with suppression of the YAG reversion up to a temperature of 1375°C. This protection was successfully demonstrated during high temperature creep up to 1375°C where microstructural stability of the bulk material was maintained by the presence of the β'/O' layer.

(d) An optimal production route for the β'/O' layer was sought. These layers has been initially formed by long term annealling at moderate temperatures (1300°C). The thickness of β'/O' layer formed in the β'/YAG materials was determined by the initial thickness of the YAG reversion in the sub-oxide layer. In this family of materials β'/O' layers of only 10-15μm typically were observed even after extended heat-treatment. This was seen to be uneconomic for practical

purposes. It was determined that in most cases the microstructural disruption incurred by these alternative methods outweighed their ability to form the β'/O' layer. It is therefore concluded that coherent β'/O' layers may only be formed without severe surface and sub-surface degredation by long term low temperature annealling.

(e) High temperature mechanical properties of LCS 201 were found to mirror the effects of complete crystallisation of the intergranular phase. Stress exponents were found to be near unity indicating a grain boundary diffusion dominated mechanism. This was supported by structural analysis which showed no evidence of cavitational effects. The effects of crystallisation was also shown to affect properties in short term fracture, where sub-critical crack growth is eliminated by the crystallisation of YAG, up to temperatures in excess of 1400°C. The high temperature fracture is very sensitive to the presence of residual glass, manifesting itself as sub-critical crack growth. Therefore, elimination of this gives a clear indication of the effectiveness of the processing philosophy adopted in this material.

(f) The high temperature stress rupture lead to the identification of a unique sub-critical crack growth mechanism. The mechanism is based upon crack propagation as a result of oxidation induced YAG reversion. This was demonstrated to cause time dependent failure at temperatures above 1350°C where YAG reversion is catastrophic.

(g) As an alternative to surface transformation to β'/O' as a method of extending the operating limit of the material, CVD coatings were investigated. Application of both silicon nitride and silicon carbide coatings was found to increase oxidation resistance by introducing a diffusion barrier between the oxide layer and the bulk

material, hence stifling YAG reversion. The oxidation kinetics were found to revert to near that observed for the single phase ceramics. This protection offered also removed time dependent stress-rupture behaviour at temperatures of 1350°C and above by inhibiting the sub-critical crack growth mechanism responsible.

8.2 Future Work

The work presented in this thesis has shown that high temperature properties may be maintained by the use of "balanced" compositions producing fully crystalline materials. However, in this case where the intergranular phase was YAG, an instability was observed at 1300°C, precluding its use above that temperature without surface treatment (either transformation or coating). Work should be done to apply the philosophy successfully used to the LCS 201 ceramic to one in which a matrix phase may be produced which is environmentally stable to 1400°C, the target application temperature for these materials. This could possibly be simply using known stable phases in the Y_2O_3-SiO_2-Al_2O_3-YN-AlN-Si_3N_4 system such as $Y_2Si_2O_7$ which is known to be highly resistant to oxidation, or may mean development of a ceramic based upon a new system.

Secondly, although "balanced" compositions provided a material whose strength retention of temperature was good, the absolute values of strength and fracture toughness were found to be generally low. For practical applications in high stress regions these are generally unsuitable. A solution to part of this problem has been the use of toughening using dispersed phases. This route constitutes the next stage of ceramic development, and the knowledge and processes gained for monolithic have now to be applied successfully to the development of composite ceramics. Many of the rules governing fabrication and properties of composites are similar to monolithics but with problems

of their own, which will have to be addressed fully before these may be applied successfully.

Finally, the use of high resolution microscopical techniques now available should be utilised to investigate the nature of the different grain boundaries ie β'-β' and β'-YAG. This will enable a greater understanding of the role these play in processes such as high temperature deformation when grain boundary processes are dominant. This will enable some interpretation of the little understood meaning of the activation energy, Q.

References

1. D. Driver, Metals and Materials, 1 (1985) 345.
2. R.W. Davidge, A.G. Evans, Special Ceramics 5, ed. P. Popper, BCRA, 1972, pg 329.
3. G. Ziegler, Sci. Ceramics, 2 (1981) 503.
4. N.E. Cother, P. Hodgson, Trans. J. Br. Ceram. Soc., 81 (1982) 141.
5. M.T. Kelly, Adv. Ceram. Mat., 1 (1986) 132.
6. J.I. Mueller, Am. Ceram. Soc. Bull., 61 (1982) 588.
7. G.B. Kenney, H. Kent-Bowen, Am. Ceram. Soc. Bull., 62 (1983) 590.
8. H. Suzuki, Mat. Sci and Eng., 71 (1985) 211.
9. R.W. Davidge, Proc. World Congress on High Tech Ceramics, Elsevier, 1986 pg.
10. T.J. Whalen, Ceram. Eng. and Sci. Proc., 7 (1986) 1135.
11. D.C. Larsen, J.W. Adams, R. Ruh, Prog. in Nitrogen Ceramics, ed. F.L. Riley, 1985, pg 695.
12. S. Dutta, J. Mat. Sci., 19 (1984) 1307.
13. R. Moussa, J.L. Chermant, F. Osterstock, J. de Physique, 47 (1986) C1-679.
14. G. Grathwol, T.H. Reets, F. Thummler, Sci. of Ceramics, 11 (1981) 425.
15. C.H. Carter, R.F. Davis, J. Bentley, J. Am. Ceram. Soc., 67 (1984) 409.
16. K.D. McHenry, R.E. Tressler, J. Am. Ceram. Soc., 63 (1980) 152.
17. R. Moussa, F. Osterstock, J.L. Cermant, "Fracture Mechanics of Ceramics - Vol. 6, Eds. R.C. Bradt, A.G. Evans, D.P.H. Hasselman, F.F. Lange, Plenum Press, New York, 1983, pg 555.
18. A.G. Evans, A.H. Heuer, J. Am. Ceram. Soc., 63 (1980) 241.
19. R.C. Garvie, R.H. Hannink, R.T. Pascoe, Nature, 258 (1975) 703.
20. M.H. Lewis, Penn. State Paper.
21. N. Claussen, G. Petzow, J. de Physique, 47 (1986) C1-693.
22. R.W. Davidge, Composites, 18 (1987) 92.
23. K.H. Jack, Metals Technology, 9 (1982) 297.
24. P. Grievson, K.H. Jack, S. Wild, "Special Ceramics 4", ed. P. Popper, BCRA, 1968, pg 237.
25. K. Kasai, S. Nagata, T. ARakawa, T. Tsukidate, Toyo Soda Kenkyu Honoku, 29 (1985) 105.
26. A.E. Pasto, Comm. J. Am. Ceram. Soc., 67 (1984) C178.
27. C.E. Bouldin, E.A. Stern., M.S. Danley, T.G. Stoebe, J. Mat. Sci., 20 (1985) 1807.
28. K. Kijma, Proc. 1st Int. Symp. "Ceramic Components for Engines" ed. S. Somiya, K.T.K. Tokyo, 1983, pg 257.
29. M. Mori, H. Inoue, T. Ochiai, in "Progress in Nitrogen Ceramics", ed. F.L. Riley, Martinus, 1983, pg 149.
30. T. Yamada, Proc. 1st Int. Symp. "Ceramic Components for Engines" ed. S. Somiya, K.T.K. Tokyo, 1983, pg 333.
31. G.G. Deeley, J.M. Herbert, N.C. Moore, Powder Metallurgy, 8 (1961) 145.
32. G.R. Twerilliger, F.F. Lange, J. Am. Ceram. Soc., 57 (1974) 26.
33. M. Shimada, M. Koizumi, A. Tanaka, T. Yamada, Comm. J. Am. Ceram. Soc., 65 (1982) C48.
34. S. Prochazka, W.A. Rocco, High Temp-High Press, 10 (1978) 87.
35. C. Greskovich, H.H. Rosolowski, J. Am. Ceram. Soc., 59 (1976) 337.
36. J.T. Barnby, R.A. Taylor, Special Ceramics 5, ed P. Popper, BCRA, 1972, pg 311.

37. F. Porz, G. Grathwol, F. Thummler, Special Ceramics 7, ed P. Popper BCRA, 1981, pg 157.
38. P.B. Noakes, P.L. Pratt, Special Ceramics 5, ed. P. Popper, BCRA, 1971, pg 299.
39. A.J. Moulson, J. Mat. Sci., 14 (1979) 1017.
40. P. Drew, M.H. Lewis, J. Mat. Sci., 9 (1974) 261.
41. F.F. Lange, S.C. Singhal, R.C. Kuznicki, J. Am. Ceram. Soc., 60 (1977) 249.
42. D.R. Clarke, F.F. Lange, J. Am. Ceram. Soc., 63 (1980) 586.
43. R.E. Loehman, D.J. Rowcliffe, J. Am. Ceram. Soc., 63 (1980) 144.
44. M.H. Lewis, A.R. Bhatti, R.J. Lumby, B. North, J. Mat. Sci., 15 (1980) 438.
45. R.L. Tsai, R. Raj, J. Am. Ceram. Soc., 65 (1982) 270.
46. P.E.D. Morgan, F.F. Lange, D.R. Clarke, B.I. Davis, Comm. J. Amm. Ceram. Soc., 64 (1981) C77.
47. W.A. Sanders, T.P. Herbell, J. Am. Ceram. Soc., 66 (1983) 835.
48. J.P. Guha, P. Goursat, M. Billy, J. Am. Ceram. Soc. 63 (1980) 119.
49. L.J. Bowen, T.G. Carruthers, R.J. Brook, J. Am. Ceram. Soc., 61 (1978) 335.
50. W.A. Sanders, D.M. Mieskowski, Adv. Ceram. Mat., 1 (1986) 132.
51. W.D. Kingery, J. App. Physics, 30 (1959) 261.
52. P. Griel, J. Weiss, J. Mat. Sci., 17 (1982) 1571.
53. J.R.G. Evans, J. Mat. Sci. Letters, 2 (1983) 19.
54. S. Hampshire, K.H. Jack, Special Ceramics 7, ed. P. Popper, BCRA, 1981, pg 37.
55. F.F. Lange, "Progress in Nitrogen Ceramics", ed. F.L. Riley, Nijhoff, 1983, pg 467.
56. R.R. Wills, M.C. Brockway, L.G. McCoy, Mat. Sci. and Res., 17 (1984) 559.
57. H. Okeda, K. Homma, T. Fujikawa, T. Kanda, "High Tech Ceramics" ed. P. Vincenzini, Elsevier, 1987, pg 1023.
58. H.T. Larker, Mat. Sci and Res., 17 (1984) 572.
59. M. Shimada, N. Uchida, M. Koizumi, Mat. Sci and Res., 17 (1984) 583.
60. R.R. Wills, M.C. Brockway, G.K. Bansal, Mat. Sci and Res., 17 (1984) 597.
61. S. Wild, P. Grievson, K.H. Jack, Special Ceramics 5, ed. P. Popper, BCRA, 1971, pg 289.
62. K.H. Jack, W.I. Wilson, Nature, 238 (1972) 28.
63. Y. Oyama, Jap. J. Appl. Physics, 10 (1971) 1637.
64. M.B. Trigg, J. Austral. Ceram. Soc., 21 (1985) 24.
65. R.J. Lumby, B. North, A.J. Taylor, Special Ceramics 6, ed. P. Popper, 1974, pg 283.
66. M.H. Lewis, R.J. Lumby, Powder Metall, 26 (1983) 73.
67. K.H. Jack, J. Mat. Sci., 11 (1976) 1135.
68. S. Hampshire, H.K. Park, D.P. Thompson, K.H. Jack, Nature, 274 (1978) 880.
69. M.D. Thouless, A.G. Evans, Acta Metallurga, 34 (1986) 23.
70. G. Grand, J. Demit, J. Ruste, J.P. Torre, J. Mat. Sci. Letters, 14 (1979) 1749.
71. M. Mitomo, F. Izumi, Y. Bando, Y. Sehikawa, Proc. of Int. Symposium on Ceram. Comp. for engines, 1983, pg 377.
72. F. Izumi, M. Mitomo, Y. Bando, J. Mat. Sci., 19 (1984) 3115.
73. F. Izumi, M. Mitomo, J. Suzuki, J. Mat. Sci. Letters, 1 (1982) 533.

74. M.H. Lewis, C.J. Reed, N.D. Butler, Mat. Sci and Eng., 71 (1985) 87.
75. M.B. Trigg, K.H. Jack, Proc. of Int. Sym. on Ceram. Comp. for Eng., Hakone, Japan, 1983, pg. 199.
76. S.M. Wiederhorn, N.J. Tighe, J. Am. Ceram. Soc., 66 (1983) 884.
77. D.R. Clarke, Ultramicroscopy, 4 (1979) 33.
78. L.K.V. Lou, T.E. Mitchell, A.H. Heuer, J. Am. Ceram. Soc., 61 (1978) 392.
79. D.R. Clarke, J. Am. Ceram. Soc., 70 (1987) 15.
80. T.M. Shaw, J. Am. Ceram. Soc., 62 (1979) 585.
81. D. Cubicciotti, K.H. Lau, J. Am. Ceram. Soc., 61 (1978) 512.
82. C. Wabner, J. Appl. Phys. 29 (1958) 1295.
83. S.C. Singhal, Ceramurgia Int., 2 (1976) 123.
84. M. Billy, 'Progress in Nitrogen Ceramics' ed. F.L. Riley, Martinus Nijhoff, 1983, pg 403.
85. R.W. Davidge, A.G. Evans, D. Gilling, P.R. Wilyman, Special Ceramics 5, ed. P. Popper, BCRA, 1971, pg 329.
86. T. Hirai, K. Niihara, T. Goto, J. Am. Ceram. Soc., 63 (1980) 419.
87. S.C. Singhal, J. Mat. Sci., 11 (1976) 500.
88. P. Vincenzini, G. Babini, 'Sintered Metal-Ceramic Composites', ed. G.S. Upadhyaya, Elsevier, 1984, pg 425.
89. W.E. Borbidge, R.V. Allen, P.T. Whelan, J. de Physique, 47 (1986) C1-131.
90. G.N. Babini, A. Bellosi, P. Vincenzini, J. Mat. Sci., 18 (1983) 231.
91. C.C. Wu, K.R. McKinney, R.W. Rice, W.J. McDonough, S.W. Freiman, J. Mat. Sci., 16 (1981) 3099.
92. G.N. Babini, A. Bellosi, P. Vincenzini, J. Mat. Sci., 19 (1984) 3487.
93. G.N. Babini, A. Bellosi, P. Vincenzini, J. Mat. Sci., 19 (1984) 1029.
94. F.F. Lange, B.I. Davis, H.C. Graham, Comm. J. Am. Ceram. Soc., 66 (1983) C98.
95. F.F. Lange, Bull. Am. Ceram. Soc., 62 (1983) 1369.
96. F.F. Lange, J. Am. Ceram. Soc., 61 (1978) 270.
97. M.H. Lewis, P. Barnard, J. Mat. Sci., 15 (1980) 443.
98. F.J. Galasso, R.D. Veltri, Comm. J. Am. Ceram. Soc., 64 (1981) C15.
99. M.H. Lewis, S. Mason, A. Szweda, Proc. Conf. on Non-oxide Technical and Engineering Ceramics, ed. S. Hampshire, Elsevier, 1985, pg 175.
100. C.E. Inglis, Trans. Inst. Naval Archit., 55 (1913) 219.
101. A.A. Griffith, Phil. Trans. R. Soc., London, A221 (1920) 163.
102. G.R. Irwin, J. Welding, 31 (1952) 450.
103. R. Maugis, J. Mat. Sci., 20 (1985) 3041.
104. M. Leon, P. Kittl, J. Mat. Sci., 20 (1985) 3778.
105. J.L. Henshall, D.J. Rowcliffe, J.W. Edington, J. Mat. Sci., 9 (1974) 1559.
106. G.R. Anstis, P. Chantikul, B.R. Lawn, D.B. Marshall, J. Am. Ceram. Soc., 64 (1981) 533.
107. P. Chantikul, G.R. Anstis, B.R. Lawn, D.B. Marshall, J. Am. Ceram. Soc., 64 (1981) 540.
108. K.Y. Chia, S.G. Seshadri, M. Srinivasan, Ceram. Eng. and Sci. Proc., 7 (1986) 795.
109. M. Srinivasan, S.G. Seshadri, "Fracture Mechanics for ceramics, rocks and concrete', ed. Frieman and Fuller, ASTM STP, 745 (1981) 46.

110. F.F. Lange, J. Am. Ceram. Soc., 56 (1973) 518.
111. S.C. Danforth, M.H. Richman, Bull. Am. Ceram. Soc., 62 (1983) 501.
112. R.K. Goliva, J. Mat. Sci., 20 (1985) 4345.
113. W.A. Sanders, D.M. Mieskowski, Bull. Am. Ceram. Soc., 64 (1985) 304.
114. S.S. Campbell, S. Dutta, Bull. Am. Ceram. Soc., 61 (1982) 854.
115. A. Tsuge, K. Nishida, M. Komatsu, J. Am. Ceram. Soc., 58 (1975) 323.
116. S.H. Knickerboker, A. Zangvil, S.D. Brown, Comm. J. Am. Ceram. Soc., 68 (1985) C99.
117. J.Y. Laval, C. Delamarre, M.C. Amamra, D. Broussaud, J. Mat. Sci., 20 (1985) 381.
118. R.W. Rice, K.R. McKinney, C.C. Wu, S.W. Frieman, W.J.M. Donough, J. Mat. Sci., 20 (1985) 1392.
119. G. Orange, J.C. Glandus, G. Fantuzzi, P. Boch, Proc. 4th European Conf. on Fracture, Leoben, Austria, 2, (1982) 609.
120. T.E. Easter, R.C. Bradt, R.E. Tressler, J. Am. Ceram. Soc., 65 (1982) 317.
121. L.A. Pierce, D.M. Mieskowski, W.A. Sanders, J. Mat. Sci., 21 (1986) 1345.
122. R.L. Tsai, R. Raj, J. Am. Ceram. Soc., 63 (1980) 513.
123. A.G. Evans, S.M. Weiderhorn, J. Mat. Sci., 9 (1974) 2070.
124. F.F. Lange, Comm. J. Am. Ceram. Soc., 65 (1982) C23.
125. B.S.B. Karunaratne, M.H. Lewis, J. Mat. Sci., 15 (1980) 449.
126. B.S.B. Karunaratne, M.H. Lewis, J. Mat. Sci., 15 (1980) 1781.
127. M.H. Lewis, G.R. Heath, S.M. Winder, R.J. Lumby, "Deformation of Ceramics II", Plenum Press, 1984, pg 605.
128. A. Tsuge, K. Nishida, Bull. Am. Ceram. Soc., 57 (1978) 424.
129. J.T. Smith, C.L. Quackenbush, Bull. Am. Ceram. Soc., 59 (1980) 529.
130. D.P.H. Hasselman, "Deformation of Ceramics II", Plenum Press, 1984, pg .
131. W.R. Cannon, T.G. Langdon, J. Mat. Sci., 18 (1983).
132. F.F. Lange, 'Progress in Nitrogen Ceramics', ed. F.L. Riley, Nijhoff, 1983, pg 467.
133. M.S. Seltzer, J. Am. Ceram. Soc., 58 (1977) 418.
134. F.F. Lange, B.I. Davis, D.R. Clarke, J. Mat. Sci., 15 (1980) 601.
135. F.F. Lange, B.I. Davis, D.R. Clarke, J. Mat. Sci., 18 (1983) 1497.
136. R.M. Arons, J.K. Tien, J. Mat. Sci., 15 (1980) 2046.
137. J.L. Besson, E. Streicher, T. Chartier, P. Goursat, J. Mat. Sci. Letters, 5 (1986) 803.
138. D.A. Bonnell, T.Y. Tien, M. Ruhle, J. Am. Ceram. Soc., 76 (1987) 460.
139. R. Kossowsky, J. Mat. Sci., 8 (1973) 1603.
140. R.L. Coble, J. Appl. Phys., 34 (1963) 1679.
141. R.L. Coble, J. App. Phys., 41 (1970) 4798.
142. A.G. Evans, W. Blumenthal, 'Francture Mechanics of Ceramics Vol. 6' ed. R.C. Bradt, A.G. Evans, D.P.H. Hasselman, F.F. Lange, Plenum, 1983, pg 423.
143. T.J. Chuang, K.I. Hagawa, J.R. Rice, L.B. Sills, Acta Metall., 27 (1979) 265.
144. B.J. Dalgleish, S.M. Johnson, A.G. Evans, J. Am. Ceram. Soc., 67 (1984) 741.
145. W. Blumenthal, A.G. Evans, J. Am. Ceram. Soc., 67 (1984) 751.
146. S.M. Johnson, B.J. Dalgleish, A.G. Evans, J. Am. Ceram. Soc., 67 (1984) 759.

147. D.C. Larsen, Progress Report, AFML/IITRI, Contract F33615-7SC-5196, 1977.
148. G.D. Quinn, Ceram. Eng. and Sci. Proc., 3 (1982) 77.
149. G.D. Quinn, AMMRC-TR-84-40, 1984.
150. R. Nathan-Katz, G.D. Quinn, 'Progress in Nitrogen Ceramics' ed. F.L. Riley, Nijhoff, 1983, pg 491.
151. G.D. Quinn, L. Swank, Comm. J. Am. Ceram. Soc., 66 (1983) C31.
152. G.D. Quinn, J. Mat. Sci., 22 (1987) 374.
153. G.G. Trantina, J. Am. Ceram. Soc., 62 (1979) 377.
154. M.D. Thouless, A.G. Evans, Acta. Metall., 34 (1986) 23.
155. M.D. Thouless, C.H. Hsueh, A.G. Evans, Acta Metall., 31 (1983) 1675.
156. M.H. Hawman, P.H. Cohen, J.C. Conway, R.N. Pangborn, J. Mat. Sci., 20 (1985) 482.
157. D. Johnson-Walls, A.G. Evans, D.B. Marshall, M.R. James, J. Am. Ceram. Soc., 69 (1986) 44.
158. J.M. Birch, B. Wilshire, D.J.R. Owen, D. Shantaram, J. Mat. Sci., 11 (1976) 1817.
159. A. Crosby, P.E. Evans, J. Mat. Sci., 8 (1973) 1573.
160. G.W. Hollenberg, G.R. Terwilliger, R.S. Gordon, J. Am. Ceram. Soc., 54 (1971) 196.
161. Z.K. Huang, P. Greil, G. Petzow, Comm. J. Am. Ceram. Soc., 66 (1983) C96.
162. K.H. Jack, 'Progress in Nitrogen Ceramics', ed. F.L. Riley, Nyhoff, 1983, pg 45.
163. G. Leng-Ward, M.H. Lewis, Mat. Sci. and Eng., 71 (1985) 101.
164. C.J. Spacie, N.S. Jameel, D.P. Thompson, Proc. of Int. Syn. on Ceram. Comp. for Engines, 1983, pg 343.
165. C. Chatfield, T. Ekstrom, M. Mikus, J. Mat. Sci., 21 (1986) 2297.
166. S. Hampshire, R.A.L. Drew, K.H. Jack, Comm. J. Am. Ceram. Soc., 67 (1984) C46.
167. R.K. Brow, C.G. Pantano, Comm. J. Am. Ceram. Soc., 67 (1984) C72.
168. G. Thomas, C. Ahn, Comm. J. Am. Ceram. Soc., 65 (1982) C185.
169. S.M. Winder, M.H. Lewis, J. Mat. Sci. Letters,
170. P. Drew, M.H. Lewis, J. Mat. Sci., 9 (1974) 1833.
171. P.W. McMillan, 'Glass-Ceramics', Academic Press, London, 1979.
172. G.R. Heath, Ph.D. Thesis, University of Warwick, 1986.
173. S.M. Winder, Ph.D. Thesis, University of Warwick, 1986.
174. C. Jasper, Private Communication.
175. W. Weibull, J. Applied Mechanics, 18 (1951) 293.
176. C.J. Reed, M.Sc. Thesis, Univeristy of Warwick, 1987.
177. V. Dworak, H. Olapinski, Ceramics for high performance application,s III: Reliability, 1983, pg 773.
178. F.F. Lange, J. Am. Ceram. Soc., 63 (1980) 38.
179. S.M. Wiederhorn, E.R. Fuller, Mat. Sci. and Eng., 71 (1985) 169.
180. D.R. Clarke, J. Am. Ceram. Soc., 66 (1983) 156.
181. R.A. Miller, S.R. Levine, S. Stecura, American Inst. of Aeronautics paper no. AIAA-80-302, 1980.
182. K. Allaert, A. van Calster, H. Loos, A. Leguesne, J. Electrochem. Soc., 132 (1985) 1763.
183. F. Fujita, H. Toyoshima, T. Ohishi, A. Sakaki, Jpn. J. Appl. Phys., 23 (1984) L144.
184. Idem, ibid, 23 (1984) L268.
185. A. Matsuda, K. Yagi, T. Kaga, K. Tanaka, ibid, 23 (!984) 1209.
186. K. Niihara, T. Hirai, J. Mat. Sci., 11 (1976) 593.

187. D.R. Biswas, J. Mat. Sci., 21 (1986) 2217.
188. K. Oda, T. Yoshio, K. O-Oka, Comm. J. Am. Ceram. Soc., 66 (1983) C-8.
189. S. Motojima, N. Iwamori, T. Hattori, J. Mat. Sci., 21 (1986) 3836.
190. O.J. Gregory, M.H. Richman, Comm. J. Am. Ceram. Soc., 67 (1984) C335.

APPENDIX

```
  10 REM++CREEP++TAPE-VERSION=4++NICK 11-85
  20 IFNOT(PAGE=&1C00)THENPRINT"TRY SETTING PAGE=&1C00!":STOP
  30 VDU4,26:MODE0:@%=10
  40 *FX230,0
  50 ?&FE62=0:?&FE6B=0:?&FE6C=192
  60 DIM XPOS%(1,1),YPOS%(1,1),F%(1),DO%(1),TO%(1),R%(1),A%(1)
  70 VDU28,0,2,79,0,24,0;0;1279;927;12,16
  80 PROCAXES
  90 REPEAT
 100 VDU23;11,0;0;0;0;12
 110 PRINT "S - START FILE  Q - QUIT"
 120 Q$=GET$
 130 IF Q$="S"THEN PROCSTART
 140 UNTIL Q$="Q"
 150 VDU23;11,255;0;0;0;12,10:PRINT"PROGRAM TERMINATED"
 160 END
 170 DEF PROCAXES
 180 VDU29,0;0;5,25,4,99;40;25,5,99;920;25,4,99;40;25,5,1279;40;
 190 XPOS%=87:FORI%=1TO5:XPOS%=XPOS%+236:VDU25,4,XPOS%;60;33:NEXT
 200 YPOS%=52:FORI%=1TO5:YPOS%=YPOS%+176:VDU25,4,99;YPOS%;45:NEXT
 210 XPOS%=79:FORI%=1TO4:XPOS%=XPOS%+236:VDU25,4,XPOS%;25;:PRINT;20*I%:NEXT
 220 YPOS%=47:FORI%=1TO5:YPOS%=YPOS%+176:VDU25,4,40;YPOS%;:PRINT;20*I%:NEXT
 230 @%=10:VDU4,29,99;40;
 240 VDU5,25,4,50;850;25,1,20;0;32,82,105,103,35,32,49,25,4,50;815;25,17,20;0;3
2,82,105,103,35,32,50,25,4,35;770;25,1,0;105;25,1,550;0;25,1,0;-105;25,1,-550;0;
4
 250 ENDPROC
 260 DEF PROCSTART
 270 VDU15,25,4,0;0;
 280 *FX140,0
 290 INPUT"TIME BETWEEN READINGS (MINS) "J
 300 PROCFILE
 310 J%=J*6000
 320 PROCHILO:IF(HI AND 192)DIV64<3THEN320
 330 TIME=0:T%=0:A%(0)=&C00:A%(1)=&C04:TO%(1)=J%:E%=0
 340 *FX12,1
 350 FOR Z%=1TO2
 360 FOR Z1%=1TO2
 370 PROCHILO:TIM%=TIME-TO%(X%):IF OVR%=1THENPRINT;CHAN%;MID$(" UNDER  OVER",6*
POL%+1,6);"-RANGE  ";
 380 PROCDRAW:PROCSTORE
 390 NEXTZ1%
 400 N%=0:M%=0:R%(X%)=HRS DIV125
 410 REPEAT
 420 IF(TIME+100)>(T%+J%) OR TIME<(T%+E%)THEN460
 430 @%=&303:VDU5:FORA%=0TO1:S%=(TIME-TO%(A%))/100:IFS%<0THENS%=0
 440 VDU25,4,470;820-35*A%;25,0,-145;0;25,83,145;30;25,83,-145;0;:PRINTS%DIV36(
0;":";(S%DIV60)MOD60;":";S%MOD60:NEXT
 450 S%=(J%-E%)/100:VDU25,4,575;785;25,0,-100;0;25,83,100;65;25,83,-100;0;25,0,
0;(1-Z%)*35;:PRINTS%DIV60;":";S%MOD60:VDU4:@%=10:E%=E%+100
 460 IF INKEY(-114) OR R%(0)=1 THEN PROCLABEL0
 470 IF INKEY(-115) OR R%(1)=1 THEN PROCLABEL1
 480 IF INKEY(-116) THEN PRINT"CLOSING ";A$:CLOSE#0:PROCFILE
 490 IF INKEY(-33) THEN VDU5:FORA%=0TO1:PROCHILO:VDU25,4,300;820-35*X%;25,0,-90
;0;25,83,90;30;25,83,-90;0;:PRINTSTR$(DTA%);"!":PROCHILO:NEXT:VDU4
 500 UNTIL TIME>=(T%+J%)
 510 T%=T%+J%:E%=0
 520 IF N%+M%>0THENTIME=TIME-TO%(1-X%):T%=T%-TO%(1-X%):TO%(X%)=TO%(X%)-TO%(1-X%
):TO%(1-X%)=0
 530 NEXTZ%
 540 GOTO 350
 550 ENDPROC
```

```
  560 DEF PROCSTORE
  570 HRS=TIM%/360000
  580 D$=(STR$(CHAN%)+STR$(DTA%))
  590 T$=(STR$(CHAN%)+STR$(TIM%))
  600 VDU2:PRINTLEFT$(D$,1);TAB(5);RIGHT$(D$,(LEN(D$)-1));TAB(12);LEFT$(T$,1);TA
B(20);HRS:VDU3
  610 PRINT£X1,D$,T$
  620 ENDPROC
  630 DEF PROCHILO
  640 ?&FE6C=240:?&FE6D=144
  650 X=(?&FE6D AND 16):IF X=0 THEN650
  660 LO=?&FE60
  670 ?&FE6C=192:?&FE6D=144
  680 X=(?&FE6D AND 16):IF X=0 THEN680
  690 HI=?&FE60
  700 CHAN%=(HI AND 192)DIV64:POL%=(HI AND 32)DIV32:OVR%=(HI AND 16)DIV16:DTA% =
(HI AND 15)*256+LO:X%=(HI AND 128)DIV128
  710 IF OVR%=1THEN DTA%=4096
  720 IF POL%=0 THEN DTA%=-DTA%
  730 ENDPROC
  740 DEF PROCDRAW
  750 IF (HI AND 64)DIV64=1 THEN ENDPROC
  760 VDU25,4,300;820-35*X%;25,0,-90;0;25,83,90;30;25,83,-90;0;5:PRINTSTR$(DTA%)
:VDU4
  770 DTA%=-(DTA%+4096)
  780 IF F%(X%)=0 THEND0%(X%)=DTA%:F%(X%)=1
  790 YPOS%(1,X%)=INT((((DTA%-D0%(X%))*0.25)/100)*880)
  800 XPOS%(1,X%)=INT((TIM%/36000000)*1180)
  810 VDU25,4,XPOS%(0,X%);YPOS%(0,X%);25,5+24*X%,XPOS%(1,X%);YPOS%(1,X%);
  820 XPOS%(0,X%)=XPOS%(1,X%):YPOS%(0,X%)=YPOS%(1,X%)
  830 IFA%(X%)<&1BF8THEN!A%(X%)=XPOS%(1,X%)+&10000*YPOS%(1,X%):A%(X%)=A%(X%)+8
  840 ENDPROC
  850 DEF PROCLABEL0
  860 IF N%=1THEN ENDPROC
  870 X%=0:T0%(0)=T%+(3-Z%)*J%
  880 LOCAL DT$,TI$
  890 DT$=STR$(-95990):TI$=STR$(TIME/360000)
  900 PRINT£X1,DT$,TI$
  910 N%=1:XPOS%(0,0)=0:YPOS%(0,0)=0:F%(0)=0:R%(0)=0
  920 CLG:PROCAXES:A%(0)=&C00
  930 VDU25,4,!&C04 MOD&10000;!&C04 DIV&10000;
  940 FOR A%=&C0C TOA%(1)-8 STEP8:VDU25,29,!A% MOD&10000;!A% DIV&10000;:NEXT
  950 ENDPROC
  960 DEF PROCLABEL1
  970 IF M%=1THEN ENDPROC
  980 X%=1:T0%(1)=T%+Z%*J%
  990 LOCAL DT$,TI$
 1000 DT$=STR$(-95992):TI$=STR$(TIME/360000)
 1010 PRINT£X1,DT$,TI$
 1020 M%=1:XPOS%(0,1)=0:YPOS%(0,1)=0:F%(1)=0:R%(1)=0
 1030 CLG:PROCAXES:A%(1)=&C04
 1040 VDU25,4,!&C00 MOD&10000;!&C00 DIV&10000;
 1050 FOR A%=&C08 TOA%(0)-8 STEP8:VDU25,5,!A% MOD&10000;!A% DIV&10000;:NEXT
 1060 ENDPROC
 1070 DEF PROCFILE
 1080 *FX21,0
 1090 INPUT"FILENAME ";A$:IFA$=""ORLEN(A$)>10THENCLS:PRINT"Silly":GOTO1080
 1100 *FX138,0,13
 1110 X1=OPENOUT(A$)
 1120 VDU2,10:PRINT"FILENAME - "A$:VDU10
 1130 PRINT"CHAN";TAB(5);"DATA";TAB(11);"CHAN";TAB(20);"TIME"
 1140 PRINT"_____":VDU10,3
 1150 ENDPROC
```

```
  5 REM CRAP PROGRAM WITH MODIFIED STRAIN-RATE CALCULATING PROCEDURE 12/2/86
 10 *XON 16
 20 MODE0
 30 DIM F%(1,750),TI(2),MIC(2),E(20)
 40 @%=10:G%=1
 50 INPUT"Specimen Length (mm) ? "L
 60 VDU26,28,0,2,79,0,24,0,0;1279;927;12,16
 70 INPUT"Max Y (um) ";Y%:PROCAXES
 80 REPEAT
 90 VDU23;11,0;0;0;0;12
100 PRINT" G - Get File      C - Display Cursor      R - Reset":PRINT" S - Sav
e File     M - Smooth File          Q - Quit";
110 C%=GET:IFC%=71 THEN PROCGET
120 IFC%=83 THEN PROCSAVE
130 IFC%=77 THEN PROCSMOOTH
140 IFC%=67 THEN PROCCURSOR
150 IFC%=82 THEN 60
160 UNTIL C%=81
170 VDU12:PRINT" Program Terminated":VDU23;11,255;0;0;0;:END
180 DEF PROCAXES
190 VDU29,0;0;5,25,4,99;40;25,5,99;920;25,4,99;40;25,5,1279;40;
200 XPOS%=87:FORC%=1TO5:XPOS%=XPOS%+236:VDU25,4,XPOS%;60;33:NEXT
210 YPOS%=52:FORC%=1TO5:YPOS%=YPOS%+176:VDU25,4,99;YPOS%;45:NEXT
220 XPOS%=-50:FORC%=1TO4:XPOS%=XPOS%+236:VDU25,4,XPOS%;25;:PRINT20*C%:NEXT
230 YPOS%=47:FORC%=1TO5:YPOS%=YPOS%+176:VDU25,4,-79;YPOS%;:PRINT20*C%*(Y%DIV10
0):NEXT
240 VDU4,29,99;40;
250 ENDPROC
260 DEF PROCDRIVE
270 INPUT"Drive No. "DR%:IF(DR%>3ORDR%<0)THEN280ELSE290
280 PRINT"Invalid Drive ! ! !":GOTO270
290 *DISC
300 ON DR%+1GOTO310,330,350,370
310 *DRIVE0
320 GOTO380
330 *DRIVE1
340 GOTO380
350 *DRIVE2
360 GOTO380
370 *DRIVE3
380 ENDPROC
390 DEF PROCCURSOR
395ST=32
400 XPOS%=638:NUMOFENTS%=0:VDU12:PRINT"Use <- keys -> to position cursor":PRIN
T"press 'COPY' key to enter value";
410 *FX4,1
420 *FX12,5
425VDU25,4,638;0;25,6,638;920;
430 REPEAT
440 @%=131594:PRINTTAB(72,0);(XPOS%/1174)*100;:@%=10
450 *FX21,0
460 C%=GET:IF(C%<135 AND C%>140)THEN450
464IFC%=139 THENST=ST*2:GOTO450
468IFC%=138 THENST=ST/2:GOTO450
470 VDU25,4,XPOS%;5;25,6,XPOS%;920;
480 IFC%=136THENXPOS%=XPOS%-ST:VDU25,4,XPOS%;5;25,6,XPOS%;920;
490 IFC%=137THENXPOS%=XPOS%+ST:VDU25,4,XPOS%;5;25,6,XPOS%;920;
500 IFC%=135THENPROCENTERVAL
510 UNTILNUMOFENTS%=2
520 *FX12,0
530 *FX4,0
540 PROCRATE
550 ENDPROC
```

```
  560 DEF PROCENTERVAL
  570 IFNUMOFENTS%=0THENCLS
  580 P%=INT(((XPOS%-99)/1180)*400):MIC(NUMOFENTS%)=ABS(F%(1,P%)*0.244):TI(NUMOF
ENTS%)=(XPOS%*100)DIV1180
  590 IFP%=0THENP%=1
  600 PRINTMIC(NUMOFENTS%),TI(NUMOFENTS%):NUMOFENTS%=NUMOFENTS%+1
  620 ENDPROC
  630 DEF PROCGET
  640 REM ONERRORGOTO720
  650 VDU29,100;40;12:I%=1
  660 INPUT"Filename - "W$
  670 PROCDRIVE:FORC%=1TO500:F%(0,C%)=0:F%(1,C%)=0:NEXT:PRINT"Inputting Data";
  680 DA=OPENIN(W$)
  690 REPEAT:INPUT£DA,F%(1,I%),F%(0,I%)
  700 I%=I%+1
  710 UNTIL EOF£DA
  720 CLOSE£DA
  730 PROCDRAW
  740 ENDPROC
  750 DEF PROCDRAW
  760 VDU25,4,0;0;:FORC%=1TOI%-1:YPOS%=ABS(INT((((F%(1,C%)-F%(1,1))*0.244)/Y%)+9
80)):XPOS%=INT((F%(0,C%)/36000000)*1179):VDU25,13,XPOS%;YPOS%;:NEXT:VDU25,4,0;0;
  770 ENDPROC
  780 DEF PROCSMOOTH
  790 VDU29,0;0;12:PRINT"Smoothing Data";
  800 FORC%=6TOI%-6:F%(1,C%)=(F%(1,C%-5)+F%(1,C%+5))DIV2:NEXT
  810 VDU12,16:PROCAXES:PROCDRAW:PRINT"Do you wish to save data on disc ?";
  820 A$=GET$:IFA$="N"THENENDPROC
  830 IFA$<>"Y"THEN820:PROCSAVE
  840 ENDPROC
  850 DEF PROCSAVE
  860 VDU12:INPUT"Filename ";W$:PROCDRIVE:PRINT"Writing Data"
  870 DA=OPENOUT(W$)
  880 FORC%=1TOI%-1:F%(1,C%)=-(F%(1,C%)*10):PRINT£DA,F%(1,C%),F%(0,C%):NEXT
  890 CLOSE£DA
  900 *DRIVE0
  910 ENDPROC
  920 DEF PROCRATE
  930 E0=(MIC(0)/L)*1E-3:E1=(MIC(1)/L)*1E-3:TI(0)=TI(0)*3600:TI(1)=TI(1)*3600:E(
G%)=ABS((E1-E0)/(TI(1)-TI(0))):PRINT;" ";G%,E(G%),LN(E(G%))
  940 IFG%=20THEN980
  950 PRINT"Do you wish to save on disc (y or n)"
  960 A$=GET$:IFA$="N"THEN1020
  970 IFA$<>"Y"THEN960
  980 VDU12:INPUT"Filename "W$:PROCDRIVE:PRINT"Writing Data";
  990 DA=OPENOUT(W$)
 1000 FORC%=1TOG%:PRINT£DA,E(C%):NEXT
 1010 CLOSE£DA:*DRIVE0
 1020 G%=G%+1
 1030 ENDPROC
```